THE PHYSICAL REVIEW

VOLUME 76 *Second Series* NUMBER 5

SEPTEMBER 1, 1949

Published for the

AMERICAN PHYSICAL SOCIETY

by the

AMERICAN INSTITUTE OF PHYSICS

Incorporated

LANCASTER, PA., AND NEW YORK, N. Y.

THE PHYSICAL REVIEW

A journal of experimental and theoretical physics established by E. L. Nichols in 1893

Published by the American Institute of Physics for the

AMERICAN PHYSICAL SOCIETY

Officers

President

F. W. Loomis
University of Illinois
Urbana, Illinois

Vice-President

I. I. Rabi
Columbia University
New York, New York

Secretary

K. K. Darrow
Bell Telephone Laboratories
Office:
Columbia University
New York 27, New York

Treasurer

G. B. Pegram
Columbia University
New York 27, New York

Local Secretary for the Pacific Coast

J. Kaplan
University of California at Los Angeles
Los Angeles, California

Managing Editor

John T. Tate
University of Minnesota
Minneapolis, Minnesota

BOARD OF EDITORS

Editor

John T. Tate

Assistant Editor

J. W. Buchta

Associate Editors

H. A. Bethe — S. A. Goudsmit — W. E. Lamb, Jr.
L. A. Ridenour — E. M. Purcell — R. G. Herb
W. H. Zachariasen — V. F. Weisskopf — J. Bardeen

Manuscripts for publication should be submitted to John T. Tate, University of Minnesota, Minneapolis, Minnesota. The authors' institutions are requested to pay a publication charge of $4 per page which, if honored, entitles them to 100 free reprints. Instructions will be sent with galley proofs.

Proof and all correspondence concerning papers in the process of publication should be addressed to the Publication Manager, American Institute of Physics, 57 East 55 Street, New York 22, New York.

Subscription Price

United States and Canada $25.00
Elsewhere $27.00

Back Numbers[1]

Yearly back number rate when complete year is available:
Prior to 1949: $20.00
Thereafter: $27.00
Single copies: $2.00 each, prior to July, 1929;
$1.00 each, July, 1929–December, 1941;
$2.00 each, January, 1942–December, 1946;
$1.00 each, January, 1947–December, 1948.
Current issues: $1.25 each.
General index, 1893–1920: $4.00.

Subscriptions and orders for back numbers should be addressed to Prince and Lemon Streets, Lancaster, Pennsylvania, or to the American Institute of Physics, 57 East 55 Street, New York 22, New York.

Changes of address in the case of members of the American Physical Society should be addressed to the Treasurer; in the case of other subscribers to the Business Manager, American Institute of Physics.

[1] For Series 1 inquire of Physics Department, Cornell University, Ithaca, New York.

The Physical Review is published semi-monthly at Prince and Lemon Streets, Lancaster, Pennsylvania.

Entered as second-class matter March 6, 1917, at the Post Office at Lancaster, Pennsylvania, under the Act of March 3, 1879.

Acceptance for mailing at special rate of postage provided for in paragraph 4, section 538, P. L. & R., authorized January 27, 1933.

THE
PHYSICAL REVIEW

A journal of experimental and theoretical physics established by E. L. Nichols in 1893

SECOND SERIES, VOL. 76, NO. 5 SEPTEMBER 1, 1949

U-235 Gamma-Radiation

R. L. MACKLIN
K-25 Research Laboratories, Carbide and Carbon Chemicals Corporation, Oak Ridge, Tennessee
(Received April 28, 1949)

Evidence for the existence of a gamma-ray accompanying the alpha-decay of U-235 is presented. The energy of the gamma-ray, as determined by several independent absorption measurements, is 162 kev.

INTRODUCTION

THE three naturally occurring uranium isotopes, U-234, U-235, and U-238, are spontaneous alpha-emitters. In a previous report[1] it was shown that the U-234 alpha-decay is accompanied by x-rays, and the present paper reports the discovery and measurement of gamma-rays accompanying the alpha-decay of U-235. The 162 kev gamma-ray found associated with the U-235 decay was discovered and clearly identified at this laboratory in April 1946.[2] A similar radiation was observed somewhat earlier at the University of Chicago, but was attributed to U-234.

Discovery of the Gamma-Radiation

Sample Preparation

The significant steps in the purification of the samples of U-235 used were as follows. The bulk of the radioactive and other impurities were removed by ether extraction of uranyl nitrate from a nitric acid solution of the original ore. Reduction and precipitation of the uranium as UF_4 probably removed few impurities other than the very volatile fluorides such as silicon tetrafluoride. The precipitated, dried UF_4 was then converted with gaseous fluorine to the volatile UF_6, which was purified by condensation and re-evaporation. The UF_6 gas was then passed through a great many fine pored filters which increased by isotopic separation the proportion of U-235 to about one-third, and the UF_6 was then condensed directly into a clean, uncontaminated nickel cylinder with quarter-inch walls. It is felt that no radioactive materials except U-234, U-235, U-238, and insignificant traces of radon were present at the time of condensation into the sample cylinder.

Radiation

A large sample of solid U-235 enriched UF_6 in a quarter-inch wall nickel cylinder was placed at a standard distance (about six inches) from a screen wall Geiger counter. An initial activity of about 1000 c/m was observed. Superimposed on this was a growing activity of 24 day half-life (UX_1, UX_2, and UZ), extrapolating to 300–400 c/m at equilibrium. To prove that a residue of the non-volatile fluoride of UX_1, possibly swept through the filters and condensed with the sample, was not the cause of the initial 1000 c/m activity, a sample of natural uranium was examined. This was prepared in the same manner as the preceding sample but was passed through only a single filter with somewhat larger pores. The initial gamma-activity of this sample was only slightly above background (net rate 24 c/m) and increased with a 24-day half-life toward 500 c/m. Since this sample contained half again as much U-238, parent of the UX_1, UX_2, and UZ, as the enriched sample, the equilibrium activity of the latter sample should have been about 330 c/m. The initial activity found then (1000 c/m) was clearly not attributable to UX_1 inclusion in the sample of enriched uranium to the extent of more than a few percent. Indeed, the initial activity (24 c/m) of the natural uranium sample with much poorer filtration led to the expectation that UX_1 dust carry over in the enriched UF_6 sample was entirely negligible.

[1] R. L. Macklin and G. B. Knight, Phys. Rev. 72, 435 (1947).
[2] R. L. Macklin and W. S. Miller, Uranium Project Report A-3640.

Energy of the Radiation

A gram sample of nearly pure U-235F_4 was used for preliminary absorption measurements. These showed a prominent gamma-ray component at about 162 kev.

For more accurate measurements, UF_6 samples such as those described above were hydrolyzed and heated to give U_3O_8 powder. This was spread on sample holders in a thin layer of measured mass. Samples of enriched uranium (one-third U-235, two-thirds U-238) were prepared at the same time and made up with equal quantities of U-238. Thus, the gamma- and beta-rays of UX_1, UX_2, and UZ at any time were equal for a pair of samples. Hence, the difference in counting rate of a pair corresponded to a known quantity of U-235 (or U-234). Absorption measurements with both lead and aluminum were made at these laboratories and later (July, 1946) at Clinton National Laboratories. The 162 kev gamma-radiation was confirmed (see Fig. 1) and two weaker radiations corresponding to *L* and *M* x-rays

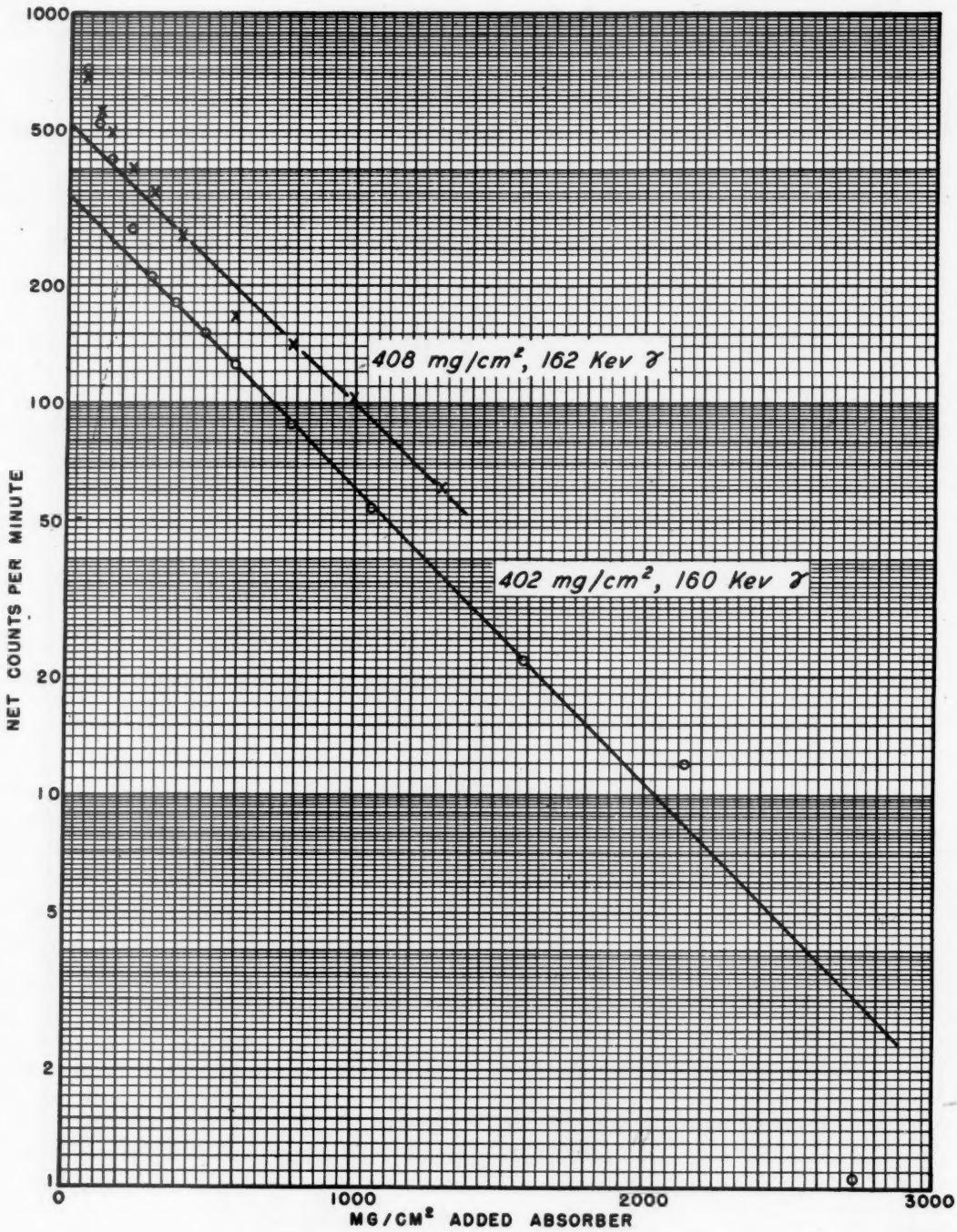

FIG. 1. Two Pb absorption curves of U-235 by difference (see text).

were found. These latter were later shown to be associated with U-234 (see reference 1).

The yield of gamma-rays per alpha-disintegration can be only roughly estimated. Values near 100 percent of the U-235 alpha-disintegration rate seem most reasonable although the gamma-counter efficiencies are so poorly known as to make this little more than a guess. One type counter yielded estimates of 10–100 percent and another gave 125–250 percent.

Origin of the Radiation

To determine which uranium isotope gave rise to the gamma-activity observed, samples of varying composition were used. The experiments with natural and enriched uranium already described showed, of course, that the 162 kev gamma-activity was not proportional to the U-238 content. Two samples were obtained which were nearly equal in U-234 content but differed by a factor of three in U-235 content as shown by mass spectrometer. These samples were several months old and hence contained virtually equilibrium quantities of UX_1, UX_2, and UZ proportional to the U-238 present.

Using the previous results for the gamma-radiation relative intensities measured through a quarter-inch of nickel, the ratio of gamma-activities of these samples (through $\frac{1}{4}''$ of nickel) was predicted on the basis of two hypotheses. If the 162 kev gamma-activity were due to the U-234, the activity ratio should be 0.63 because of the difference in U-238, UX_1, UX_2, and UZ content of the two samples. However, if the 162 kev gamma-activity were due to the U-235, the ratio would be 2.32. The ratio observed was 2.31 ± 0.04. Hence, the gamma-ray appears definitely to be associated with U-235.

DISCUSSION

The high U-234 alpha-activity of available U-235 samples has made it impossible to observe alpha-gamma-coincidences or to discover U-235 alpha-rays unaccompanied by gamma-rays. Hence, experimental confirmation of the decay scheme proposed below is not at present available.

The alpha-decay of U-235 is supposed to lead in most, perhaps all, cases to an excited state of Th-231 (UY) which rapidly omits a 162 kev gamma-ray to reach the ground state. A half-life for de-excitation longer than ten minutes would have been readily observed. The conversion of the gamma-ray has not been detected and is probably slight.

The decay of UY(Th-231) from its ground state has been investigated and reported separately.[3]

This document is based on work performed for the AEC by Carbide and Carbon Chemicals Corporation, at Oak Ridge, Tennessee.

[3] G. B. Knight and R. L. Macklin, Phys. Rev. **75**, 34 (1949).

On Penetrating Showers in Cosmic Radiation

H. A. MEYER, G. SCHWACHHEIM, A. WATAGHIN, AND G. WATAGHIN
Departamento de Fisica, Universidade de São Paulo, São Paulo, Brasil

(Received April 14, 1949)

The mean range of the radiation that generates penetrating showers has been determined in the atmosphere and in water. The results are respectively ~120 g/cm² and ~55 g/cm². The relation between the observed variation of the frequency of penetrating showers with barometric pressure and the absorption law in air for the shower producing radiation has been discussed in some detail. The east–west asymmetry of the radiation that generates penetrating showers has been studied and the results were found to be negative within the experimental errors. The penetrating power of the penetrating showers produced in air has been investigated. No appreciable absorption has been found when the lead protection of the counters has been increased from 18 to 28 cm.

INTRODUCTION

THE present work was done in order to study some of the problems related to penetrating showers in cosmic radiation. The experiments were performed at an altitude of 1750 m in Campos do Jordão from August to December 1948. We investigated the following problems: I. The altitude dependence of the frequency of meson showers. II. The absorption coefficient in water of the radiation that generates penetrating showers. III. The east–west asymmetry of the radiation responsible for penetrating showers. In addition, a complementary experiment to our work on the nature of the mesons in penetrating showers[1] has been performed.

In the following text we shall use the abbreviations *PS* for penetrating shower (meson shower) and *PSPR* for the penetrating shower-producing radiation.

I. DETERMINATION OF THE MEAN RANGE OF THE PSPR IN THE ATMOSPHERE

The study of the variation of the frequency of *PS* with altitude was initiated by Sala and Wataghin[2,3] and later continued by Wataghin.[4] They estimated the mean range of the *PSPR* to be ~100 g/cm², assuming an exponential decrease of the frequency of *PS* with atmospheric pressure. Tinlot,[5,6] working at a geomagnetic latitude of 53°N, confirmed that the dependence of the registered frequency on the barometric pressure is nearly an exponential one and found a mean range of 118±2 g/cm². The barometer effect of *PS* investigated by Janossy and Rochester[7] yields a mean range for the *PSPR* of 116±27 g/cm². The results of Janossy and Rochester can be related immediately to the measurements of the frequency of *PS* at different altitudes. Indeed, both types of experiments consist in measuring the frequency of *PS* at different barometric pressures. The variation of this pressure is obtained either by the meteorological fluctuations at a fixed altitude, or by working with the same apparatus at different altitudes.

TABLE I. Results of Experiment A.

Water thickness above the *PS* detector	Hourly rate of fourfold coincidences
0 cm	3.00±0.17
10 cm	3.59±0.20
22.5 cm	4.10±0.21
32.5 cm	4.87±0.24
42.5 cm	5.48±0.24
50 cm	5.16±0.37
58 cm	5.84±0.22
85 cm	5.11±0.16
114 cm	5.66±0.37
125 cm	5.37±0.17

The objective of the following discussions is to establish a relation between the registered variation of the frequency of *PS* with barometric pressure and the absorption law for a parallel beam of *PSPR*. In the first place, we ought to consider the generalized Gross-transformation.[8,9] We suppose that the conditions for the validity of the Gross-transformation are satisfied by the *PSPR*, i.e., we assume that there exists isotropy of the incident primary radiation at the top of the atmosphere, and that the *PSPR* does not suffer an appreciable deviation from its initial direction. In order to apply the generalized Gross-transformation we ought to know the efficiency of the *PS*-detector for each direction of incidence of the *PSPR*, but actually we can only say that the detectors used in the above experiments have a maximum of efficiency for the detection of vertical *PSPR*, so that the relative contribution of the inclined *PSPR* to the counting rate is less than for an isotropic detector (which registers the so-called integrated intensity).[10] As the intensity of the inclined radiation decreases with barometric pressure faster than the ver-

[1] Meyer, Schwachheim, Wataghin, and Wataghin, Phys. Rev. **75**, 908 (1949).
[2] O. Sala and G. Wataghin, Phys. Rev. **67**, 55 (1945).
[3] O. Sala and G. Wataghin, Phys. Rev. **70**, 430 (1946).
[4] G. Wataghin, Phys. Rev. **71**, 453 (1947).
[5] J. Tinlot, Phys. Rev. **73**, 1476 (1948).
[6] J. Tinlot, Phys. Rev. **74**, 1197 (1948).
[7] L. Janossy and G. D. Rochester, Proc. Roy. Soc. **A183**, 186 (1944).
[8] B. Gross, Zeits. f. Physik **83**, 214 (1933).
[9] L. Janossy, Zeits. f. Physik **101**, 129 (1936).
[10] For definitions and notation see B. Rossi, Rev. Mod. Phys. **20**, 537 (1948).

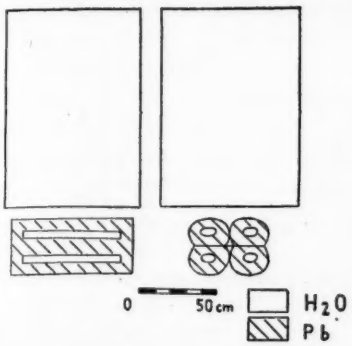

FIG. 1. Experimental arrangement used in the measurements on the transition effect in water (Experiment A).

tical radiation, the actual counting rate decreases with barometric pressure faster than the vertical intensity, but slower than the integrated intensity of the *PSPR*.

In the second place, the interpretation of the observed variation of the frequency of *PS* with barometric pressure requires the knowledge of the origin of the *PS*: We must distinguish the *PS* produced in the lead shielding of the counters from those originated in the air surrounding the detector. In the first case, the frequency of *PS* is proportional only to the intensity of the *PSPR* at the point of observation, whereas the frequency of *PS* produced in the surrounding air is also proportional to the density of the latter, because the frequency of produced *PS* is proportional to the concentration of nuclei with which the *PSPR* collides. The consideration of the density of air for the *PS* produced in it requires supplementary experiments in order to determine the contribution of atmospheric *PS* to the total number of registered *PS*.

We shall show now that the variation of the intensity of a parallel beam of *PSPR* can be represented approximately by an exponential law. We shall use the result that the variation of the registered frequency $f(x)$ of *PS* with barometric pressure x is nearly exponential, as verified by one of us[4] and confirmed by Tinlot.[6] Let us consider, for instance, the limiting case of an isotropic detector. Then we can write

$$f(x)=(k_1+k_2x)J_2(x), \tag{1}$$

where $J_2(x)$ is the integrated intensity, k_1 and k_2 are constants which give the contributions of the *PS* produced in lead and in air, respectively. Since we can write

$$f(x)\cong C\exp(-x/l), \tag{2}$$

C and l being constants, we can deduce from the well-known Gross-transformation the following absorption law $I_v(x)$ for a vertical beam of *PSPR*

$$I_v(x)\cong C(k_1+k_2x)^{-2}[k_1(1+x/l) +k_2x(2+x/l)]\exp(-x/l). \tag{3}$$

In the other limiting case of a detector registering only vertical *PSPR*, one finds

$$I_v(x)\cong C(k_1+k_2x)^{-1}\exp(-x/l). \tag{4}$$

With both types of detectors, $I_v(x)$ can fairly well be represented by an exponential, in the involved range for x, and thus we can reasonably assume that the true absorption law for the *PSPR* is approximately an exponential. Because of the uncertainties due to our lack of knowledge of the true characteristics of the detector used, we can only conclude from Tinlot's experiments that the mean range for a parallel beam of *PSPR* in air lies between the limits 95 and 145 g/cm².

In order to avoid at least the uncertainty due to the production of *PS* in air, we studied the variation with altitude of the frequency of *PS* produced locally in a given amount of water. Our detector (Fig. 1) is the same used previously in São Paulo.[11] We observed the following increase of the rate of fourfold coincidences due to 57 cm of water from São Paulo (barometric pressure 950 g/cm²) to Campos do Jordão (barometric pressure 844 g/cm², latitude 23°S): 2.78±0.51. Thus, applying the above considerations, we obtain a mean range of 113±20 g/cm² if we suppose our detector to be isotropic, and a mean range of 103±18 g/cm² if we admit that our detector registers only vertical *PSPR*.

In the above discussions we have neglected the influence, on the efficiency of the *PS* detector, of the variation with altitude of the *PSPR* energy spectrum.

A possible interpretation of the approximate validity of the exponential absorption law for the *PSPR* in air was recently discussed by one of us.[12] The mechanism of production of *PS* is probably one of cascades of showers of mesons and nucleons. One ought also to take into account that the spectral distribution of energetic nucleons may vary with altitude and that the cross section for production of *PS* is certainly dependent on the energy of the nucleons. All these facts make us think that the exponential absorption law for the *PSPR* has only an approximate validity and is due to a superposition of effects of absorption and production of mesons and nucleons, which are difficult to analyze.

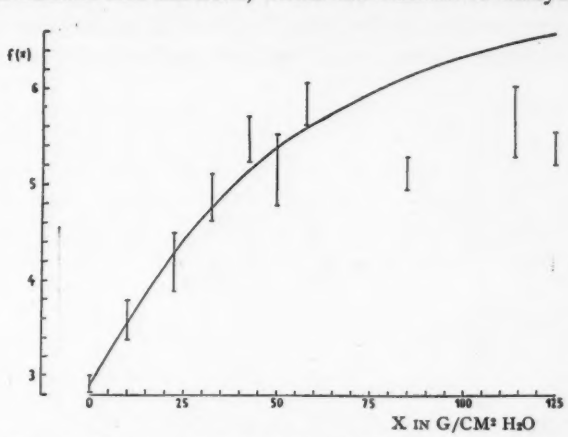

FIG. 2. Frequency of fourfold coincidences against water thickness x in Experiment A. The full curve represents formula (5) with $l=54$ g/cm².

[11] Meyer, Schwachheim, and Wataghin, Phys. Rev. **74**, 846 (1948).

[12] G. Wataghin, Phys. Rev. **74**, 975 (1948).

II. DETERMINATION OF THE MEAN RANGE OF THE PSPR IN WATER

The absorption of *PSPR* in various materials can be studied on the basis of the so-called transition effect. After some measurements of this effect in São Paulo,[11] we performed, in Campos do Jordão, more complete measurements on the transition effect in water. We used a *PS* detector consisting of two telescopes of Geiger-Müller counters completely shielded by lead (Fig. 1), so that a particle, in order to be registered by a telescope, should produce a coincidence through at least 18 cm of lead. The counter trays had an area of 600 cm² each and were connected in fourfold coincidence. The few accidental coincidences were taken into account in our results. The water was contained in a vessel of light material having a wall thickness of ~2 g/cm². In Experiment A, the water tank was placed right above the *PS* detector, as shown in Fig. 1. We increased the thickness of water to 125 cm. Our results are shown in Table I and in Fig. 2.

Experiment B was essentially the same as experiment A with the only difference that the water-containing tank was placed 90 cm higher. The results are given in Table II.

The curves obtained in Experiments A and B are the results of several factors. The first one is the exponential absorption of the *PSPR* in water. If this were the only factor, we should expect a curve given by the formula,

$$f(x)=f(0)+f_1[1-\exp(-x/l)], \qquad (5)$$

where $f(x)$ denotes the hourly rate of fourfold coincidences as a function of the water thickness x; l is the mean range of *PSPR* in water; $f(0)$ and f_1 are constants. As is well known, formula (5) describes the transition effect of a parallel beam incident normally on a plate of thickness x.

A second factor is the variation of the probability of registration of the *PS* with the position of their center of production. Experiment *B* shows the importance of this factor. Indeed, as we can see from Tables I and II,

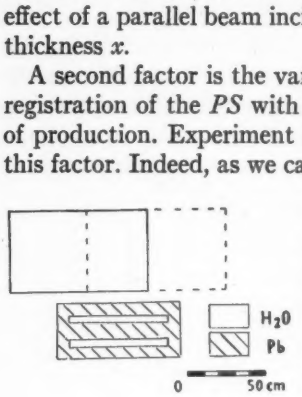

FIG. 3. Experimental arrangement for the investigation of the east–west asymmetry of the *PSPR*. The two symmetrical positions of the water containing vessel in Experiment A are represented by the the full and by the dotted rectangles.

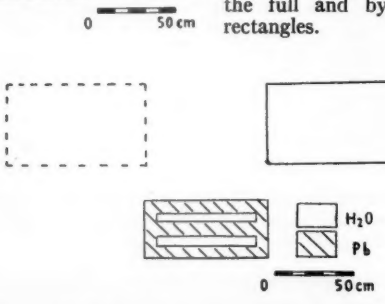

FIG. 4. Positions of the vessel in Experiment B.

TABLE II. Results of Experiment B.

Water thickness above the *PS* detector	Hourly rate of fourfold coincidences
0 cm	3.32±0.24
10 cm	3.98±0.29
30 cm	4.23±0.32
40 cm	4.49±0.25
57 cm	4.67±0.33

TABLE III. Results of Experiment C.

	Hourly rate of fourfold coincidences	
	Series 1	Series 2
No water in either tank (A_0)	3.00±0.17	3.23±0.12
Water in the lower tank (A_1)	5.81±0.29	5.11±0.16
Water in the upper tank (A_2)	4.67±0.33	4.49±0.25
Water in both tanks (A_{12})	5.66±0.37	5.37±0.17

TABLE IV. Results of the measurements on the east–west asymmetry.

	Hourly rates of fourfold coincidences	
	Experiment A	Experiment B
Background	2.79±0.14	2.79±0.14
Water at east	5.11±0.35	3.06±0.15
Water at west	4.70±0.35	3.25±0.17
Difference west–east	−0.41±0.50	0.19±0.23
Average production in water	2.11±0.29	0.36±0.18

for a given amount of water, the registered rate of production in Experiment B is only half the rate in Experiment A. This geometrical factor introduces a deviation from the saturation law (5). A third factor determining the experimental curve of the measurements is the absorption of the produced *PS* in water.

In order to avoid the influence of the geometrical factor, we devised a third experiment (Experiment C). We placed above the shielded counter arrangement described two superposed tanks. The experiment consisted in studying the influence of the water placed in the superior vessel on the production of *PS* in the water of the lower one. The diminution of the rate of production in the water of the lower tank due to the absorption of the *PSPR* allows us to calculate the mean range of the *PSPR* in water. Two series of measurements were performed. In series 1 we used 57 cm of water in both tanks. In series 2 we used 85 cm of water in the lower tank, and 40 cm in the upper one. We present our results in Table III. The mean range l is given by the relation:

$$(A_{12}-A_2)/(A_1-A_0)=\exp(-x/l), \qquad (6)$$

where x is the water thickness in the upper tank. Series 1 yields a mean range of 55±27 g/cm² for the *PSPR*, and series 2 a mean range of 53±25 g/cm². The average value resulting from series 1 and 2 is 54±19 g/cm². However in this experiment the influence of the absorption of the *PS* in water is not excluded, but it

can be shown that a mean range much larger than 55 g/cm² would be incompatible with the data of Experiments A and B. We should notice that in the latter experiment the geometrical factor is less important. In Fig. 2 we have drawn $f(x)$ with the values for the parameters: $f(0)=2.9\ h^{-1}$; $f_1=4.1\ h^{-1}$; $l=54$ g/cm². This curve is in good agreement with the experimental points if we take into account the distortion due to the geometrical factor.

We wish to point out that the mean range l measured in our experiments is only a value averaged over the energy and eventually over the types of particles constituting the *PSPR*. We should also notice that the mean range thus determined is the true mean range for absorption of *PSPR* in water. Indeed, an eventual secondary production of *PSPR* in water cannot influence our results since the secondary showers are simultaneous with the primary ones and are registered as a single event.

In conclusion, there is a definite difference between the mean range $35<l<75$ g/cm² for the absorption of *PSPR* in water and the value $95<l<145$ g/cm² for the absorption of *PSPR* in air. This difference was interpreted by one of us[12] as due to a process of secondary production of *PSPR* in the air, which would result in an apparent mean range larger than the mean range for absorption of *PSPR* in the atmosphere.

III. EAST-WEST ASYMMETRY OF THE PSPR

In order to study the east–west asymmetry of *PSPR* we performed a series of measurements using the same *PS* detector described in the preceding section. A water tank was located alternatively to the east and to the west of the *PS* detector. It seems plausible to assume that, in the average, the direction of a *PS* is the direction of the generating particle.[13] Thus, if there existed an asymmetry in the *PSPR*, we should expect different frequencies of *PS* for the east and the west positions of the tank.

We performed two experiments, A and B (Figs. 3 and 4). The asymmetry of the position of the tank was greater in Experiment B. Our results are collected in Table IV.

Neither of the experiments showed an asymmetry greater than the experimental errors. However there exist several effects which could have masked a possible magnetic deflection of the *PSPR*. In the first place, already in experiment A an asymmetry ~25 percent would be masked by statistical errors. Besides, it is possible that the *PSPR* we study are not the primaries of cosmic radiation but are secondary particles. This would attenuate any asymmetry of the primary radiation. However, at higher altitude an eventual asymmetry may become observable.

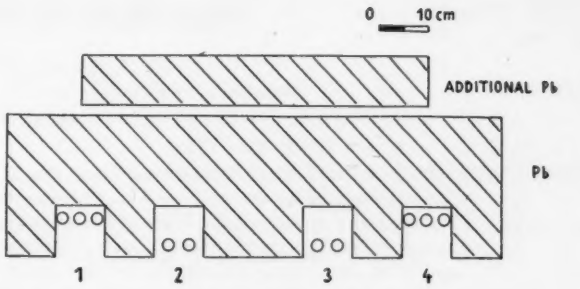

FIG. 5. Arrangement used for the study of the penetrating power of *PS* produced in the air.

IV. COMPLEMENTARY EXPERIMENT ON THE PENETRATING POWER OF PS

In a previous work[1] we discussed our experiments on the nature of the particles constituting the *PS*. We were led to conclude that the produced mesons should be π-mesons rather than μ-mesons. An essential point in our argument was the fact that when the lead protection of the counters was increased from 18 to 28 cm the rate of fourfold coincidences remained unaltered. The interpretation we gave was that the showers produced in the atmosphere were not absorbed by the additional layer of lead. We ruled out the alternative interpretation that there was a compensation between a production of *PS* in the lead and an absorption of atmospheric *PS* in this additional layer. In order to prove this point we investigated the effect of an additional layer of 10 cm of lead above the counter trays 2 and 3, on the rate of threefold coincidences due to *PS* detected by the counter arrangement shown in Fig. 5. The trays 1 and 4 were connected to the same line of the coincidence circuit. The accidental coincidences were negligible. Each counter indicated in Fig. 5 had an area of 120 cm². The geometrical disposition was planned in order to make the registration of a *PS* produced in the lead shielding of the counters more improbable than in the experimental arrangement of our previous measurements.[1] The rate of coincidences without the additional lead was $5.15\pm0.54\ h^{-1}$ and with the lead $5.00\pm0.16\ h^{-1}$. This confirms our argument.

We are indebted to Professor M. D. de Sousa Santos, Professor H. Stammreich, and to Mr. P. Saraiva de Toledo for their kind cooperation.

[13] G. Wataghin, Phys. Rev. **70**, 787 (1946).

Phase Shifts in Proton-Alpha-Scattering

C. L. CRITCHFIELD AND D. C. DODDER
Department of Physics, University of Minnesota, Minneapolis, Minnesota
(Received May 31, 1949)

Phase-shifts in S and P waves are found that fit the observed scattering of protons by helium (4) within the experimental accuracy of the recent Minnesota results. The S wave phase is negative and rather small. The $P_{\frac{1}{2}}$ and $P_{3/2}$ waves have different phase-shifts, both positive, but there are two sets of possible values, one corresponding to a normal doublet in Li^5, the other to an inverted doublet. In both cases there is resonant scattering and strong polarization of the proton beam. Measurement of the polarization would decide between the doublets. The values of the phase-shifts presented are those that minimize the sum of squares of percent differences between observed and calculated differential cross sections.

THE scattering of protons by helium (4) has been measured recently at Minnesota by Freier, Lampi, Sleator, and Williams.[1] Their results for the differential cross sections are more extensive and more accurate than those obtained in earlier investigations.[2] Within the estimated accuracy, however, there is no essential discrepancy between the earlier and the later results. The Minnesota group bombarded helium gas with protons from the electrostatic generator at eight different energies ranging from 0.95 Mev to 3.58 Mev. The scattered protons were counted at a number of angles relative to the incident beam. The angular range extended from 12.5° to 168° (in the center of mass system of coordinates) for most of the energies used.

The accuracy and completeness of the recent results make it possible to determine the phase shifts involved as functions of the energies and to an estimated accuracy of a degree or two. It is the purpose of this paper to present the phase-shift analysis for the $p-He^4$ collisions. No evidence for anomalous phase-shifts in collisions with angular momentum greater than that for P waves was found. The S wave phase-shifts are small and negative; the P wave phase shifts are double valued, but the $P_{3/2}$ and the $P_{\frac{1}{2}}$ waves are refracted very differently above 1.5 Mev. It is impossible to conclude from the differential cross sections alone whether the $P_{\frac{1}{2}}$ shift is larger than the $P_{3/2}$ (i.e., a normal doublet in Li^5) or whether the doublet is inverted.

Values of the P wave phase-shifts are of particular interest. First, it may be hoped to interpret them in terms of spin-orbit forces between nucleons. Since the nuclear forces between He^4 and a proton in a P state are attractive (the phase-shifts are positive), a normal doublet would fit, qualitatively, with Dancoff's[3] calculations based on tensor forces between nucleons, whereas, an inverted doublet would be evidence for the spin-orbit splitting from the Thomas precession as suggested by Inglis.[4] Secondly, the fact that there is definite spin-orbit splitting means that the scattered protons are partially polarized[5] and this effect is of interest not only as a possible source of fast, polarized protons but also as a means of resolving the ambiguity in the P wave phase-shifts. The polarization to be expected from the normal doublet turns out to be quite different from that in the inverted doublet.

The method of analysis of the scattering data follows the customary lines of considering the incident beam as an infinite plane wave in relative coordinates, expanding in eigenfunctions of orbital angular momentum and introducing the effects of nuclear refraction as phase shifts in the asymptotic form at large separation. In the absence of spin-orbit effects the scattered amplitude takes the familiar form

$$A(\theta,\eta,\cdots\delta_l\cdots)=k^{-1}\{-\tfrac{1}{2}\eta\csc^2\tfrac{1}{2}\theta\exp(i\eta\ln\csc^2\theta/2)+\sum_{l=0}^{\infty}(2l+1)P_l(\cos\theta)\exp(i\delta_l+i\phi_l)\sin\delta_l\},\quad(1)$$

where θ is the angle of scattering (center-of-mass system), the δ_l are the phase-shifts induced by non-Coulomb forces in the partial waves of orbital angular momentum $l\hbar$, the angular dependence of the latter being given by the Legendre polynomials $P_l(\cos\theta)$. The quantities, k, η, and ϕ_l are related to the reduced mass M and to the velocity at infinite separation, v, by

$$\begin{aligned}&k=Mv/\hbar\quad\eta=2e^2/\hbar v=0.31612E_{\mathrm{Mev}}{}^{-\frac{1}{2}}\\&k\eta=5.5450\times10^{11}\ \mathrm{cm}^{-1},\quad\phi_0=0,\\&e^{i\phi_l}=\frac{1+i\eta}{1-i\eta}\cdots\frac{l+i\eta}{l-i\eta}\quad l>0.\end{aligned}\qquad(2)$$

In Eq. (2), E_{Mev} is the energy of the proton beam in millions of electron volts and $\hbar$ is Planck's constant divided by 2π.

In the presence of spin-orbit coupling the waves will be refracted differently, depending upon the relative orientation of spin and orbital momentum. Let the normalized spin wave function be designated by $\chi_{\frac{1}{2}}$ for

[1] Freier, Lampi, Sleator, and Williams, Phys. Rev. **75**, 1345 (1949).
[2] N. Heydenburg and N. Ramsey, Phys. Rev. **60**, 42 (1941); C. B. O. Mohr and G. E. Pringle, Proc. Roy. Soc. **160**, 190 (1937).
[3] S. M. Dancoff, Phys. Rev. **58**, 326 (1940).
[4] D. Inglis, Phys. Rev. **50**, 783 (1936).
[5] L. Wolfenstein, Phys. Rev. **75**, 1664 (1949); J. Schwinger, Phys. Rev. **69**, 681 (1946); **73**, 407 (1948). The authors are indebted to Dr. Wolfenstein for the opportunity of reading his manuscript before publication and for several helpful discussions concerning the polarization.

spin pointing in the direction of the incident proton beam (z axis) and $\chi_{-\frac{1}{2}}$ for spin pointing in the opposite direction. The component of the incident beam that is proportional to $(2l+1)\chi_{\frac{1}{2}}P_l(\cos\theta)$ must be considered as a superposition of eigenstates of total angular momentum, ψ_j, with $j=l+\frac{1}{2}$ and $j=l-\frac{1}{2}$:

$$\begin{aligned}&(2l+1)\chi_{\frac{1}{2}}P_l(\cos\theta)=\psi_{l+\frac{1}{2}}+\psi_{l-\frac{1}{2}},\\&\psi_{l+\frac{1}{2}}=(l+1)\chi_{\frac{1}{2}}P_l(\cos\theta)-\chi_{-\frac{1}{2}}\sin\theta e^{i\Phi}P_l'(\cos\theta),\\&\psi_{l-\frac{1}{2}}=l\chi_{\frac{1}{2}}P_l(\cos\theta)+\chi_{-\frac{1}{2}}\sin\theta e^{i\Phi}P_l'(\cos\theta),\end{aligned}\quad(3)$$

where Φ is the azimuthal angle about the direction of bombardment and

$$P_l'(\cos\theta)=dP_l(\cos\theta)/d\cos\theta.$$

If we denote the anomalous phase-shift in $\psi_{l+\frac{1}{2}}$ by δ_l^+ and in $\psi_{l-\frac{1}{2}}$ by δ_l^-, the scattered amplitude arising from incident particles of spin $\chi_{\frac{1}{2}}$ is proportional to

$$\begin{aligned}A_{\frac{1}{2}}(\theta,\eta,\cdots)=k^{-1}\chi_{\frac{1}{2}}\{&-\tfrac{1}{2}\eta\csc^2\tfrac{1}{2}\theta\exp[i\eta\ln\csc^2\tfrac{1}{2}\theta]\\&+\sum_{l=0}^{\infty}[(l+1)\exp(i\delta_l^+)\sin\delta_l^++l\exp(i\delta_l^-)\sin\delta_l^-]\\&\times\exp(i\phi_l)P_l(\cos\theta)\}+k^{-1}\chi_{-\frac{1}{2}}\sum_{l=0}^{\infty}[\exp(i\delta_l^-)\sin\delta_l^-\\&-\exp(i\delta_l^+)\sin\delta_l^+]\exp(i\phi_l+i\Phi)\sin\theta P_l'(\cos\theta).\end{aligned}\quad(4)$$

The analogous calculation for incident particles of spin $\chi_{-\frac{1}{2}}$ leads to the scattered amplitude

$$\begin{aligned}A_{-\frac{1}{2}}(\theta,\eta,\cdots)=k^{-1}\chi_{-\frac{1}{2}}\{&-\tfrac{1}{2}\eta\csc^2\tfrac{1}{2}\theta\exp[i\eta\ln\csc^2\tfrac{1}{2}\theta]\\&+\sum_{l=0}^{\infty}[(l+1)\exp(i\delta_l^+)\sin\delta_l^++l\exp(i\delta_l^-)\sin\delta_l^-]\\&\times\exp(i\phi_l)P_l(\cos\theta)\}-k^{-1}\chi_{\frac{1}{2}}\sum_{l=1}^{\infty}[\exp(i\delta_l^-)\sin\delta_l^-\\&-\exp(i\delta_l^+)\sin\delta_l^+]\exp(i\phi_l-i\Phi)\sin\theta P_l'(\cos\theta).\end{aligned}\quad(5)$$

The differential scattering cross section for an unpolarized beam is then the average of the absolute squares of the amplitudes given by Eqs. (4) and (5), summed over spin components. In the following, we shall use only the terms involving $l=0$ and $l=1$; the formula for the cross section $\sigma(\theta,\eta)$, multiplied by k^2 then becomes:

$$\begin{aligned}k^2\sigma(\theta,\eta)=|&-\tfrac{1}{2}\eta\csc^2\tfrac{1}{2}\theta\exp[i\eta\ln\csc^2\tfrac{1}{2}\theta]+e^{i\delta_0}\sin\delta_0\\&+\cos\theta[2\exp(i\delta_1^+)\sin\delta_1^++\exp(i\delta_1^-)\sin\delta_1^-]\\&\times\exp(i\phi_1)|^2+\sin^2\theta\sin^2(\delta_1^--\delta_1^+).\end{aligned}\quad(6)$$

For convenience of calculation we define the real quantities ρ and β such that

$$\begin{aligned}\rho e^{i\beta}&=2i[2\exp(i\delta_1^+)\sin\delta_1^++\exp(i\delta_1^-)\sin\delta_1^-]\\&=2\exp(2i\delta_1^+)+\exp(2i\delta_1^-)-3.\end{aligned}\quad(7)$$

We also define three new quantities, α, ζ, and R, such that

$$\begin{aligned}\alpha&=2\delta_0-\phi_1\\R\sin(\zeta+\phi_1)&=\eta\csc^2\tfrac{1}{2}\theta\cos(\eta\ln\csc^2\tfrac{1}{2}\theta)\\R\cos(\zeta+\phi_1)&=1-\eta\csc^2\tfrac{1}{2}\theta\sin(\eta\ln\csc^2\tfrac{1}{2}\theta).\end{aligned}\quad(8)$$

In the variables defined in Eqs. (7) and (8), and multiplying by four, we obtain the equation that is used in the following analysis:

$$\begin{aligned}4k^2\sigma(\theta)=R^2&-2R\{\cos(\alpha-\zeta)+\rho\cos\theta\cos(\beta-\zeta)\}\\&+1+2\rho\cos\theta\cos(\alpha-\beta)\\&+\tfrac{1}{2}\rho^2(3\cos^2\theta-1)-3\rho\cos\beta\sin^2\theta.\end{aligned}\quad(9)$$

The unknown quantities at each energy are α, β, and ρ which are related to the desired phase-shifts by

$$\begin{aligned}\delta_0&=\tfrac{1}{2}(\alpha+\phi_1),\\2\sin2\delta_1^++\sin2\delta_1^-&=\rho\sin\beta,\\2\cos2\delta_1^++\cos2\delta_1^-&=\rho\cos+3.\end{aligned}\quad(10)$$

As a preliminary step in the reduction of the data, the cross sections at only three angles of scattering were used, *viz.*: $\theta=90°$, 54° 44′, and 125° 16′. The latter two angles are those at which the D wave component vanishes and, hence, also the term in Eq. (9) that is quadratic in ρ. By reading values for $\sigma(\theta)$ at these angles from graphs of the experimental results and by assuming a value for α, say α', we obtain a pair of equations in $\rho\sin\beta$ and $\rho\cos\beta$. Solving these and substituting in Eq. (9) as applied at $\theta=90°$, we then solve for α. By plotting the assumed values of α' against the calculated values, the roots were located. At $E=1.49$ Mev, for example, there were three sets of solutions which may be labeled by the corresponding values of α, *viz.*, $\alpha=-67.3°$, $-14.0°$, and $36.5°$. Using the values of α, β, and ρ for each set, the cross section was computed for all the angles at which observations were made.[1] In this way it was found that only the set belonging to $\alpha=-67.3°$ predicted cross sections that were close enough to the observed values to be acceptable. For example, the percent difference between calculation and observation at $\theta=25°$ was found to be -1.5, 39.6, and -39.5, in the sets with $\alpha=-67.3°$, $-14°$, and $36.5°$, respectively.

Consideration of the continuity of the phase-shifts leads one to conclude that negative α characterizes the correct set of roots at all energies. At $E=3.58$ Mev, there are four sets of roots two of which have negative α, *viz.*, $\alpha=-91.0°$ and $-132.9°$. Again comparing results of computation with the observations at various angles we found that only $\alpha=-91.0°$ gave an acceptable fit. The percent difference at $\theta=25°$ was 3.4 with $\alpha=-91.0°$

TABLE I. Results of least square reduction.

Energy (Mev)	α	$\rho\cos\beta$	$\rho\sin\beta$
0.95	-59.9 ± 5.6	-0.010 ± 0.060	0.344 ± 0.042
1.49	-65.2 ± 2.0	-0.493 ± 0.034	1.445 ± 0.020
1.70	-62.3 ± 3.1	-1.077 ± 0.053	1.914 ± 0.016
2.02	-74.3 ± 6.6	-2.238 ± 0.103	2.274 ± 0.073
2.22	-77.4 ± 2.6	-3.089 ± 0.037	2.033 ± 0.059
2.53	-78.9 ± 2.3	-3.954 ± 0.028	1.202 ± 0.072
3.04	-84.4 ± 2.2	-4.097 ± 0.018	0.068 ± 0.063
3.58	-89.4 ± 1.5	-3.958 ± 0.024	-0.374 ± 0.059

Note.—± quantities are estimated standard deviations.

TABLE II. Percent deviations in final fit.

θ	E=0.95	1.49	1.70	2.02	2.22	2.53	3.04	3.58
12° 38′	4.1	4.3	2.5	2.4	2.6	−1.5	−1.4	1.0
18 52	2.4	4.7	−0.3	3.2	−0.2	0.2	−0.8	1.1
25 3	3.3	0.8	0.4	2.3	0.6	0.6	1.2	1.3
31 13	3.1			−3.8	−1.8	−3.4	1.6	
37 20	0.6	−4.0	−1.8	3.1	1.7			0.3
43 23						−1.8	−2.2	0.1
49 23	−1.5	2.3	−0.6		2.4	4.5		
55 21							1.4	−1.0
61 10	−2.7	1.1	−0.5	−0.4		−0.4		
66 54					2.1			
72 37	−0.7	0.7		1.7		2.0	−2.3	−1.6
90 7	2.3	−1.4	2.1	0.1	0.4			2.5
94 22						0.5	1.6	
99 28	0.1							
104 36				−4.7				
110 14								3.4
114 22		−2.4	3.1	−1.2	−2.1	2.7	0.5	2.0
120 14								−2.8
132 37		1.5	3.4	0.8	−1.3	1.9	−0.5	−1.5
140 14							−2.2	2.1
149 22		0.5	−1.0	0.5	−1.7	0.6	−0.4	2.5
150 14						−3.1	−4.4	−1.3
160 14						1.1	2.2	2.1
164 59							0.5	
168 2			−2.4	0.1	−2.2	1.0	−1.2	−3.4
s	2.9	3.1	2.3	2.7	2.0	2.4	1.9	2.2

and 34.8 with $\alpha=-132.9°$. In contrast to the result at $E=1.49$, it is the next lowest value of α that gives the best fit at $E=3.58$, instead of the lowest value. Hence, it appears that the two series of negative roots cross over, there being a double root at some intermediate energy. This interpretation is corroborated by the fact that at $E=2.53$ Mev there are no real, negative roots for α, a possible result of being near the double root and making a small error in estimating the cross sections at the three angles used.

Although the method described above serves to locate the correct branch of the multiple solutions, the existence of a double root makes it useless as a way of obtaining preliminary values of α, β, and ρ at intermediate energies. With the values of α at $E=1.49$ and 3.58, however, those for the other energies can be estimated. The method used is that presented by Breit and his collaborators[6] wherein we rely on the fact that the function

$$f(\eta, \delta_0)=(e^{2\pi\eta}-1)^{-1}\pi\cot\delta_0-\ln\eta+1.202\eta^2$$

should be very closely a linear function of the energy. By drawing a line through the points obtained at $E=1.49$ and 3.58, the other δ_0's, and hence α's, were found. Then, from two observed points, preliminary values of β and ρ were obtained.

With the preliminary values of α, β, and ρ as obtained by the procedure described above, values of $4k^2\sigma(\theta)$ were computed from Eq. (9) for every angle and for every energy for which observations were made. The percent differences, ϵ_θ, between calculated and experimental values of $4k^2\sigma(\theta)$ were then taken. First-order corrections to α, $\rho\cos\beta$, and $\rho\sin\beta$ were found at each energy so as to minimize the sum of squares taken over all angles, i.e.,

$$\text{Min}\sum_\theta\left\{\frac{\partial\ln\sigma(\theta)}{\partial\alpha}\Delta\alpha+\frac{\partial\ln\sigma(\theta)}{\partial\rho\cos\beta}\Delta(\rho\cos\beta)+\frac{\partial\ln\sigma(\theta)}{\partial\rho\sin\beta}\Delta(\rho\sin\beta)-\frac{\epsilon_\theta}{100}\right\}^2.$$

No allowance is made for possible uncertainty in the value of the energy, or of angle, and all results are considered to be of the same weight. With the first-order corrections made, new values of ϵ_θ were computed and the procedure repeated. For the most part, the corrections indicated by the second calculation were of the order of one percent.

The semistatistical procedure in minimizing the sum of squares of the deviations permits rough estimates of the standard deviations of the individual observations and of the values obtained for α, $\rho\cos\beta$, and $\rho\sin\beta$. The results of the calculation are presented in Table I and the resulting percent deviations, observed less calculated, are given in Table II for each angle and energy presented in reference 1. The quantities labeled s in Table II are the estimated standard, percent deviations of the single observations. It is apparent that the magnitudes of s are in accord with the estimated probable error of 1.5 percent claimed by the experimentalists of reference 1. The fact that the deviations at the higher energies are no worse, and in fact somewhat better, than those at lower energy indicates that higher partial waves are not important to the scattering by nuclear forces.

Using the values in Table I and solving Eq. (10), we obtain the values of the phase-shifts. As remarked above, there are two sets of solutions for the P waves, one a normal doublet, the other an inverted doublet. The results are shown in Table III which includes the estimated standard deviations. In the event that the doublet is inverted, only the phase-shift of the $P_{3/2}$ wave passes through 90°, and that occurs at about 2.8 Mev. For the normal doublet, however, both P waves pass through resonance, the $P_{\frac{1}{2}}$ at a proton energy of 2.3 Mev and the $P_{3/2}$ at 3.4 Mev. The first resonance level is presumably the lowest quantum state of the Li^5 nucleus which, therefore, lacks being bound by about 1.8 Mev. The splitting caused by spin-orbit coupling would be 0.9 Mev. The width of the $P_{\frac{1}{2}}$ level at half-maximum is also about 0.9 Mev and the width of the $P_{3/2}$ levels are even larger, perhaps by 50 percent.

TABLE III. Phase-shifts in S and P waves.

Energy	S	Inverted doublet $P_{\frac{1}{2}}$	Inverted doublet $P_{3/2}$	Normal doublet $P_{\frac{1}{2}}$	Normal doublet $P_{3/2}$
0.95	−12.0±2.8	3.3± ?	3.3± ?	3.3± ?	3.3± ?
1.49	−18.1±1.0	4.1±1.8	20.4±1.0	25.8±1.7	9.6±0.8
1.70	−17.6±1.6	4.2±2.2	31.1±1.4	40.7±1.4	13.8±0.3
2.02	−24.6±3.3	8.1±1.9	47.8±0.6	63.2±2.1	23.7±0.9
2.22	−26.7±1.3	9.4±1.6	60.6±0.6	83.1±1.6	31.9±0.6
2.53	−28.2±1.2	13.1±2.7	78.8±0.8	115.3±1.4	49.6±1.1
3.04	−32.0±1.1	15.7±2.5	96.6±1.7	160.7±2.0	79.8±1.9
3.58	−35.2±0.8	20.3±4.0	105.4±6.6	181.0±5.6	95.9±2.1

[6] See G. Breit and W. G. Bouricius, Phys. Rev. **75**, 1029 (1949).

The S wave phase-shifts are similar to those that would be produced by a weak, repulsive potential of fairly long range. If the S wave potential is assumed to be independent of the energy, the phase-shifts as observed can be obtained by assuming the Coulomb repulsion to apply down to a separation, 5.75×10^{-13} cm, and substituting a constant positive potential of 3.8 Mev at smaller distances. On the other hand, the S wave interaction probably is not energy independent and the square well picture has no immediate significance.

Although the existing results on the complementary system formed by scattering neutrons in helium are not of comparable accuracy, it is of interest to compare them with our results. Staub and Tatel[7] have found that the backward scattering of the neutrons exhibits a double resonance which can be accounted for by either a normal doublet in the P waves and a negative S wave phase-shift or an inverted doublet with a positive S wave phase-shift. They preferred the former possibility which corresponds to our normal doublet if one assumes similarity between neutron-neutron and proton-proton forces. In fact, if we had imposed the condition that both P waves go through resonance in the energy range used, we should have obtained the normal doublet as a unique solution. On the other hand, the proton-alpha-scattering shows only a single maximum in the backward scattering. In any event, it is clear from the analysis above that a description by means of phase shifts will always lead to two solutions for the P waves and it is only by an additional assumption that a unique solution can be derived from the differential cross section alone.

The question as to whether the P wave doublet be normal or inverted can be settled, in principle, by determining the polarization of the scattered protons as a function of the energy of bombardment. Following the line of reasoning presented in reference 5, we compute the expectation value of the x component of the spin of the scattered proton, σ_x,

$$\sigma_x\chi_{\frac{1}{2}}=\chi_{-\frac{1}{2}} \quad \sigma_x\chi_{-\frac{1}{2}}=\chi_{\frac{1}{2}}$$

in each of the waves, Eqs. (4) and (5), average the results and divide by the cross section at the same energy and angle. This gives the fractional polarization which, since it varies as $\sin\theta$ will be near maximum at $\theta=90°$. The fractional polarization in the x direction is also proportional to $\sin\Phi$ and is therefore a maximum along the y axis. Considering only P waves and setting $\theta=\Phi=90°$, we obtain for the percent polarization p:

$$p=200\sin(\delta_1^--\delta_1^+)\{\eta\sin(\phi_1+\delta_1^-+\delta_1^+-0.69\eta) -\sin\delta_0\sin(\phi_1+\delta_1^-+\delta_1^+-\delta_0)\}/k^2\sigma(90°). \quad (11)$$

Calculations with the phase-shifts obtained above are presented in Table IV. It is evident from the numerical results that the protons scattered at 90° are almost completely polarized at energies somewhat less ($\sim$0.5 Mev) than the resonant values. It will be observed also that the direction of polarization changes sign in the case of the normal doublet. Hence, relatively inexact measurements of the proton polarization should suffice to decide which of the two solutions to the scattering problem is the correct one.

TABLE IV. Percent polarization at 90°.

Energy	Inverted doublet	Normal doublet
0.95	0	0
1.49	−70	79
1.70	−90	96
2.02	−98	80
2.22	−92	42
2.53	−68	−32
3.04	−39	−87
3.58	−15	−57

We should like to thank the members of the electrostatic generator group at Minnesota for their cooperation in the investigation reported above. This work was supported in part by the ONR.

[7] H. Staub and H. Tatel, Phys. Rev. **58**, 820 (1940).

Radioactive Tin 121, 123, 125

J. C. LEE* AND M. L. POOL
The Ohio State University, Columbus, Ohio

(Received May 18, 1949)

The 130-day activity in Sn is now assigned to Sn 123 and emits a 1.3-Mev beta-particle. No gamma-radiation is observed. A 40-minute activity emitting gamma-radiation and a 1.32-Mev beta-particle has also been assigned to Sn 123. Assigned to Sn 125 are a 10-day activity and a 9.8-minute activity which emit a 2.1-Mev beta-particle and a 1.3-Mev beta-particle, respectively. The 1.1-day Sn 121 which emits a negative particle of energy 0.35 Mev has been confirmed.

I. INTRODUCTION

NUMEROUS discrepancies and uncertainties in associating the various tin activities to definite tin isotopes are evident in the published data. The large number of stable tin isotopes and the uniformity in the percent isotopic composition of tin contribute materially to ambiguous mass assignments. The recent availability of electromagnetically enriched** tin isotopes has made it possible that accurate interpretations may be made. Table I shows the percent composition of three tin samples enriched in Sn 120, Sn 122, and Sn 124, respectively.

The first report of this region[1] stated that the bombardment of tin with 5-Mev deuterons produced activities with half-lives of 9 minutes, 40 minutes, 26 hours, 10 days, 70 days, and 400 days. These activities were also produced by slow neutron irradiation of tin. All but the 400-day activity showed emission of negative particles. The sign of the particle emitted by the 400-day activity was not established.

The 9-minute activity was not produced by fast neutrons. Since Sn 124 is the heaviest stable tin isotope, the 9-minute activity, therefore, was tentatively assigned to Sn 125 by neutron-capture. From a Sn(n, γ) reaction a 9-minute activity which emitted a 2.2-Mev negative beta-particle and gamma-radiation of energy 0.74 Mev was later reported.[2]

A recent report[3] definitely assigned to Sn 121 a 28-hour activity obtained by activating a sample enriched in Sn 120 with 18-Mev deuterons. A negative particle of energy 0.4 Mev was measured in this activity.

A 40-minute activity was placed at Sn 123 by postulating a (d, t) reaction[4] on Sn 124.

Tentative assignments for a 130-day activity[5] and a 136-day activity[6] in tin produced by uranium fission have been made at Sn 121 or 123. Associated with these long-lived activities negative beta-particles of energies 1.5 to 1.6 Mev[5] and 1.2 Mev[6] were found. Also produced by uranium fission were 11-day[7,8] and 9-day[9,10] activities tentatively assigned to Sn 123.

A 10-day activity emitting a 2.6-Mev beta-particle was found by Sn(n, γ) reaction.[11] The above-mentioned 9-minute, 26-hour, 40-minute, 130-day, and 10-day activities recently have been given the evaluations *B*, *A*, *D*, *C*, and *D*, respectively.[12]

It is the purpose of this paper to investigate more thoroughly these activities by using deuteron, slow neutron, and fast neutron bombardments of tin samples which have been electromagnetically enriched in Sn 120, Sn 122, and Sn 124, respectively.

TABLE I. Percent composition of enriched tin samples in mass numbers 112 to 114.

Sample	Mass numbers 112	114	115	116	117	118	119	120	122	124
Natural tin	1.1	0.8	0.4	15.5	9.1	22.5	9.8	28.5	5.5	6.8
Tin sample enriched in Sn 120	1.1	0.2	0.1	0.4	1.1	0.8	1.3	94.4	0.2	0.3
Tin sample enriched in Sn 122	0.1	0.2	0.1	6.2	9.1	10.3	10.8	16.4	42.9	4.3
Tin sample enriched in Sn 124	0.1	0.1	0.2	0.7	5.4	1.4	5.3	2.6	1.4	83.1

II. EXPERIMENTAL PROCEDURES

Fast neutron irradiation was produced by placing the sample near a lithium plate which was being bombarded with 10-Mev deuterons. Because of the high capture cross section of cadmium for slow neutrons, a cadmium shield around the sample was used when the elimination of lower energy neutrons was desired. Slow neutron irradiation was achieved by bombarding lithium or beryllium with deuterons and placing paraffin around the samples which were just outside the cyclotron vacuum chamber. The enriched tin samples were supplied** in the form of SnO_2. For the neutron bombardments the tin was bombarded in the form of the SnO_2 powder.

* Now at Michigan State College, East Lansing, Michigan.

** Supplied by the Y-12 plant, Carbide and Carbon Chemicals Corporation, through the Isotopes Division, U. S. AEC, Oak Ridge, Tennessee.

[1] J. J. Livingood and G. T. Seaborg, Phys. Rev. **55**, 667 (1939).

[2] W. H. Sullivan and H. E. Wyatt, Plut. Proj. Rep. Mon. No. 243, p. 3 (1947).

[3] M. Lindner and I. Perlman, Phys. Rev. **73**, 1124 (1948).

[4] A. S. Newton and W. R. McDonald, private communication to G. T. Seaborg, Rev. Mod. Phys. **20**, 585 (1948).

[5] G. R. Leader, Plut. Proj. Rep. CN 3464 (January, 1946).

[6] W. E. Grummit and G. Wilkinson, Nature **158** (1946).

[7] O. Hahn and F. Strassman, Naturwiss **31**, 499 (1943).

[8] J. Seiler, Plut. Proj. Rep. CN 2126, p. 3 (September, 1944).

[9] K. D. Coleman and M. L. Pool, Phys. Rev. **72**, 1072 (1948).

[10] Steinberg, Seiler, Goldstein, and Dudley, AECD 1860 (1948).

[11] J. Seiler, Plut. Proj. Rep. CC 2310, p. 143 (January, 1945).

[12] G. T. Seaborg and I. Perlman, Rev. Mod. Phys. **20**, 585 (1948).

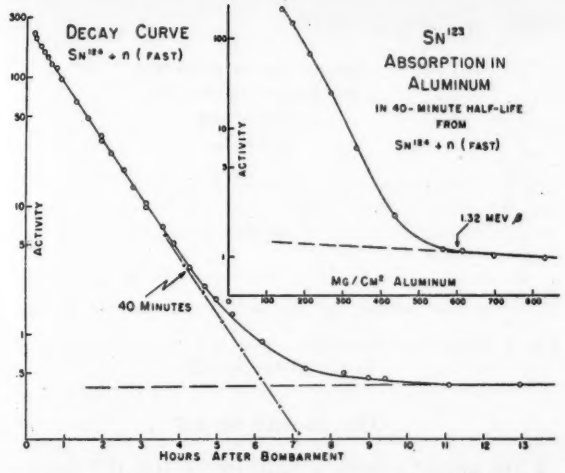

FIG. 1. Decay curve of the 9.8-minute activity of Sn 125 produced by slow neutron irradiation of Sn 124. Also is shown an aluminum absorption measurement which indicates a 1.3-Mev beta-end point in the 9.8-minute activity.

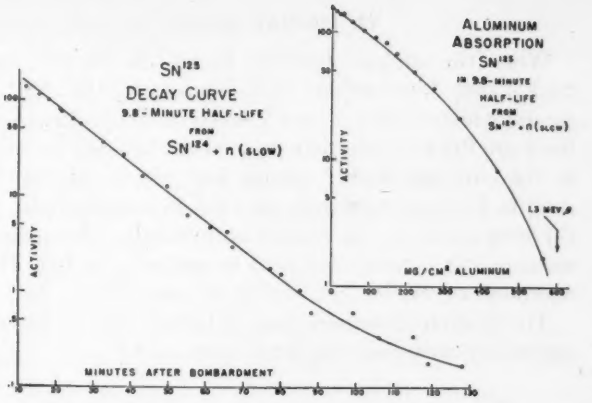

FIG. 2. Decay curve from a fast neutron bombardment of Sn 124 showing the 40-minute Sn 123 activity. Also a beta-end point of 1.32-Mev measured by absorption in aluminum is shown.

For the deuteron bombardments the SnO_2 was reduced to Sn metal in an atmosphere of hydrogen at 625°C.

For the comparison of relative yields, similar bombardments by deuterons were made by mounting samples of equal masses on either side of a specially designed cyclotron probe which could be manually rotated during the bombardment at selected intervals.

Chemical separations of bombarded materials were made by precipitations and by fractional distillations. Antimony was precipitated as Sb_2S_5 and indium as $In(OH)_3$; the tin was brought down by phenylarsonic acid.

III. 9.8-MINUTE Sn 125

Slow neutron irradiation of tin enriched to 83.1 percent in Sn 124 produced an activity which persisted for more than eight half-life periods. The half-life was 9.8±0.2 minutes. Slow neutron bombardment of samples enriched in Sn 120 and Sn 122 showed no evidence of the 9.8-minute activity. Fast neutron bombardments of Sn 120, Sn 122, and Sn 124 did not produce the 9.8-minute activity. The assignment of this activity to Sn 125 now seems definite.

Figure 1 shows aluminum absorption measurements of a 1.3-Mev beta-particle. The value of the end point is not in agreement with the previously reported value of 2.2 Mev.[2] The accompanying decay curve shows that the 9.8-minute activity is not contaminated with appreciable amount of other activities.

IV. 40-MINUTE Sn 123

When a tin sample, enriched in Sn 124, was irradiated with fast neutrons, a tin activity was measured for over five half-life periods. A half-life of 40±1 minutes was found and is in agreement with the value previously reported.[1,13] The 40-minute activity was also produced by slow neutron irradiation of a sample enriched in Sn 122 and not in samples enriched in 120 and 124. Hence, this 40-minute activity may now be logically assigned to Sn 123.

Figure 2 shows a decay curve of the 40-minute activity and also an aluminum absorption curve of the emitted beta-particles. An end point of 1.32 Mev is evident. The approximate beta-energy of 3 Mev given in a recent report[4] was in no way apparent. Gamma-radiation was also associated with this 40-minute activity.

V. 1.1-DAY Sn 121

The (d, p) reaction on tin enriched in Sn 120 makes the assignment of the 1.1-day Sn activity quite definite at Sn 121. This assignment is confirmed by fast neutron irradiation of Sn 122 and by slow neutron irradiation of Sn 120. Furthermore, the 1.1-day activity is not produced by slow neutron bombardment of Sn 122, nor fast or slow neutron bombardment of Sn 124. Both the half-life determination of 1.1±0.05 days and the assignment to Sn 121 are in agreement with a previous report.[3] Figure 3 shows a 0.35-Mev negative particle measured in this activity. This is in fair agreement with a recent report of 0.4 Mev.[3]

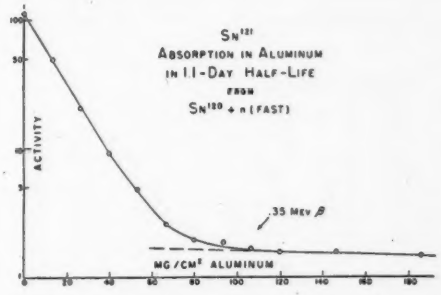

FIG. 3. Aluminum absorption curve showing a negative particle energy of 0.35 Mev in the 1.1-day Sn 121.

[13] Pool, Cork, and Thornton, Phys. Rev. 52, 239 (1937).

VI. 130-DAY Sn 123

When tin samples enriched in Sn 120, Sn 122, and Sn 124 are bombarded with deuterons, the Sn 122 sample yields a very strong 130-day activity. Neutrons from the Be(d, n) reaction induced the 130-day activity in the enriched Sn 122 sample but not in the Sn 120 sample. Fast neutrons from the Li(d, n) reaction induced the long period in the Sn 124 sample only. The assignment of this activity can thus be made to Sn 123. The reactions are $Sn^{122}(n, \gamma)$, $Sn^{122}(d, p)$, and $Sn^{124}(n, 2n)$.

The half-life determination of 130±5 days is in fair agreement with previous measurements.[5,6]

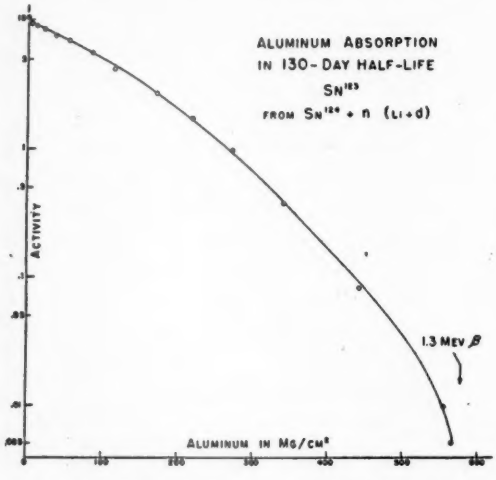

FIG. 4. Aluminum absorption curve of the 1.3-Mev beta-particles in the 130-day activity of Sn 123.

Figure 4 shows a beta-end point of 1.3 Mev in the 130-day activity of Sn 123. Previously reported values of beta-energies range from 1.2 to 1.6 Mev.[5,6] No gamma-ray activity was observed.

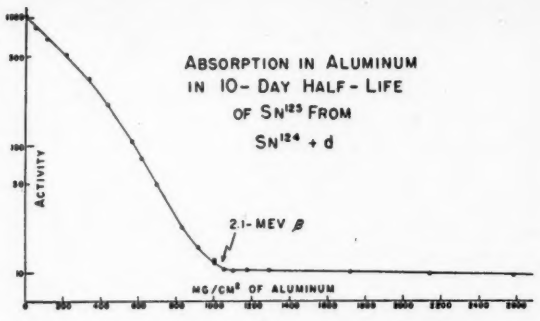

FIG. 5. Aluminum absorption curve of a 2.1-Mev beta-particle in the 10-day Sn 125.

VII. 10-DAY Sn 125

A tin activity with a half-life of 10±0.3 days was obtained by deuteron bombardments of samples enriched in Sn 120, 122, and 124, respectively, but the resulting intensity from the Sn 124 sample was much stronger than the intensities induced in the Sn 120 and Sn 122 samples. This 10-day activity is weakly, if at all, produced by slow neutron bombardment of tin. However, fast neutron irradiation of Sn 124 does produce the activity. The 10-day Sn activity may thus be assigned to Sn 125 in accordance with the reactions $Sn^{124}(d, p)$ and $Sn^{124}(n, \gamma)$.

The 10-day Sn 125 activity emits a negative beta-particle of energy 2.1 Mev. The aluminum absorption curve is shown in Fig. 5. The previously reported beta-energy of 2.6 Mev[11] is in approximate agreement with the above value.

The assistance received from the Research Foundation and the Graduate School of The Ohio State University is gratefully acknowledged. The chemical separations were ably done by H. L. Finston and R. M. Dyer.

On the Film Transfer Rate in Helium *II*

ROBERT T. WEBBER, HENRY A. FAIRBANK, AND C. T. LANE
Sloane Physics Laboratory, Yale University, New Haven, Connecticut*
(Received April 29, 1949)

In view of the wide disagreement between the two existing determinations of the flow rate of the Rollin film under a gravitational potential difference we have re-examined the matter experimentally. Our results are in substantial agreement with the earlier work of Daunt and Mendelssohn.

INTRODUCTION

ANY solid surface in contact with liquid helium *II* rapidly becomes coated with a liquid film of the order of 100 atom layers which is mobile. It is believed that this film of superfluid helium moves from points of lower temperature to places at higher temperature (up to the λ-point) and also, in the absence of a temperature gradient, from places of higher to lower gravitational potential even if this requires that the film surmount a potential barrier. Thus an impermeable test-tube or beaker with its closed end immersed in helium *II* will either fill or empty via this surface film depending on whether the liquid level in the tube is initially below or above the level of the outer bath, and this process continues until the gravitational potential difference vanishes.

The first systematic study of this latter effect was made by Daunt and Mendelssohn and reported[1] in two papers in 1939. Daunt and Mendelssohn found that the laws governing this type of liquid flow were of surprising simplicity but at the same time highly non-classical. The rate of emptying (or filling) of the beaker depended solely on:

(1) the temperature, being zero at the λ-point and increasing with decreasing temperature, and
(2) the transfer between any two levels at a given temperature being limited by the least periphery in the connecting surface *above* the higher level.

No significant dependence of the transfer rate on the gravitational potential difference of the two levels was observed and, accordingly, no classical syphon mechanism can be involved.

In a more recent communication[2] certain phases of the Daunt-Mendelssohn experiment have been repeated by Atkins but with results which are widely different. These differences were twofold:

(1) The transfer rate (emptying and filling), at a given temperature, was found to be a function of the height of the beaker rim above the higher of the two levels ("height" of the film).
(2) Even with a comparable film height, the transfer rate found by Atkins was four or five times greater than that found by Daunt and Mendelssohn.

In view of these disagreements between the only two existing experiments on this subject we felt that a third investigation would be in order.

NEW MEASUREMENTS

Our first approach was to make use of a glass beaker with a vacuum jacket (Dewar flask). The inner tube of this was a glass capillary (diameter ~1 mm) the closed end of which was of Kovar metal. Provision was made such that the tip of the outer jacket could be broken under liquid helium. We could, therefore, in the same experiment, observe the transfer effect with liquid in the tube which could either be thermally isolated from or else be in thermal contact with the outer bath. In this way we sought to repeat in a single run the two arrangements used by Daunt and Mendelssohn. We jacketed the helium Dewar with liquid nitrogen in the usual way and used a low power fluorescent light source with water shield for visual observation but, apart from this, took no other precautions to shield the test beaker from thermal radiation of which that coming from the top of the helium Dewar flask was the most important.

The results of the measurements made with this equipment agreed in order of magnitude with Daunt and Mendelssohn and not at all with Atkins. In particular, no dependence of the transfer rate on the height of the film (as reported by Atkins) was found for either type beaker for either an emptying or a filling process at the single temperature at which observations were taken (1.5°K). However, in the case of a beaker in

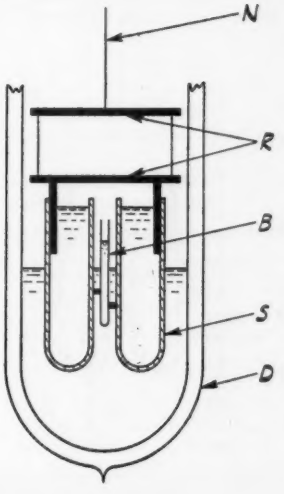

FIG. 1. Schematic drawing of the apparatus.

* Assisted by the ONR.
[1] J. G. Daunt and K. Mendelssohn, Proc. Roy. Soc. **A170**, 423 (1939); Proc. Roy. Soc. **A170**, 439 (1939).
[2] K. R. Atkins, Nature **161**, 925 (1948).

thermal contact with the outer bath, although the emptying rate was approximately double the filling rate the average value was in fair agreement with the Daunt-Mendelssohn rate at 1.5°K. In addition, the emptying rate for the thermally isolated beaker was found to be non-reproducible although the reproducibility for the other type beaker was excellent.

Examination of these data suggested that temperature gradients in the helium bath or in the vapor above the bath caused by a lack of adequate shielding against external thermal radiation might be responsible for these discrepancies and we therefore modified our apparatus. Figure 1 is a schematic drawing of the apparatus finally evolved.

The test beaker B consisting of a thin-walled glass capillary (0.74 mm diameter) was attached as shown in the inner tube of an annular glass bucket S. Above the latter were two aluminum disks R, the lower of which had two aluminum prongs extending some distance into S as shown. R, B, and S formed one rigid unit and could be raised or lowered in the helium Dewar D by means of a nylon thread N attached to a small vacuum-tight winch at the top of the cryostat. Accordingly, both B and S could be filled with liquid helium from the bath in D, and S and R formed very excellent shields for B against radiation coming from the sides or top of the flask D. The latter was fully silvered except for a pair of narrow longitudinal slits and was jacketed by a similar flask containing liquid nitrogen. The liquid level in B was observed with a cathetometer and for illumination we used a low power fluorescent lamp with a filter[3] consisting of a weak aqueous solution of $CuCl_2$.

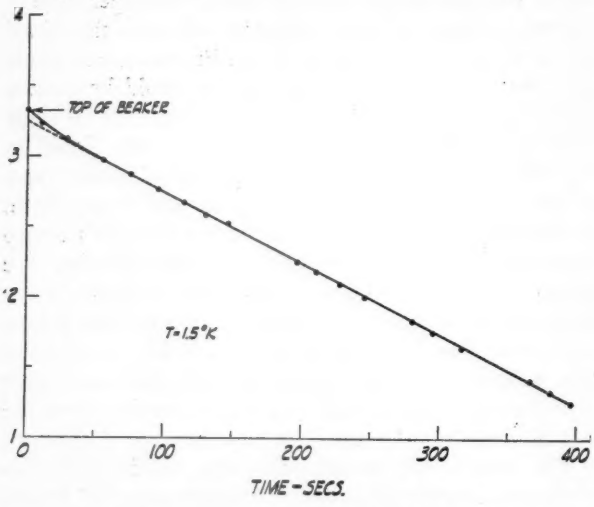

FIG. 2. The height of the liquid surface inside the beaker as a function of time during an emptying process at 1.5°K.

TABLE I. The transfer rate for various film heights H for a filling process at 1.90°K.

Rate cm³/sec. cm	H cm
5.3×10^{-5}	1.59
5.5	1.05
5.8	0.69
5.9	0.33
5.8	0.22

TABLE II. Film transfer rate (cm³/sec. cm) at various temperatures.

Temperature	Emptying	Filling	Average
2.10°K	2.3×10^{-5}	2.6×10^{-5}	2.4×10^{-5}
2.00	4.5	4.5	4.5
1.90	5.5	5.7	5.6
1.80	6.9	6.9	6.9
1.70	7.8	6.7	7.2
1.60	8.2	7.3	7.8
1.50	9.3	7.7	8.5
1.40	10.3	8.0	9.1

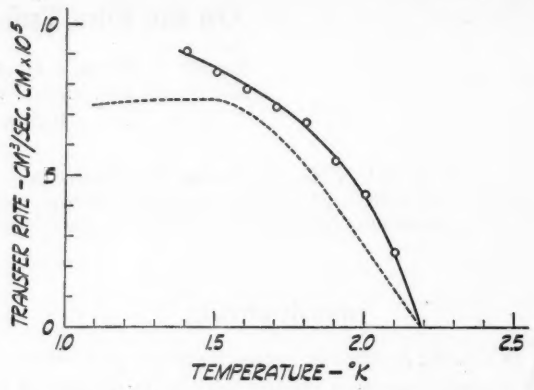

FIG. 3. The transfer rate as a function of temperature. The full curve with circles is the present experiment and the broken curve gives Daunt and Mendelssohn's results (smoothed values, reference 1).

RESULTS

The experimental procedure consisted merely in observing the fall (or rise) of the liquid surface in B as a function of time at various bath temperatures below the λ-point. This was invariably a linear function except in the initial stages of an emptying process when the liquid in B was very near the rim of the tube, an effect also observed by Daunt and Mendelssohn.[1] Figure 2 shows this—at time zero the liquid in B is flush with the top of the tube. Daunt and Mendelssohn suggested that this "end effect" might be due to a thicker surface film when the inside level was very near the rim of the beaker. It is also possible that a higher evaporation rate of the liquid in the beaker at this point could be responsible.

Within our experimental error we find no such dependence of the rate on the height of the film as reported by Atkins.[2] In Table I, for instance, is a series of measured filling rates for various values of the height

[3] John Strong, *Procedures in Experimental Physics* (Prentice-Hall, Inc., New York, 1938), p. 369.

of the beaker rim (H) above the level of the outer bath at 1.90°K. The time rate of rise of the liquid surface in the beaker was, in all cases, found to be strictly linear with no "end effect" such as was found in certain cases in an emptying process and illustrated in Fig. 2. We note, however, that this end effect of increased transfer rate on emptying always occurred when the inside level was not more than about 2 mm from the top of the beaker. The smallest observed value of H for a filling process (see Table I) was greater than 2 mm and it is possible that for smaller H the end effect would be found for the filling process also. In any event, however, these results completely disagree with Atkins.

In general, at a given temperature, the emptying rate was somewhat larger than the filling rate. We attribute this to evaporation from B, since the latter will tend to increase the emptying rate and decrease the filling rate.** On this view then, an average of the two rates should be the correct one.

A complete summary of our experimental data is given in Table II and in Fig. 3 is a plot of the transfer rate *versus* the temperature. The latter was computed from the vapor pressure of the bath using the Leiden 1932 scale. For the sake of comparison we have also plotted the Daunt-Mendelssohn data (smoothed values) in Fig. 3 and the agreement between the two sets of data is seen to be reasonably satisfactory.

** In our first experiment, it will be recalled, our emptying rate was double the filling rate indicating much poorer thermal isolation in the first apparatus.

PHYSICAL REVIEW VOLUME 76, NUMBER 5 SEPTEMBER 1, 1949

The Angular Distribution of the Photo-Neutrons from Beryllium

B. HAMERMESH, M. HAMERMESH, AND A. WATTENBERG
Argonne National Laboratory, Chicago, Illinois

(Received May 11, 1949)

The angular distribution of the photo-neutrons from beryllium has been studied for γ-ray energies of 1.70, 1.81, and 2.76 Mev. The distribution was found to be spherically symmetrical for the 1.70- and 1.81-Mev γ-rays. The 2.76-Mev gamma-ray yields a distribution of the form $a+b\sin^2\theta$ with $a/b=1.2$.

INTRODUCTION

THE threshold for the photo-disintegration of beryllium is supposed to be 1.63 Mev. Experiments[1] indicate that the (γ,n) cross section of beryllium increases to a maximum in the neighborhood of 1.7 Mev, decreases to a minimum around 2.1 Mev, and is increasing once again at 2.7 Mev. These maxima in the cross section may be explained in a naïve way by saying that the first maximum is caused by the emission of S neutrons, whereas the second maximum is caused by the emission of neutrons of higher angular momentum. One would therefore expect that the angular distribution of the photo-neutrons should be spherically symmetric just above the threshold and then have an asymmetrical component which increases with increasing energy.

Previous studies of the angular distribution of the photo-neutrons from beryllium were carried out by Chadwick and Goldhaber[2] who used γ-rays from a radon source and found a spherically symmetrical distribution. Goloborodko and Rosenkewich[3] used γ-rays from a radium source and came to a similar conclusion. In view of the complexity of the γ-rays from the radium family, it was felt more valuable information might be obtained with monoenergetic γ-ray sources.

[1] Russell, Sachs, Wattenberg, and Fields, Phys. Rev. **73**, 545 (1948).
[2] J. Chadwick and M. Goldhaber, Proc. Royal Soc. **A151**, 479 (1935).
[3] Goloborodko and Rosenkewich, Physik. Zeits. Sowjetunion **11**, 78 (1937).

APPARATUS

The apparatus shown schematically in Fig. 1 was mounted eight feet above the floor in a large room.

The detector was a BF_3 pulse ion chamber embedded in a paraffin cylinder 20-cm in diameter and 20-cm long. The chamber was filled to a pressure of one atmosphere with enriched BF_3. The amplifier bias was chosen to discriminate between pulses caused by gamma-rays and those caused by neutrons.

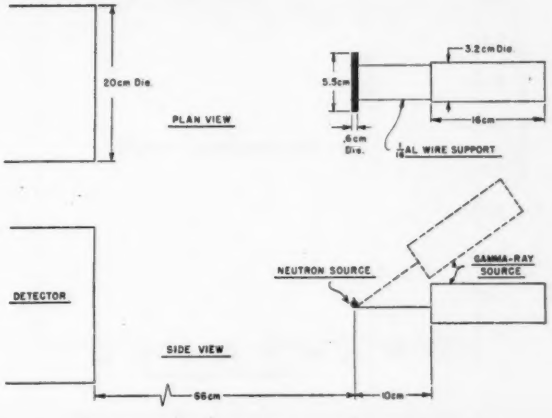

FIG. 1. A schematic diagram of apparatus.

The source holder supported the beryllium target by means of two $\frac{1}{16}$-inch aluminum wires. The beryllium target was a cylinder 5.5-cm long and 0.6-cm in diameter. The source holder could be rotated about an axis that coincided with the axis of the target so as to change the angle between the bombarding gamma-rays and the detected neutrons. Readings were taken at 0°, 20°, 40°, 55°, 75°, and 90°. A set of electrical contacts on the rotating arm attached to the source holder made it possible to make an accurate setting of the angles. The source and detector subtended half-angles of less than 9° at the target.

The sources used were approximately 20 curies in strength. As gamma-ray sources Sb^{124} (γ-ray energy 1.70 Mev), Mn^{56} (γ-ray energies 1.81 and 2.13; nearly 80 percent of the neutron intensity is caused by the 1.81-Mev γ-rays), and Na^{24} (γ-ray energy 2.76 Mev) were used. The source materials were in thin walled aluminum cans for the purposes of handling and irradiation in the heavy water pile at this laboratory. The aluminum activity was allowed to die out before measurements were started. By the use of mirrors, pulleys, and strings all operations during the experiments were carried out with the experimenters located behind adequate shielding material.

EXPERIMENTAL PROCEDURE

The counting rate at any angle included in addition to the desired beryllium photo-neutron intensity, (E), a background consisting of four components—namely:

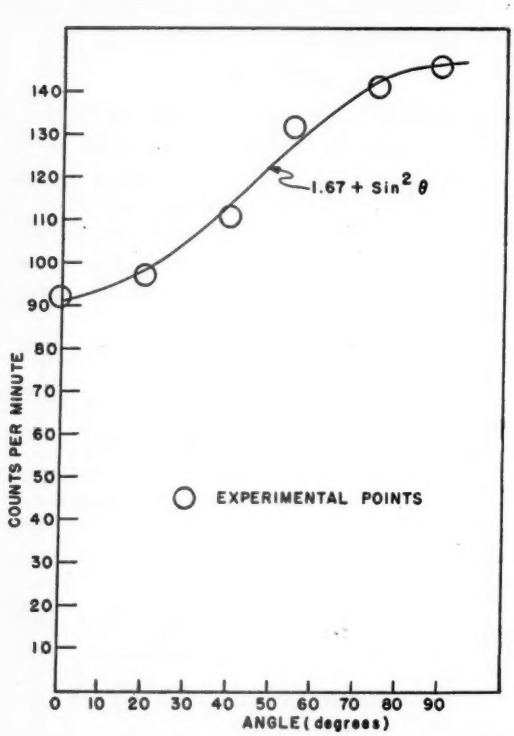

FIG. 2. The angular distribution of photo-neutrons from beryllium at 2.76 Mev.

b—the natural background of the counter.

S—the room scattered neutrons, i.e., those neutrons that reach the counter because they have been scattered by the walls, floor, and ceiling of the room.

C—the neutrons that were produced in the paraffin surrounding the counter. These arise from the photo-disintegration of the deuterium contained in the paraffin in its natural isotopic abundance.

W—the wall-produced neutrons. These arise from the photo-disintegration of the deuterium contained in the walls, floor, and ceiling.

C and W are only present to an appreciable extent when the Na^{24} source was used.

The counting rate, due to the room scattered neutrons, S, was determined by interposing a tapered lead plug 30-cm long between the target and detector. The plug prevented the detector from seeing any portion of the beryllium target.

The experimental procedure was to go through a cycle of four measurements at each angle. The natural background, b, was determined at the beginning and end of a run. The cycle was as follows:

I—Beryllium target present, no lead plug,
II—No target, no lead plug,
III—Beryllium target present, lead plug in,
IV—No target, lead plug in.

These four measurements are related to E, C, W, S, and b in the following way:

$$\begin{aligned} \text{I} &= E+S+C+W+b, \\ \text{II} &= C+W+b, \\ \text{III} &= S+W+b, \\ \text{IV} &= W+b. \end{aligned}$$

The effect we are interested in is E=I–II–(III–IV). When W and C are zero or negligible, only measurements I and III are necessary.

DATA

(1) Sb^{124} and Mn^{56} gamma-rays.

The angular distribution of the photo-neutrons was found to be spherically symmetrical within the limits of the experimental errors for both Sb^{124} and Mn^{56} gamma-rays.

(2) Na^{24} gamma-rays.

Table I gives the average of a set of cycles obtained with a source of Na^{24} gamma-rays. The last column gives the counting rate caused by the effect we are trying to study after all the backgrounds have been subtracted. (In this table an average of (III–IV) for all angles was used in calculating the last column, E.)

Figure 2 shows a least square fit of the data to a curve of the form $A+B\sin^2\theta$. There seems to be good correlation between the experimental data and the curve. If one accepts the conclusion that the angular distribution is of the above form, then the most important parameter that is desired is the ratio A/B. This ratio can be most readily obtained by obtaining good data at 0° and 90°. An average of three runs, each

extending over periods greater than fifteen hours, gave $A/B=1.58$. This value is not the value for the actual distribution emitted by the beryllium nuclei; one must correct for two important effects.

CORRECTIONS

The observed angular distribution, $A+B\sin^2\theta$ requires correction for the following:

(1) The geometry employed, i.e., the finite size of the target, source, and detector result in a spread around the listed central angle.

(2) Neutron scattering effect, i.e., a small percentage of the neutrons undergo scattering in the beryllium target, and these neutrons are shifted from one angular range to some other before escaping from the beryllium.

The geometrical effect, (1), is comparatively small and can be estimated by numerical integration. It turns out that if the angular distribution of the neutrons leaving the beryllium target is of the form $a'+b'\sin^2\theta$, then with the geometry employed here, the distribution that will be observed is

$$A+B\sin^2\theta,$$

where $A=a'+0.034b'$ and $B=a'+0.99b'$.

The effect on the distribution of those neutrons that are scattered before leaving the target is more difficult to estimate. It tends to make the observed neutron distribution appear more spherically symmetric. The correction was estimated graphically for the targets employed here and has been roughly checked experimentally in the course of similar experiments on D_2O which are still incomplete.

If the probability distribution for the emission of the neutrons by a nucleus is of the form $a+b\sin^2\theta$ and due to the scattering within the target the neutrons leaving the beryllium target have a distribution of the form $a'+b'\sin^2\theta$, then the relationships between these quantities are

$$a'=1.02a+0.12b, \quad b'=0.90b,$$

for the targets employed in these experiments and for the neutrons from Na^{24}+Be.

Applying the above correction to the experimentally observed values of A/B, we obtain a corrected value of a/b of 1.22 for the Na^{24}+Be source.

TABLE I. Average counting rate obtained from Na^{24} source.

Angle	I Be target (counts/min.)	II No target (counts/min.)	III Be target and lead plug (counts/min.)	IV No target and lead plug (counts/min.)	E Effect (counts/min.)
0°	213.5	98.6	36.1	11.4	91.6
20°	239.6	116.2	37.6	11.8	97.4
40°	266.4	129.7	36.9	9.7	110.7
55°	298.4	140.5	39.1	11.3	131.9
75°	322.4	154.6	42.6	18.8	141.1
90°	352.1	180.3	54.8	25.4	145.8

COMPARISON WITH THEORY

For the lower energy γ-rays an isotropic distribution is expected because of their proximity to the photo-disintegration threshold.

The angular distribution can be calculated for the simple model discussed by Guth and Mullin.[4] The Be^9 is regarded as an inert Be^8 (2α-particle) core, with a "valence" neutron in the ground $P_{3/2}$ state. On this model, no magnetic dipole transitions are possible. Electric dipole transitions to S states will give a spherically symmetric distribution, while transitions to D states lead to a distribution of the form $a+b\sin^2\theta$, with $a/b=17/12\simeq 1.4$. The rise in total cross section is ascribed[4] to the $P-D$ transition; the residual effect of the transition to S states increases slightly the expected a/b value.

A splitting of the D levels will decrease the value of a/b for the $P-D$ transition. In this way Guth and Mullin[5] obtain a value that is in agreement with the value for Na^{24} γ-rays found in this experiment.

ACKNOWLEDGMENTS

It is a pleasure to acknowledge the valuable assistance of John Dalman in the construction of the equipment employed in this experiment and his help in obtaining the data. We also wish to thank Rena Levy for carrying out the numerical integration needed to determine the corrections.

[4] E. Guth and C. J. Mullin, Phys. Rev. 74, 833 (1948).
[5] E. Guth and C. J. Mullin, Phys. Rev. 76, 682 (1949).

K Capture of Be^7 and the Excited State of Li^7

R. M. WILLIAMSON AND H. T. RICHARDS
University of Wisconsin, Madison, Wisconsin
(Received May 23, 1949)

The fraction of Be^7 K capture to the 478 kev excited state of Li^7 has been experimentally determined to be 0.107 ± 0.02. The experimental method consisted in measuring the number of Be^7 atoms by counting neutrons from the $Li^7(pn)Be^7$ reaction, and in observing the subsequent number of 478 kev gammas by use of a counter calibrated by beta-gamma-coincidences from Au^{198}. Implications concerning the character of the 478 kev Li^7 level are discussed.

UNTIL recently it has been usually assumed that the 478 kev excited state of Li^7 was the $P_{\frac{1}{2}}$ branch of a spin multiplet with the ground state being the $P_{3/2}$ branch since the observed total angular momentum of the ground state is $\frac{3}{2}$. Such an assignment was consistent[1,2] with the one published measurement[3]† of the fraction (3 percent–30 percent) of Be^7 K captures to the excited state of Li^7. When, however, the total angular momentum of the ground state of B^{10} was measured[4] to be 3 instead of 1, it became difficult to understand why the disintegration of B^{10} by thermal neutrons, $B^{10}(n,\alpha)Li^7$, should leave the Li^7 in the 478 kev excited state in 93 percent of the disintegrations.[5]

To explain the boron disintegration branching, Inglis[6] has postulated that the excited state of Li^7 was a $F_{5/2,7/2}$ spin multiplet. Such an F state is hard to reconcile with the above branching of K capture in Be^7 if the ground states of Be^7 and Li^7 are to be regarded as primarily P states. However, there were large experimental uncertainties in the old branching ratio measurement, and hence an independent and more direct determination of this branching ratio seemed desirable.

Our method for determination of the branching ratio consisted in (1) measuring the number of Be^7 nuclei formed in the $Li^7(p,n)Be^7$ reaction by counting the neutrons in a calibrated neutron counter, and (2) in observing the number of K captures to the excited state by counting the 478 kev gammas from the subsequent decay of the excited state.

The calibration of the gamma-counter can be made quite accurate because of the fortunate circumstance that the simple beta-decay of Au^{198} is followed by a single gamma-ray[7–12,*] whose energy of 411.2 kev[11] is nearly the same as the 478 kev gamma from lithium so that only a small correction is required for the change in gamma-counting efficiency as a function of gamma-ray energy. The efficiency (including solid angle) of the gamma-counter was determined in the conventional manner[13] by counting simultaneously the single counts in a beta-counter and the beta-gamma-coincident counts between the beta- and gamma-counters which were located on opposite sides of a $\frac{1}{8}$-inch diameter piece of activated 0.003 inch gold foil. For this geometry, it was shown experimentally that small variations in the position, size and thickness of the gold source had negligible effects on the efficiency determinations. We believe that the calibration of the gamma-counters was good to about 6 percent.

The determination of the number of neutrons (hence Be^7 nuclei) was more difficult, though we may hope for only a 10 percent uncertainty in this factor by making proper choice of neutron detector and bombarding conditions. An energy insensitive shielded "long counter"[14] one meter from the target and at 0° to the proton beam was the neutron detector. This long counter was then calibrated in position by placing a calibrated Ra-Be neutron source at the target. The relative efficiency for counting the Ra-Be neutrons is the same as that for counting 500 kev neutrons according to Fig. 5 of reference 14.

Two different thin (30 kev and 15 kev) lithium targets were bombarded by about 6 microampere hours of 2.3 Mev protons. At this voltage, the neutron energy in the forward direction is about 500 kev and the laboratory angular distribution is very asymmetric. The total neutron flux was obtained by use of Taschek and Hemmindinger's data[15] on the angular distribution at this energy. Since the neutron detector is at 0°, the strong forward bunching of the neutrons makes the integrated

[1] G. Breit and J. Knipp, Phys. Rev. **54**, 652 (1938).
[2] E. Konopinski, Rev. Mod. Phys. **15**, 209 (1943).
[3] Rumbaugh, Roberts, and Hafstad, Phys. Rev. **54**, 657 (1938).
† *Note added in proof.*—C. M. Turner, in a recent letter in Phys. Rev. **76**, 148 (1949), reports a preliminary value of 10 to 13 percent for the fraction of Be^7 K captures to the excited state of Li^7. This value is in good agreement with the present work.
[4] Gordy, Ring, and Burg, Phys. Rev. **74**, 1191 (1948).
[5] C. W. Gilbert, Proc. Camb. Phil. Soc. **44**, 447 (1948); J. K. Boggild, Kgl. Danske Vid. Sels. Math. Fys. Medd. **23**, 4 (1945).
[6] D. R. Inglis, Phys. Rev. **74**, 1876 (1948).
[7] D. Saxon and R. Heller, Phys. Rev. **75**, 909 (1949).
[8] K. Siegbahn and A. Hedgran, Phys. Rev. **75**, 523 (1949).
[9] E. Jurney, Phys. Rev. **74**, 1049 (1948).
[10] R. Wilkinson and C. Peacock, Phys. Rev. **74**, 1250 (1948).
[11] DuMond, Lind, and Watson, Phys. Rev. **73**, 1392 (1948).
[12] P. Levy and E. Greuling, Phys. Rev. **75**, 819 (1949).

* References 11 and 12 take exception to this statement and report the presence of low intensity 208 kev and 157 kev gamma-rays. However, were the decay scheme advocated by Levy and Greuling to be substantiated, a rough estimate shows that our counter calibration would be changed by about 8 percent. The change would raise our values of $(\lambda^*/\lambda+\lambda^*)$ in Table I by about 8 percent.
[13] A. C. G. Mitchell, Rev. Mod. Phys. **20**, 296 (1948).
[14] A. O. Hanson and J. L. McKibben, Phys. Rev. **72**, 673 (1947).
[15] R. F. Taschek and A. Hemmindinger, Phys. Rev. **74**, 373 (1948).

TABLE I. Summary of measurements on the fraction of Be^7 K captures which leave the Li^7 nucleus in the 478 kev excited state.

Lithium Target	No. 1	No. 2	No. 3
Thickness (kv)	90	30	15
Bombarding proton energy in Mev	2.0	2.3	2.3
Total counts (C_n) in neutron detector	1.71×10^6	3.12×10^6	0.691×10^6
Relative efficiency (μ) for detection of neutrons from Ra-Be and from $Li^7(pn)Be^7$	1.04[a]	1.00[a]	1.00[a]
$\alpha=\sigma/4\pi\sigma(0°)$ where $\sigma(0°)$ is the differential cross section of the $Li^7(pn)Be^7$ reaction and σ is the total cross section	0.64[b]	0.34[b]	0.33[b]
Total number of Be^7 atoms, $N_{Be^7}=[\mu C_n\alpha/(\epsilon_n\omega_n)_{RaBe}]$ where $(\epsilon_n\omega_n)_{RaBe}=0.757\pm0.01\times10^{-6}$ is the observed neutron detection efficiency, including solid angle, for the calibrated Ra-Be source	1.50×10^{12}	1.40×10^{12}	0.302×10^{12}
Observed Be^7 gamma-activity, A_{Be^7} (corrected for decay) in counts per sec.	16.8±0.2	16.9±0.2	3.45±0.2
Fraction $(\lambda^*/\lambda+\lambda^*)$ of Be^7 K captures which lead to Li^7 excited: $(\lambda^*/\lambda+\lambda^*)=[A_{Be^7}/N_{Be^7}(\lambda+\lambda^*)(\epsilon\gamma\omega\gamma)_{Be^7}]$ where $\lambda+\lambda^*=\log2/T_{\frac{1}{2}}$ and $T_{\frac{1}{2}}=52.93\pm0.22$ days[c] $(\epsilon\gamma\omega\gamma)_{Be^7}=7.1\pm0.4\times10^{-4}$ = gamma-counting efficiency (including solid angle) for the Be^7 activity $=(478/411)(\epsilon_\gamma\omega_\gamma)_{Au^{198}}=(478/411)(N_{\beta\gamma}/N_\beta)_{Au^{198}}$	0.104±0.006	0.112±0.007	0.106±0.007

[a] From Fig. 5 of reference 14.
[b] From Figs. 2–4 of reference 15.
[c] Reference 16.

neutron flux relatively insensitive to possible uncertainties in the angular distribution at the large angles.

A third lithium target was bombarded by 2.0 Mev protons. At this energy the angular distribution in the laboratory is much more nearly spherically symmetric.[15]

Any neutron induced activity in the 0.010 inch tantalum target backings was shown experimentally to be less than 2 percent of the Be^7 activity and hence negligible for these measurements. It should also be pointed out that no Be^7 activity is lost by recoiling Be^7 nuclei leaving the target. Since the reaction is endothermic, the velocity of the center of mass system is always large compared to Be^7 center of mass velocity, and hence in the laboratory system all Be^7 recoils are toward the tantalum backing.

All measured Be^7 activities were corrected to the initial activities by using Segré and Wiegand's precise value[16] of the half-life, $T_{\frac{1}{2}}=52.93\pm0.22$ days.

Results for the three targets are shown in Table I where the indicated errors are only statistical. The agreement of the data for targets bombarded with different proton energies indicates absence of large errors arising from uncertainties in the angular distribution of the neutrons. The major error in absolute number of neutrons probably is associated with the Ra-Be neutron standard. This Ra-Be source was calibrated last August at the Argonne National Laboratories as emitting 0.998×10^6 neutrons per second. However, in view of the difficulties in absolute flux measurements, we doubt whether our number of Be^7 atoms is known to better than 10 percent.

A mean value from all three targets would therefore give for the fraction (f) of transitions to the excited state, $f=0.107\pm0.02$, where the indicated error now includes an estimate of the uncertainty in both the neutron and gamma-calibration.

[16] E. Segré and C. Wiegand, Phys. Rev. **75**, 43 (1949).

DISCUSSION

Experimentally Be^7 K capture is an "allowed" transition.[2] In the discussion of our experimental data, we will follow Rosenfeld's[17] treatment of allowed transitions on Wigner's approximation. On Wigner's "first approximation" only transitions between the "fine structure" components of a multiplet are "allowed" and all terms have a definite L but not necessarily a definite S. The general expression for the lifetime is

$$1/T_{\frac{1}{2}}=(1/\tau_0\log2)\sum_f|G_{if}|^2I(W_{if}),$$

where τ_0 is the characteristic time constant of beta-decay, G_{if} is the matrix element for the transition from an initial state i to a final state f and $I(W_{if})$ for our case of K capture is

$$I(W_{if})=2\pi(Z_{\text{eff}}/137)^3W_{if}^2,$$

where W_{if} is the difference in energy (in units mc^2) between the initial and final state. $Z_{\text{eff}}=3.7$ for Be.

For Be^7 K capture the sum is taken over the transition to the ground state of Li^7 and to the 478 kev level. The differences in energy between the initial and final states are now known very accurately from the recent absolute voltage determination[18] of the $Li^7(p,n)Be^7$ threshold (±0.1 percent) and the $n-H$ mass difference[19]

[17] L. Rosenfeld, *Nuclear Forces* (Interscience Publishers, Inc., New York, 1949), Vol. II, Appendix I, p. 377.
[18] Herb, Snowdon, and Sala, Phys. Rev. **75**, 246 (1949).
[19] Tollestrup, Jenkins, Fowler, and Lauritsen, Phys. Rev. **76**, 181 (1949).

(=0.800±0.004 Mev) and energy of the gamma-ray (478±1.5 kev)[20] from the excited state of Li^7. The resulting W's are given in Table II.

For the assumption of the Gamow-Teller interaction, the matrix elements can be calculated by the usual procedures of atomic spectroscopy.[21] The results are displayed in Table II for various assumptions concerning the character of the states involved.

From Table II it is seen that transitions (2) and (3) are definitely excluded by the present measurements. Transition (1) almost agrees with the present experiment but of course the $P_{\frac{1}{2}}$ assignment to the excited level of Li^7 is in disagreement[6,22] both with the branching of $B^{10}(n\alpha)Li^7$ and with the variation[3] with deuteron energy of the $Li^6(dp)Li^7$ reactions. Transition (4) does not quite satisfy the present experimental data, and furthermore the assumed difference in total angular momentum of the ground states of the mirror nuclei Be^7 and Li^7 is very unlikely according to current ideas of nuclear structure.

The existence of tensor forces may be expected to produce a mixing of states. In transition (5) we assume that the ground states of Be^7 and Li^7 are identical and primarily $P_{3/2}$ but contain an unspecified admixture of $D_{3/2}$. On the further assumption that the excited state is predominantly $D_{5/2}$, we may use the experimentally determined branching ratio to estimate roughly the amount of admixture required. The result is a 25 percent $D_{3/2}$ probability. The approximate character of this result should be emphasized since among other things, the matrix elements may be sensitive to detailed assumptions concerning the respective wave functions. It will be noted that transition (5) is also consistent with the $B^{10}(n\alpha)Li^7$ branching and with the dependence on deuteron energy of the $Li^6(dp)Li^7$ reactions.

It is possible that this large admixture of $D_{3/2}$ may give trouble in understanding the magnetic moment of Li^7. However, the pure $P_{3/2}$ state usually assumed does not in itself predict[23] a value of the magnetic moment in very good agreement with experiment. Furthermore, the neglect of contributions from exchange currents may not be justified. Therefore, perhaps the possibility of a large $D_{3/2}$ admixture warrants further consideration.

Two other hypotheses might reconcile all the experimental data:

(a) Two different excited levels of Li^7 may be involved.

TABLE II. Comparison of possible allowed transitions.

Transition assumed	$\lvert G_{if}\rvert^2$ on GT interaction	W_{if}	Branching ratio $\frac{\lambda^*}{\lambda}=\frac{\lvert G^*\rvert^2 I^*(W)}{\lvert G\rvert^2 I(W)}$	Fraction to excited state $\frac{\lambda^*}{\lambda+\lambda^*}$	τ_0 (sec.)
(1) $P_{3/2}\rightarrow P_{1/2}$	4/9	0.725	0.152	0.13	1.44×10^3
(1) $P_{3/2}\rightarrow P_{3/2}$	5/9	1.66			
(2) $P_{1/2}\rightarrow P_{1/2}$	1/9	0.725	0.024	0.023	
(2) $P_{1/2}\rightarrow P_{3/2}$	8/9	1.66			
(3) $D_{3/2}\rightarrow D_{5/2}$	12/15	0.725	0.759	0.43	
(3) $D_{3/2}\rightarrow D_{3/2}$	3/15	1.66			
(4) $D_{5/2}\rightarrow D_{5/2}$	7/15	0.725	0.166	0.14	1.40×10^3
(4) $D_{5/2}\rightarrow D_{3/2}$	8/15	1.66			
(5) $aP_{3/2}+bD_{3/2}\rightarrow D_{5/2}$	$b(12/15)$	0.725	0.120	0.107	1.69×10^3
(5) $aP_{3/2}+bD_{3/2}\rightarrow aP_{3/2}+bD_{3/2}$	$a^2(5/9)+b^2(3/15)$	1.66			

(a=0.75; b=0.25, chosen to give correct experimental value)

[20] L. G. Elliot and R. E. Bell, Phys. Rev. **74**, 1869 (1948).
[21] For example see Rosenfeld, reference 17, p. 380. In his formula (13) of Section A1.131 replace $2(L-1)$ by $(2L-1)$.
[22] L. R. Hafstad and E. Teller, Phys. Rev. **54**, 681 (1938).
[23] For a summary discussion and references see Rosenfeld, reference 17, p. 413.

(b) The total orbital angular momentum L may not be a good quantum number.††

Hypothesis (a) seems unlikely in view of the recent determinations[20,24] of the equivalence in energy of the excited state independent of the reaction producing it.

An experimental measurement of the angular momentum and magnetic moment of Be^7 would be of great help in choosing between various hypotheses, as also would a measurement of the electric quadrupole moment of Li^7.‡

In Table II is also included a calculation of τ_0, the characteristic time constant of beta-decay, which employs the very accurate data on $I(W)$ and $T_{\frac{1}{2}}$ which is now available.

This work has been supported in part by the Wisconsin Alumni Research Foundation and in part by the AEC.

†† *Note added in proof.*—This hypothesis is discussed by S. S. Hanna and D. R. Inglis in a recent letter to Phys. Rev. **75**, 1767 (1949).

[24] Rasmussen, Lauritsen, and Lauritsen, Phys. Rev. **75**, 199 (1949); Zaffarano, Kern, and Mitchell, Phys. Rev. **74**, 105 (1948); F. N. D. Kurie and M. Ter-Pogossian, Phys. Rev. **74**, 677 (1948); Buechner, Strait, Stergiopoulos, and Sperduto, Phys. Rev. **74**, 1569 (1948); Fowler, Lauritsen, and Rubin, Phys. Rev. **75**, 1463, 1471 (1949).

‡ *Note added in proof.*—The sign of the electric quadrupole moment of Li^7 has been recently found (Kusch, Phys. Rev. **76**, 138 (1949)) to be positive instead of negative as expected on past nuclear models. According to recent unpublished calculations of R. Avery and C. Blanchard at the University of Wisconsin, both the magnetic moment and electric quadrupole moment of Li^7 can be accounted for correctly in sign and approximate magnitude by assuming that the ground state of Li^7 is predominately $D_{3/2}$.

PHYSICAL REVIEW VOLUME 76, NUMBER 5 SEPTEMBER 1, 1949

Neutron-Capture Cross Section of 85-Minute Ba^{139}

L. Yaffe, B. W. Sargent, M. Kirsch,* S. Standil,** and Jean M. Grunlund
Atomic Energy Project, National Research Council of Canada, Chalk River, Ontario, Canada

(Received May 9, 1949)

Four samples of barium carbonate were irradiated with neutrons at three different times and at three different positions in the heavy water pile. A few days after an irradiation, lanthanum separations were made until no further La^{140} activity could be detected. The lanthanum was discarded. At intervals of 4 to 9 days the La^{140} grown from the Ba^{140} was separated and its number of atoms determined with a calibrated Geiger-Müller counter. The fluxes of thermal neutrons were obtained by experiment as far as possible; the maximum used was 2.0×10^{13} neutrons/cm²/sec. The final value for the capture cross section of Ba^{139} is 4.7 ± 1.2 barns.

I. INTRODUCTION

CROSS SECTIONS for the capture of thermal neutrons by stable elements have been measured in numerous investigations. A nucleus of mass A transforms to one of mass $A+1$ when a neutron is captured. This nucleus is radioactive in some cases and stable in others. Some methods of measuring capture cross sections that require little or no knowledge of scattering cross sections are (1) the activation method, (2) the pile reactivity method, and (3) the mass spectrographic method. The activation method is applicable when the nuclei formed by neutron-capture are radioactive. The number of thermal neutrons captured per second is equal to and in practice obtained from the number of β-disintegrations per second at saturation. This method of measuring capture cross sections has been applied, for instance, by Seren, Friedlander, and Turkel,[1] who discussed it in detail and presented a long list of measurements. When the nucleus of mass $A+1$ is stable, the number of thermal neutrons captured per second has to be determined in some other way such as by the change in the reactivity of a chain-reacting pile.[2] If the capture cross section is high, the mass spectrograph shows a measurable change in the relative abundances of the isotopes before and after a prolonged irradiation.[3] Numerical values of cross sections could be obtained in favorable cases.

The combination of high flux of thermal neutrons in a pile and the activation method permits capture cross sections to be measured even for β-active nuclei. A stable isotope of atomic number Z and mass A is irradiated with neutrons in a pile, producing β-active isotopes of masses $A+1$, $A+2$, $\cdots$ in succession. The amounts of these successive isotopes produced in a given time are in rapidly decreasing orders of magnitude. It is clear that if the neutron flux is sufficiently high, the amount of isotope of mass $A+2$ produced by neutron bombardment can, in many cases, be either directly measured, or obtained from a measurement on

* Now at the Department of Chemistry, University of Manitoba, Winnipeg, Manitoba.
** Now at the Department of Physics, Queen's University, Kingston, Ontario.

[1] Seren, Friedlander, and Turkel, Phys. Rev. **72**, 888 (1947).

[2] Anderson, Fermi, Wattenberg, Weil, and Zinn, Phys. Rev. **72**, 16 (1947).

[3] Lapp, VanHorn, and Dempster, Phys. Rev. **71**, 745 (1947). A. J. Dempster, Phys. Rev. **71**, 829 (1947).

the separated daughter substance $(Z+1, A+2)$ if it is radioactive, by the very sensitive method of β-particle detection. This may be related to the capture of neutrons by the β-active isotope of mass $A+1$. If, in addition, the amount of the latter formed in the given time is similarly measured or calculated from the known weight of isotope of mass A and its capture cross section, and if the neutron flux is known, the capture cross section of isotope of mass $A+1$ can be deduced. The method may be complicated by the formation of $(Z+1, A+2)$ by neutron-capture in $(Z+1, A+1)$, and by other β-activities if the stable element that is introduced into the pile consists of several isotopes.

An extensive knowledge of the neutron-capture cross sections of both stable and radioactive nuclei may show further interesting regularities[4] and may assist in accounting for the abundances of elements and of their isotopes found in nature.[5] The present paper is one of a series giving measurements of neutron-capture cross sections of β-active nuclei. It is concerned with Ba^{139}, a β-emitter of half-period 85 minutes, which occurs with high yield in fission initiated by slow neutrons.

II. DETAILED NUCLEAR REACTIONS

It is preferable to produce the Ba^{139} by neutron-capture in stable Ba^{138} than to separate it from mixed fission products. The pertinent nuclear reactions that occur when natural barium is irradiated in a pile are as follows:

$_{56}Ba^{138}$ (71.66 percent of natural barium)

(n,γ)

$$Ba^{139} \xrightarrow[85\text{ min.}]{\beta^-} {}_{57}La^{139}\text{ (stable)}$$

$$Ba^{140} \xrightarrow[12.8\text{ days}]{\beta^-} La^{140} \xrightarrow[40\text{ hr.}]{\beta^-} {}_{58}Ce^{140}\text{ (stable)}; \qquad \text{(I)}$$

Ba^{130} (0.101 percent of natural barium)

(n,γ)

$$Ba^{131} \xrightarrow[12.0\text{ days}]{K} {}_{55}Cs^{131} \xrightarrow[9.6\text{ days}]{K} {}_{54}Xe^{131}\text{ (stable)}; \qquad \text{(II)}$$

Ba^{132} (0.097 percent of natural barium)

(n,γ)

$$Ba^{133*} \xrightarrow[38.8\text{ hr.}]{I.T.} Ba^{133} \xrightarrow[20\text{ yr.}]{K} Cs^{133}\text{ (stable)}. \qquad \text{(III)}$$

Let P, Q, R, U, and V represent, respectively, the numbers of atoms of Ba^{138}, Ba^{139}, Ba^{140}, La^{139}, and La^{140} present at any time t during neutron irradiation at a constant flux $\rho v(\approx 10^{13}$ neutrons/cm^2/sec.). The subscripts 0, 1, 2, 3, and 4 will be used to designate the respective neutron-capture cross sections σ and transformation constants λ of these nuclei. The differential equations that apply during the irradiation are as follows:

$$dQ/dt=\rho v\sigma_0 P-\lambda_1 Q-\rho v\sigma_1 Q \approx \rho v\sigma_0 P-\lambda_1 Q; \qquad (1)$$

$$dR/dt=\rho v\sigma_1 Q-\lambda_2 R-\rho v\sigma_2 R \approx \rho v\sigma_1 Q-\lambda_2 R; \qquad (2)$$

$$dU/dt=\lambda_1 Q-\rho v\sigma_3 U; \qquad (3)$$

$$dV/dt=\rho v\sigma_3 U+\lambda_2 R-\lambda_4 V-\rho v\sigma_4 V \approx \rho v\sigma_3 U+\lambda_2 R-\lambda_4 V. \qquad (4)$$

P is assumed to be constant. At $t=0$, $Q=R=U=V=0$. At the end of the irradiation of duration T, the desired formulas are as follows:

$$Q_T=\frac{\rho v\sigma_0 P}{\lambda_1}(1-e^{-\lambda_1 T}); \qquad (5)$$

$$R_T=\frac{(\rho v)^2\sigma_0\sigma_1 P}{\lambda_1\lambda_2}(1-e^{-\lambda_2 T})-\frac{(\rho v)^2\sigma_0\sigma_1 P}{\lambda_1(\lambda_1-\lambda_2)}(e^{-\lambda_2 T}-e^{-\lambda_1 T}); \qquad (6)$$

$$U_T=\frac{\sigma_0 P}{\sigma_3}(1-e^{-\rho v\sigma_3 T})-\frac{\rho v\sigma_0 P}{\lambda_1-\rho v\sigma_3}\times(e^{-\rho v\sigma_3 T}-e^{-\lambda_1 T}) \approx \rho v\sigma_0 PT; \qquad (7)$$

$$V_T \approx \frac{(\rho v)^2\sigma_0\sigma_3 PT}{\lambda_4}+\frac{(\rho v)^2\sigma_0\sigma_1 P}{\lambda_4\lambda_4}(1-e^{-\lambda_4 T})-\frac{(\rho v)^2\sigma_0\sigma_1 P}{\lambda_1(\lambda_4-\lambda_2)}(e^{-\lambda_2 T}-e^{-\lambda_4 T}). \qquad (8)$$

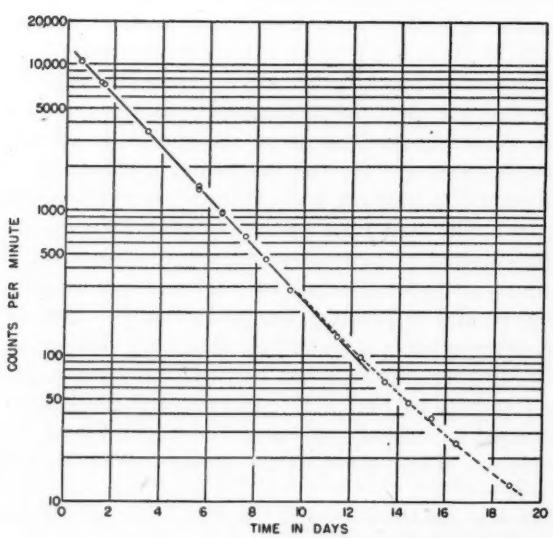

FIG. 1. Decay of separated lanthanum. Half-period is 41 hours when allowance of 10 counts per minute (i.e., 0.1 percent of initial activity) is made for barium contamination.

[4] M. G. Mayer, Phys. Rev. 74, 235 (1948).
[5] R. A. Alpher, Phys. Rev. 74, 1577 (1948); R. A. Alpher and R. C. Herman, Phys. Rev. 74, 1737 (1948).

In formula (8) the first term arises from the neutron-capture by La^{139} and the other terms from the β-decay of Ba^{140}.

An examination of formulas (5)–(8) suggests that the following four methods should be considered in determining σ_1, the neutron-capture cross section of Ba^{139}.

1. Determine the ratio of the β-counting rates of Ba^{140} and Ba^{139} at the end of the irradiation. (Formulas (5) and (6).) This method has the advantages of being independent of σ_0, the capture cross section of Ba^{138}, which is not accurately known, and of the solid angle subtended at the Geiger-Müller counter.
2. Determine the absolute β-counting rate of Ba^{140} at the end of the irradiation. (Formula (6).)
3. Determine the absolute β-counting rate of La^{140} separated at the end of the irradiation. (Formula (8).)
4. Determine the absolute β-counting rate of La^{140} that grows from the Ba^{140} after the irradiation has stopped.

Methods 1 and 2 cannot be used owing to the Ba^{131} that is formed in nuclear reaction II. The similarity in the half-periods of Ba^{140} and Ba^{131} and the complexity of their decay chains make it difficult, if not impossible, to determine their separate activities. Method 3 is ruled out by the fact that the La^{140} formed from La^{139} (first term, formula (8)) is much greater than the La^{140} formed from Ba^{140} (second and third terms, formula (8)). In fact, assuming $\sigma_1=\sigma_3$, the ratios of these contributions are 1220 after one day, 350 after 10 days, and 450 after 30 days irradiation. Consequently, method 4 was adopted. At the end of the irradiation, lanthanum was separated from barium and discarded. The La^{140} grown from Ba^{140} during successive intervals was separated and measured. While the La^{140} formed during the irradiation, mainly from La^{139} of known capture cross section, could have been used to determine the neutron flux, this was not done as a La^{139} impurity of even one part per million in the original barium sample would have caused a large error.

Suppose the La^{140} is separated at a time t_1 measured from the end of the irradiation and new La^{140} grows during the subsequent time t_2. The formula for the new La^{140} separated at this time is

$$V=\lambda_2/(\lambda_4-\lambda_2)R_T e^{-\lambda_2 t_1}(e^{-\lambda_2 t_2}-e^{-\lambda_4 t_2}), \qquad (9)$$

which is used in the calculation of σ_1.

III. EXPERIMENTAL PROCEDURE

Barium carbonate (analytical reagent grade) was irradiated in high flux positions in the heavy water pile. To free the barium from lanthanum after irradiation, the procedure was in each case to dissolve the sample in dilute hydrochloric acid, and take an aliquot from which the barium content was determined as barium sulfate. About 300 mg lanthanum nitrate was added to the main sample and a hydroxide precipitation was made. This step was repeated, lanthanum carrier being added each time, until no La^{140} activity could be detected in the precipitate. The lanthanum hydroxide samples were discarded.

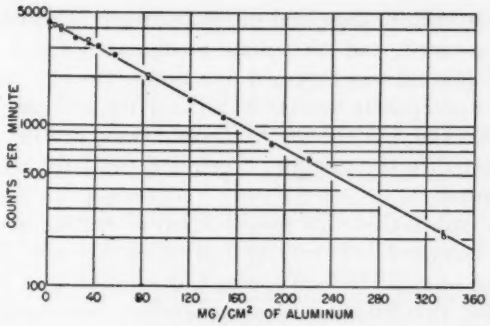

FIG. 2. Absorption of β-rays of La^{140} in aluminum. Crosses refer to lanthanum extracted from irradiated barium, circles to spectroscopically pure lanthanum after irradiation in the pile.

For collecting and separating the lanthanum that grows subsequently, the barium-containing solution was acidified and a weighed amount (about 300 mg) of lanthanum nitrate was added as a carrier. At a known time later (4 to 9 days), lanthanum hydroxide was precipitated from the solution. The precipitate was dissolved in dilute hydrochloric acid, barium chloride carrier added, and barium sulfate precipitated. Barium and caesium hold-back carriers were added to the centrifugate, and lanthanum hydroxide was again precipitated. The precipitate was washed with dilute

TABLE I.

Sample $BaCO_3$	Time in pile, days	Thermal neutron flux (neutrons/cm²/sec.) $\times 10^{-12}$	Elapsed time to first La separation, days
D	27.30	3.5	1.3
E	10.95	18	6.2
F	17.97	20	4.1
G	17.97	20	4.1

Note.—Samples *F* and *G* were irradiated together. The La^{140} separated at the time after irradiation given in column 4 was discarded.

TABLE II.

La^{140} sample measured	Gm $BaCO_3$	La^{140} growth time, days	La^{140} atoms formed $\times 10^{-8}$	$\sigma_1(Ba^{139})$, barns	
*D*1	5.38	5.6	2.23	5.12	
*D*2	5.19	5.9	1.42	4.58	
*D*3	5.19	6.1	1.11	4.93	
*E*1	1.20	4.0	5.53	4.40	
*F*1a	1.32	5.9	15.2	5.56	5.15
*F*1b	1.32	5.9	14.5	5.30	
*F*1c	1.32	5.9	12.6	4.60	
*F*2a	1.28	6.05	9.03	4.70	3.87
*F*2b	1.32	6.05	6.92	3.49	
*F*2c	1.29	6.05	6.59	3.39	
*F*2d	1.29	6.05	7.54	3.89	
*G*1	8.88	8.97	85.2	5.02	
*G*2	7.72	3.96	41.2	4.37	
*G*3	7.96	5.97	37.8	4.63	
*G*4	8.08	8.00	24.8	4.31	
*G*5	7.85	6.00	19.6	5.18	
*G*6	7.59	7.04	13.2	5.09	
				Average	4.72

Note.—The samples of La^{140} grown and measured are numbered in their natural order. Samples *F*1 and *F*2 were split into smaller samples *F*1a, *F*1b, etc., and the La^{140} separated and measured separately.

barium nitrate, dissolved in hydrochloric acid, barium carrier added, and the sulfate precipitated again. This cyclic process was repeated five times. The last barium sulfate precipitate was tested for activity, and none was found. The lanthanum hydroxide was precipitated, converted to the formate, dried, and the La^{140} activity measured.

To ensure that this precipitation of lanthanum had been complete, 300 mg lanthanum nitrate was added to the original barium-containing solution and a hydroxide precipitation was performed. No significant activity was ever found in this precipitate.

About 300 mg lanthanum nitrate carrier was again added to the solution, which had been acidified. The solution was allowed to stand until it was time for another La^{140} separation.

The La^{140} samples were mounted on aluminum trays, 7.1 cm^2 area, and the activity measured with a previously calibrated Geiger-Müller counter having a mica end-window of mass 2.8 mg per cm^2.

The decay curve of a lanthanum sample was followed for some time. This was corrected for the residual background due to barium contamination, which amounted to about one percent of initial La^{140} activity. The counting rate of the La^{140} at the time of precipitation was obtained by extrapolation. The number of disintegrations per minute was estimated from the counting rate by applying the following corrections:*** self-absorption of β-rays in the sample ($\sim$5 percent), external absorption by the air gap and counter window ($\sim$3 percent), back-scattering by the aluminum tray ($\sim$20 percent), counter efficiency, and percentage chemical recovery. The counter efficiency was found to be 7.5 percent using a standard Co^{60} source.

IV. RESULTS

The β-activity was identified as La^{140} by measurement of half-period and absorption of the β-rays in aluminum. Figure 1 shows a typical decay curve, which has a half-period of 41 hours when corrected for barium contamination. Figure 2 shows absorption measurements on the β-activities of the lanthanum separated from the irradiated barium and of La^{140} obtained by irradiating spectroscopically pure lanthanum in the pile.

The experimental results are shown in Tables I and II. Four samples of barium carbonate were irradiated at three different times and at three different positions in the pile.

The flux of thermal neutrons was determined by separate activations at the position for sample *D*. Five samples of lanthanum yielded a flux of 3.5×10^{12} neutrons/cm^2/sec. based on a capture cross section of 8.4 barns[1] for La^{139}. The variations from the mean were less than 3 percent. Two samples of barium carbonate yielded 1.67×10^{-12} and 1.75×10^{-12} neutron/sec./atom Ba^{138} for $\rho v\sigma_0$. Assuming $\sigma_0=0.511$ barn[1] for Ba^{138} the values of ρv are 3.3×10^{12} and 3.4×10^{12} neutrons/cm^2/sec., in good agreement with the measurements using lanthanum. It should be noted that σ_1 of Ba^{139} depends on the product of ρv and $\rho v\sigma_0$. The uncertainty in σ_1 arising from the error in $(\rho v)^2\sigma_0$ is somewhat reduced by the direct measurement of $\rho v\sigma_0$.

The fluxes of thermal neutrons for samples *E*, *F*, and *G* could not be conveniently measured by the activation method. The fluxes were therefore estimated from the measured heat output of the pile when operating, known pile constants, and the known spatial distribution of neutron density.

The irradiations of the samples were interrupted a number of times by the pile being shut down. The amounts of Ba^{139} and Ba^{140} built up have been accurately determined by a step by step application of Eqs. (1) and (2) over the times of operation (ρv tabulated) and shutdown ($\rho v=0$).

The final value of the capture cross section of Ba^{139} is 4.7 barns. The internal agreement of the various measurements is very satisfactory. Actually cadmium differences were not taken, but some rough experiments using cadmium to shield the samples indicate that the contribution of epicadmium neutrons to the activation is small. The measured cross section is therefore assumed to refer to neutrons of speed 2200 m/sec. for which the fluxes are quoted.

It is difficult to assess the error that should be associated with the measured cross section. Seren, Friedlander, and Turkel[1] assign a probable error of 20 percent to their measured cross sections of Ba^{138} and La^{139}, which were used here. We feel that 1.2 barns is sufficient for the probable error in our measured value of 4.7 barns.

Since this work was done we have learned that Katcoff[6] obtained 3.8 barns for the capture cross section of Ba^{139} in a previous measurement. He separated and measured La^{140} three times from a sample of irradiated barium carbonate. The agreement between the two independent measurements is satisfactory. Katcoff's result also depends on the accuracy of 0.511 barn assumed for the cross section of Ba^{138}.

We wish to thank Miss A. R. Rutledge for assistance in computing.

*** These were carefully determined in subsidiary experiments. The values in brackets are given only to indicate their magnitudes.

[6] S. Katcoff, Report CC-2908 of the Manhattan Project (1945).

Temperature Dependence of Susceptibility of Zinc, Cadmium, and Gamma-Brass*

JULES A. MARCUS**
*Sloane Physics Laboratory, Yale University,*** New Haven, Connecticut*
(Received May 9, 1949)

The temperature dependence (14°K–373°K) of the diamagnetic susceptibility of zinc and cadmium single crystals and several polycrystalline gamma-brasses has been investigated. For zinc, pronounced maxima occur in the susceptibility parallel to the hexagonal axis ($\chi_{\parallel}$) at 40°K and 105°K, and minima occur at 60°K and 180°K. The susceptibility perpendicular to the hexagonal axis ($\chi_{\perp}$) is independent of temperature from 14°K to 100°K and then decreases linearly as the temperature is increased. For cadmium, $\chi_{\parallel}$ decreases by a factor of three between 14°K and 373°K while $\chi_{\perp}$ increases by 7 percent in the same temperature interval. Measurements on polycrystals of copper-zinc alloys in the gamma-phase show that the temperature coefficient of susceptibility changes from positive to negative as copper content is increased, in agreement with previously reported measurements above room temperature. At the copper rich end of the phase, the susceptibility increases by 10 percent between 14°K and 293°K; at the zinc rich end of the phase, the susceptibility decreases by 3 percent in the same temperature interval.

WHILE the temperature dependence of the susceptibility of weakly paramagnetic and diamagnetic metallic elements has been extensively investigated for polycrystalline specimens,[1] data for single crystals and alloys is meager, particularly at low temperatures. Measurements which have been made on single crystals and alloys are however of considerable interest: the temperature dependence of susceptibility of bismuth,[2] antimony,[3] and graphite[4] single crystals, exhibits a marked anisotropy which of course is not apparent from data on polycrystals; for bismuth[2] and antimony alloys,[5] a slight change in composition produces a reversal in sign of the temperature coefficient of susceptibility and a similar effect has been observed at high temperatures for copper-zinc alloys in the gamma-phase.[6] As yet, these results have only been accounted for in a qualitative way. Further research along the same lines should yield information about the electronic structure of metals and prove useful in formulating a quantitative theory of the temperature dependence of susceptibility.

In the research reported here, the variation of susceptibility with temperature was investigated from 14°K to 300°K for single crystals of zinc and cadmium and for a series of polycrystalline copper-zinc alloys in the gamma-phase. The results for zinc were briefly reported in a previous communication.[7]

EXPERIMENTAL PROCEDURE

Single crystals of zinc and cadmium were grown by the Bridgman[8] method of slowly lowering a Pyrex tube containing the molten, outgassed metal through an electric furnace having a large temperature gradient. The resulting crystal was roughly 0.5 cm in diameter and 5 cm long. To obtain small cylindrical specimens suitable for measurements by the Faraday method, the rods were cut into sections 0.5 cm long by coating with paraffin, circumscribing notches in the paraffin at appropriate intervals and etching with acid. Where, as in some of the zinc rods, the cleavage plane was almost perpendicular to the axis of the rod, specimens of the desired dimensions were obtained by cleavage. While cutting with acid undoubtedly involved less deformation than cleavage, measurements on specimens prepared in the two ways differed by less than the experimental error. The cadmium and zinc used were Johnson, Matthey & Company H. S. metals for which the supplier's analysis indicated 99.999 percent purity.

Small polycrystalline specimens of copper-zinc alloys in the gamma-phase were synthesized and annealed by the method fully described by Lane.[6] Having obtained five alloys with compositions fairly well distributed

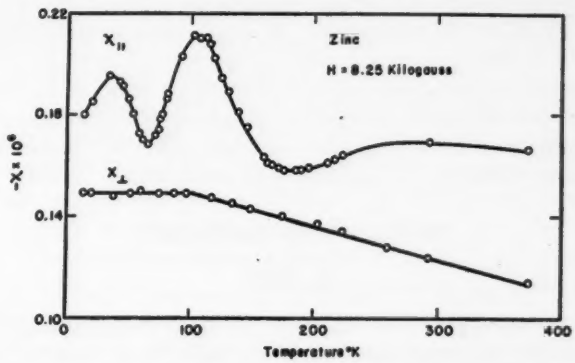

FIG. 1. Temperature dependence of the principal susceptibilities of zinc at a constant field strength of 8.25 kilogauss.

* Part of this work was included in a dissertation submitted in 1947 to the faculty of the Graduate School of Yale University in candidacy for the degree of Doctor of Philosophy.

** Now at the Institute for the Study of Metals, University of Chicago, Chicago, Illinois.

*** Assisted by the ONR under contract N6ori-44.

[1] K. Honda, Ann. d. Physik **32**, 1027 (1910); M. Owen, Ann. d. Physik **37**, 657 (1912); W. J. de Haas and P. M. van Alphen, Comm. Phys. Lab. Leiden, No. 225b (1933).

[2] D. Shoenberg and Z. M. Uddin, Proc. Roy. Soc. **A156**, 687 (1936).

[3] D. Shoenberg and Z. M. Uddin, Proc. Roy. Soc. **32**, 499 (1936).

[4] N. Ganguli and K. S. Krishnan, Proc. Roy. Soc. **A177**, 168 (1941).

[5] S. H. Browne and C. T. Lane, Phys. Rev. **60**, 899 (1941).

[6] C. T. Lane, J. App. Phys. **8**, 693 (1937).

[7] J. A. Marcus, Phys. Rev. **71**, 559 (1947).

[8] P. W. Bridgman, Proc. Am. Acad. **60**, 305 (1925).

across the phase, it was intended that measurements be made on both polycrystals and single crystals. However, attempts to grow single crystals failed and measurements were confined to polycrystalline specimens. The composition of the alloys was determined from the initial weight of the constituents and final weight of the castings, any loss in weight during the alloying process being ascribed to vaporization of zinc. No further chemical analysis was deemed necessary since at room temperature, the variation of susceptibility with composition was in sufficiently good agreement with the results

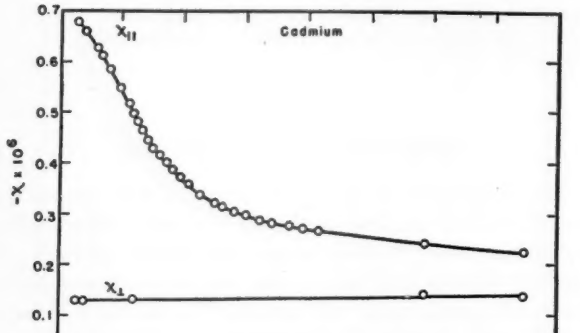

FIG. 2. Temperature dependence of the principal susceptibilities of cadmium.

of Smith[9] and Lane.[6] The materials used were Johnson, Matthey & Company H. S. brand copper (99.999 percent purity) and New Jersey Zinc Company S. P. zinc (99.999 percent purity). Mass susceptibilities were determined by the Faraday method employing a Sucksmith ring balance as described in a previous paper.[10]

Fixed temperatures were obtained by the use of liquid hydrogen, oxygen, nitrogen, air, methane, and ethylene, and were determined from vapor pressure measurements. Data at intermediate temperatures were obtained by allowing the specimen to warm up after the evaporation of the refrigerant, three and one-half hours being required for the specimen to reach room temperature after the evaporation of liquid hydrogen. During the warm-up, temperatures were measured with a calibrated copper-constantin thermocouple soldered to the copper tube surrounding the specimen. Readings agreed with those at fixed temperatures to within ± 1°K in the range where both methods were employed.

RESULTS AND DISCUSSION

A. Zinc

The temperature variation of the principal susceptibilities was measured from 14°K to 373°K in a magnetic field of 8.25 kilogauss, and the curves of Fig. 1 obtained.[11] For the susceptibility parallel to the hexagonal axis ($\chi_{\parallel}$), pronounced maxima occur at temperatures of 40°K and 105°K and minima at 65°K and 180°K. Below 64°K, $\chi_{\parallel}$ is field dependent[10] with the result that this part of the curve is of little significance for the present discussion.

TABLE I. Principal susceptibilities of cadmium at room temperature.

	$-\chi_{\parallel} \times 10^6$	$-\chi_{\perp} \times 10^6$	$\chi_{\parallel}/\chi_{\perp}$
McLennan, Ruedy, and Cohen[a]	0.261	0.160	1.63
Rao[b]	0.223	0.163	1.34
Present work	0.243	0.142	1.71

[a] McLennan, Ruedy, and Cohen, Proc. Roy. Soc. **A121**, 9 (1928).
[b] S. R. Rao and S. Sriraman, Proc. Roy. Soc. **A166**, 325 (1938).

In contrast, the temperature dependence of the susceptibility perpendicular to the hexagonal axis ($\chi_{\perp}$) is normal, having a constant value of -0.150×10^{-6} from 14°K to 100°K and then decreasing linearly to -0.114×10^{-6} at 373°K.

The peculiar temperature dependence of $\chi_{\parallel}$ does not seem to have been observed in other metals although Shoenberg[2] has found a single maximum or minimum in some bismuth alloys. For bismuth alloyed with 0.4 percent to 4 percent lead, a maximum occurs in $\chi_{\perp}$ at a temperature which increases from 100°K to 300°K as the lead content is increased, and a similar maximum occurs for bismuth-tin alloys. Where bismuth is alloyed with 0.11 percent tellurium, $\chi_{\perp}$ has a minimum in the neighborhood of 200°K. While the diamagnetism of these alloys is from five to fifteen times greater than that of free bismuth ions, the diamagnetism of zinc is less than that of free zinc ions (-0.23×10^{-6}) for temperatures down to 14°K and the net effect of the valence electrons must be paramagnetic. It therefore seems likely that the temperature dependence of the electron paramagnetism is of relatively greater importance for

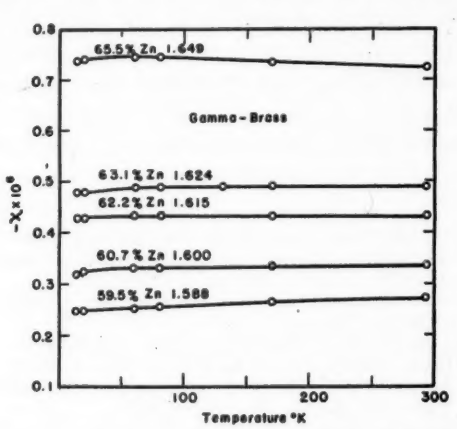

FIG. 3. Temperature dependence of the susceptibility of several gamma-brasses. The parameters are zinc content by weight and the electron ratio.

[9] C. S. Smith, Physics **6**, 47 (1935).
[10] J. A. Marcus, Phys. Rev. **76**, 413 (1949).

[11] For a comparison of our room temperature values of the principal susceptibilities with the results of other investigators, see Table I of reference 10.

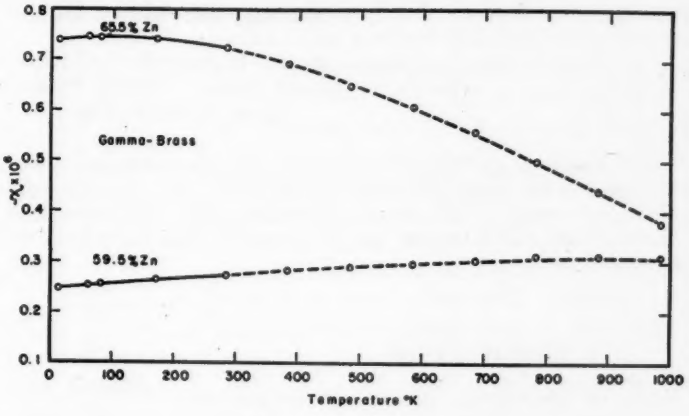

FIG. 4. Temperature dependence of the susceptibility of two gamma-brasses. The dashed part of the curves is taken from Lane's measurements.

zinc and may account for the more complicated susceptibility-temperature curves of Fig. 1.

B. Cadmium

The principal susceptibilities were measured at room temperature and 14°K in fields ranging from 3 to 9 kilogauss. No field dependence was observed at either temperature, indicating the absence of ferromagnetic impurities. Results at room temperature together with those of other investigators are given in Table I. The discrepancies are larger than can be accounted for by calibration errors and are most probably due to a difference in purity. Figure 2 shows the variation of the principal susceptibilities with temperature. The susceptibility parallel to the hexagonal axis ($\chi_{\parallel}$) increases by a factor of three from -0.225×10^{-6} at 373°K to -0.679×10^{-6} at 14°K and the increase apparently continues to lower temperatures. In the same temperature range, the susceptibility perpendicular to the hexagonal axis ($\chi_{\perp}$) decreases linearly to -0.130×10^{-6} at 14°K. The average susceptibility as calculated from these results using the formula $\bar{\chi}=\frac{1}{3}(\chi_{\parallel}+2\chi_{\perp})$, is 76 percent greater at 14°K than at room temperature which is in good agreement with the 78 percent increase observed in measurements on a polycrystal by de Haas and van Alphen.[1]

The striking difference in the susceptibility-temperature curves for cadmium and zinc indicates that the electronic structure of the two metals is significantly different despite a similarity in crystal structure. This is further borne out by the observation of an anomalous field dependence of susceptibility[10] and resistance[12] at low temperatures for zinc but not for cadmium. Bismuth[2] and antimony[3, 13] parallel zinc and cadmium with respect to these phenomena and the combined results should prove useful in determining the detailed electronic structures of these metals.

C. Gamma-Brass

The susceptibility of five polycrystalline specimens of copper-zinc alloys in the gamma-phase was measured at room temperature and 14°K in fields ranging from 3 to 9 kilogauss. No field dependence of susceptibility was observed and the room temperature values were in good agreement with those of Smith[9] and Lane.[6] Figure 3 shows the variation of susceptibility with temperature from 14°K to 293°K for the alloys where the curve for each specimen is identified by the weight percent of zinc and the electron ratio. At the copper rich end of the phase, the susceptibility decreases with decrease in temperature, the total change being 10 percent; at the zinc rich end of the phase, the susceptibility increases with decrease in temperature showing a total change of 3 percent.

Results for the most diamagnetic and least diamagnetic alloys are shown in Fig. 4 together with Lane's measurements on specimens of the same composition taken above room temperature. For the 65.5 percent Zn alloy, the temperature coefficient decreases considerably at low temperatures while for the 59.9 percent Zn alloy, very little change is observed.

Since no significantly new features were observed at low temperatures, Lane's[6] discussion of the thermomagnetic properties of gamma-phase alloys at high temperatures appears to be applicable over the extended temperature range.

The author wishes to thank Professor C. T. Lane and Dr. Henry Fairbank for their generous advice and assistance.

[12] Lazarev, Nachimovich, and Parfenova, C. R. Acad. Sci. U.R.S.S. **24**, 855 (1939).

[13] L. Schubnikov and W. J. de Haas, Comm. Phys. Lab. Leiden Nos. 207a, 207d (1930).

Energy Levels of Si^{30}

JOHN E. BROLLEY, JR., M. B. SAMPSON, AND ALLAN C. G. MITCHELL
Department of Physics, Indiana University, Bloomington, Indiana

(Received May 23, 1949)

The distribution in range of the protons arising when aluminum is bombarded by 22-Mev alpha-particles, produced in the cyclotron, has been investigated. Seven groups of protons, having energies up to 17 Mev, have been measured. The energy levels of the resulting Si^{30} nucleus have been calculated and are found to be 0.0, (2.28), 3.49, 7.18, 8.20, 9.26, 9.87, and 10.86 Mev. Inelastic scattering of protons from aluminum has also been measured.

1. INTRODUCTION

THE study of the energy of the various proton groups, arising when aluminum is bombarded by high energy alpha-particles, shows that, aside from the ground state of the residual Si^{30} nucleus—associated with the longest range particles—several excited states of the Si^{30} nucleus, associated with shorter range proton groups, are formed. The reaction has been studied by Chadwick and Constable[1] who established the existence of several proton groups. They also showed that the number of protons in a given group varied with the energy of the oncoming alpha-particles and that resonance effects existed at certain alpha-particle energies. This reaction was further studied by Duncanson and Miller[2] who established the ground state and three excited states of the Si^{30} nucleus at 0, 2.28, 3.66, and 4.6 Mev. Work of a similar nature was performed by Haxel[3] and Meerhaut,[4] with substantially similar results. All of the above authors used alpha-particles from radioactive sources as the bombarding particle. Benson[5] used alpha-particles of 7.3 Mev, produced in a cyclotron, to investigate the reaction, and found results essentially in agreement with the earlier authors. In addition, by measuring coincidences between protons and gamma-rays, he established that gamma-rays were emitted from the excited states of Si^{30}.

In all of the above investigations, alpha-particles of less than 8.6 Mev were used. Since the Indiana University cyclotron produces a good beam of 22 Mev alpha-particles, the reaction $Al^{27}(\alpha, p)Si^{30}$ was reinvestigated with the purpose of looking for protons from higher energy levels in the Si^{30} nucleus and also to investigate the spacing of these energy levels at higher excitation energy.

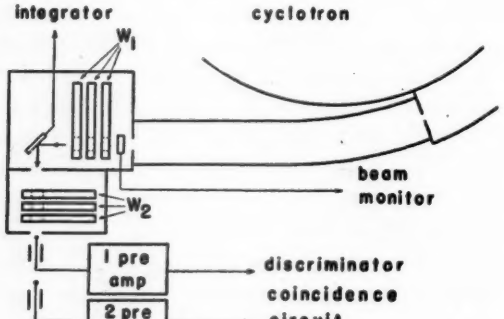

FIG. 1. Cyclotron attachment.

2. METHOD AND APPARATUS

The principle of the method is essentially the same as that used by the earlier investigators. An aluminum foil was bombarded in vacuum with 22 Mev alpha-particles from the cyclotron. The protons produced in the reaction, emerging from the aluminum foil at 90° to the incident beam, were counted with the help of two proportional counters in series, arranged for coincidence counting. The range of the various proton groups was determined by allowing the protons to pass through aluminum absorbers into the counting system.

Figure 1 shows the arrangement of the apparatus at the cyclotron. The cyclotron beam was conducted a distance of 43 inches from the gate chamber of the cyclotron by means of a 4-inch i.d. tube. The tube was curved to accommodate the alpha-particle trajectory in the fringing field of the magnet. At the gate end, there were placed a set of stainless steel slits. Upon entering the bombardment chamber the beam passed through an aluminum foil of 1.06 mg/cm² surface density and holes in three wheels W_1, designed to carry absorber foils, and thence to the target. The holes in the absorber wheels, gate slit and fringing magnetic field formed a beam analyzer which tended to monochromatize the beam.

The target was an aluminum foil of 1.06 mg/cm² surface density cemented to a brass ring in such a manner that the beam could not strike the ring. The ring was supported by a brass rod which emerged from the vacuum through a well-insulated Wilson seal. The current to the target was measured by an integrating meter which has been previously described.[6]

[1] J. Chadwick and J. E. R. Constable, Proc. Roy. Soc. London A135, 49 (1932).
[2] W. E. Duncanson and H. Miller, Proc. Roy. Soc. London A146, 396 (1934).
[3] O. Haxel, Zeits. f. Physik 83, 323 (1933); 88, 346 (1934); 90, 373 (1934).
[4] O. Meerhaut, Zeits. f. Physik 115, 77 (1940).
[5] B. B. Benson, Phys. Rev. 73, 7 (1948).
[6] J. E. Brolley, Jr., Rev. Sci. Inst. 19, 405(L) (1948).

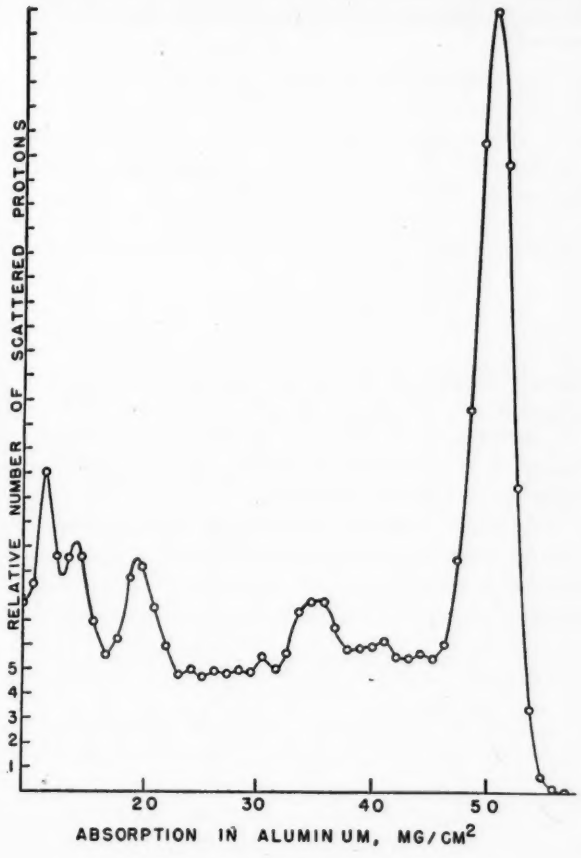

FIG. 2. Protons inelastically scattered from Al.

The protons emerging from the target pass through three wheels, designed to carry a number of absorbers, and into the proportional counters. All absorbers, except one of lead, were laminae of a basic sheet of aluminum of surface density 1.06 mg/cm² and were cemented to the wheels. The wheels could be viewed through windows and rotated to give any desired combination of absorbers.

The counter tubes were $\frac{7}{8}$-inch long and $\frac{1}{2}$-inch inside diameter. The inner wires of tungsten were 0.005-inch in diameter with bronze spheres on the ends. Both tubes were housed in a brass box containing argon at 8 cm Hg pressure. The window was of aluminum alloy, 0.001-inch thick, cemented to the box. The output of the counter tubes was boosted by preamplifiers of the Los Alamos type and fed into a conventional discriminator coincidence circuit. After mixing, the signal was counted on a scale of 128 set which also furnished the high voltage for the counter tubes.

3. EXPERIMENTAL DETAILS AND RESULTS

The apparatus was first tested to see whether sharp peaks could be obtained for protons at the end of their range. Hydrogen molecule ions were accelerated in the cyclotron. These have very nearly the same resonance conditions as deuterons. The beam was then passed through a monitor foil where the ion was stripped of its electron. The protons emerging from the monitor foil were then elastically scattered into the counter tube by the aluminum target. Absorption curves on the scattered protons were taken. The gain of the second channel associated with the last counter tube was varied until optimum peaking was found. The absorption curve is shown in Fig. 2.

The aluminum target was then bombarded with alpha-particles and minor adjustments made to the gain to secure a good compromise between peaking and counting rate. The whole proton absorption curve for alpha-particle bombardment was then run.

In order to calibrate the instrument, the target was replaced with a thin source of thorium C′ alpha-particles. This was prepared by collecting thorium active deposit on a ground stainless steel button from a mesothorium source. Air was used as absorber and the counter adjusted for the best alpha-particle peaks. Since the distance between the source and counter was known, the range spent in the counter was easily obtained. This was found to be 5.79 cm.

The energy of the impinging alpha-particles was obtained by several methods. The direct method consisted of measuring the energy of alpha-particles elastically scattered by a gold foil, of 0.17 mg/cm² surface density, in place of the aluminum target. A value of 21.80 Mev was obtained for alpha-particles entering the bombardment chamber. This quantity could also be computed indirectly from the scattering of protons from the cyclotron by aluminum; a value of 22.00 Mev being obtained.

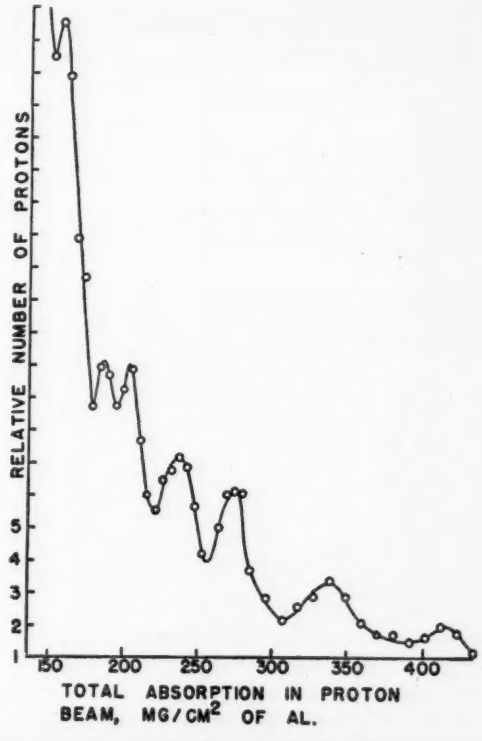

FIG. 3. Protons from $Al(\alpha, p)Si^{30}$.

TABLE I. Energies and Q-values of proton groups in the reaction $Al^{27}(\alpha, p)Si^{30}$.

Proton energy (Mev)	Q (Mev)
16.85	−1.27
14.96	−3.22
13.28	−4.96
12.29	−5.98
11.27	−7.04
10.68	−7.65
9.72	−8.64

The mean of these two measurements 21.90 was taken as the final value. Messrs. R. G. Cochran and A. D. Schelberg, of this laboratory, have measured the energy of the alpha-particle beam, under similar conditions, by magnetic deflection and obtain a value of 21.84 Mev. The half-width of the alpha-particle beam is less than 200 kev.

After these tests, the aluminum target was bombarded with alpha-particles and the distribution in the range of the protons measured. The results of the measurements are shown in Fig. 3 in which the number of protons per unit beam intensity is plotted against the range of the protons.

To obtain the energy of the maxima shown in Fig. 3, the calculations of Smith[7] on the range energy relation for protons in aluminum were used. In Table I these proton energies and associated Q values are compiled. In these calculations, the energy of the alpha-particles striking the foil was taken as 21.54 Mev. This takes into account the absorption in the monitor foil and the mean loss in the target.

There are indications of additional higher energy levels. However, with the present technique, they are

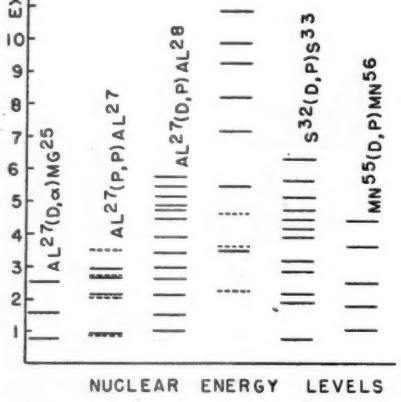

FIG. 4.

[7] J. H. Smith, Phys. Rev. 71, 32 (1947).

TABLE II. Energy levels of Si^{30} in Mev.

Present work	Benson's
	0
	2.28
3.49	3.66
	about 4.6
5.44	
7.18	
8.20	
9.26	
9.87	
10.86	

difficult to measure in the presence of a background of apparently continuously distributed protons. The proton background rises very rapidly with diminishing energy of the protons. At 2 Mev it is nearly 10,000 times greater than at 17 Mev.

The range of the most energetic protons from this reaction could not be well-determined in this experiment. The counting rate in the 17 Mev region was extremely low, only 25 to 50 counts per point being obtained. For this reason the Q-value associated with those protons which go to the ground state was taken from the work of Benson,[5] who gives the value 2.22 Mev. Using this value, the positions of the energy levels of Si^{30} are given in Table II.

TABLE III. Energy levels of Al^{27} in Mev.

Present work	Dicke and Marshall
0.95	0.87
2.14	2.03
2.65	
2.93	2.70
	about 3.5

In the present work, the level reported by Benson at about 4.6 Mev does not appear to be excited. As Benson points out, however, the proton group associated with this level in his experiment comes at almost the same place as that to be expected from hydrogen contamination. Moreover, he finds fewer gamma-rays associated with this group than with the others. Furthermore, he has not resolved the group but obtains it by extrapolation. It is possible that this group is too weak to be observed in the present experiment.

From an inspection of Table II, it will be seen that the level spacing does not appear to decrease significantly with increasing energy. The spacing remains approximately constant at about 1 Mev.

4. INELASTIC SCATTERING OF PROTONS FROM Al^{27}

In the calibration experiments, mentioned earlier, in which protons from the cyclotron were scattered from aluminum, it was possible to observe, in addition to the main group of elastically scattered protons, several groups of protons inelastically scattered from aluminum.

From the results, shown in Fig. 2, a few low lying levels of Al^{28} were calculated.

Table III compares the present results with those of Dicke and Marshall.[8] The first two levels are in fair agreement. It is suggested that the third level reported by Dicke and Marshall as 2.70 Mev may possibly be two at 2.65 and 2.93 Mev. In the present experiment the protons available were not sufficiently energetic to observe the level reported by them at about 3.5 Mev.

5. DISCUSSION OF RESULTS

In the present experiments, evidence has been presented for the existence of excited states of Si^{30} up to about 11 Mev excitation energy. There also appear to be higher levels above 11 Mev, but the proton groups from which the energy levels are derived ride on a continuous background of protons thus making the measurement at this energy difficult. The most striking feature of the results is the large spacing between energy levels and the fact that the spacing does not appear to decrease with increasing excitation energy, at least up to 11 Mev. The results are shown graphically in Fig. 4, along with certain other energy levels to be discussed later.

The liquid drop model and statistical theories predict a much closer spacing and also that the spacing should get closer as the excitation increases. Weisskopf,[9] using a thermodynamical theory of the nucleus, gives the following equation for the level density as a function of energy for nuclei in the neighborhood of Si^{30}.

$$D = 10^6 \exp[-2(E)^{\frac{1}{2}}].$$

The values given by this formula for various excitation energies are listed in Table IV. It is interesting to compare this with Fig. 4. There is no apparent agreement.

The wide spacing of the energy levels observed in this and all other experiments of this type is difficult to reconcile with the predictions of the liquid drop and other statistical models. This is especially true when, as in the case here, some of the observed levels lie above the neutron binding energy. The fact that the proton groups appear to ride on a continuous background of protons whose intensity increases as one goes to lower proton energies has led to some speculation on the nature of these groups. It has been suggested that this continuous background of protons may be an unresolved series of proton groups with very small energy level spacing and that the proton groups observed, associated with the higher energy levels, may be an envelope of more closely spaced levels. From the experimental point of view there is no doubt about the existence of the groups, and hence the validity of the energy levels, since the observed spacing of the groups is roughly 1 Mev and the resolving power about 200 kev. The theoretical explanation of the wide level spacing observed is at present not clear from the usual considerations of the liquid drop model. Its solution may lie more in the direction of considering certain other modes of vibration of the nucleus, possibly somewhat similar to the considerations of Goldhaber and Teller.[10]

TABLE IV.

Excitation energy	Spacing
2 Mev	59 kev
4	18
6	7.5
8	3.5
10	1.5

Figure 4 also shows, for comparison, the energy levels of Mg^{25} obtained from $Al^{27}(d\alpha)$,[11] Al^{27} from inelastic scattering of protons,[12] Al^{28} from $Al^{27}(dp)$,[11] S^{33} from $S^{32}(dp)$,[13] and Mn^{56} from $Mn^{55}(dp)$.[14] The levels drawn in with dashed lines in Al^{28} are those of Dicke and Marshall and those similarly indicated in Si^{30} are those of Benson. It will be noticed at once that the level spacing in the Si^{30} nucleus is greater than in any of its near neighbors. This phenomenon seems to have no very obvious explanation.

The authors wish to thank Mr. William Stefanich and the other members of the cyclotron crew who have given generously of their time and skills. This work was assisted by the joint program of the ONR and the AEC.

[8] R. H. Dicke and J. Marshall, Phys. Rev. **63**, 86 (1943).
[9] H. A. Bethe, *Elementary Nuclear Theory* (John Wiley and Sons, Inc., New York), p. 117.
[10] M. Goldhaber and E. Teller, Phys. Rev. **74**, 1046 (1948).
[11] Pollard, Sailor, and Wyly, Phys. Rev. **75**, 725 (1949).
[12] R. H. Dicke and J. Marshall, Phys. Rev. **63**, 86 (1943).
[13] P. W. Davison, Phys. Rev. **75**, 757 (1949).
[14] A. B. Martin, Phys. Rev. **72**, 378 (1947).

High Energy Induced Fission of Bismuth and Lead

R. H. GOECKERMANN AND I. PERLMAN
Radiation Laboratory and Department of Chemistry, University of California, Berkeley, California
(Received June 1, 1949)

A study has been made of the characteristics of the fission induced in bismuth and lead by irradiation with the high energy deuterons using radiochemical methods for the determination of yields of the fission products. The fission yield curve resulting from 190-Mev deuteron fission of bismuth was found to be a single symmetrical peak with a maximum fission yield of 5.0 percent at a mass number of approximately 100. The ratio of neutrons to protons was observed to be nearly constant for all nuclides formed in relatively good yield. The excitation function of the Mo^{99} yield in two lead samples enriched, respectively, in Pb^{204} and Pb^{208} showed that the fission cross section is larger and decreases less rapidly as the deuteron energy decreases in the lead sample which has a higher proportion of the light isotopes. A mechanism has been postulated for the nuclear reaction which involves prior neutron evaporation from the initial highly excited nucleus followed by fission with unchanged charge distribution.

INTRODUCTION

IN two previous communications, the observation of fission of elements in the bismuth region of the periodic table with high energy particles was reported;[1,2] and the characteristics and a theory of the reaction were briefly described.[2] In this paper is presented a more detailed account of the observations which suggested this picture of high energy induced fission. In particular the results of the irradiation of bismuth with 190-Mev deuterons are summarized. The irradiations of bismuth and lead at several energies are included to complete the description.

The distribution of fission products in the fission of bismuth with 190-Mev deuterons was determined by studying the activities of 27 elements from $Z=20$ to $Z=63$—Ca, Cr, Fe, Ni, Cu, Zn, Ga, As, Se, Br, Rb, Sr, Y, Zr, Cb, Mo, Ru, Pd, Ag, Cd, Sb, Te, I, Cs, Ba, Ce, and Eu. The yields of 48 radioactive nuclides from mass numbers 45 to 149 were measured.

PROCEDURE

Bismuth of high purity was cut into 1-mm thick strips which were mounted on the probe to intercept the circulating beam of the 184-inch frequency-modulated cyclotron. Most of the irradiations were for one to three hours with deuteron currents of approximately one microampere. For the measurement of long-lived activities, a similar target was irradiated in this manner intermittently over a period of several weeks. In general, a 10- or 20-mg portion of carrier of the element being investigated was added to an aliquot of the nitric acid solution of the target, the element was separated and purified from all others, and the chemical yield was determined by weighing a compound of the recovered carrier. The chemistry used was based on fission product procedure reports of the Plutonium Project[3] with modifications in many cases because of the presence in large quantities of spallation products covering the region from bismuth to the rare earths. The final precipitates were filtered onto 1-cm^2 area papers, mounted on cardboard, and covered with ~3-mg cellophane for measuring the decay characteristics on ~3-mg mica end-window Geiger-Müller tubes. Wherever sufficient activity was encountered, identification of the radiation by means of absorption methods or with a simple beta-ray spectrometer was carried out in addition. Also, where applicable, identification was made more certain by observation of parent-daughter relationships. The chemistry and isotope identification will be summarized in the appendix.

RESULTS

One of the graphical methods for describing some of the features of the fission process is to plot against the mass number of a fission fragment the incidence with which that mass number appears. This *fission yield curve* of U^{235} with slow neutrons as determined by the exhaustive measurements made by members of the Plutonium Project[4] is reproduced as the familiar double-hump curve in Fig. 1. It should be recalled that the primary fission products in this system have considerable neutron excess and beta-decay toward stability with a general increase in half-life in the members of the decay sequence. For any mass number there is a distribution of *primary* fission products with respect to element but those nearest stability appear in low yield and by inference the probability of producing a stable nuclide as a primary fission product is low. As a consequence the yield of beta-emitting nuclides one or two removed from stability represents, with fair accuracy, the total yields for their respective mass numbers if sufficient time is elapsed to permit accumulation of yield through decay of the shorter lived antecedents. The fission yield curve for uranium with slow neutrons is therefore accurately defined by such measurements.

[1] Perlman, Goeckermann, Templeton, and Howland, Phys. Rev. 72, 352 (1947).
[2] R. H. Goeckermann and I. Perlman, Phys. Rev. 73, 1127 (1948).
[3] National Nuclear Energy Series—Plutonium Project Record Vol. 9B, Chapter 8 (to be issued).
[4] See "Nuclei Formed in Fission," J. Am. Chem. Soc. 68, 2411 (1946).

In Fig. 1 is also shown a curve to represent the fission yield *vs.* mass number dependence for the fission products from bismuth induced by 190-Mev deuterons. In contrast to the curve for uranium with slow neutrons the highest yields appear in the symmetrical cleavage. Without belaboring this point further for the present another important feature should be discussed, namely, that although there is good evidence to believe that this curve represents in essence the mass number distribution, not many of the measured radioactive fission products actually fall on the curve. It will be necessary to anticipate some of the points which will be brought out in the later discussion in order to explain how this fission yield curve was constructed from the measured fission products.

One striking difference between bismuth fission products and those from the slow neutron fission of uranium is that in the case of bismuth the fission products do not necessarily have a high excess of neutrons; in fact, they may lie on the neutron deficient side of stability. Besides the general propensity of the primary fission products to lie close to stability, it was noted that the lighter fission fragments are β^--emitters while those on the high mass side of the distribution are neutron deficient and decay by β^+-emission or electron-capture. In accounting for these and other observations it was found possible to set up conditions which define the most probable primary fission products for each mass number. It is first of all assumed that about 10 neutrons are boiled out of the nucleus before it undergoes fission. While it is recognized that the fission of no single nuclear species describes all of the events, for the sake of simplicity it is assumed that an excited state of Po^{199} is the immediate nucleus which undergoes fission. This would arise from the reaction: $Bi^{209}(d,12n)Po^{199*}$. It is further assumed that the Po^{199} undergoes cleavage without charge redistribution so that each fragment retains the same neutron/proton ratio as the parent nucleus.

One may now attempt to construct a fission product distribution curve using the measured yields of the fission products. One has but to select the various mass numbers and calculate from the neutron/proton ratio for Po^{199} what will be the most probable charge which will appear with that mass number. This has been done in Table I in which the second column lists the most probable primary fission products. In a number of cases the predicted value for Z falls well between two integers and so two elements are listed. It will be noted that up to mass number ~110 the predicted primary fission products are predominantly β^--emitters, in the mass number range 110–125 they are to a large extent stable, while above 125 most are on the neutron deficient side of stability. Turning to Fig. 2 in which the points may be identified from the mass numbers and yields as listed in Table I, the low mass arm of the curve is constructed by drawing a smooth curve through points of maximum yield. When this is done it is found that the points which fall closest to the curve are indeed those which the theory would predict to be the most probable fission products for each mass number. These are shown as solid circles. The high mass arm of the curve may be obtained by reflecting the low mass arm through mass number 99 as the line of symmetry. As predicted from the theory there will be relatively few measurable isotopes which should fall on the curve since most of the primary fission products in this range are stable. In a few cases one would predict a radioactive fission product to be the most probable and here it was found that these particular species did fall on the curve with one apparent exception which will be discussed below. The open circles in Fig. 2 represent yields of fission products predicted to arise in rare modes of fission since they do not fulfill the conditions set for the most probable events. The half-closed circles are points for which the theory predicts sharing of yield in that the most probable value of Z lies between integers.

Considering the manifest oversimplification in this model for the fission process the agreement between measured yields and predictions is considered good. Individual points will be discussed below which will serve to indicate that agreement may be better than indicated by a cursory examination of Fig. 2. Furthermore there is a considerable amount of other evidence

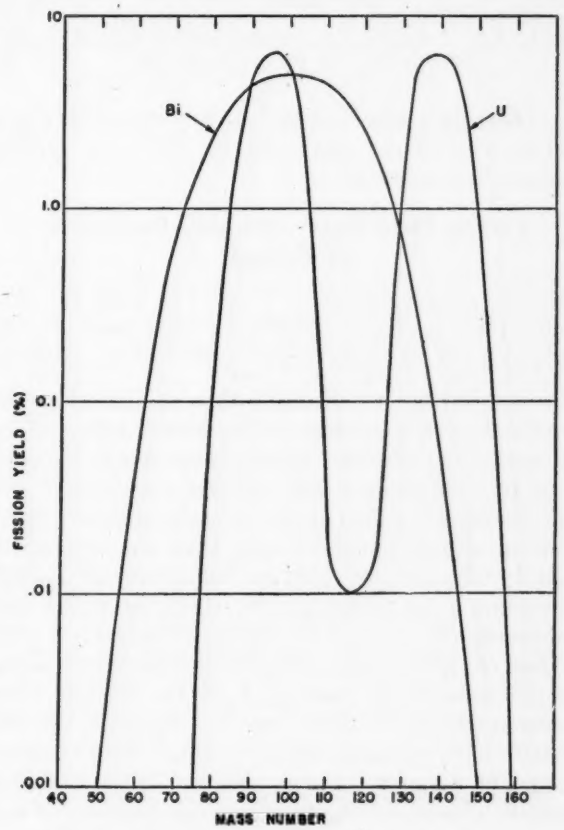

FIG. 1. Fission yield for U^{235} with slow neutrons and bismuth with 190-Mev deuterons.

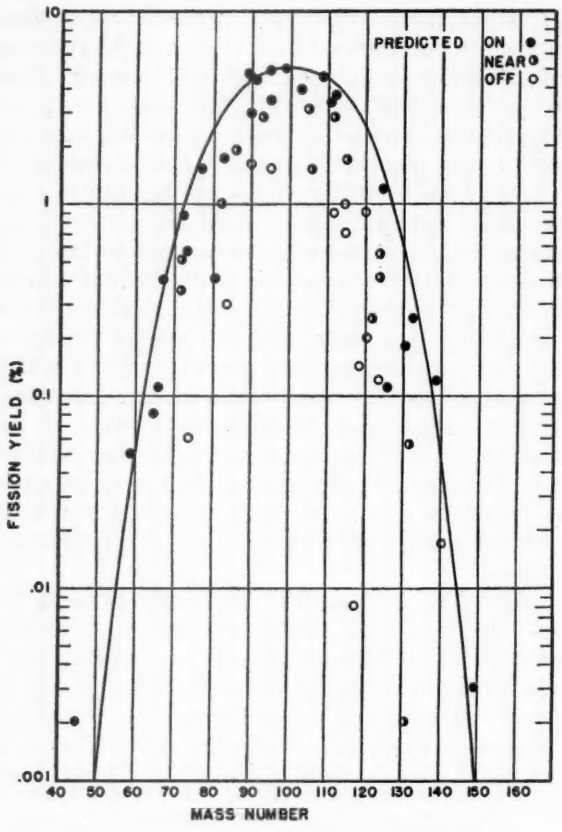

FIG. 2. Yields for products of the irradiation of bismuth with 190-Mev deuterons.

to support the general picture both in terms of the shape and position of the curve and the ability to predict primary fission products.

Fission Yield Data—190-Mev Deuterons on Bismuth

In the second column of Table I is listed the predicted primary fission product for each mass number for which one or more activities have been measured. The designation $A \xrightarrow{\beta^-} B$ means that element A is the predicted primary product but its yield was determined by measuring the daughter activity B much in the same sense that the primary fission products in the slow neutron fission of uranium are not usually measured. For a number of mass numbers more than one measurable nuclide exist and the yields are followed by an asterisk in column 4 for those cases in which the yields were independently determined. Column 5 presents a summation of yields of measured activities and these values should agree with those read off the smooth curve (column 6) only in those instances in which the predicted fission products are those which could be measured. For example, at mass number 72 the predicted primary charge for the fragment lies between 30 and 31 so that one would predict that the 49-hr Zn^{72} and 14-hr Ga^{72} would share the bulk of the yield for this mass number. The yields of the two activities were independently measured as 0.35 and 0.51 percent respectively, the sum of which agrees within experimental error with the value 0.93 percent for mass number 72 as read off the smooth curve. On the other hand for mass number 74 the predicted fission product Ga^{74} was not measured and is an unknown, presumably short-lived, activity. It decays to stable Ge^{74} which blocks the possibility of detecting it through a daughter activity. For mass number 74, the 17.5-day As^{74} activity was measured and since this is two units of atomic number removed from the theoretical primary product it should appear in low yield. As expected its yield is very low, accounting for only 5 percent of the yield taken off the curve for mass number 74. Not all of the data agree so well with the predictions as the examples just cited. However, before ascribing these descrepancies to shortcomings of the theory, one should rule out several factors which produce apparent low yields. The difficulties of absolute measurement of β-emitters and especially of isotopes which decay by electron-capture are well recognized. Of those encountered in these studies, a number do not have well worked out decay schemes and the possible errors lie principally in the direction of indicating low yields. Continued study of radioactive species over the past several years has turned up more and more cases of nuclear isomerism. As a result it is not always possible to ascribe the entire yield of an isotope to the measured species since an undetected isomer may contribute. A well known case of isomerism, namely Cd^{115}, was measured and it was found that the two isomers are formed in comparable yields. Arnold and Sugarman[5] have uncovered some cases of isomerism in uranium fission products which explain previous yield descrepancies among members of a decay chain. Another phenomenon which can give an apparently low fission yield is that of delayed neutron emission. In the case of bismuth fission it would be predicted that such species would lie on the light wing of the distribution where nuclides with considerable neutron excess are expected.

The following gives a brief discussion of the yield data according to mass number. The yields of the lightest and heaviest nuclides measured, Ca^{45} and Eu^{149}, were so low that the position of the yield curve as determined by these values has little significance. References to almost all of the activities mentioned will be found in a compilation of nuclear data.[6]

Mass 59.—The predicted primary fission product for this mass number is manganese. Mn^{59} is not known and is probably a short-lived β^--emitter whose yield can be determined through its decay product 46-day Fe^{59}. None of the other chemical fractions would be expected to contain a measurable activity of this mass number.

[5] J. R. Arnold and N. Sugarman, J. Chem. Phys. **15**, 703 (1947).
[6] G. T. Seaborg and I. Perlman, Rev. Mod. Phys. **20**, 585 (1948).

Mass 65.—No activities corresponding to the mass number range 60–64 were measured. Significantly no appreciable yields of Cu^{64} were found which is in agreement with the prediction that Co^{64} is the primary fission product for this mass number.

The predicted primary fission product for mass number 65 is divided between Co^{65} and Ni^{65}. It would be expected that Co^{65} is sufficiently short-lived to allow the accumulated yield to be measured as Ni^{65}. The next neighboring isobar is stable Cu^{65}. The measured yield for Ni^{65} is about a factor of three below the curve.

Mass 66.—For this mass number nickel would be expected and a new 56-hr. period was found in the nickel fraction and identified as the parent of the 5-min. Cu^{66}. The radiation from Ni^{66} was not itself measured but the yield was determined from the hard β^--particles of Cu^{66}. The yield so determined falls below the curve and the discrepancy is thus far not explained.

Mass 67.—This is another case in which the predicted primary fission product is a previously unknown isotope, Cu^{67}. The copper fraction contained a 56-hr. period with a 0.5-Mev β^--particle which does not have an active zinc daughter. The assignment to Cu^{67} is reasonable in view of its radioactive properties and is in keeping with its preparation from zinc by the γ-p reaction.[7]

Mass 72.—The sharing of this mass number between Zn^{72} and Ga^{72} as predicted has already been mentioned.

Mass 73.—The measured yield of Ga^{73}, which should be the major primary fission product of this mass number, is about a factor of two below the curve.

Mass 74.—The predicted charge for this mass number lies near gallium, element 31. The only activity of mass number 74 measured was As^{74} and as expected the yield fell well below the curve indicating its appearance in only about 5 percent of the events producing this mass number.

Mass 77 (and 76).—The measurement of 40-hr. As^{77} was made at a time in which the 12-hr. Ge^{77} would have decayed into it so the yield as determined is cumulative. The predicted primary product lies between germanium and arsenic and the cumulative yield of As^{77} lies close to the curve. It was possible to resolve a small amount

TABLE I. Fission yields in 190 Mev deuteron fission of bismuth.

Mass number	Predicted primary product	Product measured	Measured yield (%)	Total measured yield for mass number (%)	Predicted fission yield (%)
45	$K \xrightarrow{\beta^-} Ca$	Ca	0.002	0.002	0.0002
59	$Mn \xrightarrow{\beta^-} Fe$	Fe	.05	.05	.04
65	$Co \xrightarrow{\beta^-} Ni$	Ni	.08	.08	.23
66	Ni	Ni	.11	.11	.32
67	$Ni \xrightarrow{\beta^-} Cu$	Cu	.40	.40	.40
72	Zn	Zn	.35	.86	.93
	Ga	Ga	.51*		
73	Ga	Ga	.55	.55	1.1
74	Ga			.06	1.2
		As	.06		
77	$Ge \xrightarrow{\beta^-} As$	As	1.5	1.5	1.9
81	Se			.41	2.8
	Se^m	Se^m	.41		
82	Br	Br	1.0*	1.0	3.0
	Se(stable)	—			
83	Br	Br	1.7	1.7	3.2
84	Br			0.3	3.4
	Kr(stable)	—			
		Rb	0.3		
86	Kr(stable)	—		1.9	3.8
	Rb	Rb	1.9*		
89	$Rb \xrightarrow{\beta^-} Sr$	Sr	4.7	4.7	4.4
90	Sr	Sr	2.9	4.5	4.5
		Y	1.6*		
91	$Sr \xrightarrow{\beta^-} Y$	Y	4.4	4.4	4.6
93	Y	Y	2.8	2.8	4.8
	Zr				
95	Zr	Zr	3.4	4.9	4.9
		Cb	1.5*		
99	Mo	Mo	5.0	5.0	5.0
103	$Tc \xrightarrow{\beta^-} Ru$	Ru	3.9	3.9	4.95
105	Ru	Ru	3.1	3.1	4.9
	Rh				
106	Rh			1.5	4.8
	Ru	Ru	1.5		
109	Pd	Pd	4.6	4.6	4.6
111	Ag	Ag	3.4	3.4	4.2
112	Ag	Ag	2.8*	3.7	4.1

TABLE I.—(*Continued*).

Mass number	Predicted primary product	Product measured	Measured yield (%)	Total measured yield for mass number (%)	Predicted fission yield (%)
	Cd(stable)	—			
		Pd	.9		
115	In(stable)	—		1.7	3.6
	Cd(2.3 *d.*)	Cd(2.3 *d.*)	1.0		
	Cd(43 *d.*)	Cd(43 *d.*)	.7		
118	Sn(stable)	—		.008	3.0
		Te	.008		
119	Sn(stable)	—		.14	2.7
		Te	.14		
120	Sb(6 *d.*)	Sb(6 *d.*)	.90	.9	2.5
	Sb(17 *m.*)				
	Sn(stable)	—			
121	Sb(stable)	—		.2	2.3
		Te(143 *d.*)	.20		
122	Te(stable)	—		.25	2.0
	Sb	Sb	.25*		
124	Te(stable)	—		.55	1.6
	I	I	.43*		
		Sb(60 *d.*)	.12		
125	I	I	1.2	1.2	1.4
126	I	I	.11*	.11	1.2
131	Cs	Cs	.002*	.18	.54
	Ba	Ba	.18		
132	Ba(stable)	—		.06	.45
	Cs	Cs	.056*		
133	Ba(39 *h.*)	Ba	.25	.25	.35
	K				
139	$Pr \xrightarrow{} Ce$	Ce	.12	.12	.07
140	Pr			.0004	.05
		Ba	.0004		
141	Pr(stable)	—		.017	.03
	Nd				
		Ce	.017		
149	Eu	Eu	.003	.003	.0015

* Independent yields.

[7] R. B. Duffield and J. D. Knight, private communication.

of shorter-lived activity, probably 27-hr. As^{76}. The yield was about ten-fold lower than As^{77} which is to be expected since stable Ge^{76} is the calculated fission product for this mass number.

Mass 81.—The predicted atomic number is close to 34 (selenium) with some of the yield to be shared by stable Br^{81}. The selenium fraction was removed too late to observe the 17-min. Se^{81} ground state but a moderate amount of 58-min. Se^{81m} was measured amounting to 15 percent of the total yield predicted for this mass number.

Mass 82.—This mass number is predicted to be shared between stable Se^{82} and the shielded isotope 34-hr. Br^{82}. The yield of Br^{82} is one-third of the total yield for this mass number as taken off the curve. Some difficulties were experienced with the bromine chemistry so that the actual yield may be higher than that measured.

Mass 83.—The yield of the predicted product 24-hr. Br^{83} is almost a factor of two below the curve but, as mentioned, some bromine may have been lost in isolating the bromine fraction.

Mass 84.—The most probable nuclides for this mass number are stable Kr^{84} and 30-min. Br^{84} which was not measured. The rubidium fraction showed a 40-day period which is probably that for which positrons were observed and assigned to Rb^{84} by Barber.[8] The predominant mode of decay appears to be by electron-capture and the yield as estimated from the 12-kev x-rays was only about 8 percent of that for this mass number taken from the curve. The low yield would be expected since Br^{84} and Kr^{84} should be the most abundant fission products.

Mass 86.—This mass number should be shared between stable Kr^{86} and 20-day Rb^{86}. The measured yield of Rb^{86} is about one-half that taken from the curve for this mass number. Positrons in low abundance were observed to decay with a 20-day half-life which indicates some positron branching in the decay of Rb^{86}.

Mass 89.—The predicted product, Sr^{89}, was found in slightly higher yield than the point on the smooth curve.

Mass 90.—The yield of the predicted primary product 25-yr. Sr^{90} fell about 30 percent below the curve and the independent yield of 62-hr. Y^{90} made up the difference.

Mass 91.—The measured yield of 57-day Y^{91} also included that from the decay of 10-hr. Sr^{91} and these are the two nuclides which should appear with this mass number. The cumulative yield of Y^{91} fell on the curve.

Mass 93.—The predicted nuclides are 10-hr. Y^{93} and the unobservable long-lived Zr^{93}. The measured yield of Y^{93} accounted for over half of that expected for this mass number.

Mass 95.—The principal primary product is predicted to be 65-day Zr^{95} with a small contribution by 33-day Cb^{95}. The total measured yield lies on the curve with the Zr^{95} accounting for 70 percent of the yield. The columbium fraction was removed too late to observe any Cb^{96}.

Mass 99.—Mo^{99}, predicted to be the primary product for this mass number, represents the highest yield of any fission product and lies at approximately the point of symmetry in the cleavage.

Mass 103.—The yield of 42-day Ru^{103} should include that of the unknown Tc^{103} and these two nuclides are predicted to share mass number 103 as primary fission products. The yield so determined falls about 20 percent below the curve.

Mass 105.—This mass number should be shared between 4.5-hr. Ru^{105} and 36.5-hr. Rh^{105}. Rhodium could not be isolated and the yield of Ru^{105} accounted for about 60 percent of the expected total yield.

Mass 106.—The principal primary fission product should be Rh^{106} with a moderate contribution by 1.0-yr. Ru^{106}. The yield of Ru^{106} amounted to about 30 percent of the total expected for this mass number while Rh^{106} could not be independently measured.

Mass 109.—The 13-hr. Pd^{109} is predicted to be the primary fission product and its yield helps define the yield curve in this region.

Mass 111 (and 110).—Mass 110 is expected to be shared between stable Pd^{110} and the isomers 24-sec. Ag^{110} and 225-day Ag^{110}. Some long-lived silver was observed but a reliable yield could not be calculated. Ag^{111} is expected to be the principal fission product for mass 111 and its measured yield is about 80 percent of the value from the curve.

Mass 112.—For this mass number 3.2-hr. Ag^{112} is predicted to account for the major amount for the yield with moderate contribution by stable Cd^{112}. It was found that Ag^{112} did account for most of the yield but that the 21-hr. Pd^{112} contributed significantly.

Mass 115.—The 2.3-day and 43-day isomers of Cd^{115} should share the mass number yield with In^{115}. The sum of the yields for the cadmium isomers is about half the total yield for this mass number. A point of importance is that the two Cd^{115} isomers are formed in almost equal yield. The ratio of 2.3-day Cd^{115}/43-day Cd^{115} is 14 in the slow neutron fission of uranium which is presumably the ratio which ensues from the β^--decay of Ag^{115}. The interpretation is that in the fission of bismuth, Cd^{115} is formed as a primary fission product as the theory demands.

Mass 118 and 119.—The predicted major element for both of these mass numbers is tin, element 50. In the case of 118 the favored value of Z is slightly below 50 and for 119 it is slightly above. The only activities measured which are attributed to these mass numbers are two isotopes of tellurium, element 52. One would predict low yields for both, with Te^{118} being more rare than Te^{119}. The yields of Te^{118} and Te^{119} are respectively 0.3 percent and 5 percent of the expected total yields for the mass numbers.

[8] W. C. Barber, Phys. Rev. **72**, 1157 (1947).

Mass 120.—The predicted primary fission product is the shielded nuclide Sb^{120} (of which two isomers apparently exist) with some contribution by stable Sn^{120}. Only the 6.0-day isomer of Sb^{120} could be measured, and its yield was estimated from the x-ray counting rate as about 40 percent of that read from the smooth curve.

Mass 121.—Stable Sb^{121} should be the primary product with slight contribution by Te^{121}. The yield of the 143-day isomer of Te^{121} was measured as about 10 percent that expected for the mass number.

Mass 122.—This mass number should be shared between stable Te^{122} and shielded 2.8-day Sb^{122}. The yield of Sb^{122} was somewhat lower than expected amounting to about one-tenth that for the mass number.

Mass 124.—This represents an interesting case in that the principal predicted product, stable Te^{124} lies between a recognized β^--emitter and β^+-emitter. The prediction actually would indicate appreciable contribution by 4.0-day I^{124} and very little by 60-day Sb^{124}. The measured yield for I^{124} is about 25 percent the expected yield for the mass number while Sb^{124} contributes about 7 percent.

Mass 125.—The 56-day iodine which has been assigned to I^{125} was obtained in good yield. There is the difficulty in this case, as well as others in which yields are determined by counting x-rays, in estimating the x-ray counting efficiencies. If the counting efficiency is assumed to be 0.5 percent then I^{125} falls near the curve as would be predicted.

Mass 126.—According to prediction the shielded isotope 13.0-day I^{126} should account for most of this mass number. The yield as determined is a factor of 10 below the curve and this is the farthest deviation from prediction that is known. It is worth examining this activity to see if it actually decays largely by electron-capture.

Mass 131 and 132.—The determination of yields of the predicted activities for mass number 131 (Cs^{131} and Ba^{131}) was unsatisfactory because of difficulties with cesium chemistry and in the estimation of counting efficiencies of both activities. Nevertheless the yields as estimated accounted for one-third of the total for this mass number and, significantly, 8.0-day I^{131} which is two units of Z removed from the predicted value, could not be detected at all.

Mass number 132 is predicted to fall principally on stable Ba^{132} with moderate contribution by 7-day Cs^{132}. The yield of the latter was estimated at over 10 percent of the total expected for mass 132.

Mass 133.—The predicted nuclide is Ba^{133} of which two isomers are known. Only the 39-hr. Ba^{133m} could be measured and its yield alone could account for almost all that was expected for this mass number.

Mass 139.—The position of the fission yield curve becomes rather indeterminate in this range so it is difficult to say whether or not measured yields conform with the theory. For mass 139 the predicted primary fission products are Pr^{139} (unknown) and 140-day Ce^{139}. On the assumption that Pr^{139} would have decayed into Ce^{139}, the yield of the latter determines the yield for both. This measured yield fell somewhat above the smooth curve.

Mass 140.—The predicted product Pr^{140} could not be measured and its decay product is stable. A careful search was made for 12-day Ba^{140} by identifying its 40-hr. La^{140} daughter. Since barium is three units of Z removed from praseodymium one would expect a very low yield, and it was found to occur in less than 1 percent of the expected number of events giving this mass number.

Mass 141.—The major predicted primary fission product is stable Pr^{141} with some contribution by Nd^{141}. The only species of this mass number measured was 28-day Ce^{141} whose yield was about half that given by the curve. A small displacement of the curve in this region makes great differences in yield so that measurements here can only show whether the predicted nuclear types are appearing.

Cross Section for Bismuth Fission

In the short bombardments comprising this study the yield of Mo^{99} was determined in each case to serve as a standard for comparison between bombardments. These irradiations were carried out with probe targets in the circulating beam in which it is not possible to measure accurately the beam current which strikes the target. The fission yields shown in Table I and Fig. 1 were determined by integrating the smooth fission yield curve and by this means Mo^{99} was found to occur in 5.0 percent of the fissions.

A single experiment was carried out in this laboratory in which the 190-Mev deuteron beam was deflected outside the vacuum chamber and a well collimated beam of 3.0×10^{-5} microamperes was measured. A bismuth foil 1-mm thickness was irradiated and the Mo^{99} measured. The absolute value for the Mo^{99} yield along with its fission yield gave a fission cross section of 0.20×10^{-24} cm^2. The uncertainties of this cross section are largely that of estimating the shape of the fission yield curve and the value is probably accurate within 20 percent.

Fission of Separated Lead Isotopes

In order to explain the distribution of the fission products of bismuth it was necessary to postulate the emission of some 10 or 12 neutrons so that the actual nuclei undergoing fission lie close to Po^{199}. It is perhaps significant that the fissionability parameter, Z^2/A, for this nucleus lies in the same range as the naturally occurring uranium isotopes. One would expect that the fission of lead would be governed by a mechanism similar to that of bismuth and that the lighter isotopes of lead would undergo fission more readily than the heavier isotopes. Thus Pb^{204} should not require the loss of so

many neutrons as Pb^{208} before fission begins to compete with other modes of energy dissipation. As will be discussed, it is not to be expected that there exists a sharp energy threshold for fission so the effect to be looked for is a difference in yield at relatively low deuteron energies.

Two samples of isotopically enriched lead were irradiated with deuterons from 30 to 100 Mev and the yields of Mo^{99} compared. In both samples the yields decreased with decreasing deuteron energy; the sample enriched in Pb^{204} showed the higher cross section at all energies and the difference became greater at lower energies. The results are shown in Fig. 3 in which the relative cross sections between the two samples are indicated by the factors between them. The absolute cross sections plotted as ordinates should not be considered accurate because of the uncertainty in estimating the deuteron beam. In Fig. 3 are also shown the compositions of the two lead samples. In order to make certain that the observed differences of Mo^{99} yields were proportional to fission yields and did not merely reflect a shifting of the fission product distribution, two other fission products were measured representing points on both arms of the distribution curve. These nuclides Cu^{67} and Ba^{133} could only be measured with 50, 75 and 100 Mev deuterons because of low yields. Within the limits of error both of these showed parallel changes with that noted for Mo^{99}.

It should be mentioned that the yields shown in Fig. 3 are for the lead compositions indicated. The yield differences between pure Pb^{204} and Pb^{208} should be even greater. Also, in the case of Pb^{208} with 30 Mev deuterons the yield was so low that it could have resulted from 0.1 p.p.m. uranium in the lead, an amount which could conceivably have been present.

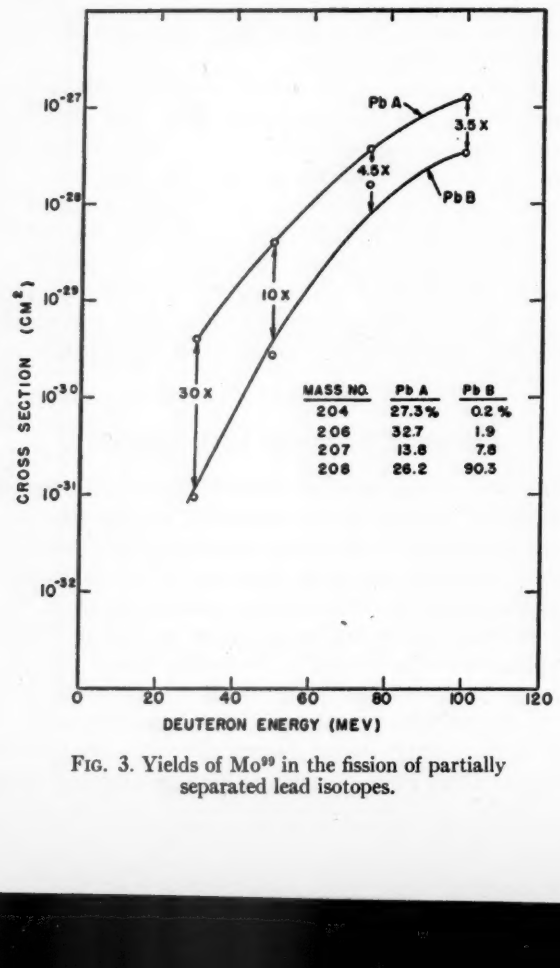

FIG. 3. Yields of Mo^{99} in the fission of partially separated lead isotopes.

DISCUSSION

In developing the mechanism for the fission of bismuth it is convenient to refer to the process as "high energy fission" since it is probable that a similar mechanism is at play in the fission of all heavy elements with high energy particles. It is also profitable to contrast this process with that observed for nuclei which undergo fission with slow neutrons and to correlate this information with fragmentary data obtained at intermediate energies. A number of aspects of the high energy reaction demand examination and these include the excitation function, mass and charge distribution between the fragments, neutron emission and competitive reactions.

Excitation Function

It is not possible to define a threshold energy for the fission of bismuth as the true excitation energy or threshold is undoubtedly considerably lower than that at which an appreciable cross section is observed. Since the question of levels of excitation with high energy particles is itself complicated by nuclear transparency[9] it may be well first of all to consider this point. With deuteron energies up to at least 50 Mev the interaction is probably accurately described by compound nucleus formation. Even at 190 Mev, the probability for complete transparency is low so that events in which some nuclear excitation occurs approximate the geometric cross section. It has been calculated[10] that collisions with 190-Mev deuterons in which less than 100 Mev is transferred occur in only about 25 percent of the cases. Since the proposed mechanism to account for bismuth fission with 190-Mev deuterons postulates the evaporation of about 12 neutrons it is probable that these 25 percent of the events cannot produce the fissions observed. (This contradiction in terms in view of the observed fission of bismuth at 50 Mev is only apparent, since for the present we are discussing reactions which occur with cross section of 0.2 barn while the cross section for 50-Mev neutrons is less than 10^{-3} barn.[11]) Of the remaining 75 percent of the events let us assume that there is a broad maximum probability for excitation at about 150 Mev. The cross section for such excitations is then about 2 barns which is approximately ten times the observed fission cross section. Since we assume that any excited nucleus which is degraded to Po^{199} has a high probability of undergoing fission, it follows that about 90 percent of the 2 barns is taken up by reactions in which some charged particles are

[9] R. Serber, Phys. Rev. **72**, 1114 (1947).
[10] L. W. Baumhoff, private communication.
[11] E. L. Kelly and Clyde Wiegand, Phys. Rev. **73**, 1135 (1948).

emitted or which fall short of the necessary neutron emission by the emission of high energy neutrons. It may be pointed out that on the present theory it is not possible to account for the formation in good yield of such shielded nuclides as Sb^{120} and Br^{82} and of the Cd^{115} isomers in the observed ratio if as many as two protons are lost giving Pb^{199} instead of Po^{199} as the nucleus responsible for most of the fissions.

With regard to a threshold energy for bismuth fission it has already been mentioned that any observed threshold will probably be that at which fission can compete appreciably with other forms of energy dissipation. The liquid drop model which leads to the deformation or fissionability parameter Z^2/A predicts an increased tendency for fission for decrease in A. For $Z=84$, the fission threshold is calculated to be ~ 12 Mev at $A=210$ and ~ 6 Mev for $A=200$.[12] We know from observations in the vicinity of uranium that when the excitation energy is around the binding energy of a neutron, i.e., ~ 6 Mev, that fission is capable of using up a considerable portion of the geometric cross section (see, for example, Klema[13]). From the results of the present study it is to be inferred that if the excitation energy for fission is about twice this value, excitation near or even considerably above the threshold results in a very poor competition by fission and instead neutron emission is favored. It is only when the threshold for fission is decreased through the ejection of neutrons that the rate for fission increases. Further emission of neutrons only serves to produce a nucleus which is even more susceptible to fission. From this picture one would expect to observe fission of bismuth with increasing yields as the projectile energy increases. There is good evidence that this is the case. Figure 3 shows the effect for lead isotopes up to 100 Mev, and Kelly and Wiegand[11] have counted fissions of bismuth with neutrons in which an increase by a factor of about fifty was observed between 50 and 85 Mev. In a series of experiments not recorded above, the yields from bismuth fission were measured for Cu^{67}, Mo^{99} and Ba^{133} with 100-Mev deuterons, 190-Mev deuterons, and 380-Mev alpha-particles. There was a progressive increase in yield for all three nuclei with increase in projectile energy. That the fission product distribution also broadens is evidenced in that, whereas Mo^{99} yield increased about threefold between the 100 Mev and the 380 Mev irradiations, the yields of Cu^{67} and Ba^{133} increased tenfold. In summary, it will be expected that the distribution of fission products of bismuth as shown in Table I and Fig. 2 is that for reactions produced by sufficient excitation to result in high fission cross section, in this case about one-tenth the geometric cross section. If it were possible to measure the rare events which occur at low excitation energy, the distribution could be quite different.

[12] S. Frankel and N. Metropolis, Phys. Rev. **72**, 914 (1947).
[13] E. D. Klema, Phys. Rev. **72**, 88 (1947).

Charge Distribution

The ratio of charge to mass in the asymmetrical cleavages from slow neutrons on U^{235} and Pu^{239} can be described by the postulate that the beta-decay chains from the two fission fragments are of equal length.[14] This demands a redistribution of charge in the fission process and probably permits the maximum amount of energy to be directed toward the separation of the fission fragments. This demand for energy economy in order to allow maximum kinetic energy for the slow neutron process is in sharp distinction with the observations for high energy fission. One of the requirements to explain the types of fission products in the high energy reaction is that there be no redistribution of charge, that is, both fragments bear the same neutron to proton ratio as the parent nucleus. Obviously this mechanism does not in general produce maximum kinetic energy of the fission fragments in the asymmetrical cleavages since it would be more economical to form two stable products instead of one which is β^--unstable and the other β^+-unstable. These observations indicate that the high energy fission process takes place from a slightly supra-threshold energy state in which the further energy which would accure from rearrangement of neutrons and protons is not important, and that by the same token the reaction is faster than slow neutron fission in which such rearrangements do take place.

There is some evidence that this same mechanism is at play in the high energy fission of uranium. Here it is not so easy to observe the effect as in the case of bismuth in which positron emitters are actually produced, but measurements in this laboratory show the ratio of Cd^{115} isomers to be different from that produced in slow neutron fission and the 28.7-hr. barium tentatively assigned to Ba^{135m} is found in good yield.[15]

Mass Distribution

One of the outstanding features of slow neutron fission is the low probability for symmetrical cleavage. In the high energy reaction the most favored cleavage is symmetrical and this apparently applies to uranium[16] as well as to bismuth. That the fission of bismuth with high energy particles has symmetrical cleavage as the most prominent mode is evidenced not only by the identification of fission products. Jungerman and Wright have measured the fission pulses from neutrons on bismuth and found the most prominent mode that in which the fragments have equal energy.[17]

It would be consistent with the other observations on high energy fission to correlate the preponderance of symmetrical cleavages with the rapid reaction rate and the unimportance of small economies of energy.

[14] Coryell, Glendenin, and Edwards, Phys. Rev. **75**, 337 (1949).
[15] O'Connor, Seaborg, and Folger, private communication.
[16] P. R. O'Connor and G. T. Seaborg, Phys. Rev. **74**, 1189 (1948).
[17] J. Jungerman and S. C. Wright, Phys. Rev. **75**, 1470 (1949).

Conversely one might associate asymmetrical fission with a slower reaction rate and with the necessity for putting as much energy as possible into kinetic energy of the fragments. In the case of slow neutron fission the ranges and energy distribution of the fission fragments have been measured[18–20] but there is no evidence that the highly asymmetric cleavages produce greatest total fission product energies. On the contrary the greatest energies appear to result from nearly equal mass distribution. As a result it is probably not possible to state with certainty the reasons for asymmetric fission. What appears to be fairly certain is that as the nuclear excitation becomes greater than the fission threshold the tendency toward splitting into equal fragments increases. Besides the present studies this is evidenced by the shallower valley of the distribution curve for Pu^{239} as compared with U^{235},[21,22] presumably due to lower fission threshold with increase in Z, and the similar effect when Th^{232} is irradiated with fast neutrons[23] and with charged particles.[24]

Neutron Emission

The distribution of the fission fragments in the case of 190-Mev deuterons on bismuth indicates that about 10 neutrons are lost in the reaction. It is most reasonable to assume that these neutrons precede the fission reaction because of the expected faster rate of neutron emission from a nucleus in which the barrier toward fission demands excitation energy several times that of neutron binding energies. However one might expect essentially the same distribution of fission products if fission resulted in highly excited fragments which subsequently boiled off nucleons.

The measurements of Jungerman and Wright[17] of the energy of the fission fragments of bismuth indicate that the fragments come apart with kinetic energy within a few Mev of predictions on the basis of fission with near threshold energy. This is in agreement with deductions made from the present findings, namely, that almost all of the nuclear excitation imparted by the high energy projectile is used in evaporating neutrons.

ACKNOWLEDGMENTS

We are grateful to Mr. J. T. Vale and members of the 184-inch cyclotron operating staff for their cooperation in making the irradiations for these studies. It is also a pleasure to acknowledge the continued interest in this problem and helpful discussions with Professor G. T. Seaborg and Professor E. O. Lawrence. This work was carried out under the auspices of the U. S. Atomic Energy Commission.

[18] W. Jentschke, Z. Physik **120**, 165 (1943).
[19] Katcoff, Miskel and Stanley, Phys. Rev. **74**, 631 (1948).
[20] D. C. Brunton and G. C. Hanna, Phys. Rev. **75**, 990 (1949).
[21] J. L. Fowler and L. Rosen, Phys. Rev. **72**, 926 (1947).
[22] Steinberg, Seiler, Goldstein, and Dudley, U. S. AEC Report MDDC-1632 (Jan. 1948).
[23] A. Turkevich, U. S. AEC Report MDDC-1568 (Dec. 1947).
[24] A. S. Newton, Phys. Rev. **75**, 17 (1949).

APPENDIX

For each element investigated, the essentials of the chemical procedure and isotope identification used are summarized. The chemistry steps listed were usually repeated several times in cycles. In some cases the amount of activity encountered is mentioned without reference to irradiation conditions solely for the purpose of indicating the limitations in accuracy of identification and yield determinations.

Calcium—Precipitated as CaC_2O_4; separations of sulfides insoluble in 0.5 N HCl, hydroxides insoluble in NH_3, and $Ba(NO_3)_2$ and $Sr(NO_3)_2$ with fuming HNO_3.

Particles, which had a rate of 30 counts per minute initially, were observed to decay with ~155-day half-life and were assumed to be from Ca^{45}.

Chromium—Precipitated as $Cr(OH)_3$ and extracted into ether as H_2CrO_8; separations of Bi_2S_3 and Sb_2S_3 in 1 N HCl, $Fe(OH)_3$ from H_2O_2-NaOH solution.

No activity was observed in the sample but short-lived ($T_{\frac{1}{2}}$<one week) activities would have been missed.

Iron—Extracted into isopropyl ether as $FeCl_3$ and precipitated as $Fe(OH)_3$ with NH_3; separations of acid-insoluble sulfides, $BaSO_4$, AgI, Zr phenylarsonate, and Ru by distillation.

A 46-day β^--emitter of ~0.36 Mev was observed and identified as Fe^{59}.

Nickel—Precipitated with dimethylglyoxime in neutral solution; separation of acid-insoluble sulfides, $Fe(OH)_3$ with NH_3, Pd dimethylglyoxime from 0.5 N acid, and AgI in ammoniacal solution.

The decay curve resolved into a 3-hour and a 57-hour component. The 3-hour period was taken to be Ni^{65}; the 57-hour period was shown to be Ni^{66} by separation of its 5-minute Cu^{66} daughter.

Copper—Precipitated as CuCNS and CuS; separations of $Fe(OH)_3$ plus $BaCO_3$ with NH_3, CdS in cyanide solution, and AgCl.

The main component of the decay curve was a 57-hour ~0.5 Mev β^--emitter assigned to Cu^{67}.

Zinc—Precipitated as $ZnHg(CNS)_4$ and ZnS; separations of Bi_2S_3 and $Fe(OH)_3$ plus $BaCO_3$ from NaOH solutions.

The decay curve showed the growth of a 14-hour daughter and then a 49-hour decay. Separation of Ga^{72} identified the isotope as Zn^{72}.

Gallium—Extracted into ether as $GaCl_3$; separations of Mo α-benzoin oxime, Bi_2S_3, and $Fe(OH)_3$ plus $BaCO_3$ from NaOH solution.

The decay curve resolved into a 4.9-hour and a 14-hour component. The 5-hour period was identified as Ga^{73}; the 14-hour period was identified as Ga^{72}.

Arsenic—Precipitated with H_2S from concentrated HCl and dissolved in NH_3 solution, distilled as $AsCl_3$; separation of $GeCl_4$ by distillation.

Components of 40 hours and 19 days were resolved from the decay curves. The 40-hour β^- had an energy of ~0.6 Mev and was identified as As^{77}. The 19-day activity, which was ~50 percent positrons, was identified as the shielded As^{74}. These was evidence of the hard positrons of As^{76} in the absorption curve.

Selenium—Distilled as $SeBr_4$, and precipitated as Se° with SO_2 in cold concentrated HCl.

The activity observed two hours after the midpoint of the bombardment decayed to background with a 57-minute period and was identified as the 58-minute isomer of Se^{81}.

Bromine—Oxidized to Br_2 and extracted into CCl_4 after $NaNO_2$ oxidation of I^- to I_2 and prior extraction, extraction of Br_2 into CCl_4 with $NaHSO_3$ solution, precipitation of AgBr.

The activity observed three hours after the midpoint of the bombardment resolved into 2.7-hour and 35-hour periods. The 2.7-hour period was identified as Br^{83}; the 35-hour period was identified as the shielded Br^{82}.

Rubidium—Precipitated as $RbClO_4$, Rb_2PtCl_6; separation of insoluble sulfides, hydroxides, carbonates, and Cs silicotungstate.

A 21-day 2.0 Mev β^-, 23-day 1.5 Mev β^+, ~40-day 12 kev x-ray and ~40-day 0.6 Mev γ were observed. The ~20-day periods were associated with shielded Rb^{86} and the ~40-day periods were associated with shielded Rb^{84}.

Strontium—Precipitated as $Sr(NO_3)_2$ with fuming HNO_3, and SrC_2O_4; separations of $Fe(OH)_3$ and $BaCrO_4$.

The activity observed a month after the bombardment consisted of a 55-day 1.6 Mev β^- which was identified as Sr^{89}. The presence of Sr^{90} was detected by separation of its 62-hour Y daughter.

Yttrium—Precipitated as YF_3, $Y(OH)_3$, and $Y_2(C_2O_4)_3$; separations of Bi_2S_3.

Components of 10-hour, 62-hour, and 57-day periods were resolved from activity separated soon after the bombardment. The 10-hour period was identified as Y^{93}. The 62-hour period was identified as Y^{90}. The yield of 57-day Y^{91} was measured in a Y fraction separated three weeks after bombardment. The rare earth activities present in the Y fraction did not interfere because their yields are much less.

Zirconium—Precipitated as $BaZrF_6$, and Zr cupferrate in 1 *M* HCl; separations of LaF_3 and $BaSO_4$.

The 68-day ~0.4 Mev β^- observed was identified as Zr^{95}.

Columbium—Precipitated as Cb_2O_5 from a high acidity solution and from NH_4F solution; separations of $BaZrF_6$, Bi_2S_3, and Te°.

The activity consisted of a soft β^- and γ decaying with a 35-day half-life which was identified as the lower state of Cb^{95}.

Molybdenum—Extracted into ether from 6*N* HCl after Br_2 oxidation, precipitated as α-benzoin oxime from 3*N* HCl after Br_2 oxidation, precipitated as α-benzoin oxime from 3*N* HNO_3 containing $H_2C_2O_4$, and as Ag_2MoO_4; separations of $Fe(OH)_3$.

The activity observed a few hours after bombardment consisted of a 67-hour 1.2 Mev β^- identified as Mo^{99}.

Ruthenium—Distilled from fuming $HClO_4$ containing H_3PO_4, precipitated as a lower oxide by ethyl alcohol in NaOH solution, and as Ru° by Mg in HCl; separations of OsO_4 by distillations from HNO_3.

The decay curve of activity from a short bombardment resolved into a 4.5-hour, a 36-hour, and a long-lived component. The 4.5-hour and 36-hour periods were identified as Ru^{105} and Rh^{105} daughter. In a Ru fraction from a long bombardment a 42-day ~0.2 Mev β^- and a much longer-lived very hard β^- were observed. The 42-day period was identified as Ru^{103}. The long period is probably the 1-year Ru^{106} detected by counting the 4 Mev β^- of its 30-second Rh^{105} daughter.

Palladium—Precipitated as dimethylglyoxime from 0.5*N* HCl; separations of $Fe(OH)_3$, AgI, and AgCl.

The decay curve resolved into a 13-hour and a 21-hour component. The 13-hour period was identified as Pd^{109} by separation of its 40-second Ag^{109} daughter.

Silver—Precipitated as AgCl and Ag_2S; separations of $Fe(OH)_3$.

The decay curve consisted of a 3.5-hour component identified as Ag^{112}, and a 7.5-day 1.0 Mev component identified as Ag^{111}. The 225-day isomer of Ag^{110} was also observed in small amounts. 5.3-hr. Ag^{113} would not have been resolved.

Cadmium—Precipitated as CdS from 0.2 *N* HCl and from NH_3 solution, and as $CdNH_4PO_4$; separations of basic ferric acetate, $In(OH)_3$, PdS, and Sb_2S_3.

The decay curve consisted of a 2.3-day and a 43-day component, and a 4.5-hour In daughter was separated. The activities were identified as the two isomers of Cd^{115}.

Antimony—Precipitated as Sb_2O_3, and as Sb_2S_3 from hot 3 *N* HCl; separations of As_2S_3, MoS_3, Te°, $Fe(OH)_3$ from KOH solution, and Bi_2S_3 from K_2S solution.

An Sb fraction from a short bombardment contained a 2.7-day 1.7 Mev β^- which was taken to be Sb^{122}. A 6-day x-ray activity observed in another bombardment was tentatively identified as the 6-day isomer of Sb^{120}. A 60-day β^- was also observed and identified as Sb^{124}.

Tellurium—Precipitated as Te° by SO_2 in 3 *N* HCl; separations of Se°, $SeBr_4$ by distillation, and $Fe(OH)_3$ from NaOH solution.

Observation of a 6-day β^+ activity suggested the presence of the 6-day electron capturing Te^{118} which was confirmed by separation of its 3-minute β^+-emitting Sb^{118} daughter. Te^{119} was detected by separating the 40-hour x-ray activity of its Sb^{119} daughter. The ~130-day activity observed consisted of ~0.2 and ~1.2 Mev electrons, 27 kev x-ray, and 185 and 650 kev γ. This activity was identified as the 143-day isomer of Te^{121} and its daughters.

Iodine—Distilled as I_2 from HNO_3, extracted as I_2 into CCl_4 after $NaNO_2$ oxidation, and precipitated as AgI.

Positrons, x-rays and γ's of 4.5-day half-life were observed and identified as I^{124}. A 13-day 1.0 Mev β^- was identified as I^{126}. The third component of the decay curve was a 55-day x-ray emitter identified as I^{125}.

Cesium—Precipitated as $CsClO_4$, Cs_2PtCl_6, and Cs silicotungstate from 6*N* HCl; separations of insoluble sulfides, hydroxides, and carbonates.

The fraction contained a 6-day 0.65 Mev γ, 10.5-day x-ray, 19-day 1.9 Mev β^-, and a small amount of ~30-day and ~300-day tails. The 6-day activity was identified as Cs^{132}; the 10.5-day activity was identified as Cs^{131} and the other activities could not be identified as Cs isotopes.

Barium—Precipitated as $Ba(NO_3)_2$ with fuming HNO_3, $BaCrO_4$, and $BaCl_2$ with ether—HCl mixture; separations of $Fe(OH)_3$.

A 38-hour 280 kev ϵ^- activity was identified as the 38-hour isomer of Ba^{133}. A 40-hour La activity was separated from the Ba, showing the presence of Ba^{140} in very low yield. The presence of Ba^{131} was shown by growth in the x-ray decay curve and the separation of Cs^{131} daughter.

Cerium—Precipitated as CeF_3, $Ce(OH)_3$ with carbonate-free ammonia, $Ce_2(C_2O_4)_3$, $Ce(IO_3)_4$, and $Ce_3(PO_4)_4$; separations of Bi_2S_3.

A 30-day ~0.6 Mev β^--activity was identified as Ce^{141}. The other component of the decay curve was a ~140-day activity of soft electrons and x-rays which was identified as Ce^{139}.

Europium—Precipitated as EuF_3, $Eu(OH)_3$ with carbonate-free ammonia, and $Eu_2(C_2O_4)_3$; separations of Bi_2S_3, and $Ce(OH)_3$ after zinc amalgam reduction of Eu.

An initial activity of 500 particles, 32 γ, and 5 x-ray counts per minute decayed with a 21-day half-life and was tentatively identified as Eu^{149}.

Nuclear Gyromagnetic Ratios II

WILLIAM H. CHAMBERS AND DUDLEY WILLIAMS
Mendenhall Laboratory of Physics, Ohio State University, Columbus, Ohio
(Received May 27, 1949)

By means of super-regenerative oscillator techniques, magnetic resonance absorption peaks have been observed for Be^9, P^{31}, Cl^{36}, Rb^{85}, Cs^{133}, and La^{139}. By simultaneous observation of each of these resonances and of the proton absorption peak in the same magnetic field, the ratio of the resonance frequency ν of each of these nuclei to the proton frequency ν_p in the same applied field has been determined. The experimental results are as follows:

Nucleus	ν/ν_p
Be^9	0.14034 ± 0.00007
P^{31}	0.40490 ± 0.00011
Cl^{35}	0.09799 ± 0.00007
Rb^{85}	0.09661 ± 0.00004
Cs^{133}	0.13093 ± 0.00014
La^{139}	0.14116 ± 0.00014

From these experimental results, the gyromagnetic ratio for each nucleus can be determined in terms of the gyromagnetic ratio of the proton provided suitable corrections for the diamagnetism of the electrons are applied.

THE determination of nuclear gyromagnetic ratios by magnetic resonance absorption measurements in the radio frequency range has been discussed in detail in the recent literature. The present paper is concerned with results obtained for several nuclear species by a method involving a super-regenerative oscillator circuit.[1] This method involves the observation of the change in the amplitude of the output of the oscillator when the Larmor condition $h\nu=(\mu H/I)=gH$ is realized. A tube containing a solution of a salt containing the nuclei of interest is placed in the tank coil of the oscillator, the coil being mounted with its axis at right angles to a strong magnetic field, which can be varied. The Larmor condition is realized by varying the strong magnetic field. The resonance absorption line can be displayed on an oscilloscope by applying a small 60-cycle modulation to the strong magnetic field.

In order to obtain the absolute value of a nuclear gyromagnetic ratio g, the value of the resonance frequency ν and the value of the strong field H must both be determined with high precision. As the precise determination of magnetic fields is a matter of considerable difficulty, a different procedure giving gyromagnetic ratios in terms of the known proton gyromagnetic ratio g_p was adopted.[2] This procedure involved the comparison of the resonance frequency ν of a given nucleus with the resonance frequency ν_p of the proton in the same magnetic field. In order to make this comparison a second oscillator tank circuit containing a proton sample was mounted in the strong magnetic field close to the coil containing the unknown. The outputs of the two oscillators were displayed on the same oscilloscope by means of an electronic switch. The frequency of the second oscillator was varied until the absorption peaks for the proton and the unknown nucleus appeared at the same position on the oscilloscope trace. When the two absorption peaks are properly matched, the gyromagnetic ratio g of the unknown can be determined in terms of the gyromagnetic ratio of the proton g_p from the relations

$$h\nu=gH$$
$$h\nu_p=g_pH. \quad (1)$$

Thus, g is determined in terms of a frequency ratio (ν/ν_p) which is readily determined:

$$g=(\nu/\nu_p)g_p. \quad (2)$$

The frequencies ν and ν_p were determined by zero-beat with a General Radio 805C signal generator calibrated at 100 kc/sec. intervals with a crystal-controlled multivibrator; the 100th harmonic of the multivibrator was adjusted to zero-beat with the 10 Mc/sec. carrier signal from WWV.

The experimental values of the frequency ratios ν/ν_p for Be^9, P^{31}, Cl^{35}, Rb^{85}, Cs^{133}, La^{139} are given in Table I. The observed frequency ratios have been corrected for a small field inhomogeneity; this correction takes account of the fact that the applied field at the proton sample position is slightly different from the field at the unknown-sample position. Each frequency ratio given in the table is the average of ten independent measurements, each of which was made at a different radio frequency. The indicated uncertainty is the average

TABLE I. Experimental results: frequency ratios.

Nucleus	Sample	Resonance frequency/ Resonance frequency of proton
Be^9	$BeCl_2$	0.14034 ± 0.00007
P^{31}	H_3PO_4	0.40498 ± 0.00011
Cl^{35}	LiCl	0.09799 ± 0.00007
Rb^{85}	Rb_2CO_3	0.09661 ± 0.00004
Cs^{133}	CsCl	0.13093 ± 0.00014
La^{139}	$LaCl_3$	0.14116 ± 0.00014

[1] J. R. Zimmerman and D. Williams, Phys. Rev. (to be published).
[2] Thomas, Driscoll, and Hipple, Phys. Rev. **75**, 902 (1949).

TABLE II. Summary of recent resonance measurements in solids and liquids.

Nucleus	Resonance frequency / Resonance frequency of proton	Calculated from	Ref.
n^1	0.68479 ±0.0004		(a)
	0.685001 ±0.00003		(b)
H^2	0.153506 ±0.000001		(c)
	0.15355 ±0.00005		(d)
	0.1535105±0.000005		(e)
	0.153501 ±0.00007		(f)
H^3	1.066636 ±0.00001		(g)
	1.06666 ±0.00010		(h)
Li^7	0.38862 ±0.00002		(d)
	0.388625 ±0.00004		(i)
Be^9	0.14034 ±0.00007		
B^{10}	0.10745 ±0.00011	$(B^{10}/B^{11})(B^{11}/H^1)$	(i)
B^{11}	0.32085 ±0.00006		(i)
	0.32076 ±0.00009		(d)
C^{13}	0.25143 ±0.00005		(j)
F^{19}	0.94086 ±0.00018		(d)
	0.94077 ±0.0001		(j)
	0.94079 ±0.00010		
Na^{23}	0.26454 ±0.00007		(d)
	0.26450 ±0.00003		(i)
Al^{27}	0.26062 ±0.00007		(d)
	0.26056 ±0.00003		(i)
P^{31}	0.40498 ±0.00011		
	0.40481 ±0.00004		(i)
	0.40495 ±0.0003	$(P^{31}/Na^{23})(Na^{23}/H^1)$*	(k)
Cl^{35}	0.09799 ±0.00007		
	0.09800 ±0.00014	$(Cl^{35}/Na^{23})(Na^{23}/H^1)$	(i)

value of the individual deviations from the mean with the sign of the deviation neglected. In the table the compound used for each nuclear species is indicated; in each case, a saturated solution was used and a small amount of magnetic catalyst was employed.

In general, the values for ν/ν_p given in Table I are in fair agreement with those obtained by other investigators employing different methods of observing the resonances. The only exception is the value for P^{31}; the value obtained for P^{31} is in good agreement with the value reported by Pound[3] but is somewhat larger than the value reported by Bitter.[4] The value for La^{139} has not been determined by other methods. Where a check is available, it is found that the frequency ratios reported here are in some cases slightly higher and in some cases slightly lower than those obtained by other methods; this would seem to indicate that there is no systematic error in the super-regenerative oscillator method.

The uncertainties listed in Table I are somewhat greater than those reported for other nuclei in the earlier paper.[1] As pointed out in the earlier paper, the arrangement for frequency measurement may introduce errors as large as 0.02 percent; the uncertainties listed for the nuclei reported here are somewhat larger than this and are as large as 0.1 percent for Cs^{133} and La^{139}. The primary source of additional error in the work reported here lies in the somewhat ambiguous matching of the proton resonance peak with the resonance peak for the other nucleus. For the six nuclei studied in the present experiment, the resonance signal was weak and broad. The width of the resonance signal was several gauss as compared with about 0.5 gauss for the proton. As the resonance signal was poorly defined, it was difficult to select a resonance "peak" with which to match the proton. The large line widths can be attributed only in part to field inhomogeneities.

From the observed values of ν/ν_p, it would appear that the gyromagnetic ratio g for each nucleus could be determined in terms of the recent measurement of the absolute value[2] of g_p from relation (2). However, it must be recalled that although the resonances are observed in the same *applied* magnetic field, the actual fields at the nuclei are not necessarily the same. The chief correction to be applied is a small correction for the diamagnetism of the electrons. The Lamb correc-

[3] R. V. Pound, Phys. Rev. **73**, 1112 (1948).
[4] F. Bitter, Phys. Rev. **75**, 1326 (1949).

TABLE II.—*Continued.*

Nucleus	Resonance frequency / Resonance frequency of proton	Calculated from	Ref.
Cu^{63}	0.26515 ±0.00005		(d)
	0.26506 ±0.00005		(i)
	0.26508 ±0.0002	$(Cu^{63}/Na^{23})(Na^{23}/H^1)$*	(l)
Cu^{65}	0.28393 ±0.0004	$(Cu^{65}/Cu^{63})(Cu^{63}/Na^{23})(Na^{23}/H^1)$*	(l)
	0.28391 ±0.00006		(i)
	0.28404 ±0.00009		(d)
Ga^{69}	0.24009 ±0.0008	$(Ga^{69}/Ga^{71})(Ga^{71}/Na^{23})(Na^{23}/H^1)$*	(k)
Ga^{71}	0.30494 ±0.0004	$(Ga^{71}/Na^{23})(Na^{23}/H^1)$*	(k)
Br^{79}	0.25059 ±0.00005		(d)
	0.25054 ±0.0006	$(Br^{79}/Br^{81})(Br^{81}/Na^{23})(Na^{23}/H^1)$*	(m)
Br^{81}	0.27014 ±0.00005		(d)
	0.27003 ±0.00008		(i)
	0.27003 ±0.0003	$(Br^{81}/Na^{23})(Na^{23}/H^1)$*	(m)
Rb^{85}	0.09661 ±0.00004		
	0.09657 ±0.00011		(i)
Rb^{87}	0.32718 ±0.00016		(d)
	0.32718 ±0.00007		(i)
I^{127}	0.20003 ±0.00007		(d)
	0.20013 ±0.0002	$(I^{127}/Na^{23})(Na^{23}/H^1)$*	(k)
Cs^{133}	0.13093 ±0.00014		
	0.13113 ±0.00014	$(Cs^{133}/Li^7)(Li^7/H^1)$	(i)
La^{139}	0.14116 ±0.00014		
Tl^{203}	0.571499 ±0.00005**		(j)
	0.5714 ±0.0001		(n)
Tl^{205}	0.577135 ±0.00005**		(j)
	0.5770 ±0.0001		(n)

* Value for Na^{23}/H^1 taken from 3 for calculation.
** Values for Tl^{203}/H^1 and Tl^{205}/H^1 interchanged.
[a] W. R. Arnold and A. Roberts, Phys. Rev. **70**, 766 (1946).
[b] Bloch, Nicodemus, and Staub, Phys. Rev. **74**, 1025 (1948).
[c] Bloch, Levinthal, and Packard, Phys. Rev. **72**, 1125 (1947).
[d] See reference 1.
[e] Bitter, Alpert, Nagle and Poss, Phys. Rev. **72**, 1271 (1947).
[f] A. Roberts, Phys. Rev. **72**, 979 (1947).
[g] Bloch, Graves, Packard, and Spence, Phys. Rev. **71**, 551 (1947).
[h] H. L. Anderson and A. Novick, Phys. Rev. **71**, 372 (1947).
[i] See reference 3.
[j] H. L. Poss, Phys. Rev. **75**, 600 (1949).
[k] See reference 4.
[l] R. V. Pound, Phys. Rev. **73**, 523 (1948).
[m] R. V. Pound, Phys. Rev. **72**, 1273 (1947).
[n] W. G. Proctor, Phys. Rev. **75**, 522 (1949).

tion[5] for diamagnetism has been employed by many investigators but its use for heavier elements is somewhat questionable. Hence, we shall not list values for gyromagnetic ratios; when a reliable diamagnetism correction has been developed, values for nuclear gyromagnetic ratios can be obtained from the observed values of ν/ν_p and the then accepted value of g_p. For purposes of comparison of data obtained by various methods we have assembled the published data and reduced it to frequency ratios ν/ν_p. These values of ν/ν_p are given in Table II. In cases where the original comparison was not made with the proton, the indicated calculation has been made.

In connection with the question of internal fields, one might raise questions concerning the effects of small amounts of magnetic catalysts. Thus far, we have not detected any variations in resonance frequency when catalysts are added. However, this problem is receiving further attention.

The writers wish to express their appreciation to Dr. John R. Zimmerman for his able assistance in designing apparatus, to Mr. R. E. Sheriff for assistance in taking data, and to the Graduate School, Research Foundation, and Development Fund of the Ohio State University for research grants.

[5] W. E. Lamb, Phys. Rev. **60**, 817 (1941).

Beta-Spectra of Forbidden Transitions

LAWRENCE M. LANGER AND H. CLAY PRICE, JR.
Department of Physics, Indiana University, Bloomington, Indiana
(Received April 26, 1949)

The beta-spectra of the forbidden transitions of Y^{91}, Sr^{89}, Y^{90}, Cs^{137}, RaE, Au^{198}, Re^{186}, and P^{32} have been measured with thin sources and high resolution. Forbidden type spectra are found for the first five. Au^{198}, Re^{186}, and P^{32} yield spectra with the allowed shape. Evidence is advanced for the reliability of the nuclear shell structure model and for the validity of G.-T. selection rules. End points found are: Y^{91}, 1.537±0.007 Mev; Sr^{89}, 1.463±0.005 Mev; Y^{90}, 2.180±0.007 Mev; Cs^{137}, 0.51±0.01 Mev; Au^{198}, 0.956±0.005 Mev; Re^{186}, 1.063±0.006; and P^{32}, 1.689±0.01 Mev.

I. INTRODUCTION

SINCE the energy dependence in the allowed form of beta-spectra is mainly determined by the statistical distribution of momentum between the electron and the neutrino, the experimental evidence from measurements of such spectra does not yield information regarding the uniqueness of the Fermi theory or of the possible forms which can be given to it.[1] The spectra of forbidden transitions, however, may, at least in some cases, be expected to have shapes different from that of an allowed transition. The exact form of the momentum distribution in such cases will be determined by the form of the particular interaction between the nucleon and the electron-neutrino field which is assumed. It should be kept in mind, however, that since the forbidden factor may be dominated by terms which are not dependent on energy, it is thus quite possible for once forbidden and even twice forbidden spectra to have the allowed shape. It must also be remembered that selection rules other than those on spin and parity change may operate so as to increase effectively the comparative half-life.[2] Empirical classification of forbiddenness on the basis of such ft values alone may therefore be too high.

Until recently, the beta-spectrum of RaE has been the only distribution which was reported to have a shape unambiguously different from that of an allowed transition.[3]

Although the shape of the RaE spectrum can be accounted for fairly satisfactorily,[2] the explanation involves considerable arbitrariness in the evaluation of the several matrix elements that appear in the forbidden factor. As a result, one cannot come to any definite conclusions regarding the type of interaction on the basis of the RaE results alone.

The present paper reports the results of detailed measurements on the spectra of several transitions, which are empirically classified as forbidden because of their long comparative half-lives. These investigations were instituted for the purpose of determining whether any transition other than RaE might yield a distribution distinctly different from the allowed shape. In particular, it was hoped that some forbidden transition might be discovered which would be consistent with a more specific theoretical description. Such transitions might be expected to occur for example, according to Gamow-Teller selection rules, when the disintegration involves a spin change of one unit higher than the degree of the forbiddenness. For such cases, all but one of the nuclear matrix elements vanish, so that a unique spectrum distribution is predicted. Moreover, the nuclear shell structure analysis[4] can, for certain elements close to the stable configurations, predict the spin and parity of the initial and final states.

The shapes of the spectra reported below for Y^{91} and Sr^{89} are indeed in exact agreement with what is to be expected for transitions involving a spin change of two units and a parity change. These spectra, therefore, are to be classified in terms of spin and parity change as once forbidden in spite of the fact that their comparative half-lives ($ft \sim 5\times10^8$) would classify them empirically as twice forbidden. These results furnish good evidence for the reliability of the shell model. They also provide evidence for the validity of the G.-T. selection rules, based on spectra shapes. Y^{90} and Cs^{137} are also found to yield forbidden spectra similar to those of Y^{91} and Sr^{89}.

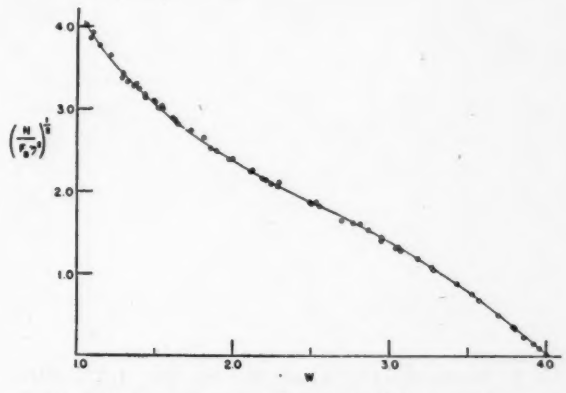

FIG. 1. Conventional Fermi plot for the Y^{91} beta-spectrum.

[1] E. J. Konopinski and G. E. Uhlenbeck, Phys. Rev. **60**, 308 (1941).
[2] E. J. Konopinski, Rev. Mod. Phys. **15**, 209 (1943).
[3] G. J. Neary, Proc. Roy. Soc. **A175**, 71 (1940). L. M. Langer, Phys. Rev. **75**, 328 (1949). R. Morrissey and C. S. Wu, Bull. Am. Phys. Soc. **24**, D14 (1948).
[4] E. Feenberg and K. C. Hammack, Phys. Rev. **75**, 1877 (1949).

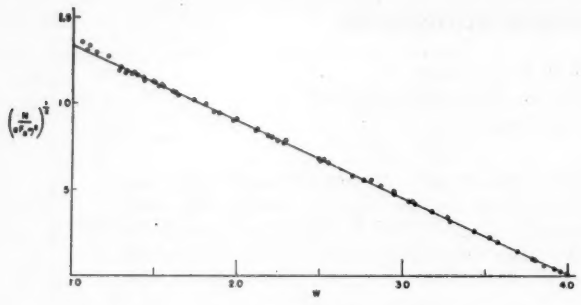

FIG. 2. Forbidden Fermi plot for the Y^{91} beta-spectrum. $a \sim (W^2-1)+(W_0-W)^2$.

The spectra of Re^{186} and Au^{198} were studied because they involve high Z elements in which the half-lives and end points are very similar to those of RaE. Both, however, were found to yield distributions indistinguishable from that of an allowed transition. P^{32} was also found to have the allowed shape.

II. EXPERIMENTAL METHOD

All of the spectra were studied in the 40-cm radius of curvature, shaped field magnetic spectrometer described previously.[5] All sources were 0.4-cm wide and 2.5-cm high. The detecting slit was set at 0.4 cm and the defining slit was set to transmit all particles emerging from the source within an angle of 32 degrees. Under these conditions the resolution is such that, with a thin source, the full width at half maximum for an internal conversion line is 0.5 percent. With such resolution, the influence of the "line" width on the shape of a spectrum is quite negligible.[6] Both grid supported Zapon, and unsupported mica window counters were used in appropriate and overlapping energy regions. Tests show that the presence of the supporting grid, when it is properly designed, does not affect the spectrum distribution. All the sources were supported on a backing of Zapon and LC600 of about 0.02 mg/cm² total thickness. The sources were prevented from acquiring a high electric potential either by means of a grounded graphite covered hair or by a narrow strip of 0.18 mg/cm² aluminum, layed down next to but not touching the end of the radioactive deposit. Insulin was used to help spread the activity over the desired area.[7] The sources were made as thin as was compatible with the activity. Energy determinations are in terms of the 0.5108 Mev annihilation radiation and the 0.411 Mev Au^{198} internally converted gamma-ray.

III. RESULTS

A. Yttrium 91

The source of Y^{91} was obtained carrier free from Oak Ridge, and was further separated from the alkaline earths. The sources used had an average thickness of about 0.15 mg/cm². Our measurements of the decay in terms of a uranium monitor, seem to be in better agreement with the half life of 61 days reported by Grummitt and Wilkinson,[8] than with the previously reported value of 57 days.

The results obtained[9] on the Y^{91} spectrum are shown in terms of the conventional Fermi plot of the data shown in Fig. 1. N is the number of particles per minute per unit momentum interval normalized to constant detector slit acceptance by dividing the actual number detected at any magnetic field strength by the value of

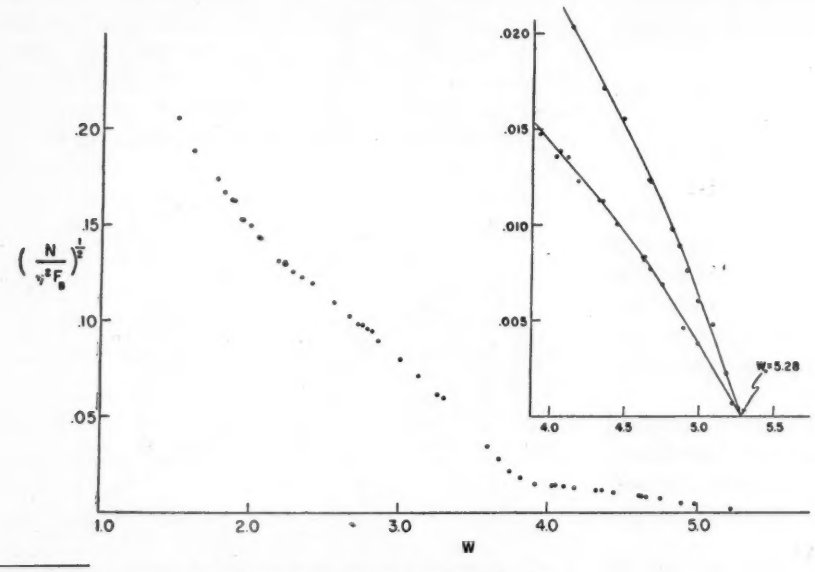

FIG. 3. Conventional Fermi plot for the spectra of Sr^{89} and Sr^{90} in secular equilibrium with Y^{90}. The Y^{90} tail is shown on a larger scale along with data obtained with a stronger source.

[5] L. M. Langer and C. S. Cook, Rev. Sci. Inst. 4, 257 (1948).
[6] G. E. Owen and H. Primakoff, Phys. Rev. 74, 1406 (1948).
[7] L. M. Langer, Rev. Sci. Inst. 20, 216 (1949).
[8] W. E. Grummitt and G. Wilkinson, Nature 158, 163 (1946).
[9] L. M. Langer and H. C. Price, Jr., Phys. Rev. 75, 1109 (1949) is a preliminary report of these results.

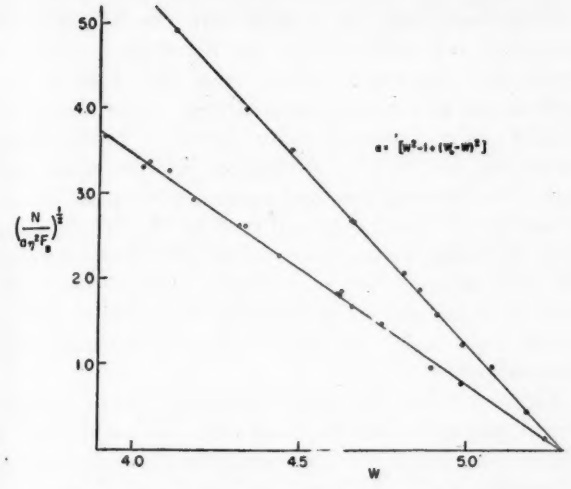

FIG. 4. Forbidden Fermi plot for the Y^{90} spectrum.

the field. η is the electron momentum in units of m_0c and W is the electron energy in units of m_0c^2. F_B is the Coulomb function which has been evaluated by means of the very good approximation given by Bethe and Bacher.[10]

It is apparent from Fig. 1 that the Fermi plot is not the usual straight line which is characteristic of allowed transitions; it is, instead, definitely curved.

Now, according to its comparative half-life ($ft=4.7\times10^8$), one might expect this transition to be twice forbidden. However, Feenberg and Hammack's[4] analysis of nuclear shell structure leads to the prediction of a spin change of 2 units together with a parity change. According to G.-T. selection rules, such a transition is theoretically classified as once-forbidden. According to the theory of forbidden spectra,[1,2] it also has the special property that only one type of nuclear matrix element fails to vanish for it. Thus a unique energy dependence is predicted, differing from the allowed shape by the factor

$$a\sim(W^2-1)+(W_0-W)^2$$

where W_0 is the maximum energy, which in this case is 4.01.

Thus, when the ordinates of the curve of Fig. 1 are divided by $a^{\frac{1}{2}}$, one should obtain a straight line if the above theory is correct. The result of such a plot is shown in Fig. 2.

It is seen that a very good straight line fit is obtained from the end point down to extremely low energies. The slight rise above the straight line below 100 kev may or may not be real.

Y^{91} has been reported as having no γ-radiation.[11] It is found, however, that measurements on a sample which was separated chemically and also by means of an ion exchange column, indicate the presence of extremely weak gamma-radiation with a period of 61 days. Absorption measurements of the gamma-radiation and coincidence absorption of Compton recoils indicate the existence of two quanta, one of 1.22 Mev and the other of about 0.2 Mev. Gamma-gamma-coincidence measurements indicate that these two quanta are in cascade following a beta-transition of less than 0.1 percent the intensity of the main group.† The presence of this feeble gamma-radiation therefore does not affect the interpretation that the main body of the data, reported in Fig. 2, represents the transition directly to the ground state. The Y^{91} end point occurs at 1.537 $\pm$0.007 Mev.

B. Strontium 89 and Yttrium 90

In this case, the source was obtained from Oak Ridge as a mixture of Sr^{89} and about 10 percent Sr^{90} in equi-

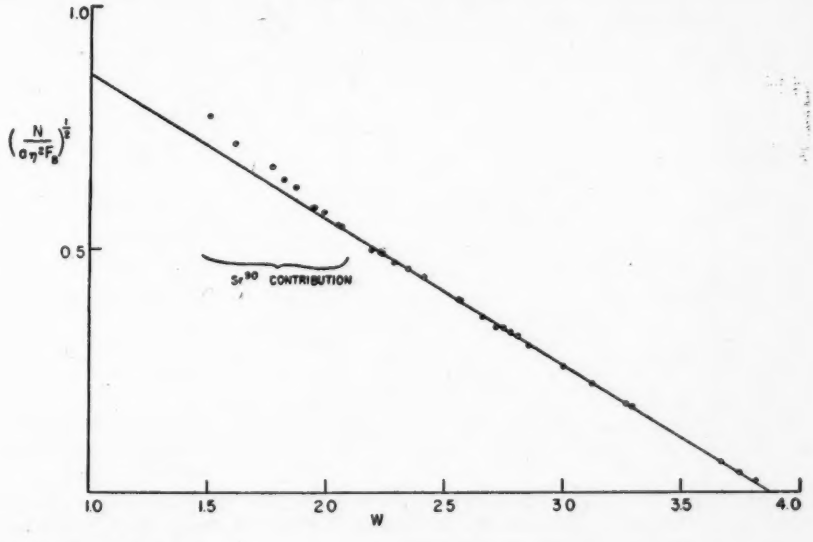

FIG. 5. Forbidden Fermi plot for the Sr^{89} spectrum obtained after correcting for the Y^{90} contribution.

[10] H. A. Bethe and R. F. Bacher, Rev. Mod. Phys. 8, 194 (1936).
[11] N. E. Ballou, Plut. Proj. Report CC298D, 4 (1942).
† We are indebted to Mr. E. T. Jurney for kindly making the coincidence measurements and calculations.

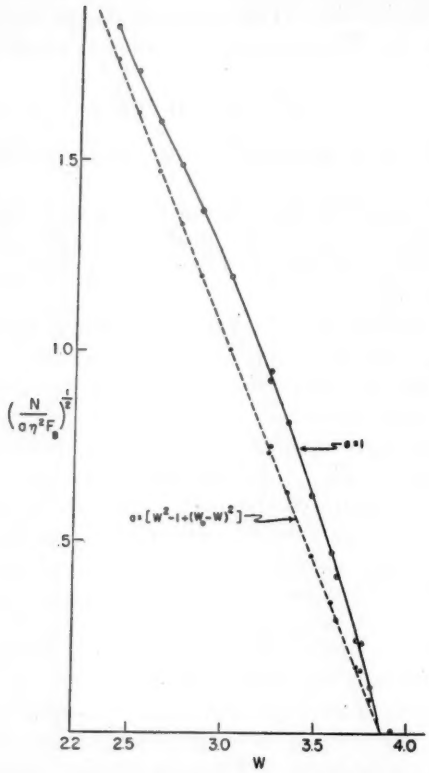

FIG. 6. Conventional and forbidden Fermi plots for data obtained with a source of Sr^{89} from which the Y^{90} had been chemically extracted.

librium with its daughter Y^{90}. Figure 3 shows the conventional Fermi plot of the data obtained with a source of about 0.02 mg/cm² average thickness. A second stronger source was used to obtain somewhat better statistics for the Y^{90} tail.

It is clear from Fig. 3 that both the Y^{90} and Sr^{89} spectra do not yield straight line Fermi plots. Figure 4 shows that application of the same forbidden factor, appropriate to a transition involving a spin change of 2 units and a change of parity, fits the Y^{90} data. After correcting for the Y^{90} contribution in accordance with such a forbidden shape, and again applying the appropriate factor, a, one obtains Fig. 5 for the Sr^{89} distribution. No attempt was made to obtain information about the Sr^{90} shape by means of further subtraction, since such information can be obtained much better with a source from which the shorter lived Sr^{89} isotope has decayed out.[12]

Figure 6 shows both the conventional and forbidden Fermi plots for the Sr^{89} spectrum obtained with a source from which the Y^{90} fraction had been chemically extracted.

It is clear that both Y^{90} and Sr^{89} have forbidden spectra consistent with their being transitions involving a spin change of 2 units and a parity change.

The value of the Sr^{89} end point is 1.463±0.005 Mev. For Y^{90}, we get 2.180±0.007 Mev. This value is somewhat lower than the value recently reported by Meyerhof.[13] His value was obtained on the basis of a straight line interpretation of the conventional Fermi plot, obtained with a thicker source and poorer resolution.*

C. Cesium 137

The data on the Cs^{137} distribution were obtained with several sources, the thinnest of which had an average thickness of 0.03 mg/cm² and the thickest was 0.2 mg/cm². The Fermi plot of the data is shown in Fig. 7. In spite of the fact that there is a very strongly internally converted gamma-ray of 0.663 Mev and a weak

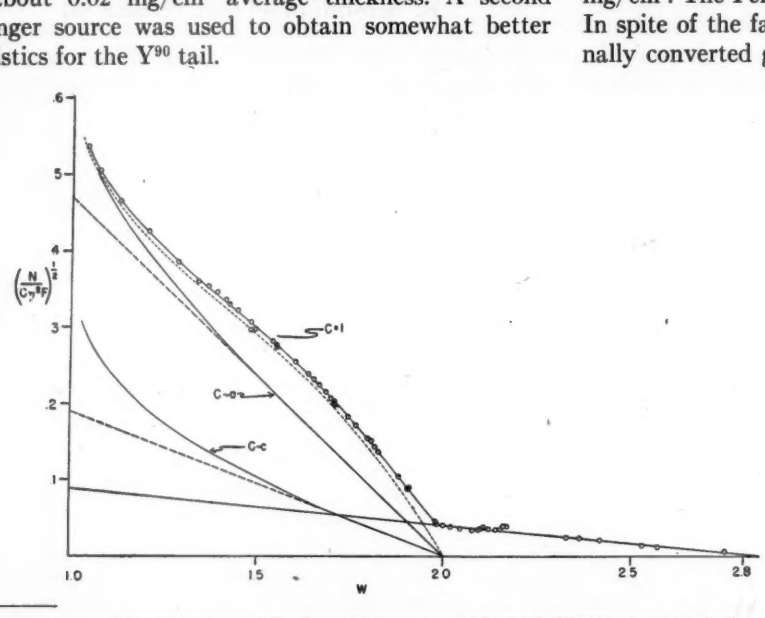

FIG. 7. Conventional and forbidden Fermi plots for the spectrum of Cs^{137}.

[12] Measurements by Jensen and Laslett, Phys. Rev. 75, 1949 (1949), do indeed show that Sr^{90} too has the same forbidden shape satisfied by the factor, a. They are also in agreement with our results on Y^{90}. We are grateful to Dr. Laslett for having made available these results to us prior to publication.

[13] W. E. Meyerhof, Phys. Rev. 74, 621 (1948).

* It is perhaps indicative of the perversity of nature, that thick sources and poor resolution can make straight line Fermi plots appear curved as well as curved Fermi plots appear straight.

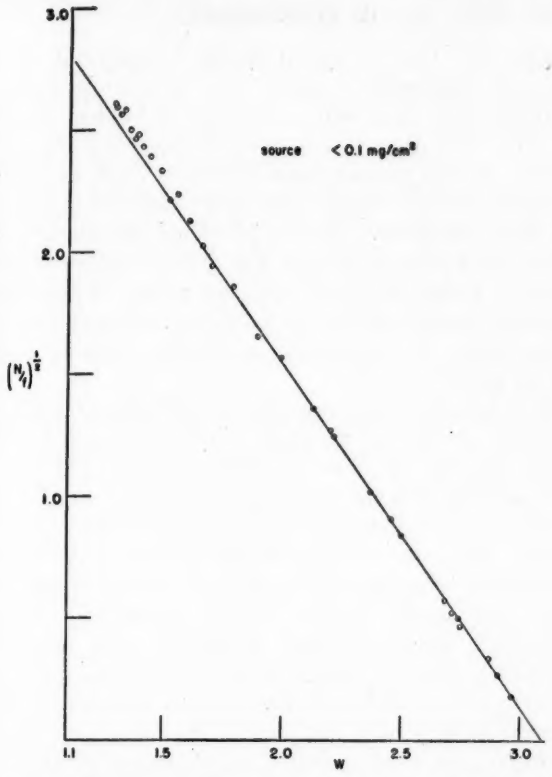

FIG. 8. Conventional Fermi plot for the spectrum of Re^{186}. The Coulomb factor was evaluated by expansion of the complex Γ function.

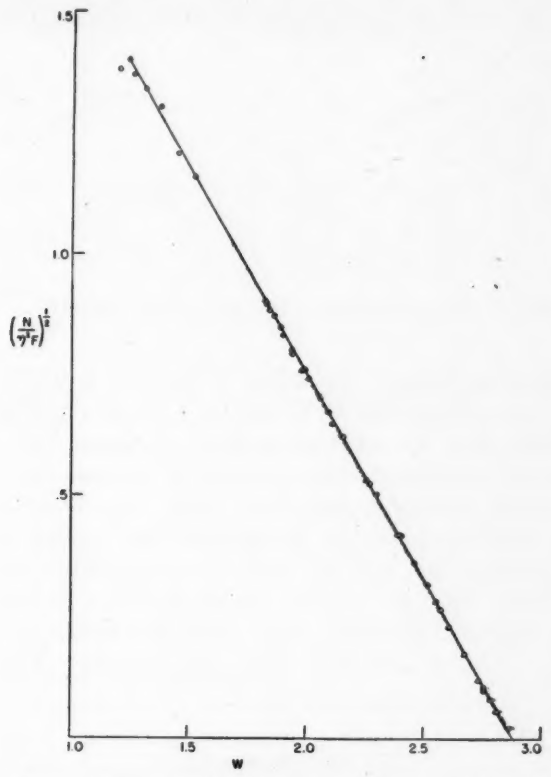

FIG. 9. Conventional Fermi plot for the spectrum of Au^{198}.

high energy group, it is quite apparent that the main spectrum does not give a straight line for the conventional Fermi plot ($C=1$). A detailed investigation of the high energy group seemed to indicate that it might be complex. An ion exchange column separation indicated that at least part of the high energy tail is associated with cesium. Poor statistics prevented a better investigation of this point with a thin source. For purposes of calculation, the high energy contribution has been deducted by assuming that its distribution follows a straight line Fermi plot. The resultant dotted curve obtained for the main transition is not very sensitive to this assumption.

The comparative half-life for Cs^{137} is $\sim 3\times 10^9$. If this transition were twice forbidden with a spin change of 3 units and no parity change, the forbidden factor would again be unique and would have an energy dependence given by

$$C\sim c\sim 3(W^2-1)^2+3(W_0-W)^4+10(W^2-1)(W_0-W)^2.$$

Figure 7 shows the results of applying both $C\sim c$ and $C\sim a$ to the data. It appears that the factor, a, gives a better fit although the agreement is not too good at very low energies.[14] The end point for the main transition to the 0.663 Mev level in Ba^{137} is 0.51 ± 0.01 Mev.

[14] See C. L. Peacock and A. C. G. Mitchell, Phys. Rev. **75**, 1272 (1949).

D. Rhenium 186 and Gold 198

The spectra of Re^{186} and Au^{198}, as mentioned above, were investigated because they are both high atomic number isotopes whose comparative half-lives are very similar to that of RaE. The source of Au^{198}, obtained from Oak Ridge, was chemically separated, particularly from mercury. Sources used for both elements were of the order of 0.1 mg/cm² thick. Figures 8 and 9 show that for both Re^{186} and Au^{198} the ordinary Fermi plot is indistinguishable from a straight line over almost the

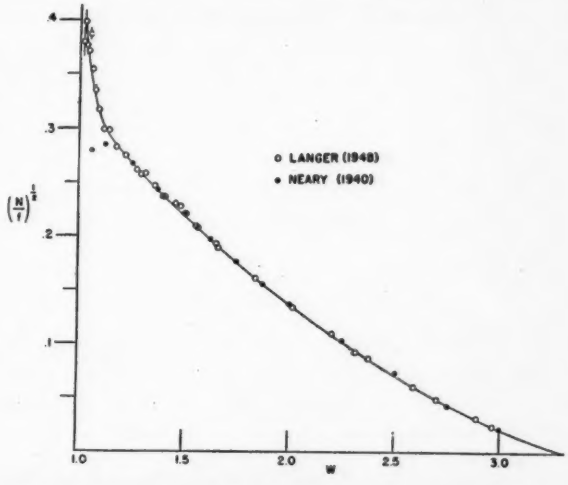

FIG. 10. Conventional Fermi plot for the spectrum of RaE.

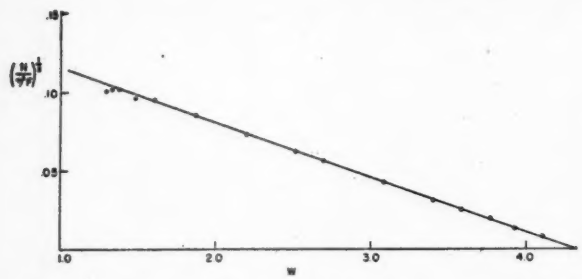

FIG. 11. Conventional Fermi plot for the spectrum of P^{32}.

entire distribution. The value of the end point for Au^{198} is 0.956±0.005 Mev. For Re^{186} we obtain 1.063 ±0.006 Mev. The spectrum of RaE was remeasured in the same apparatus using an essentially massless source extracted electrolytically from RaD. The ordinary Fermi plot shown in Fig. 10 shows excellent agreement with the earlier work of Neary[3] over the entire distribution. The plot is indeed not satisfied by a straight line. The fact that Neary's curve falls off at low energies may be due to an error in estimating the effect of absorption in the counter window.

E. Phosphorus 32

The spectrum of P^{32} was obtained with an Oak Ridge source of average thickness about 0.2 mg/cm². Here again, a straight line Fermi plot, Fig. 11, is obtained for this apparently forbidden transition. The end point obtained is 1.689±0.01 Mev.

IV. CONCLUSION

The fact that certain forbidden transitions have spectral distributions which can be completely accounted for by means of the forbidden factor $a\sim(W^2-1)+(W_0-W)^2$ is good evidence for the reliability of the nuclear shell structure analysis which predicts a parity change and a spin change of two units for those transitions. It is also evidence for the validity of the G.-T. selection rules. For once-forbidden transitions, a forbidden factor with an energy dependence specified completely by the factor, a, indicates that in those cases, the interaction is of the tensor or axial vector form.

The fact that some apparently forbidden transitions yield spectra having the allowed form, is expected to be quite common for once forbidden transitions. Although it is possible, only for very special conditions should one expect twice forbidden transitions to yield the allowed shape. Since the comparative half-lives may be increased by selection rules other than those applying to spin and parity change, certain apparently twice-forbidden transitions may indeed be only once-forbidden. It would therefore be of interest to examine the spectra of very definitely higher order transitions. The spectra of K^{40}, Be^{10}, Rb^{87}, and Tc^{99} should yield interesting results when measured with high specific activity sources.

We are greateful to Professor E. J. Konopinski for many helpful discussions. This work has been assisted by a grant from the Frederick Gardner Cottrell Fund of the Research Corporation and by the joint program of the ONR and AEC.

Pressure Broadening in the Microwave and Infra-Red Regions*

P. W. ANDERSON†
Harvard University, Cambridge, Massachusetts‡
(Received May 12, 1949)

In this paper a generalized theory of collision broadening is developed, adequate for predicting line breadths in the microwave and infra-red regions. This theory differs from previous ones in taking into account transitions among quantum states caused by collisions, although it is limited to a classical picture of the relative motion of the colliding molecules as a whole. Formulas are derived for computing approximate line broadening collision cross-sections from known intermolecular interactions, and the results of the theory are successfully compared with experiments on self-broadening in the ammonia inversion spectrum and the vibrational band spectra of HCl and HCN. Some cases of foreign gas broadening in the microwave region are examined, but it is concluded that in general the Van der Waals interaction, commonly assumed to be the force important in causing foreign gas broadening, is not adequate to cause the observed broadenings. The more complicated types of forces which become important at short range would have to be taken into account to give good agreement with experiment in these cases.

PART I. THEORY

A. Introduction

THE theories of pressure broadening presented up to this time can easily be shown to be inapplicable in the microwave and infra-red regions of the spectrum. The primary purpose of this paper is, therefore, to develop a theory which can give accurate results in these regions, and to compare these results with the available experimental data.

The older theories, in particular the Fourier integral treatment developed primarily by Lorentz, Lenz, and Weisskopf,[1–4] have given good results in the optical region.[4,5] However, this theory is essentially in contradiction to the theory of dielectric relaxation developed by Debye and others,[6–8] which treats broadening in the limiting case of a spectral line of zero frequency.[8] Both theories involve computing the spectrum due to a radiating molecule randomly interrupted by collisions with other molecules. However, the mechanism by which the interruption is effected is essentially different in the two theories. Debye's relaxation theory considers interruptions due only to reorientations of the radiating molecule; in a quantum theory, this is equivalent to considering transitions among the various spacially degenerate quantum states. Contrariwise, the Fourier integral theory explicitly assumes that no transitions are caused by collisions. Then the effect of a collision is computed by means of the adiabatic approximation and is equivalent to a relative phase-shift of the radiation before and after the collision, with no amplitude change.

B. Generalization of the Fourier Integral

It is clear that it is necessary, in order to compute pressure broadening in any frequency range, to develop an expression for the spectral shape of a pressure-broadened line which encompasses the two limiting cases of high and low frequencies. In other words, a formula must be obtained which includes the effects both of phase-shifts and of transitions. Before presenting this formula, we should emphasize the physical picture upon which it is based. This picture is equivalent to that employed by Foley[9] in his re-derivation of the standard Fourier integral formula by means of quantum radiation theory. The basic assumption we call the "assumption of a classical path": we assume that for all collisions of interest the colliding molecules can be taken to be point dipoles following definite paths; thus their interaction is a definite function of the time $H_1(t)$. The justification for this lies in the fact that one can think of the motion of the molecules in terms of packets of translational wave functions; by the uncertainty principle the allowable spreads Δp and Δq in position and momentum space are $\Delta p \Delta q \doteq h$. We seldom or never consider in detail collisions in which the molecules under consideration pass at distances less than the kinetic theory diameter, $\doteq 5$A. Then an uncertainty in position of 1A will lead to no great ambiguity in magnitude or type of intermolecular forces. The corresponding uncertainty in velocity is

$$\Delta v/v \doteq 0.3/(\text{molecular weight})^{\frac{1}{2}} \qquad (1)$$

which is a small percentage for most molecules. Calculations carried out by Lindholm[10] for many optical problems, not using this assumption, have indicated that the assumption is normally valid, in consideration

* The material in this paper is a part of the author's thesis submitted in partial fulfillment of the requirements for the degree of Doctor of Philosophy at Harvard University.
† National Research Council Predoctoral Fellow.
‡ Now at Bell Telephone Laboratories, Murray Hill, New Jersey.
[1] H. A. Lorentz, Proc. Amst. Acad. Sci. **8**, 59 (1906).
[2] W. Lenz, Zeits. f. Physik. **80**, 423 (1933).
[3] V. F. Weisskopf, Phys. Zeits. **34**, 1 (1933).
[4] E. Lindholm, Ark. Mat. Astron. Och Fys. **32**, 17 (1945).
[5] H. Margenau and W. W. Watson, Rev. Mod. Phys. **8**, 22 (1936).
[6] P. Debye, *Polar Molecules* (Chemical Catalog Company, New York, 1929), Chapter V.
[7] W. Kauzmann, Rev. Mod. Phys. **14**, 12 (1942).
[8] J. H. Van Vleck and V. F. Weisskopf, Rev. Mod. Phys. **17**, 227 (1945).
[9] H. M. Foley, Phys. Rev. **69**, 616 (1946).
[10] E. Lindholm, Dissertation, Uppsala, 1942.

of the large quantum numbers of the partial waves whose contributions were important.

The problem is reduced, by this assumption, to finding the spectrum radiated by a molecule, whose unperturbed Hamiltonian we designate by H_0. This molecule undergoes random perturbations due to collisions, representable by a time-dependent interaction Hamiltonian $H_1(t)$. The problem can be solved following Foley's method, by the use of general radiation theory; or it is possible to extend the correspondence-principle radiation theory of Klein and Pauli to our problem by analogy. Either method leads directly to the following formula, which we present without proof:**

$$I(\omega)=\text{const.}\times\omega^4\, Tr\Big[\rho_0\int_{-\infty}^{\infty}dt e^{i\omega t}\mu_z(t)\times\int_{-\infty}^{\infty}dt' e^{-i\omega t'}\mu_z(t')\Big]. \quad (2)$$

Here ω is the angular frequency for which we desire the spectral intensity $I(\omega)$; ρ_0 is an assumed initial density matrix for molecules in the gas, in fact essentially the density matrix for the time $t=-\infty$; $\mu_z(t)$ is the Heisenberg time-dependent operator (see reference 12) for the z-component of the dipole moment (if we consider radiation polarized in the z-direction); and the "Tr" means that one must take the diagonal sum of the indicated matrix product. $\mu_z(t)$, of course, satisfies the Heisenberg time equation

$$i\hbar\dot{\mu}=[H\mu-\mu H], \quad (3)$$

where

$$H=H_0+H_1(t). \quad (4)$$

Finally, we have omitted all numerical factors other than the frequency-dependent one ω^4. These factors can easily be shown to come correctly from the general theory.

The formula (2) gives the intensity for spontaneous emission. The approach through spontaneous emission is chosen in order to avoid the use of a time-dependent density matrix.†† The intensity for absorption must be derived from (2) by use of the Einstein relations.[11] Some confusion as to whether the correct Einstein relations come out of the theory actually does appear when the classical path method, or equivalent absorption methods, are used;[8] we have been able to clarify this point to some extent, but our work on this point will not be reported in this paper.

It is interesting to rewrite (2) for the case in which the standard Fourier integral of Foley and his predecessors is valid. This is the case in which the perturbing Hamiltonian $H_1(t)$ is either diagonal already, or can be made so in a simple manner (following Foley) by replacing transitions to high-energy levels by their second-order effects; that is, we replace the so-called Van der Waals forces, a second-order phenomenon, by a first-order Hamiltonian. This, too, can be shown to be valid from the general equations of motion and the radiation theory. Then Eq. (3) integrates explicitly; a typical matrix element is

$$\mu_{mn}(t)=\mu_{mn}(0)\exp\Big\{1/i\hbar\Big[(E_m-E_n)t+\int_0^t[(m|H_1|m)-(n|H_1|n)]\Big]\Big\}=\mu_{mn}(0)\exp[-i\omega_{nm}t-i\eta_{nm}(t)]. \quad (5)$$

The unperturbed frequency is ω_{nm}, given by

$$\hbar\omega_{nm}=E_m-E_n.$$

E_m is the mth eigenvalue of the unperturbed Hamiltonian H_0. Equation (5) defines the relative phase-shift η_{nm} for the two levels n and m. We can then use the Boltzmann density matrix

$$(n|\rho_B|m)=\delta_{nm}\exp(-E_n/kT)\times[\textstyle\sum_n\exp(-E_n/kT)]^{-1}, \quad (6)$$

for ρ_0, and I in (2) separates into the following contributions I_{mn} for each of the various spectral lines m and n:

$$I_{mn}(\omega)=\omega^4\exp(-E_m/kT)\times\Big|\mu_{mn}\int_{-\infty}^{\infty}dt\exp\{-i[(\omega-\omega_{mn})t+\eta_{mn}(t)]\}\Big|^2 \quad (7)$$

This is the form of the Fourier integral used by Weisskopf, etc.‡‡

** The intensity in classical theory is given by the average over-all states of

$$\omega^4\Big|\int_{-\infty}^{\infty}\mu_z(t)e^{i\omega t}dt\Big|^2$$

The corresponding quantum-mechanical quantity is obtained by replacing all observables (in this case $\mu(t)$) by quantum-mechanical operators, in multiplying by the density matrix, and taking the trace. Thus Eq. (21) is reasonable; a rigorous proof can be given. For this procedure see W. Pauli, Handbuch der Physik, 2. Aufl., Band 24, 1. Teil, p. 149.

†† See, for instance, R. Karplus and J. Schwinger, Phys. Rev. 73, 1020 (1948).

[11] A. Einstein, Verh. d. D. Phys. Ges. 18, 318 (1916); Phys. Zeits. 18, 121 (1917).

‡‡ It is interesting to note that the derivation of (7) employed by Foley fails to lead to the correct external frequency factor ω^4. If carefully followed, Foley's theory gives a factor here of $\omega^2\omega_{nm}^2$, which is by no means correct at low or zero frequencies, where the line-breadths are comparable to ω_{mn}. Even if Foley's "adiabatic assumption" (H_1 diagonal) were correct at low frequencies, these factors would be in error. The reason is that the general theory must be retained, at least until the point where a partial integration can be performed analogously to that which one would use in the classical theory to go from the Fourier integral of the vector potential $A(\sim\dot{\mu})$ to that of $\mu(t)$ itself.

C. Introduction of the Time-Development Matrix T

It is well known that it is possible to write the time-dependent operators $\mu(t)$ in Eq. (2) in the following manner:[12]

$$\mu(t)=U^{-1}(t)\mu_0 U(t), \tag{8}$$

where

$$ih(d/dt)U=(H_0+H_1(t))U. \tag{9}$$

If μ_0 is the value of μ at a time t_0, then $U(t_0)=1$ is the initial condition on Eq. (9). The time-development operator U is not as useful to us as another operator T, which is defined in much the same way. However, in deriving T one uses a Heisenberg representation in relation to the unperturbed energy H_0. Therefore the equation for $\mu(t)$ is

$$\mu(t)=T^{-1}(t)\exp(-H_0t/ih)\mu_0\exp(H_0t/ih)T(t), \tag{8'}$$

and that for T is

$$ih\dot{T}(t)=H_1'(t)T. \tag{9'}$$

H_1' is the interaction Hamiltonian with the time-dependence due to H_0 inserted:

$$(m|H_1'|n)=(m|H_1(t)|n)\exp[(E_m-E_n)t/ih]. \tag{10}$$

The diagonal elements of T give the phase-shifts due to the interaction H_1, while the off-diagonal elements—or their squared absolute values—give the transition probabilities due to this interaction. In terms of eigenstates of H_0, (8') is

$$(m|\mu(t)|n)=\sum_{k,l}(m|T^{-1}|k)\times\exp(-i\omega_{kl}t)(k|\mu_0|l)(l|T|n). \tag{8''}$$

We may now insert this explicit form for $\mu(t)$ into the Fourier integral formula (2), and obtain the following complicated expression:

$$I(\omega)=\text{const.}\times\omega^4\sum_{abcdefg}(a|\rho_0|b)\times\int_{-\infty}^{\infty}dte^{i\omega t}(b|T^{-1}(t)|c)(c|\mu_0|d)\times\exp(i\omega_{cd}t)(d|T(t)|e)\times\int_{-\infty}^{\infty}dt'e^{-i\omega t'}(e|T^{-1}(t')|f)(f|\mu_0|g)\times\exp(-i\omega_{fg}t')(g|T(t')|a). \tag{11}$$

D. Re-expression in Correlation-Function Form, and Simplification Using the Assumption of Short Collisions

Formula (10) can be simplified greatly by the insertion of a new time-development matrix

$$T(t\to t')=T(t')T^{-1}(t). \tag{12}$$

This operator is the solution of (9') with initial condition $T(t)=1$; it answers the question "what happens in the time-interval $t\to t'$?". In addition, we use the fact that the density matrix, as a function of time, transforms according to $T(t)$ but inversely to other matrices. Then (11) becomes:

$$I(\omega)=\text{const.}\times\omega^2\int_{-\infty}^{\infty}dt\int_{-\infty}^{\infty}dt'e^{i\omega(t-t')}\times\sum_{abcde}(a|\rho(t)|b)(b|\mu_0|c)\exp(-i\omega_{bc}t)\times(c|T^{-1}(t\to t')|d)(d|\mu_0|e)\times\exp(-i\omega_{de}t')(e|T(t\to t')|a). \tag{13}$$

In order to use the considerable simplification made available by the Wiener-Khintchine relations in evaluating our formulas,[13] it is expedient to re-express them in correlation-function form. By means of the simple substitution

$$t'=t+\tau,$$

we obtain

$$I(\omega)=\omega^4(\text{const.})\sum_{de}\int_{-\infty}^{\infty}d\tau\exp[i(\omega-\omega_{de})\tau]\varphi_{de}(\tau), \tag{14}$$

where

$$\varphi_{de}(\tau)=\int_{-\infty}^{\infty}dt\sum_{abc}\exp[-i(\omega_{bc}+\omega_{de})t]\times(a|\rho(t)|b)(b|\mu_0|c)(c|T^{-1}(t\to t+\tau)|d)\times(d|\mu_0|e)(e|T(t\to t+\tau)|a). \tag{15}$$

We observe that (15) has the form of an average over the time t. It consists of three essentially different terms: $\rho(t)$, which depends on the state of the molecule at t; the $T(t\to t+\tau)$ factors, which depend on the collisions which occur between t and $t+\tau$; and the phase-factor. At this point we first limit ourselves to the "impact" type of theory: we assume that the collisions are short compared to the time between them. Under this assumption, it is easy to show that unless $\omega_{bc}+\omega_{de}$ is less than $1/\tau$, the inverse of the time between collisions, (15) will essentially vanish. For this reason, and for other reasons which we shall not consider here, it is considered legitimate to drop from (15) all terms for which $\omega_{bc}+\omega_{de}\neq 0$. This is equivalent to assuming that all lines considered are either not resolved at all compared to the line-breadth—in which case we treat them as degenerate—or are well separated.***

It is also legitimate, since the phase and T-factors are independent of the actual state of the molecule, to take the average of $\rho(t)$ over the history of the molecule

[12] Born u. Jordan, *Elementare Quantenmechanik* (Verlag J. Springer, Berlin, 1930).

[13] See, for instance, M. C. Wang and G. E. Uhlenbeck, Rev. Mod. Phys. **17**, 323 (1945).

*** In Section H we will discuss further the terms which are here dropped.

separately. Clearly, we obtain for ρ_{Nv} the Boltzmann distribution (6). Let us now introduce a degenerate index m. Each state will be designated by a non-degenerate index $(a, b, c, d\cdots)$ and a degenerate index $(m, m'\cdots)$. Then, letting the "initial" state be designated by i, the final by f, (14) and (15) are

$$I=\sum_{i,f}\int_{-\infty}^{\infty} d\tau \exp[i(\omega_{if}-\omega)\tau](i|\rho_B|i)\varphi_{if}(\tau), \quad (16)$$

where

$$\varphi_{if}(\tau)=\sum_{m,m',m'',m'''}\int_{-\infty}^{\infty} dt(i, m|\mu|f, m') \times(f, m'|T^{-1}(t\to t+\tau)|f, m'') \times(f, m''|\mu|i, m''')(i, m'''|T(t\to t+\tau)|i, m), \quad (17)$$

or

$$\varphi_{if}(\tau)=Tr\left[\int_{-\infty}^{\infty} dt\mu^{if}(T^{-1}(t\to t+\tau))^f \times\mu^{fi}(T(t\to t+\tau)^i\right], \quad (17')$$

where the superscripts designate "Teilmatrices" for the given non-degenerate indices.

E. Solution for the Correlation Function in the Standard Optical Case

To illustrate our method of finding the correlation function and to furnish some introduction to the line-shapes to be expected, we shall re-derive the impact theory solution of the standard Fourier integral (7). This formula, re-written in correlation-function form by means of (13), and exclusive of numerical factors, is

$$I(\omega)=\int_{-\infty}^{\infty} d\tau \exp[i(\omega_{if}-\omega)\tau]\varphi(\tau),$$
$$\varphi(\tau)=\int_{-\infty}^{\infty} dt \exp\{i[\eta_{if}(t+\tau)-\eta_{if}(t)]\}. \quad (18)$$

The assumption of the impact theory is that the collisions are short compared to the time between them. Then

$$\eta_{if}(t+\tau)-\eta_{if}(t)=\sum_{\substack{\text{collisions from}\\ t \text{ to } t+\tau}}\eta_c, \quad (19)$$

where η_c are the phase-shifts due to the various collisions occuring in the interval $t\to t+\tau$:

$$\eta_c=\int_{\substack{\text{collision}\\ \text{"}c\text{"}}} dt[(i|H_1'(t)|i)-(f|H_1'(t)|f)]. \quad (20)$$

We divide the types of collisions into classes according to the paths followed by the molecules; then, corresponding to each "element of cross section" $d\sigma_k$ we can assume that there is a definite phase-shift η_k. Then the probability that a collision in $d\sigma_k$ occurs in a given, short time dt is given by

$$\rho(d\sigma_k)=nvdtd\sigma_k, \quad (21)$$

where n is the number of molecules per cc, and v is their velocity (assuming, as is always justifiable for collision-broadening problems, that all molecules have the average velocity $\bar{v}$).

Consider the integrand of the expression (18) for $\varphi(\tau)$:

$$f(t, \tau)=\exp\{i[\eta_{if}(t+\tau)-\eta_{if}(t)]\}. \quad (22)$$

If in the time $d\tau$ after τ a collision of type k occurs, we have

$$f(t, \tau+d\tau)=\exp(i\eta_k)f(t, \tau),$$
$$f(t, \tau+d\tau)-f(t, \tau)=[\exp(i\eta_k)-1]f(t, \tau). \quad (23)$$

Now let us take the integral, which is equivalent to averaging over all times t:

$$\varphi(\tau+d\tau)-\varphi(\tau)=d\varphi(\tau) =\langle[\exp(i\eta_k)-1]f(t, \tau)\rangle_{\text{average over } t}. \quad (24)$$

This is the point at which the impact theory assumption is vital. We must be able to say that the time $d\tau$ is short compared to the interval between collisions, and so contains at most one collision; on the other hand, $d\tau$ must be quite long compared with the duration of a collision, so that there is no correlation between what happens in the interval $d\tau$ and what happens in the preceding or following times. Then we can take the averages in (24) separately, and have

$$d\varphi(\tau)=\varphi(\tau)\langle\exp(i\eta_k)-1\rangle_{\text{average over collisions}} =\left[nvd\tau\int d\sigma_k(\exp(i\eta_k)-1)\right]\varphi(\tau), \quad (25)$$

so that

$$\varphi(\tau)=e^{-nv\sigma\tau}, \quad (26)$$

where

$$\sigma=\int d\sigma(1-e^{i\eta})=\sigma_r+i\sigma_i.$$

It is easy to see that

$$\varphi(-\tau)=\varphi^*(\tau)$$

as is required for the reality of $I(\omega)$; then we get for the intensity distribution

$$I(\omega)=\text{const.}\times\frac{2(nv\sigma_r)}{(\omega-\omega_{if}-nv\sigma_i)^2+(nv\sigma_r)^2}. \quad (27)$$

This is a dispersion line-form with half-width

$$2\pi(\Delta\nu)_{\frac{1}{2}}=nv\sigma_r, \quad \text{shift } 2\pi\Delta\nu_{if}=nv\sigma_i. \quad (28)$$

F. Solution for the Correlation Function in the Classical Debye Case

Since the classical Debye problem of the spectrum of a rotating dipole perturbed by collisions has frequently been considered by absorption methods,[6-8] in particular the very general method in the appendix of the paper by Van Vleck and Weisskopf, it is of interest to show how easily this problem is solved by correlation function methods. Here we can see that the spectrum is

$$I(\omega)=\int_{-\infty}^{\infty} d\tau e^{i\omega\tau}\varphi(\tau),$$
$$\varphi(\tau)=\int_{-\infty}^{\infty} dt\mu_z(t+\tau)\mu_z(t), \tag{29}$$

where $\mu_z(t)$ is the z-component of the rotator's dipole moment at a time t. Again we consider the function

$$f(t,\tau)=\mu_z(t+\tau)\mu_z(t),$$
$$f(t,\tau+d\tau)-f(t,\tau)=\mu^2(\cos\psi(t+\tau+d\tau)-\cos\psi(t+\tau))\cos\psi(t), \tag{30}$$

where $\mu_z(t)=\mu\cos\psi(t)$, ψ being the angle of the dipole relative to the z-axis.

Our basic assumptions will be (a) that the probability of a collision taking the rotator from the element of solid angle $d\omega$ into $d\omega'$ in a time $d\tau$ is

$$nvd\sigma_{\omega\to\omega'}d\tau, \tag{31}$$

and (b) that this probability is obviously independent of the azimuthal angle φ between $d\omega$ and $d\omega'$, and therefore is a function only of the polar angle θ between these two directions. We know that

$$\cos\psi(d\omega')=\cos\psi(d\omega)\cos\theta+\sin\psi(d\omega)\sin\theta\cos\varphi. \tag{32}$$

Since, upon averaging the difference of cosines in (30) over all possible collisions, the last term in (32) will vanish because of the factor $\cos\varphi$, we can use

$$\cos\psi(t+\tau+d\tau)-\cos\psi(t+\tau)=\cos\psi(t+\tau)(\cos\theta-1). \tag{33}$$

Then we actually perform the average of (30) over all times, using again our impact theory assumption of short collisions. It is clear that the result is:

$$d\varphi(\tau)=\left[nvd\tau\int d\sigma_{\omega\to\omega'}(\cos\theta-1)\right]\varphi(\tau),$$
$$\varphi(\tau)=e^{-nv\sigma\tau}, \tag{34}$$
$$\sigma=\int d\sigma(1-\cos\theta)\ \text{(real)}.$$

This gives, with the correct external factor ω, the Debye line form:

$$I(\omega)=nv\sigma\omega/[\omega^2+(nv\sigma)^2]. \tag{35}$$

The two terms in σ (34) correspond to the γ and δ of the Van Vleck-Weisskopf paper.

G. The General Quantum-Mechanical Case

It is possible to do the quantum-mechanical nonresonant, or Debye, case by a generalization of the above arguments similar to that employed in the paper by Van Vleck and Weisskopf. However, the arguments for this and for the general quantum-mechanical case involving spacial degeneracy are quite equivalent. We shall give only the latter, regarding the Debye case as an obvious special application.

We want to find the breadth of the line corresponding to a dipole transition between two states i and f, of angular momenta j_i and j_f, with $j_f=j_i\pm1$ or j_i.††† Equation (17) for the correlation function applies here, with the spectrum given by (16). Before proceeding farther, we must prove a theorem about the expression (17), or rather about the following part of it:

$$\sum_{m',m''}\langle(m|T^{i-1}(t\to t+\tau)|m')(m'|\mu_z{}^{if}|m')\times(m''|T^f(t\to t+\tau)|m''')\rangle_{\text{average over } t}$$
$$=(m|\langle T^{i-1}(t\to t+\tau)\mu_z{}^{if}T^f(t\to t+\tau)\rangle_{\text{average over } t}|m''') \tag{36}$$

Suppose we apply a rotation of the coordinate axes to (36) in the sense that we do all of our computations with respect to a new set of axes x', y', $z'=R(x,y,z)$. We must use the fact that, since in the course of the time average we consider collisions from all conceivable directions and of all possible types in equal number, the affect of the $\langle T^{i-1*}T^f\rangle$ factor is essentially an isotropic one. (This is equivalent to the step (32)→(33).) Mathematically,

$$R\langle T^{-1}\mu_zT\rangle_{Av}=\langle(RT^{-1})(R\mu_z)(RT)\rangle_{Av}$$
$$=\langle T^{-1}(R\mu_z)T\rangle_{Av}$$
$$=\lambda_{z'x}\langle T^{-1}\mu_xT\rangle_{Av}+\lambda_{z'y}\langle T^{-1}\mu_yT\rangle_{Av}+\lambda_{z'z}\langle T^{-1}\mu_zT\rangle_{Av}, \tag{37}$$

where the λ's are the direction cosines of the new axis system with respect to the old. Thus the quantity (36) has the transformation property of a vector component. But the i, f matrix elements of any vector component are determined, exclusive of a constant factor, by the transformation property.[14] Thus we can say

$$(m|\langle T^{i-1}(t\to t+\tau)\mu_z{}^{if}T^f(t\to t+\tau)\rangle_{\text{Av over } t}|m''')=F(\tau)(m|\mu_z{}^{if}|m'''), \tag{38}$$

where $F(\tau)$ is a scalar.

We are now in a position to set up the differential

---

††† The case of higher multipole transitions is easily worked out and, interestingly, leads usually to a different breadth.

[14] E. U. Condon and G. H. Shortley, *Theory of Atomic Spectra* (Cambridge University Press, Cambridge, 1935), Chapter III.

equation for $\varphi(\tau)$, or, equivalently, for $F(\tau)$, since

$$\varphi(\tau)=\sum_{m,m'''}|(m|\mu_z{}^{if}|m''')|^2F(\tau),$$

$$d\varphi(\tau)=\sum_{m,m'''}|(m|\mu^{if}|m''')|^2dF(\tau),$$

$$=Tr\left\{\int_{-\infty}^{\infty}dt\mu_z{}^{fi}[T^{i-1}(t\to t+\tau+d\tau)\mu_z{}^{if}\times T^f(t\to t+\tau+d\tau)-T^{i-1}(T\to t+\tau)\mu_z{}^{if}\times T^f(t\to t+\tau)]\right\}. \quad (39)$$

We introduce a matrix $T_d=T(t+\tau\to t+\tau+d\tau)$ (the notation T_d indicates that this matrix is not a differential); then

$$T(t\to t+\tau+d\tau)=T(t\to t+\tau)T_d. \quad (40)$$

Again we can make use of the reasoning of Section E, (24)→(25): we use the assumption of short collisions to enable us to take independent averages of the happenings in $t\to t+\tau$ and $t+\tau\to t+\tau+d\tau$. Then we introduce Eq. (40), Eq. (38) for $F(\tau)$, and get for (39):

$$\sum_{m,m}|\{m|\mu_z(m')|^2dF(\tau)=F(\tau)Tr[\langle\mu_z{}^{fi}T_d{}^{i-1}\mu_z{}^{if}T_d{}^f-\mu_z{}^{if})]\rangle_{\text{Av. over all }d\tau}\}. \quad (41)$$

Now we introduce the probability assumption (21) for types of collisions:

$$p(d\sigma \text{ in } d\tau)=nvd\sigma d\tau.$$

If a collision of type $d\sigma$ occurs in $d\tau$, the T matrix T_d will be characteristic of the collision $d\sigma$. In fact, T is obtained by integrating Eq. (9′) from $t=-\infty$ to $+\infty$, using for $H_1'(t)$ the time-dependent interaction Hamiltonian for just one collision of type $d\sigma$ occurring in the whole range of t. The initial condition is $T(-\infty)=1$. This integration is legitimate because of our assumption that $d\tau$ can be chosen long compared to the duration of one collision. We call the resulting T matrix $T(d\sigma)$; then the average in (41) gives the following equation for F.

$$[dF(\tau)/d\tau]=-nv\sigma F(\tau), \quad F(\tau)=e^{-nv\sigma\tau}, \quad (42)$$

$$\sigma=\int d\sigma\left[\frac{Tr(T^i(d\sigma)^{-1}\mu_z{}^{if}T^f(d\sigma)\mu_z{}^{fi})}{Tr(\mu_z{}^{if}\mu_z{}^{fi})}-1\right]. \quad (43)$$

It is obvious that the shift in frequency and the linebreadth follow from the real and imaginary parts of the number σ, precisely according to (28). Thus the problem of the line-shape is solved in principle.

Before proceeding further with the evaluation of σ, the "collision cross section for line-broadening," it is necessary to generalize formula (43) to a case which we shall frequently treat—that in which the interaction Hamiltonian $H_1'(t)$ is a matrix involving the quantum-mechanical states of both the perturbing molecule and the radiating molecule. The line of reasoning is practically identical, except, of course, that the radiation occurs according to the operator

$$\mu_z(1)+\mu_z(2). \quad (44)$$

The two molecules of interest are called (1) and (2). It is clear that it is legitimate to use only the first half of (44), regarding, therefore, molecule (1) as the radiator, (2) as a perturber (the line-shape for molecule (2) will be included in the implicit average over all molecules in the gas). Then, in place of the transformation property "vector component," we use essentially "vector"$_{\text{molecule (1)}}$ "scalar"$_{\text{molecule (2)}}$. Without going through the reasoning for the case of two molecules, which differs from the preceding only in that the Boltzmann factors for molecule (2) must be included and that T-matrices involving any transition whatever for molecule 2 are of interest, we present the correct result for σ:

$$\sigma=\int d\sigma\{[\sum_{\substack{m_1,\,m_1'\\ m_1'',\,m_1'''\\ a_2b_2}}(m_1a_2|T^{i-1}(d\sigma)|m_1'b_2)(\rho_B)_{b_2}\times(m_1'|\mu_z{}^{if}|m_1'')(m_1''b_2|T^f(d\sigma)|m_1'''a_2)\times(m_1'''|\mu_z{}^{fi}|m_1)]\times[\sum_{m_1m_1'}|(m_1|\mu_z{}^{if}|m_1')|^2]^{-1}-1\}. \quad (45)$$

a_2, b_2 designate the various states of the second molecule. Two possible cases occur in which this expression can be simplified to a usable form. First we have the case in which no transitions occur in molecule (2) quantum numbers, except perhaps for degenerate ones; second, that case in which transitions in molecule (2) quantum numbers can occur only simultaneously with those of molecule (1), so that T^i and T^f are still essentially diagonal in molecule (2) because they are so in molecule (1) (this is the interesting case corresponding to resonant interactions). In either case, σ reduces to the following simple form:

$$\sigma=\sum_{a_2}\sigma_{a_2},$$

$$\sigma_{a_2}=(\rho_B)_{a_2}\times\int d\sigma\left[\frac{Tr(T^{i,a_2}(d\sigma)^{(-1)}\mu_z{}^{if}T^{f,a_2}(d\sigma)\mu_z{}^{fi})}{Tr(\mu_z{}^{if}\mu_z{}^{fi})(2j_{a_2}+1)}-1\right]. \quad (46)$$

The trace includes a summation over m_2, the molecule (2) degenerate index, and $2j_{a_2}+1$ is the degeneracy of the a_2 level.

H. Reduction of σ to Computable Form

1. Use of Rotational Invariance to Relate Matrix Elements to "Collision Axes"

In the form (43) it is still practically impossible to compute σ, since we must find the T-matrices not only

for every impact parameter, or distance of closest approach of the two molecules during collision, but for every set of direction angles of the colliding molecules relative to the polarization direction. It is possible to use the fact that the $\int d\sigma$ implies an average over all conceivable sets of direction angles to remove this latter difficulty. We do not do this rigorously, since it involves some rather long group theory. The following argument, however, indicates the method.

The integrand of (43) is, as it stands, rotation invariant, since it is a trace. Essentially, this means that the component of μ we deal with is immaterial. Suppose we can compute the T-matrices for one specific set of direction angles (for instance, suppose we know them for a system quantized along b, the impact parameter). Then it is possible to leave these T-matrices as they stand and to take the direction average by rotating the z-axis, i.e., the component of μ which is used in (43). Since (43) is quadratic in μ_z, it is allowable merely to average over the x, y, and z-directions. Then we get simply

$$\sigma\, Tr(\mu_z^{ij}\mu_z^{j'i}) = \tfrac{1}{3}\textstyle\sum_{x,\,y,\,z}\int_0^\infty 2\pi b db \times Tr[T^{i(-1)}(b)\mu_{x,y,z}^{ij}T^{j}(b)\mu_{x,y,z}^{j'i} - \mu_{x,y,z}^{ij}\mu_{x,y,z}^{j'i}], \quad (47)$$

where $T^i(b)$ designates the T-matrix in the "collision-axis" coordinate system.

Since a great deal of further manipulation with (47) is necessary, we shall use an alternative form for it, based on the identity between the vector matrix and the Wignerian coefficients.[12]

$$(m|\mu_z^{ij}|\mu) = (j_f 1 j_i m | j_f 1 \mu 0) \quad (48)$$

and similarly for $1/\sqrt{2}(\mu_x \pm i\mu_y)$, with 0 replaced by ± 1. Then it is easy to show that (47) is the same as

$$\sigma = \int_0^\infty 2\pi b db \sum_{\substack{M,\,m,\,m' \\ \mu,\,\mu'}} \frac{(j_f 1 j_i m | j_f 1 \mu M)}{(2j_i+1)} (j_f 1 j_i m' | j_f 1 \mu' M) \times [\delta_{mm'}\delta_{\mu\mu'} - (m|T^{i-1}(b)|m')(\mu'|T^{j}(b)|\mu)]. \quad (47')$$

A similar formula can be written in the two molecule case of Eq. (46).

2. *Introduction of an Approximate Form for T.*

For the purpose of computing σ from (47), an expression for the T-matrices in terms of the interatomic forces must still be found. This cannot be done exactly. However, a device which has been frequently used is the following expansion of T in successive approximations with the assumption that $\int H_1' dt/\hbar$ is small. We use the following procedure:

$$T = T_0 + T_1 + T_2 + \cdots, \quad T_0 = 1,$$

$$i\hbar \dot{T}_1 = H_1' T_0; \quad T_1(t) = \int_{-\infty}^{t} \frac{H_1'(t')}{i\hbar} dt', \quad (49)$$

$$i\hbar \dot{T}_2 = H_1' T_1; \quad T_2(t) = \int_{-\infty}^{t} \frac{H_1'(t')}{i\hbar} dt' \int_{-\infty}^{t'} \frac{H_1'(t'')}{i\hbar} dt'', \text{ etc.}$$

If we could assume that $H_1'(t')$ commuted with $H_1'(t'')$ at all times, the result of this process would be simply the scalar solution of the linear differential Eq. (9′):

$$T(t) = \exp\left[\int_{-\infty}^{t} \frac{H_1'(t')}{i\hbar} dt'\right]. \quad (50)$$

On the other hand, it is clear from the definition (10) of H_1' that it does not commute with itself at all times, but only because H_1 and H_0 do not commute. $H_1(t)$ is a function of the coordinates only, in general, and will always commute with itself.

An investigation was made into the size and meaning of the "non-commuting" terms by which (50) differs from the accurate solution of (49). Those terms involving high frequency elements of H_1' ("high" compared to the rate of change of H_1) were found to be precisely equivalent to the terms obtained in (50) by including, in H_1 itself, the 2nd-, 3rd-, etc., order forces due to the high frequency elements of H_1'. On the other hand, such terms are small if they involve low frequency elements of H_1'.

Therefore it seems permissible to ignore the non-commuting terms and to use (50) for T, including at least the second-order (Van der Waals') forces in H_1. These terms have not been computed accurately according to (49), because they appear first in the successive terms T_2 (shift) and T_4 (broadening). The Van der Waals' procedure introduces the second-order forces in the same manner as the first-order ones in T_1 and T_2 where they are much easier to handle. It is an interesting check on our method to note that the second order effects of high levels would derive naturally in the correct form from the general theory.

For simplicity we limit ourselves to the first three terms of (50). These are

$$T(b) \cong T_0 + T_1 + T_2, \quad T_0 = 1; \quad T_1 = -iP; \quad T_2 = P^2/2, \quad (51)$$

where

$$P = \frac{1}{\hbar}\int_{-\infty}^{\infty} H_1'(t)dt. \quad (51')$$

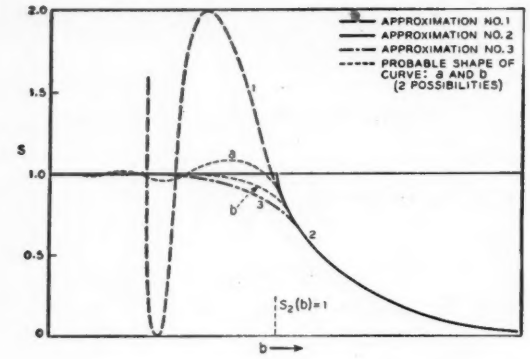

FIG. 1.

3. *Use of the Approximation for T in Computing σ and Line-Broadening*

Let us repeat the formula (47) here, in a slightly different form:

$$\sigma=\int_0^\infty 2\pi b\,db\,S(b),$$

$$S(b)=\sum_{\substack{m,\,m',\,M\\ \mu,\,\mu'}}\frac{(j_f 1 j_i m\,|\,j_f 1\mu M)(j_f 1 j_i M\,|\,j_f 1\mu' M)}{2j_i+1} \times(\delta_{\mu\mu'}\delta_{mm'}-(m\,|\,T^{i-1}(b)\,|\,m')(\mu'\,|\,T^f(b)\,|\,\mu). \tag{52}$$

We are going to expand $S(b)$ in powers of the P-matrix of Eq. (51′):

$$S=S_0+S_1+S_2+\cdots. \tag{53}$$

In order to get terms of the zero'th order in P, we must pick $T^i=T_0{}^i$, $T^f=T_0{}^f$, and we get

$$S_0=0. \tag{54a}$$

The first-order terms are obtained by including either $T^i=T_0$, $T^f=T_1$ or *vice versa*. The result is

$$S_1=-\sum_{\substack{M,\,m,\,m'\\ \mu\mu'}}\frac{(j_f 1 j_i m\,|\,j_f 1\mu M)}{2j_i+1}(j_f 1 j_i m'\,|\,j_f 1\mu' M) \times[(m\,|\,T_1{}^{i-1}\,|\,m)\delta_{\mu\mu'}+(\mu'\,|\,T_1{}^f\,|\,\mu)\delta_{mm'}].$$

This is greatly simplified by the fact that the Wignerian coefficient $(j_f 1 j_i m\,|\,j_f 1\mu M)$ vanishes unless $m=\mu+M$; thus if $\mu=\mu'$, $m=m'$, or *vice versa*, and S_1 is simply

$$S_1=-\sum_M\sum_{m\text{ or }\mu}|(j_f 1 j_i m\,|\,j_f 1\mu M)|^2 \times[(m\,|\,T_1{}^{i-1}\,|\,m)+(\mu\,|\,T_1{}^f\,|\,\mu)].$$

The sums over M are easily performed, one by the unitarity of the Wignerian coefficients, and one by this and the "permutation of indices" property of these coefficients which appears most easily from Racah's paper.[15] Also using the fact that $T_1{}^{-1}=-T_1$, we get

$$S_1=i\left[\sum_{m=-j_i}^{j_i}\frac{(m\,|\,P^i\,|\,m)}{2j_i+i}-\sum_{\mu=-j_f}^{j_f}\frac{(\mu\,|\,P^f\,|\,\mu)}{2j_f+1}\right]. \tag{54b}$$

Referring to the definition (51) of P, it appears that this, the first "shift" term in σ, is just the first term in the simple phase-shift approach, averaged over all directions.

There are two possibilities for obtaining second-order terms in the S sum. We have the choice of taking $T_0{}^i\times T_2{}^f$ or *vice versa*, or of taking the terms involving $T_1{}^i\times T_1{}^f$. The former pair of terms follow precisely as did the S_1 terms; we call these (S_2) outer.

$$(S_2)_{\text{outer}}=-\left[\sum_m\frac{(m\,|\,T_2{}^{i(-1)}\,|\,m)}{2j_i+1}+\sum_\mu\frac{(\mu\,|\,T_2{}^f\,|\,\mu)}{2j_f+1}\right] =\frac{1}{2}\left[\sum_m\frac{(i,m\,|\,P^2\,|\,i,m)}{2j_i+1}+\sum_\mu\frac{(f,\mu\,|\,P^2\,|\,f,\mu)}{2j_f+1}\right]. \tag{54c′}$$

The second type of term, however, must be left in its original form; we call the sum of these $(S_2)_{\text{middle}}$:

$$(S_2)_{\text{middle}}=-\frac{1}{2j_i+1}\sum_{\substack{M,\,m,\,m'\\ \mu,\,\mu'}}(j_f 1 j_i m\,|\,j_f 1\mu M) \times(j_f 1 j_i m'\,|\,j_f 1\mu' M)(im\,|\,P\,|\,im')(f\mu'\,|\,P\,|\,f\mu). \tag{54c″}$$

Further terms are prohibitively difficult; in any case, the "non-commuting" part of T can no longer be neglected in T_3.‡‡‡

4. *The Interpolation Process*

Since the expansion (53) of $S(b)$ is valid only for small P, and P increases very strongly with decreasing b (r^{-3} for first-order, r^{-6} for second-order forces), obviously the first two non-vanishing terms of S, derived above, are of no help for collisions for which b is small. For this range of b we must use physical reasoning, based on the fact that "strong" collisions such as these must have an effect equivalent to complete interruption of the radiation. The T-matrix for complete interruption

[15] G. Racah, Phys. Rev. **62**, 438 (1942).

‡‡‡ It is clear that in (54c) the degenerate and non-degenerate levels play essentially different parts. One can interpret these terms by saying that transitions to non-degenerate levels act like complete interruptions of the radiation, while transitions among degenerate levels take on the character of phase-shifts to a greater or lesser extent, whence the terms (54c″). This phenomenon, and the question of when a level is or is not "degenerate," are allied to the general problem of coherence of radiation of different frequencies which crops up in many fields.

In this case, the problem is fairly simple. It is easy to see that the different behavior of degenerate and non-degenerate levels follows from the step of dropping the terms of finite frequency in Section D, Eqs. (13) and (14). We noted there that this step was allowable if the frequency difference of the levels was much greater than $1/\tau$. In addition, (54c″) can be shown to vanish for first-order dipole-dipole interactions in any case, so that observable effects of this cause seldom appear.

can have two forms: For the pure phase-shift case, that of an arbitrary phase-factor, averaging to zero; for the transition case, that of complete off-diagonality, meaning that the molecule has certainly changed its state. In either case $S(b)$ contains only the $\delta_{mm'}\delta_{\mu\mu'}$ factors, and a simple summation shows that

$$S(b \text{ small})=1 \text{ or averages to } 1. \tag{55}$$

The problem of interpolating between the region of large b, where $S(b)$ is small and satisfies (54), and that of small b, or (55), is insoluble in principle. However, several simple models and some general reasoning have led us to conclude that a definite upper limit for the real part of σ, and a probable lower limit, can be assigned on the basis of two rather arbitrary choices of $S(b)$, while a third choice gives a good working approximation.

Figure 1 illustrates the various possibilities. Our three approximate "ideas" for curves are labeled "approximation #1, 2, 3." #1 is essentially the $S(b)$ curve used in the phase-shift theory.

$$S\#_1(b)=1-\cos(2S_2(b))^{\frac{1}{2}}. \tag{56}$$

It is easy to show that because of the factor b in (52a) this is an upper limit for all conceivable shapes. One can look upon the true curve as an average of several curves like #1, with different asymptotic strengths; then it might well resemble curve (a) or (b). #2 is the approximation obtained by using $S_2(b)$ from (54c) to the point at which $S=1$; then we use exactly (55). #3 is a rather arbitrarily set lower limit

$$S\#_3(b)=1-\exp[-2S_2(b)]. \tag{56'}$$

We will find that the three approximations are never more than 20 percent from each other, which is usually less than experimental error. Where the experiments are more accurate, #2 does indeed seem to be the best choice.

5. *Some Remarks on the Matrix "P"*

Before concluding the theoretical part of this work it is well to make some remarks about the magnitude of the a, b elements of P as a function of the separation in energy of the levels a, b. An element of P is given by

$$(a|P|b)=\int_{-\infty}^{\infty} dt \exp(i\omega_{ab}t)(a|H_1(t)|b). \tag{57}$$

$H_1(t)$ will always be either a first- or second-order dipole-dipole interaction; therefore it will have a form like

$$H_1(t)=Kr^{-3} \text{ or } Kr^{-6}. \tag{58}$$

We can always assume that the paths followed by the colliding molecules are straight lines, since one can show that if the molecules collide with sufficient strength to have curved paths it is quite certain that the radiation will be completely interrupted. Then

$$r^2=b^2+v^2t^2, \tag{59}$$

and

$$(a|P|b)=K\int_{-\infty}^{\infty} dt \exp(i\omega_{ab}t)(b^2+v^2t^2)^{-1 \text{ or } -3}. \tag{60}$$

Now we define

$$x=vt/b, \quad k=b\omega_{ab}/v, \tag{61}$$

following Foley;[9] then (60) becomes

$$(a|P|b)=\frac{k}{b^2v \text{ or } b^5v}\int_{-\infty}^{\infty} dx \frac{e^{ikx}}{(1+x^2)^{3 \text{ or } 1}}. \tag{60'}$$

These integrals can easily be done by contour integration; however, the main features of the two solutions are the same. Both integrals have nearly the same value as at $k=0$ ("fast" collisions or degenerate levels) for a fairly large region of the parameter k (relating speed of collision to frequency) approaching $k=1$. Then there is quite a rapid falling off until at $k=4$ or 5 (60') essentially vanishes.

We may interpret this according to the uncertainty principle. As long as the collisions are sufficiently fast ($k<1$), the energy-difference corresponding to ω_{ab} acts as though it were negligible: $\Delta E\Delta t>h$ implies that there is a region of "vagueness in energy" of the width $h/\Delta t$, with Δt the time in which a collision occurs. Since the P-matrix element gives, by (51), the probability of occurrence of transitions between the states a and b, these transitions will occur as though these states were resonant throughout the region $k<1$. This is a point which is frequently ignored in the theory; qualitatively, it was previously made by Foley. We shall find opportunity to use the "region of resonance" idea repeatedly in the applications of our theory. On the other hand, for large k—slow collisions—no non-adiabatic transitions will occur, since the motion is adiabatic.

SUMMARY OF THE THEORY

At this point it will clarify the exposition to present a summary of the theory up to this point. We have, essentially, found the line shape of a pressure-broadened spectral line under the following assumptions:

(a) that the relative motion of the molecules is classical; this enables us to write down the generalized Fourier integral (2).

(b) that the time between collisions is long compared to the duration of the collisions; this enables us to separate the Fourier integral into component parts referring to the separate spectral lines ((16) and (17)), to find a general expression for the correlation function (42), and to write down the broadening cross-section σ occurring in this expression in terms of collision operators T (43).

(c) that the collision operators are smooth functions of the collision parameter b between large b (where we have the expansion (51)) and small b, where complete interruption occurs. Then we are able to apply the interpolation process, and obtain for σ the expression (52), $S(b)$ given by the formulas (56) fitted to the large $-b$ expansion (54).

TABLE I. Comparison of theory and experiment.

	Theory			Experiment
Approx.	#1	#2	#3	
$\Delta\nu_{\frac{1}{2}}=$	0.86	0.77	0.68 cm^{-1}/atmos.	0.74 cm^{-1}/atmos.

TABLE II. Comparison of theory with experiment—relative breadths in the ammonia spectrum.

$J=$ (a)	$K=$ (b)	Theoretical breadths: this thesis (c)	Experimental data: Bleaney (d)	Quasi-empirical formula: Bleaney (e)
2	1	2.6	2.6	2.7
3	1	2.3	2.4	2.2
3	2	3.3	3.2	3.4
3	3	4.5	4.5	4.5
4	4	4.6	4.5	4.6
5	1	1.8	1.8	1.6
5	2	2.5	2.6	2.5
5	3	3.3	3.3	3.3
5	5	4.8	4.7	4.65
6	3	2.8	3.1	3.1
6	4	3.5	3.6	3.6
6	6	4.8	4.7	4.7
7	5	3.7	4.1	3.8
7	6	4.3	3.9	4.3
8	7	4.3	4.1	4.35
10	9	4.5	4.2	4.5
11	9	4.1	2.9	4.2

Data are half-widths in $cm^{-1}\times10^{-4}$ at 0.5 mm Hg pressure.

The procedure to be followed in computing line shapes is this: given an assumed type of intermolecular forces, one computes the matrix P (51′) in the collision-parameter coordinate system. The interaction energy H_1' is given by (10). The elements of this matrix involving the initial and final states are then averaged over directions according to (54b) and (54c′ and c″). The S_2 averages (54c) are employed in the approximations (56) and the σ-integral (52) to obtain a broadening cross-section, which gives the line-breadth from (28); a shift, if present, can be computed similarly from S_1 (54b), (52), and (28).

PART II. APPLICATIONS OF THE THEORY TO SPECTRA

A. Cases Involving Permanent Dipole Interactions

1. Ammonia Self-Broadening

We shall begin with various problems involving permanent dipole interactions, since there is much experimental work on them and since, in general, the "difficult" term $(S_2)_{\text{middle}}$ vanishes in these problems. Self-broadening in the inversion spectrum of ammonia has been studied most extensively.

The states of the ammonia molecule, exclusive of vibrational and electronic quantum numbers, are specified by four quantum numbers: J(total angular momentum), M(equatorial), K(symmetric top quantum number), and $\pm$, denoting the symmetry of the wave-function with respect to inversion.

$$\sqrt{2}\psi_+=\psi_{+K}+\psi_{-K},\quad \sqrt{2}\psi_-=\psi_{+K}-\psi_{-K}. \tag{1}$$

Here $+K$ and $-K$ denote the "single-ended" states, whose degeneracy is raised by the well-known inversion or "tunnel effect."

First we consider the interaction between two ammonia molecules (first-order only). The Hamiltonian of this interaction is

$$H=\left[\boldsymbol{\mu}_1\cdot\boldsymbol{\mu}_2-3\frac{(\boldsymbol{\mu}_1\cdot\mathbf{r})(\boldsymbol{\mu}_2\cdot\mathbf{r})}{r^2}\right]r^{-3}, \tag{2}$$

where $\boldsymbol{\mu}_1$ and $\boldsymbol{\mu}_2$ are the dipole moment matrices of the two molecules considered, and $\mathbf{r}$ is the distance between the molecules. Equation (2) can easily be expanded in terms of direction-angles in a system of reference in which the impact parameter b is the polar axis of spherical coordinates for each molecule. Then θ_1, φ_1 and θ_2, φ_2 are the polar angles of μ_1 and μ_2 referred to b, while $\psi=\tan^{-1}[(vt)/(b)]$ is the angle which $\mathbf{r}$ makes with b. The result for H is

$$H=\mu^2/r^3[\cos\theta_1\cos\theta_2(1-3\cos^2\psi)+\sin\theta_1\sin\theta_2\times(\cos(\varphi_1-\varphi_2)-\sin^2\psi\cos\varphi_1\cos\varphi_2)+\text{terms in }\cos\psi\sin\psi]. \tag{3}$$

We must obtain the matrix elements of the combinations of functions of θ and φ which occur here. One theorem simplifies this problem greatly. All matrix elements vanish between states which are both $+$ or both $-$, while the $(+|\boldsymbol{\mu}|-)$ elements are precisely those of the ordinary symmetrical top for states of the correct J, K and M. The proof is obvious upon observing that

$$(K|\boldsymbol{\mu}|K)=-(-K|\boldsymbol{\mu}|-K);\quad (K|\boldsymbol{\mu}|-K)\cong0. \tag{4}$$

The latter holds true within the order of the tunnel frequency compared to a vibrational frequency, or 10^{-3}. Then (1) leads directly to our theorem.

We present here a tabulation of the required matrix elements:[16]

$$(J\,K\,M|\cos\theta|J\,K\,M)=KM/J(J+1)$$

$$(J\,K\,M|\sin\theta e^{\pm i\varphi}|J\,K\,M\pm1)=\mp K/J(J+1)((J\pm M+1)(J\mp M))^{\frac{1}{2}},$$

$$(J\,K\,M|\cos\theta|J+1\,K\,M)=\frac{\{[(J+1)^2-K^2][(J+1)^2-M^2]\}^{\frac{1}{2}}}{(J+1)[(2J+1)(2J+3)]^{\frac{1}{2}}},$$

$$(J\,K\,M|\cos\theta|J-1\,K\,M)=-\frac{[(J^2-K^2)(J^2-M^2)]^{\frac{1}{2}}}{J[(2J+1)(2J-1)]^{\frac{1}{2}}},$$

[16] R. de L. Kronig, and I. Rabi, Phys. Rev. **29**, 262 (1927).

$$(J\,K\,M|\sin\theta e^{\pm i\varphi}|J-1\,K\,M\pm1)$$
$$=\frac{[(J^2-K^2)(J\mp M-1)(J\mp M)]^{\frac{1}{2}}}{J[(2J-1)(2J+1)]^{\frac{1}{2}}},$$
$$(J\,K\,M|\sin\theta e^{\pm i\varphi}|J+1\,K\,M\pm1)$$
$$=\frac{\{[(J+1)^2-K^2](J+1\pm M)(J+2\pm M)\}^{\frac{1}{2}}}{(J+1)[(2J+1)(2J+3)]^{\frac{1}{2}}}.$$

Of course, these elements are to be understood, according to our theorem above, as always off-diagonal in the index $\pm$, which is not explicitly written in.

There are two kinds of matrix elements of the "interaction matrix" P which do not vanish, for all practical purposes: (a) those corresponding to a simple "first-order Stark effect" interaction involving the $J\rightarrow J$ elements of (5), and (b) those corresponding to rotational resonance and involving $J\rightarrow J\pm1$ elements of (5). All others are negligible because of the large energy-changes (order of 10 cm^{-1}) involved; we neglect the second order effects and vibrational resonances, the latter because few vibrationally excited molecules are present.

However, it is necessary to observe that there is no resonance effect as far as the inversion frequency is concerned. The parameter k of Section H-5, Part I, is small for the inversion frequency, and therefore collisions of + molecules with + molecules or of − with −, in which each type must undergo a $+\rightarrow-$ transition (total energy change about 1.6 cm^{-1}) are as effective in broadening as the truly resonant $\left\{\begin{matrix}+\rightarrow-\\-\rightarrow+\end{matrix}\right\}$ collisions. This applies as far as both effects (a) and (b) are concerned. The parameter k is actually

$$k=\frac{b\omega}{v}\doteq\frac{b(\mathrm{A})\times10^{-8}\times3\times1.6\times10^{18}\times2\pi}{8\times10^4}\doteq b(\mathrm{A})\times0.035. \tag{5}$$

We shall never consider impact parameters b greater than 15A. A k of 0.5 may lead to an error of a few percent.

These considerations lead us to the following procedure: we shall calculate the P-matrix (Part I, Eq. (51)) ignoring the exponential time factors entirely, and then substitute the resulting P-matrix into the sum S_2 (I, Eq. (54c)). Since we are ignoring the time-factor, it is permissible to perform the time-integral of (3) previously to taking the matrix elements. We use the formulas:

$$r^2=b^2+v^2t^2 \qquad \cos\psi=b/r \qquad \sin\psi=vt/r, \tag{6}$$

and the result is

$$\int_{-\infty}^{\infty}\frac{H_1dt}{\hbar}=\frac{2\mu^2}{b^2v\hbar}[-\cos\theta_1\cos\theta_2 -\sin\theta_1\sin\theta_2\sin\varphi_1\sin\varphi_2]. \tag{7}$$

At this point it is very easy to calculate the correct S_2 sums. We present merely the result, which includes the identical sums for initial and final states. For the simple Stark effect we get the following S_2 sum, applicable to collisions of the radiating molecule, quantum numbers J_1 and K_1, with molecules of any J_2 and K_2 (n_2 in the general formula (46) of Part I for the two-molecule case being here J_2, K_2).

$$S_2(J_2,K_2)=\frac{8}{9}\frac{\mu^4}{b^4v^2\hbar^2}\frac{K_1^2K_2^2}{J_1(J_1+1)J_2(J_2+1)}$$
(Stark effect). (8)

For the two rotational resonance S_2's, in case the radiating molecule J_1, K_1 collides with a molecule with $J_2=J_1\pm1$, we get

$$S_2(J_1-1,K_2)=\frac{8}{9}\frac{\mu^4}{b^4v^2\hbar^2} \times\frac{(J_1^2-K_1^2)(J_1^2-K_2^2)}{J_1^2(2J_1+1)(2J_1-1)}(\text{rot. res.}) \tag{9a}$$

$$S_2(J_1+1,K_2)=\frac{8}{9}\frac{\mu^2}{b^4v^2\hbar^2} \times\frac{[(J_1+1)^2-K_1^2][(J_1+1)^2-K_2^2]}{(J_1+1)^2(2J_1+1)(2J_1+3)}. \tag{9b}$$

For collisions with molecules of $J_2=J_1\pm1$, one must add (9a) or (9b) and (8) together to get the total S_2 sum. These are $(S_2)_{\text{outer}}$ sums; no $(S_2)_{\text{inner}}$ sums enter in this problem because the elements of $\mathfrak{y}$ are all off-diagonal in the non-degenerate index $\pm$.

We must now obtain the quantity σ (or rather the separate $\sigma(J_2,K_2)$ to average over J_2 and K_2 by Part I, Eq. (46)). Without bothering to do the integrals,[17] we present here the three possible σ's for our three approximations of Part I, Section H-4. We use the notation

$$S_2(J_2,K_2)=A^2/b^4. \tag{10}$$

Then the three approximations give

$$\begin{aligned}&\#1.\quad \sigma_1(J_2,K_2)=\rho_B(J_2,K_2)2\pi(1.11A),\\ &\#2.\quad \sigma_2(J_2,K_2)=\rho_B(J_2,K_2)2\pi A,\\ &\#3.\quad \sigma_3(J_2,K_2)=\rho_B(J_2,K_2)2\pi(0.885A),\end{aligned} \tag{11}$$

or

$$\sigma(J_2,K_2)=2\pi A\rho_B(J_2,K_2)\times C,$$

where C has the values

$$\begin{aligned}&C=1.11 \quad \#1,\\ &C=1.00 \quad \#2,\\ &C=0.885 \quad \#3.\end{aligned} \tag{11'}$$

[17] H. Jensen, Zeits. f. Physik. **80**, 448 (1933).

Then we have Eq. (46) of Part I

$$\sigma = \sum_{J_2 K_2} \sigma(J_2, K_2),$$

and

$$(\Delta\nu)\ \mathrm{cm}^{-1} = (nv/2\pi c)\sigma \qquad (12)$$

which determine the line-breadth from Eqs. (8)–(11).

Two types of experimental information are available. The most extensively measured single line in the ammonia inversion spectrum is the $J_1=3$, $K_1=3$ line.[18,19] For this line we can neglect, with one or two percent error, the effect of the rotational resonance sums (9a) and (9b). Then we can compare our theoretical values from (8)–(12) with the experimental results.§ The result shown in Table I (all breadths are half-widths in cm^{-1}/atmos. at 0°C). This shows the agreement of our theory with experiment as far as absolute values of the broadening are concerned. Certainly the experimental value lies within our computational error, and it is interesting that the working approximation #2 is fairly close.

The second type of experimental data available is that on the relative breadths for all the lines in the ammonia spectrum, taken by Bleaney and Penrose.[20] In Table II we present our theoretical results on relative values. In order to avoid the ambiguity due to the interpolation procedure, we have normalized the theoretical value for the 33 line to fit the experimental value precisely. Columns (*a*) and (*b*) give the J and K values for the various lines; column (*c*) gives our values using the Stark effect, from Eq. (8), plus an approximately computed correction for the rotational resonance effect, from Eq. (9). These values are normalized as explained above. Column (*d*) gives Bleaney and Penrose's experimental data, and column (*e*) gives predictions from a theoretical formula of Bleaney based on the arbitrary assumption that the broadening effect of a collision depends on the *maximum* interaction energy of the two molecules. This formula is

$$(\Delta\nu)_{\frac{1}{2}} \sim (K^2/(J(J+1))^{\frac{1}{2}}.$$

It does not seem very well based since it takes no account of rotational resonance. All breadths are in 10^{-4} cm^{-1} at 0.5 mm pressure.

The computational error in our approximate method for the rotational resonance is about 0.1 $\mathrm{cm}^{-1}\times 10^{-4}$. Bleaney states that his experimental error is of the order of 0.2 $\mathrm{cm}^{-1}\times 10^{-4}$. Within these errors, our agreement is excellent, except for the last four lines, which seem to allow no reasonable explanation. The fortuitous agreement of Bleaney's formula (*e*) with experiment is interesting, but not, apparently, significant.

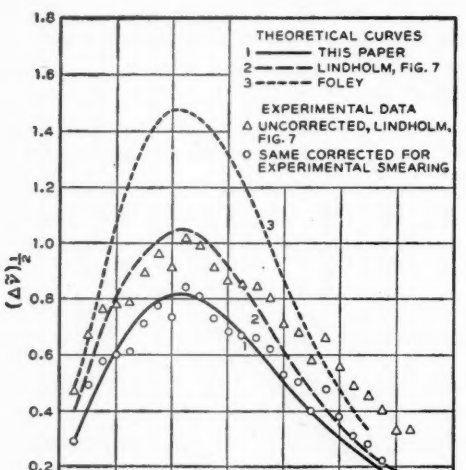

FIG. 2. Comparison of theoretical and experimental results.

B. Other Cases: HCN and HCl Vibrational Band Spectra

Lindholm[21,16] has taken a great deal of experimental data on line-breadths in the vibrational bands of HCl and HCN. He has also made theoretical calculations of the line-breadths for these spectra, as has Foley.[9] Before giving our own theory, it will make our procedure somewhat clearer to indicate how these older theories worked.##

For cases in which resonances occur, as in the molecules under consideration, the standard practice has been to find a mean square direction-averaged energy perturbation due to resonance, for instance[22]

$$(\langle V^2\rangle_{\mathrm{Av}})^{\frac{1}{2}}(J\to J-1) = \left(\frac{2}{3}\right)^{\frac{1}{2}}\left[\frac{J^2}{(2J-1)(2J+3)}\right]^{\frac{1}{2}}\frac{\mu^2}{R^3} \qquad (13)$$

in the case of rotational resonance of dumbell molecules. Then this energy change is inserted as the diagonal $H(t)$ in the simple phase-shift theory. This is for precise resonance; if imprecise resonance occurs, the "quasi-resonance" type of calculation such as the following is used. If two levels are separated by a small difference in energy Δ, and an interaction V_{ik} is assumed between them, the energy E of the perturbed levels is computed from the secular equation

$$\begin{vmatrix} (\Delta/2)-E & V_{ik} \\ V_{ik} & (-\Delta/2)-E \end{vmatrix} = 0. \qquad (14)$$

[18] B. Bleaney and R. P. Penrose, Proc. Roy. Soc. **A189**, 358 (1947).
[19] C. H. Townes, Phys. Rev. **70**, 166 (1946).
§ Bleaney's experimental value seems the soundest.
[20] B. Bleaney and R. R. Penrose, Proc. Phys. Soc. London **59**, 424 (1947); **60**, 540 (1948).
[21] E. Lindholm, Zeits. f. Physik **109**, 223 (1938).
Lindholm in reference 10 himself stated that he found this type of theory very bad in atomic resonance problems and that he used it only because his own rigorous theory was too difficult in these cases.
[22] H. Margenau, Rev. Mod. Phys. **11**, 1 (1939).

Then

$$E=\pm((\Delta/2)^2+(V_{ik})^2)^{\frac{1}{2}}.$$

In the application of the method used by these authors, a mean square perturbation such as (13) is introduced as V_{ik}, and that solution of (14) chosen which reduces to the correct level at $V_{ik}=0$. Then this E is used in the phase-shift method.

Two objections can be made to this idea, considered simply as an interpolation method between the first order, resonance region and the second-order, r^{-6} force region for V. In the first place, the criterion for the point at which the change in type of forces occurs is whether $V\doteq\Delta$, apparently independent of the speed of collisions, which enters into the criterion for our own theory. This can be shown to be not a serious discrepancy, using the fact that on both theories a collision must be both long and strong enough to cause a certain P-matrix element before it has an appreciable effect. However, the two criteria are not identical; the quantitative results of the two theories differ considerably.

The second objection is more fundamental. A particular choice of the solution of (14) is made; thus in general it appears that a center-frequency shift should be expected, larger the closer to resonance the levels come. However, experimentally and theoretically it can be shown that there is no shift due to precisely resonant collisions: both signs in (14) occur when $\Delta=0$. This contradiction is a true defect in the quasi-resonance theory.

We are not able to present a good theory of the interpolation region between first order (r^{-3}) forces and r^{-6} forces, or even, in the particular case of the rotator, of the second-order, r^{-6}, region. Therefore, since the answers for HCl depend strongly on how these regions are treated, we do not present detailed work on this molecule. We are able to attain fair (30 percent) agreement with Lindholm's observed widths for this spectrum, but no better agreement than that of his quasi-resonance theory. However, his theory predicts much greater breadths for the P than the R branch, which are not observed; our method of treating near-resonance could never lead to such a great difference, and thus agrees better with experiment.

We have been able to make fairly quantitative calculations for the HCN molecule. This molecule is a dumbell rotator with a large dipole moment 2.65×10^{-18} esu. The observed spectra are the P-branches of the two bands at 11500 cm^{-1} ($v_1=1$, $v_3=3$) and 12500 cm^{-1} ($v_3=4$). There are several types of interactions to be considered.

(1) Vibrational resonance; this is neglected because the dipole moment for this interaction is quite small.

(2) Rotational resonance of the ground state ($J=J_1$) with unexcited colliding molecules, having $J=J_1\pm1$.

(3) Rotational resonance of the excited state ($J=J_1-1$) with unexcited colliding molecules having $J=J_1$, $J_1=2$.

(4) Second-order Keesom alignment forces, operative primarily when the colliding molecule is not in resonance with either state of the radiator.

Effect (1) is ignored. Effect (2) we can compute on much the same basis we have already used for ammonia: in fact, we can take over the S_2 sums (9) bodily from the ammonia problem, if we specialize to $K=0$ and realize we must take only half of the sum there used, since only one state of the two involved in the radiation is undergoing the first-order perturbation.

$$\begin{aligned}S_2(J_2=J_1+1)&=\frac{4}{9}\frac{\mu^4}{b^4v^2\hbar^2}\frac{(J_1+1)^2}{(2J_1+1)(2J_1+3)},\\ S_2(J_2=J_1-1)&=\frac{4}{9}\frac{\mu^4}{b^4v^2\hbar^2}\frac{J_1^2}{(2J_1-1)(2J_1+1)}.\end{aligned}\tag{15}$$

The effect (3) is not a precise resonance, because the moment of inertia of the HCN molecule depends on vibrational quantum number. If we express the rotational energy approximately as

$$E_R(J)=B_vJ(J+1).\tag{16}$$

Then[23]

$$B_v=1.4878-0.0093(v_1+\tfrac{1}{2})+0.0007(v_2+1)-0.0108(v_3+\tfrac{1}{2}).$$

B is therefore about 0.04 cm^{-1} different in excited and normal states. Since the quantum exchanged in the rotational resonance is about $2BJ$ wave numbers, the total amount by which the excited and ground states fail to be in resonance is approximately

$$\Delta\omega(\text{off resonance})=0.08J\text{ cm}^{-1}.\tag{16}$$

Then our parameter k is

$$k=b\Delta\omega/v=2.9\times10^{-3}b(\text{A})J.\tag{17'}$$

The maximum collision parameters for this problem are about 30A; then

$$k\leq0.09J\tag{17''}$$

and it is only for values of $J\sim10$ that an appreciable correction for failure to resonate should appear. We shall ignore this correction entirely, both because it should not be large for the interesting lines and because it is extremely difficult to compute. Then for the effect (3) we also use Eqs. (15), except that J_1 must be replaced by J_1+1.

Lindholm finds a large correction for quasi-resonance in this case, not depending much on J. We do not agree with this result. In addition, this is the point in which his HCl treatment differs greatly from ours: we find that if (as is necessary for most lines) a correction is to be applied for this effect, it should be fairly symmetric between the P and R branches of the band.

[23] G. Herzberg, *Infrared and Raman Spectra* (D. Van Nostrand New York, 1945), p. 393.

Effect (4) we have not been able to treat rigorously by our own methods, since the sums required become quite difficult for the second-order alignment forces. It seems likely that the results for these forces obtained by the simple direction-averaged phase-shift theory should not be very far wrong; in order to include this important effect, we have simply borrowed the result of Lindholm and Foley for these forces (they agree) and added their line-breadths for these forces to our own for resonant forces. This simple addition is legitimate, since the important contributions these forces make come from different collisions from those contributing to the resonant line breadth.

We use the "working approximation" number (2). Then the cross section is given by (11) with $C=1$, and A defined by (10). We use S_2 from (15). The line breadth can then be computed from (12) and Eq. (46) of Part I, for all resonant collisions (effects (2) and (3): sum over $J_2=J_1-2$, J_1-1, J_1, J_1+1) with a contribution computed from Lindholm's figure (7) added in for the alignment forces.

Before comparing our results with Lindholm's experiments in Fig. 2, we should like to make some comments about his experimental data. These were taken in the photographic infra-red, by means of densitometer analysis of plates. His best data are those on the 11.5 $\times 10^3$ cm^{-1} band at pressures of 25 cm and 58 cm Hg; he also has data on the 12.5×10^3 cm^{-1} band at three pressures, 25, 40, and 58 cm Hg. The most obvious fact about his original breadth data is that they are not proportional to the pressure, as one would expect on any theory at these pressures, but that instead they are given by

$$\delta\nu = \text{const.} + (\text{const.}) \times \text{pressure}, \qquad (18)$$

within the experimental fluctuations. One can interpret the constant in this expression as an experimental broadening due to slit width, finite resolving power, etc.; this would be the case if these effects were summarized by a dispersion form of curve, to be smeared with the true line breadth. This constant is about 0.13 cm^{-1} in half-width, a very reasonable value for experimental effects. To get the true width one should subtract this constant from all data.****

In Fig. 2 we present both sets of experimental data: the actual observations at 58 cm extrapolated to 1 atm. pressure using simple proportionality to pressure, and the same with the constant term in (18) subtracted, which we expect to be the true impact theory line breadth. The legend explains that the lower (o) values are the corrected data. In addition, we present three theoretical curves for comparison: (1) is our own theory for resonance, borrowing the Lindholm-Foley values for the small contribution of alignment forces; (2) is Lindholm's curve for this spectrum; and (3) is Foley's published values for the HCN spectrum. Lindholm's curve is appreciably lower than Foley's for two reasons. He has a correction for quasi-resonance, which is, in our opinion, unfounded. Foley need not use this correction in any case, since his theory applied to the 14μ fundamental band. In addition, it seems that even taking into account this correction Foley's values are some 20 percent higher than Lindholm's; perhaps this is a numerical error in Foley's work, since we get agreement with Lindholm's values upon re-computing by their common method.

Two forms of agreement can be claimed for our curve: (a) excellent agreement with the experimental variation with J, a factor which is unchanged by any method of correcting for experimental error; and (b) good agreement quantitatively with the corrected data.

TABLE III. Comparison of measured and computed diameters.

Molecules		Line-breadth (a) Computed collision diameter A	(b) Measured diameter A	(c) Kinetic theory diameter(A)
Radiator	Perturber			
NH_3	He	1.5	2.4	3.2
NH_3	H_2	1.9	3.5	3.4
NH_3	N_2	2.6	6.4	3.4
NH_3	O_2	2.5	4.8	3.5
NH_3	A	2.6	4.6	3.7
H_2O	Air	3.3	5.6	3.5

C. Foreign Gas Broadening: Van der Waals Interactions

Broadening of microwave lines by pressures of foreign gases has been the subject of some experimental investigations.[20,24] The theoretical approach to the problem of foreign gas broadening has generally been that of computing the Van der Waals interactions between the molecules concerned and using these to obtain broadening cross sections. We have followed this procedure with our more accurate theory. In general, it can be shown that the r^{-6} term in the interaction between two molecules is, for the Debye induction type of forces:

$$H_{\text{ind.}} = (\alpha_2\mu_1^2/2r^6)(1+3\cos^2\theta), \qquad (19a)$$

where α_2 is the polarizability for the non-polar molecule, assumed isotropic, μ_1 the dipole moment of the polar molecule, and θ the angle which $\boldsymbol{\mu}_1$ makes with the intermolecular distance $\mathbf{r}$. Very similarly, the London dispersion forces for two interacting non-polar molecules, one assumed isotropic, are approximately given

**** In a private communication, Lindholm suggests that while there must be some error of the type suggested here, he cannot agree that it could be quite so large. One may consider that the correction for experimental error is uncertain by perhaps half its total value, and thus that the data is uncertain by 0.06 cm^{-1}/atmos. Gordy has recently reported microwave measurements on the HCN rotational spectrum (Rev. Mod. Phys. **20**, 668 (1948)) and it is to be hoped that the observation of one or two of these lines will definitely settle the question.

[24] G. E. Becker and S. H. Autler, Phys. Rev. **70**, 300 (1946).

by

$$H_{\text{disp.}}=\frac{I_1I_2}{I_1+I_2}\frac{3\alpha_2}{4r^6}(3\alpha'+\alpha''+(\alpha''-\alpha')\cos^2\theta), \quad (19b)$$

where α_2 is still the polarizability of the isotropic molecule, I_1 and I_2 are the fundamental frequencies from one-term dispersion formulas, or the ionization potentials, for the two molecules, and α' and α'' are the polarizabilities along the two different axes of the polarizability ellipsoid of the non-isotropic molecule, assumed to be an ellipsoid of rotation. (A somewhat similar formula holds in case the anisotropic molecule has three different polarizabilities.) θ is the angle between the axis of the polarizability ellipsoid and the intermolecular distance $\mathbf{r}$.

For states separated by microwave frequency differences, the isotropic parts of (19) make no contribution to broadening, and one need consider only an interaction of the form

$$H=\text{const.}\times(\cos^2\theta/r^6). \quad (20)$$

S_2 sums can be computed using this interaction, and inserting appropriate constants for various cases. These sums are quite difficult, both because the $\cos^2\theta$ term introduces essentially a second-order Legendre polynomial symmetry into the matrix P, and because the difficult term $(S_2)_{\text{inner}}$ does not vanish. They are evaluated easily only by using the group-theoretical methods of Racah;[15] however, using these methods they can be done in general, even for forces of more complicated symmetry.

We do not present this evaluation because the results, in general, do not have any relation to experimental results. It is found that the collision broadening cross sections σ calculated by means of the known Van der Waals forces come out usually to be considerably smaller than the kinetic theory cross sections computed from viscosity, etc. This means that the forces which cause broadening must be the higher order and exchange forces which come into prominence at the diameter corresponding to the kinetic theory cross-section. As would be expected, the measured broadening cross sections are at least as great as the kinetic theory ones in most cases.

Table III summarizes the situation very well. Column (b) is from Bleaney and Penrose's paper,[22] except the H_2O line, which comes from Becker and Autler.[24] Column (c) is from Stuart's book.[25]

One more problem was computed. The microwave spectrum of oxygen has been measured[26] in some detail. This case is even more complicated that the preceding, because transitions among states having different total angular momenta (J) but the same K, or molecular quantum number, must be considered. $\mathbf{J}=\mathbf{K}+\mathbf{S}$, where $\mathbf{S}$ is the spin angular momentum of O_2, $|S|=1$. The splitting of the states $J=K\pm1$, K is very small, since this is the line observed at microwave frequencies, and thus this type of transition occurs easily upon collision. Another theorem of Racah was used to simplify this computation. Here the agreement with experiment was somewhat better than would be expected from the kinetic theory diameters and Table II, but this is not significant since the experimental data are only on the entire unresolved set of lines near 2 cm^{-1}.

I should like to express my gratitude for the wise direction, help, and encouragement given me in my work on this problem by Professor J. H. Van Vleck.

[25] H. A. Stuart, *Molekulstruktur* (Verlag J. Springer, Berlin, 1934), Table II.

[26] J. H. Van Vleck, Phys. Rev. **71**, 413 (1947).

Interferometric Studies of Faster than Sound Phenomena. Part II. Analysis of Supersonic Air Jets*

R. LADENBURG, C. C. VAN VOORHIS, AND J. WINCKLER
Palmer Physical Laboratory, Princeton University, Princeton, New Jersey
(Received April 4, 1949)

A study of supersonic air jets has been made by the use of the Mach interferometer. The density distribution in axially symmetric jets with several tank-receiver pressure ratios has been determined, with special emphasis on the 3.7–7 range of ratios. In terms of the dimensionless quantities ρ/ρ_0 (ratio of jet density to tank density) and Z/D (ratio of distance from orifice to orifice diameter), all jets are closely the same in a region bounded by the orifice and an oblique line from the orifice edge. This line marks an inflection point in the streamlines, and probably indicates the low pressure termination of a three-dimensional Prandtl-Meyer expansion region which reduces the pressure at this point below that of the receiver. The strength of the stationary shock wave in general agrees with that predicted by the Rankine-Hugoniot equations. Recent theoretical computations of the density in the axis of the jets by Owen and Thornhill are in satisfactory agreement with the experimental results, but so far no suggestion has appeared for a theory to predict the three-shock configuration in jets.

Experiments with two-dimensional jets confined between parallel glass walls demonstrated that the *stationary* three-shock configuration could not be studied in this way, presumably because of boundary layer effects on the glass which destroy the two-dimensional quality of strong shock waves.

I. INTRODUCTION

THE study of the flow of gases from a reservoir through an orifice into a receiver dates back to the original work of St. Venant and Wantzel[1] more than a century ago. The existing knowledge of the compressible flow of gases through pipes and orifices is summarized in most textbooks on gas dynamics.[2]

A significant advance was made by Osborne Reynolds,[3] who discovered in 1885 that, if the ratio of the receiver to reservoir pressure drops below a certain critical value $P/P_0=[2/(\gamma+1)]^{\gamma/\gamma-1}$, the velocity of the gas at the narrowest part of the passage reaches the local velocity of sound, but up to the point of reaching the constriction, the flow is unaffected by the receiver conditions. If the pressure ratio P/P_0 is lower than the critical value, the jet expands into the receiver, attaining supersonic velocity. In such supersonic jets stationary patterns, consisting of expansions and constrictions accompanied by shock waves,[a] appear, under certain conditions repeating themselves many times as the jet proceeds out from the orifice.

Since this is the most prominent feature of such jets, it was the first to be studied by various authors, originally by E. Mach and Salcher,[4] later by Emden,[5] and Prandtl,[6,7] by means of the schlieren and shadowgraph technique, and recently by Hartmann and Lazarus.[8] Theoretical explanations for the periodic structure were given by Prandtl,[7] von Karman,[9] and Lord Rayleigh.[10] An account of the mathematical ideas involved (especially those of Rayleigh) and a bibliography on the subject are given by Bateman.[2] Such derivations assume that the gas velocity normal to the jet direction is small, or, in other words, that the jet expands very little, its pressure being about the same as the receiver, and that conditions throughout the jet are nearly constant. The adiabatic law, or the existence of a velocity potential is also assumed throughout the flow. Under these assumptions a wave-length, λ, representing the distance between the successive "disks" or periods of expansion and contraction as shown in Mach's and Emden's photographs, is obtained, in more or less agreement with some of the experiments. These derivations are certainly not applicable when the jet undergoes an appreciable radial expansion. Also, the existence of standing discontinuities which make the flow non-isentropic, and the turbulent mixing of the jet stream with the surrounding air, along with the other effects of viscosity and heat conduction, are neglected in these treatments.

It is evident that more knowledge, both theoretical and experimental, must be forthcoming before a general treatment, which holds over a wide range of pressure and expansion ratios, can be made.

The proper approach to the subject would seem to be to study in detail the structure of only the first section, or period, and such is the purpose of this paper. L.

* The present work as well as that described in Part I (Phys. Rev. 73, 1358 (1948)) was done under Contract NORD 9240 with the Bureau of Ordnance, Navy Department.

[1] B. De Saint-Venant and L. Wantzel, J. de l'Ecole Polytechnique 16, 85 (1839).

[2] See, for example, J. Ackeret, *Handbuch der Physik* (Verlag. Julius Springer, Berlin, 1927), Vol. 7, Chapter 5; H. Bateman, Committee on Hydrodynamics, Part 4: "Compressible fluids" (Bull. Nat. Res. Council, No. 84, February 1932); G. I. Taylor and J. W. Maccoll, *Aerodynamic Theory* (Verlag. Julius Springer, Berlin, 1935), edited by W. F. Durand, Vol. 3, Division H.

[3] Osborne Reynolds, Phil. Mag. 21, 185–199 (1886).

[a] The shocks, or sudden discontinuities in the density, pressure, temperature, and velocity of the air in the jet are fundamentally the same as those arising from an explosion.

[4] E. Mach and P. Salcher, Wien. Ber. 98, 1303–1309 (1889).

[5] R. Emden, Ann. d. Physik 69, 264–269, 426–455 (1899).

[6] L. Prandtl, Physik. Zeits. 5, 599–601 (1904). See also his book, *Strömungslehre* (Friedrich Vieweg & Sohn, Braunschweig, 1944), second edition, Abschnitt II.

[7] L. Prandtl, Physik. Zeits. 8, 23–30 (1907); E. Magin, Forschungsheft Ingenieurwesen 62, 1–32 (1908).

[8] J. Hartmann and F. Lazarus, Phil. Mag. 31, 35–50 (1941).

[9] Th. von Karman, Physik. Zeits. 8, 209–211 (1907).

[10] Lord Rayleigh, Phil. Mag. 6, 177–187 (1916).

Mach[11] made such a study in some detail qualitatively, using schlieren and interferometric techniques for the optical examination. He showed that standing "sound" waves of conical shape (called *schiefer Verdichtungsstoss* in German literature), similar to those observed ahead of a projectile in flight, existed in the jet, and that these waves could be reflected at the free boundary between the jet and the atmosphere due to the sudden change in velocity of the gas at this point. Furthermore, at low reservoir pressure he showed that these conical "sound" waves intersected in a simple way to form an X, but at higher pressures they become stronger and a flat shock wave normal to the stream appeared (called *gerader Verdichtungsstoss*). This he interpreted to be the same kind of interaction as observed and studied in detail earlier by E. Mach[12] when two explosion waves collided, or when an explosion wave was reflected from a surface.[b] L. Mach also found from a rough quantitative evaluation of the interference photographs that the air density in the jet at emergence was, in general, higher than that of the atmosphere, but that at distances out from the orifice the density dropped far below atmospheric density in many cases.

Cranz and Glatzel[13] made a study of jets at very high pressures formed by the ejection of powder gases from an 8-mm gun. They measured the Mach number distribution with probes and made shadowgrams of the shock formations. It has been shown in connection with the present work that these velocity measurements are in error, however, due to boundary layer phenomena.[c] W. Pupp, working in Cranz's laboratory, made what is probably the first quantitative evaluation of the density in a supersonic jet by interferometry. This is described in Cranz's *Ballistik* (Vol. II, p. 192), but in insufficient detail for comparison with the present study, as only axial pressure values are given.

Stanton[14] investigated certain properties of jets, particularly the conditions just at the orifice, by using static pressure probes and pitot tubes. He determined the exact position of the minimum cross section, the effect of scaling, and measured the pressure distribution along the axis of the jet. His results are not complete enough to determine the flow pattern and shock wave formation of the jet, however. His values of P/P_0 were in the vicinity of the critical value.

Hartmann and Lazarus[8] explored the pressure distribution along the axis of jets at reservoir pressures up to 7 kg/cm^2 using a pitot tube. Axial pressure curves were obtained in jets exhibiting both the simple X and the more complex shock interaction observed by Mach. The pitot measurements were in agreement with measurements of the Mach number using probes, in the case of the simple X interaction. These measurements constitute the best quantitative data we have found so far for supersonic jets, but are not complete as only the axial region is explored. The schlieren photos made by Hartmann and Lazarus are valuable for qualitative examination.

Prandtl[7] was the first to interpret the formation of a free jet by determining what shape and direction a very weak shock wave, or sound wave ("Mach line"), would

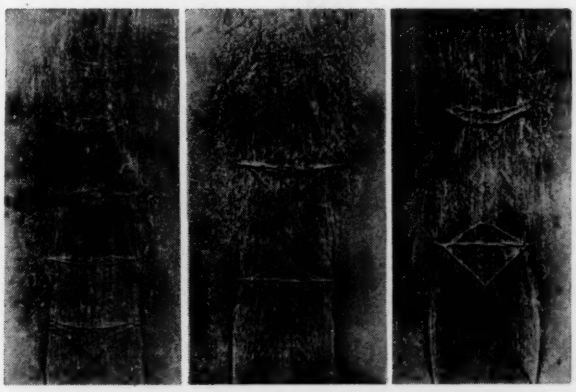

a b c

FIG. 1A. Shadowgrams of axially symmetric air jets flowing upward from a round orifice of 10-mm diameter. The black lines are generally the outlines of standing shock wave formations. The tank gauge pressure in a, b, and c are 20, 30, and 40 lb./in.^{2}, respectively.

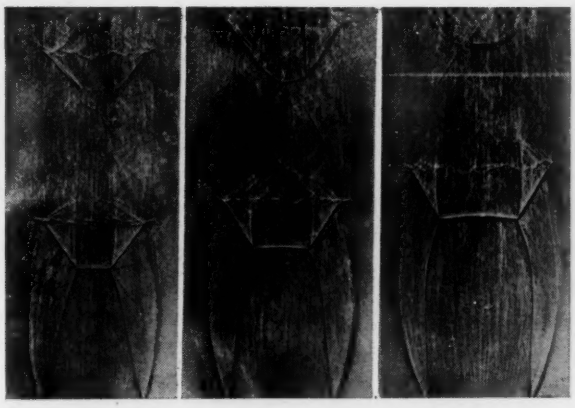

d e f

FIG. 1B. Shadowgrams as in Fig. 1A, the tank gauge pressures in d, e, and f are 60, 80, and 110 lb./in.^{2}, respectively.

[11] L. Mach, Wien. Ber. **106-II**, 1025–1074 (1897).

[12] E. Mach and J. Wosyka, Wien. Ber. **72-II**, 44–50 (1875). W. Rosicky, Wien. Ber. **73-II**, 629–650 (1876). E. Mach and J. Sommer, Wien. Ber. **75-II**, 101–130 (1877). Mach, Tumlirz, and Kogler, Wien. Ber. **77-II**, 7–32 (1878). E. Mach, Wien. Ber. **77-II**, 819–838 (1878). E. Mach and G. Gruss, Wien. Ber. **78-II**, 467–480 (1878). E. Mach and J. Simonides, Wien. Ber. **80-II**, 476–486 (1879). E. Mach and L. Mach, Wien. Ber. **98-II**, 1333–1336 (1889).

[b] The importance of E. Mach's discovery of such "triple shocks" to modern studies of shock waves and their interaction, was pointed out by J. von Neumann, R. J. Seeger, and others (reference 15).

[13] C. Cranz and B. Glatzel, Ann. d. Physik **43**, 1186 (1914).

[c] In regions where strong standing shock waves exist, the boundary layers along the probes used for the measurements of Mach numbers suffer separation and lead to diversion of the flow. Details of these disturbing effects are published in Part III of our interferometric studies NAVORD Report 7–47. See also Fig. 13 of reference 16b.

[14] T. E. Stanton, Proc. Roy. Soc. **111-A**, 306 (1926).

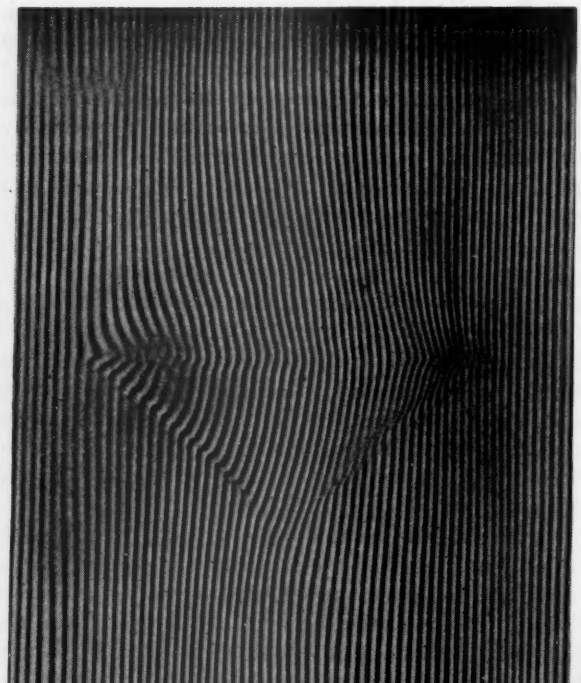

FIG. 2. Interferogram of an air jet issuing upward from a tank at 40-lb./in.² gauge through a 10-mm-diameter round orifice. (Compare with the shadowgram *c* of Fig. 1A.) The exposure (~300 μsec.) was too long to show turbulence.

assume at various parts of the jet. He showed that the wedge-shaped expansion region which arises from the orifice edge as the gas stream turns outward into the atmosphere (see especially his Figs. 7 and 9), is reflected from the opposite free boundary of the jet with a change of phase, and proceeds onward as a compression region, is again reflected as an expansion region, and so on, producing the periodic structure of the jet. Prandtl does not discuss the shock formations observed by Mach in jets.[11,15]

The present investigations as well as two others[16,17] originated during the war when the senior author (R. L.) studied at the Ballistic Research Laboratory of Aberdeen Proving Ground the behavior of powder gases ejected from guns in connection with the formation and elimination of gun flash. When it became clear that the typical shocks in the ejected gases, through the increase of pressure and temperature, were essential for the gun flash, at least for the "primary" flash, the interferometric method was suggested for the quantitative study of the physical conditions of jets, since this method had been used extensively by R. L. for the investigation of the dispersion, especially the "anomalous" dispersion of gases (see Rev. Mod. Phys. **5**, 248, 1933). The experiments described in this paper were carried out in the years 1945 and 1946.

II. DESCRIPTION OF EXPERIMENTS

A. Axially Symmetric Jets at Pressure Ratios from 2:1 to 8:1

The techniques developed by the writers and described elsewhere (references 16, 17) have been used in studying axially symmetric air jets over a wide range of pressure ratios. In these experiments dry air from a pressure tank discharged through a valve and a cylin-

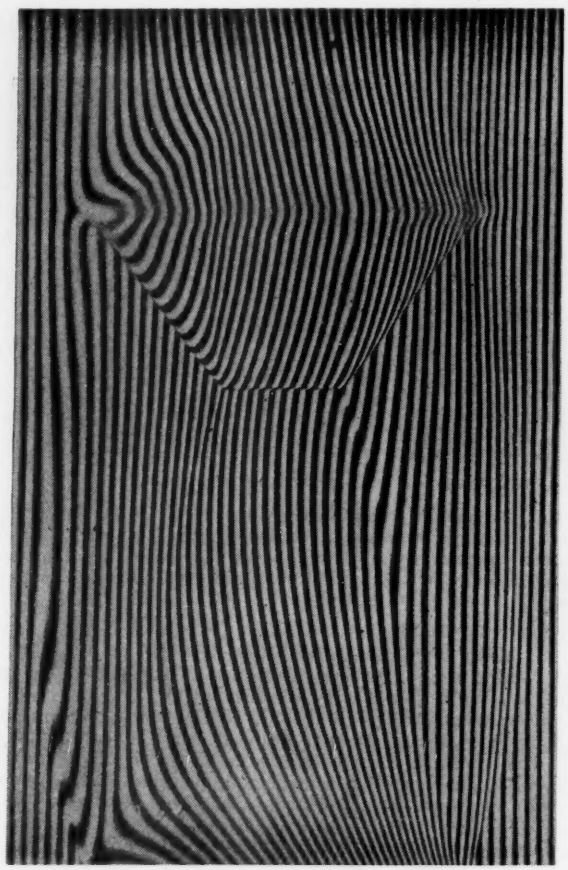

FIG. 3. Interferogram of an air jet at 60-lb./in.² gauge tank pressure (compare with shadowgram *d* of Fig. 1B). Exposure ~300 μsec.

[15] Seeger, von Neumann, and Polachek, Phys. Rev. **69**, 677 (1946); H. Polachek and R. J. Seeger, Phys. Rev. **69**, 677; L. G. Smith, Phys. Rev. **69**, 678; A. H. Taub and L. G. Smith, Phys. Rev. **69**, 678. See also H. W. Liepmann and A. E. Puckett, *Introduction to Aerodynamics of a Compressible Fluid*, GALCIT Aeronautical Series (John Wiley & Sons, Inc., New York, 1947), p. 60.

[16] (a) Ladenburg, Van Voorhis, and Winckler, NAVORD Report 69–46 (Navy Bureau of Ordnance publication). (b) J. R. Winckler, Rev. Sci. Inst. **19**, 307 (1948).

[17] Ladenburg, Winckler, and Van Voorhis, Phys. Rev. **73**, 1372 (1948).

drical tube with a streamlined orifice into the open atmosphere, forming an air jet. The orifice was placed in one light beam of a Mach interferometer (see Fig. 9; also Figs. 2 and 10 of reference 16b). The valve was either opened quickly by hand and a spark as light source flashed by an automatic switch when the tank pressure dropped to a predetermined value, or the valve was opened to synchronize with a rotating shutter when using a mercury arc. This instrumentation has been used without modification to study jets at various tank pressures between 20 and 100 lb./in.^{2} gauge, or a tank÷room pressure ratio of about 8 maximum. Some experiments were carried out with a modified orifice having a much more gradual constricting section than that described in reference 16b, Fig. 10, but the geometrical shape of the jet and of the shock formations did not change appreciably. To extend the ratio to higher values, the jet was discharged into a vacuum chamber equipped with nearly plane-parallel windows (see Part II-B). Some measurements were also attempted with a two-dimensional jet confined between such windows.

The characteristic features of such air jets are shown qualitatively by shadowgrams (Figs. 1A and 1B, made with a fast light source of about 10 μsec. duration (mercury arc)). Any discontinuities in density, such as shock waves and slip streams, appear as dark and light bands. The interesting feature is the development of the shock wave formation, which up to nearly 40 lb. pressure is conical. At greater pressures, a normal shock appears, accompanied by a slip stream extending upward from the three-shock intersection. The air emerges upward from a round orifice constricted smoothly from the valve opening (25 mm) to the orifice diameter (10 mm). (For details, see reference 16). It seems, according to these shadowgrams, as if a continuous shock starts at the edge of the orifice and extends up to the edge of the normal shock. But this is actually not so. As will be explained in more detail in Section III, the apparently continuous line consists of a density "valley" extending up from the orifice, joining in some cases to a shock wave which forms farther up in the jet. The "valley" has an optical effect in schlieren and shadow photographs identical with a shock wave. The difference is shown only by interferometer photographs and analysis.

Figures 2, 3, and 4 are interferograms of air jets at 40, 60, and 80 lb./in.^{2}, respectively, and are typical of the jets studied. The unsymmetrical appearance of the fringes is due to the fact that a density decrease, for example, moves the fringes perpendicular to themselves always in the same direction, therefore they crowd on one side of the axis and expand at a symmetrical point on the other side of the axis, although the change of density is the same at symmetrical points. In addition, interferograms were also made and analyzed at 20, 30, and 100 lb./in.^{2}. An interferogram of a 60-lb./in.^{2} jet emerging from a 4-mm diameter orifice similar to the 10-mm was also analyzed. The shock waves are revealed by sudden displacements of the fringes and are seen to correspond in position to the light and dark bands shown in the shadowgrams. One sees also that many portions of the jets, especially at 80 lb./in.^{2} pressure, are very turbulent as shown by irregular variations in the fringes. This effect is probably in the boundary which surrounds the entire jet. The narrow horizontal sections in Fig. 4 contain undisplaced fringes for reference, which are superposed photographically on the main part of the interferogram by two sets of grids.

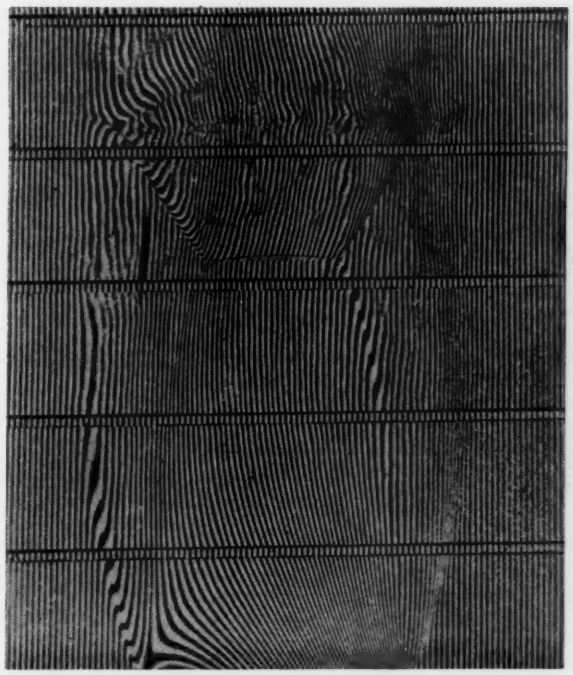

FIG. 4. Interferogram of an air jet at 80-lb./in.^{2} gauge tank pressure (compare with shadowgram *e* of Fig. 1A.) Undisplaced fringes are superimposed in the narrow bands by means of grids. Note the turbulence, probably in the jet boundary, shown by irregularities in the fringes. Exposure 1 μsec.

Figures 2 and 3 were photographed with a powerful mercury arc and fast shutter (~300 μsec.), while for Fig. 4 an air spark of only 1-μsec. duration between magnesium electrodes was used. (Light sources are described in reference 16.)

The interferograms obtained on spectroscopic plates were measured with great care on a comparator with accurate scales in two perpendicular directions. Between 20 and 30 separate cross sections were measured and evaluated on each interferogram, spaced very close together in the triple-shock intersection region, and wider elsewhere. The fringe shifts were calculated and plotted in the usual way, using the scheme described in reference 16, averages being taken of the two symmetrical halves of each section. Reduction of fringe shift values to densities was carried out at the Navy Department, Bureau of Ordnance, in accordance with a

mechanized scheme developed for axially symmetric flows. This procedure is described in reference 17, and has replaced the slower methods discussed in reference 16 for this phase of the reduction.

The density contours resulting from an analysis of the 40-, 60-, and 80-lb. jets are given, respectively, in Figs. 5, 6, and 7.[d] The numbers on the charts are in mg/cm³. A glance at these charts and at the shadowgrams of Figs. 1A and 1B indicates that the analysis has preserved the shock contours reasonably well. One observes that the density drops rapidly from its value at the orifice as the air expands into the jet.

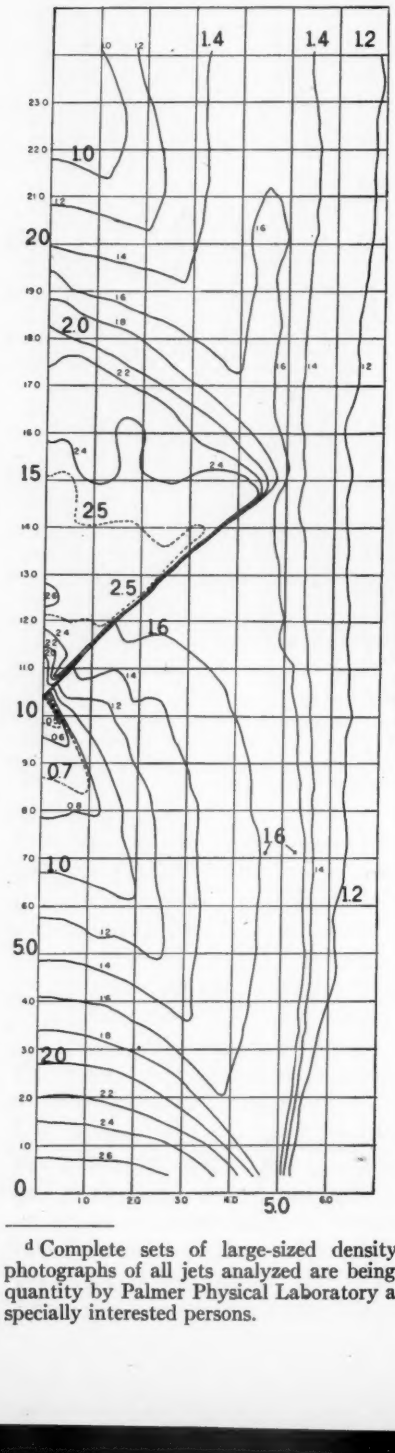

FIG. 5. Density contours for an axially symmetric supersonic air jet. Tank gauge pressure 40 lb./in.² (compare shadowgram *c* of Fig. 1A and interferogram Fig. 2). The isopycnic lines are labeled in units of mg/cm³. Corresponding values of pressure etc. are given in Table I.

[d] Complete sets of large-sized density charts and original photographs of all jets analyzed are being prepared in a limited quantity by Palmer Physical Laboratory and will be available to specially interested persons.

There is a sudden, apparently discontinuous increase across the various shock fronts, and a gradual transition to normal density at the jet boundary. If one is willing to assume an isentropic expansion of the air from the pressure tank up to regions in the jet bounded by the orifice, the tubulent boundary and the shock waves, then the pressure, temperature, and velocity may be calculated from well-known hydrodynamical relations since the stagnation pressure P_0, temperature T_0 and density ρ_0 are known. Tables I, II, and III have been prepared using these relations, with the various constants applying to the 40-, 60-, and 80-lb. jets, and enable one to obtain the pressure and other variables directly from the jet density within the region bounded by the orifice, the turbulent boundary and the shock waves. The additional application of the Rankine-Hugoniot relations permits one to determine changes in these variables across shocks, where the flow is not isentropic.[e] Especially remarkable are the deep minima in the isopycnic curves which mark also regions of minimum pressure, the line connecting these minima will be designated as "valley" in the following discussions in Section III.

B. Axially Symmetric Jets at Pressure Ratios up to 200:1

The 1.5-m³ tank used primarily for the jet studies had a maximum working pressure of 100 lb./in.², which provided a jet discharging into the atmosphere at a pressure ratio of about eight. To increase the pressure ratio, a vacuum tank was added to the system, and the jet was discharged into a chamber at various degrees of evacuation. The chamber was located in one beam of the interferometer, and light was admitted through glass windows of the best optical quality. Compensating glass plates were added to the other interferometer beam. A sketch of the arrangement is shown in Fig. 8, and Fig. 9 gives a photographic view of the actual apparatus. The vacuum chamber is a circular tube of 10-cm inside diameter, which is connected by a 90° elbow and a sylphon bellows to a vacuum tank of about $\frac{3}{4}$-m³ capacity. The orifice, valve and pressure tank are the same as before.

Face plates containing openings were welded to the sides of the tube, and their surfaces were carefully ground. The window glasses are held against these face plates directly and sealed from the side with rubber gaskets. The compensating chamber is a tube in a horizontal position, also with ground end plates against which the compensating windows are held. The vacuum chamber window glasses are 2 in.×4 in., while those on the compensating chamber are 2 in.×2 in. All four plates were cut from a plane disk of 7½-in. diameter and ½-in. thickness, which had a wedge error of about two wave-lengths. The wedge error was compensated by mounting the windows in a reverse position to that originally occupied in

[e] For a derivation of these relations see textbooks such as Liepmann and Puckett, *Introduction to the Aerodynamics of a Compressible Fluid* (John Wiley & Sons, Inc., New York, 1947); or R. Sauer, *Theoretische Einführung in die Gasdynamik* (Verlag. Julius Springer, Berlin, 1943), English translation published by Edwards Brothers, Ann Arbor.

the circular plate. The result was that the introduction of the vacuum chamber and compensating chamber into the interferometer produced no perceptible distortion of the interference fringes.

The chamber could be raised or lowered by a telescoping section, with a number of cylindrical spacer rings equal in diameter to the inner tube. The inside wall surface between tank and orifice was thus kept smooth, while utilizing the full area of the 4-in. high window with the 1-in. high field of view of the interferometer.

The camera consisted simply of a 3-in. diameter, 60-cm lens of good quality, a mirror to reduce the space needed, and a plate holder. Images of the interference fringes at the jet were produced in exactly natural size on the photographic plate.

The vacuum chamber was not suited to shadow photography as the photographic plate could not be brought near to the jet, and also because the low air density gave very weak effects. Schlieren studies were made by turning the vacuum chamber by 90°, which, on removal of the compensating chamber, provided a clear path for light between the interferometer mirror supports. Two schlieren lenses, a knife edge and a suitable camera objective were used in the conventional manner.

The pressure in the vacuum chamber was determined by a calibrated vacuum gauge connected to a manifold with four tubes leading to four points near the bottom of the chamber. The compensating chamber was ordinarily kept at atmospheric pressure.

The temperature within the vacuum chamber was in general lower than normal due to cooling by the expanding gas of the jet. The density, which had to be known in the region outside the jet proper for interpreting the interferograms, could therefore not be calculated from the pressure alone. The density was determined by moving film records made with a General Radio Recording Camera (see reference 16). A known vacuum was produced in the chamber, the camera was started, and the jet produced by opening the valve. The shift Δs of the fringes from the known initial condition could be determined, and the density ρ' in the homogeneous region outside the jet calculated, using the known length d of the light path, through the chamber, from the relation $\rho' = \rho_0 + \Delta s\lambda/Kd$. K is the Gladstone-Dale factor, λ the light wavelength and ρ_0 the density of air in the other interferometer beam.

The 4-mm streamlined orifice mentioned in Section II-A was used in the vacuum chamber, as the smaller size permitted the observation of larger expansions without exceeding the limits of the field of view.

Interferograms were made and reduced in the usual manner for cases of axial symmetry.

In Fig. 10 a series of schlieren photographs of jets at various expansion ratios is presented. The knife edge was perpendicular to the flow, with the result that the jet appears symmetrical, but shows the large Z-gradient near the orifice. At the higher ratio the density drops to so low a value near the shock region that the optical effect is quite small. The sharpness and contrast of the shocks decrease at higher expansion ratio, as the overall density and consequently the optical effect is smaller.

Figure 11A is an interferogram of a jet at an expansion ratio of 210. Due to its large extension, two sections obtained by changing the height of the chamber have been fitted together. Figure 11A, as well as 11B and 11C, were made with an initial adjustment of the interferometer so that one fringe covered the entire field, i.e., so that the field had a uniform color. Fringes then appear if the density is not uniform when the jet is turned on. Each fringe represents a line of constant integrated density through the jet. Such interferograms can be interpreted directly in two-dimensional flow, but for axial symmetry they give qualitative results only. This will be known, henceforth, as the method of *fringe contours*.

In Figures 11B and 11C the jet expanded at a ratio of

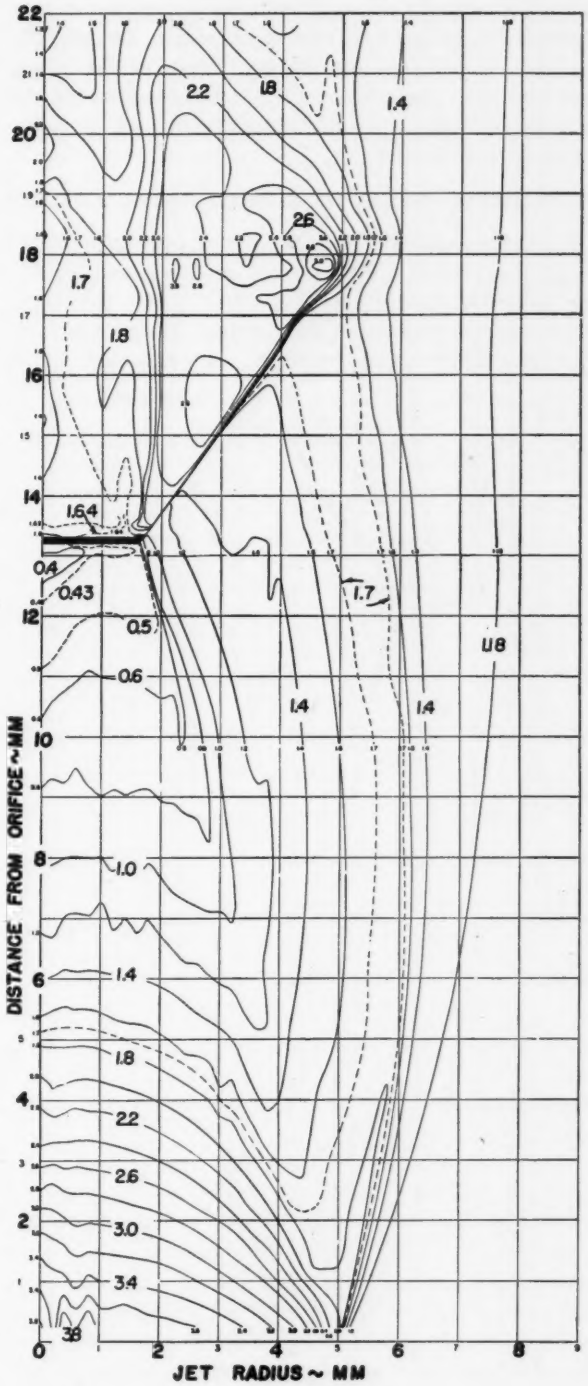

FIG. 6. Density contours for an axially symmetric supersonic air jet at a tank gauge pressure of 60 lb./in.² (compare shadowgram *d* of Fig. 1B and interferogram Fig. 3). The isopycnic lines are labeled in units of mg/cm³. Corresponding values of pressure etc. below the strong normal shock are given in Table II.

nearly 60, but the tank pressure in 11C was 17.7 lb./in.² gauge whereas it was 103 lb./in.² in 11B.

Figure 12 is an interferogram at ratio 60 with the field initially filled with straight vertical fringes. This interferogram has been completely analyzed in the usual manner, but the isopycnal chart is not reproduced here; due to the very low density, the relative accuracy is poor especially at points near the shock region. In fact, the analysis yielded negative density values in the region near the axis, probably due to the turbulence at the boundary between jet and surrounding air or some asymmetry in the jet.

III. INTERPRETATION OF EXPERIMENTAL RESULTS

From the isopycnal charts of jets at various pressures (Figs. 5, 6, and 7) as well as from shadowgrams (Fig. 1) and schlieren photographs (Fig. 10), it is seen that there is a regular dependence of jet structure on tank pressure. The jet progressively enlarges, accompanied by a characteristic system of stationary shock waves, which at low ratios appear on the photographs as oblique lines crossing at the jet center. At higher ratios the shocks appear much stronger and a normal shock appears in the central part of the jet, accompanied by a slip stream extending downstream from the intersection point of the three shocks.

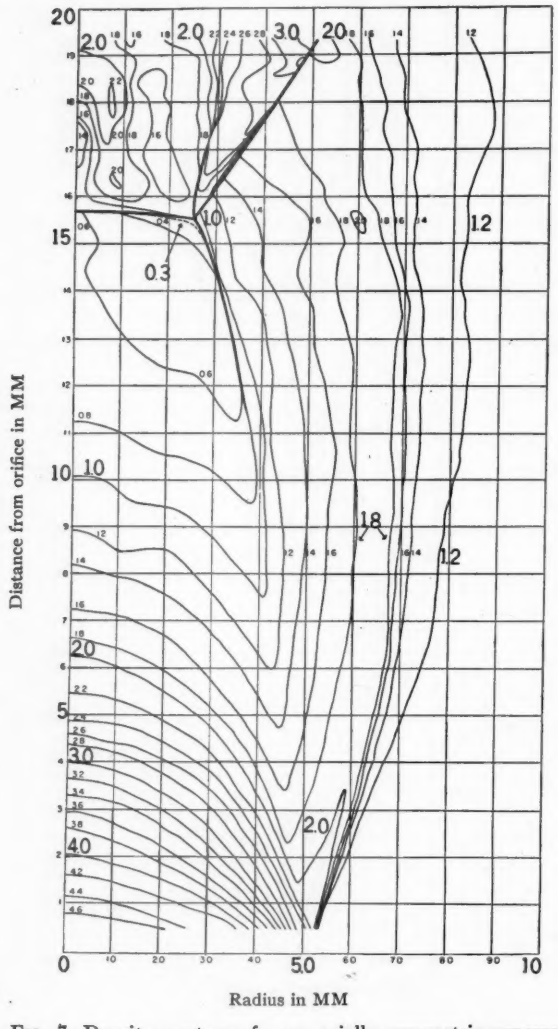

FIG. 7. Density contours for an axially symmetric supersonic air jet at a tank gauge pressure of 80 lb./in.² (compare shadowgram *e* of Fig. 1B and interferogram Fig. 4). The isopycnic lines are labeled in units of mg/cm³. Corresponding values of pressure etc. below the strong normal shock are given in Table III.

For the interpretation of the structure of the various jets the following ideas are helpful:

(A) The assumption of isentropic flow from the tank through the valve and orifice and out into the jet, up to the point where shock waves occur;

(B) the fact that most features of the jets are functions of the dimensionless quantity ρ/ρ_0, where ρ is the density of points in the jet and ρ_0 is the tank density;

(C) the assumption of a Prandtl-Meyer expansion region at the edge of the orifice, where the jet expands into the lower pressure region of the receiver;

(D) the applicability of the Rankine-Hugoniot relations to all shock waves in the jets;

(E) the possibility of applying to the jet shocks the shock wave theory for the reflexion of shocks in ideal gases as developed by von Neumann, Polachek and Seeger (reference 15);

(F) the construction of streamlines and Mach lines computed by the numerical-graphical integration of the general flow equations.

Some of these ideas are discussed also by Pack in a recent paper,[18] where he computes the formation of shock waves in jets for two-dimensional flow.

Let us now consider the various points.

A. The Assumption of Isentropic Flow

This assumption has been used in calculating pressure, temperature, Mach number and velocity, for example in the Tables I, II, and III; the well known equations are given in Table I. The Mach number values were checked experimentally by probes in several instances, and good agreement was found except in the boundary layer, where turbulence and mixing occur, and some distance upstream of the strong normal shock.[f] Changes of entropy occur across shock waves, so the above assumption holds in the jets only between orifice and shock wave region.

B. Dependence of Most Features of Jets on ρ/ρ_0

If one plots ρ/ρ_0 as a function of the ratio Z/D with R/D constant, where Z is the distance from the jet orifice, D the jet diameter and R the distance from the jet axis, it is found that all jets fall on one curve,[g] and depart therefrom at a definite value of Z depending

[18] D. C. Pack, Quart. J. of Mech. and App. Math. **1**, Part 1, (1948).

[f] Details of these disturbing effects are published in Part III of our interferometric studies NAVORD Report 7-47.

[g] The theoretical justification for this "scaling" is given, for example, in the recent paper by Pack (reference 18).

TABLE I. Pressure, etc., as adiabatic functions of density (40-lb./in.² jet). $P/P_0=(\rho/\rho_0)^\gamma$; $T/T_0=(\rho/\rho_0)^{\gamma-1}$; $M^2=V^2/a^2=2(T_0-T)/T(\gamma-1)$; $V^2=2C_p(T_0-T)$; $\gamma=C_p/C_v=1.404$; $C_p=1.00\times10^7$ erg/g °K; $\rho_0=4.41$ mg/cm³; $P_0=3.74$ atmos.; $T_0=298$°K.

Density ρ (mg/cm³)	Pressure P (atmos.)	Temperature T (°K)	Mach No. M	Velocity V (meter/sec.)
0.2	0.05	85	3.51	652
0.3	0.08	101	3.12	628
0.4	0.13	113	2.85	607
0.6	0.22	133	2.48	573
0.8	0.34	149	2.21	545
1.0	0.46	163	2.03	520
1.2	0.60	175	1.85	494
1.4	0.74	186	1.71	472
1.6	0.89	196	1.58	450
1.8	1.05	206	1.47	428
2.0	1.22	216	1.36	405
2.2	1.39	224	1.27	385
2.4	1.57	232	1.18	364
2.6	1.76	239	1.09	344
2.8	1.95	246	1.00	322

on the reservoir pressure. This value of Z corresponds to a shock wave or compression region. Figure 13 is a typical example of such a curve compounded from the isopycnal charts of all jets analyzed except the jet at the expansion ratio 60.

The plotted points are the values of ρ/ρ_0 on a line at $R/D=0.1$ parallel to the axis. It is seen that the experimental points for various jets group closely around the mean curve, up to the point where a shock or compression occurs in each case (see Section III-D below). Similar curves were drawn in addition at values of $R/D=0.0$, 0.2, 0.3, 0.4, and 0.45, all of which behave in a way similar to Fig. 13. From this set of curves a new composite chart representing all jets at once was constructed (Fig. 14). The contours represent points of constancy of the ratio ρ/ρ_0. The figure shows that this ratio and all values such as pressure, temperature, Mach numbers, etc., dependent on it, are identical in the various jets in a region bounded by the orifice and a line (dotted in Fig. 14) drawn from the orifice edge through the minima in the isopycnic charts. This is the "valley" mentioned at the end of Section II-A. These lines either meet the jet axis some distance from the orifice or they meet the triple-shock intersection away from the axis. In the latter case the line of the normal shock wave closes the region. Values of pressure ratio $P/P_0=(\rho/\rho_0)^\gamma$ are given in Fig. 14 on each contour, as well as the geometrical shape and location of the shock formations for the 40-, 60-, 80-, and 100-lb./in.² jets. It is to be understood that the over-all figure is for the 100-lb./in.² jet, but that this represents also the other pressures up to the position of the dotted line referred to above.

These considerations and conclusions have been confirmed recently to some extent by a paper by Owen and Thornhill of the Armament Research Establishment, British Ministry of Supply,[19] who calculated by the

[19] P. L. Owen and C. K. Thornhill, A. R. E. Report No. 30/48, Fort Halstead, Kent (September 1948).

Table II. Pressure, etc., as adiabatic functions of density (60-lb./in.² jet). (For equations used, see Table I.) $C_p=1.00\times10^7$ erg/g °K; $\rho_0=6.06$ mg/cm³; $P_0=5.08$ atmos.; $T_0=297$°K.

Density ρ (mg/cm³)	Pressure P (atmos.)	Temperature T (°K)	Mach No. M	Velocity V (meter/sec.)
0.2	0.043	76	3.81	664
0.4	0.112	99	3.14	629
0.6	0.197	116	2.76	602
0.8	0.295	131	2.51	575
1.0	0.409	145	2.30	551
1.2	0.524	155	2.14	532
1.4	0.645	164	2.00	516
1.6	0.782	173	1.88	498
1.8	0.929	181	1.77	482
2.0	1.078	189	1.67	465
2.2	1.225	197	1.58	447
2.4	1.398	205	1.50	428
2.6	1.552	212	1.42	412
2.8	1.730	218	1.35	397
3.0	1.883	224	1.28	382
3.2	2.065	230	1.21	366
3.4	2.26	236	1.14	350
3.6	2.44	241	1.08	334
3.8	2.63	246	1.02	319
4.0	2.80	250	0.96	306

TABLE III. Pressure, etc., as adiabatic functions of density (80-lb./in.² jet). (For equations used, see Table I.) $C_p=1.00\times10^7$ erg/g °K; $\rho_0=7.68$ mg/cm³; $P_0=6.44$ atmos.; $T_0=296$°K.

Density ρ (mg/cm³)	Pressure P (atmos.)	Temperature T (°K)	Mach No. M	Velocity V (meter/sec.)
0.2	0.04	68	4.08	675
0.3	0.07	80	3.66	657
0.4	0.10	90	3.37	642
0.6	0.18	106	2.98	616
0.8	0.27	119	2.71	595
1.0	0.37	130	2.51	576
1.2	0.48	140	2.35	558
1.4	0.59	149	2.21	542
1.6	0.71	157	2.09	527
1.8	0.84	165	1.98	512
2.0	0.97	172	1.89	498
2.2	1.11	179	1.80	484
2.4	1.26	185	1.72	471
2.6	1.41	191	1.65	458
2.8	1.56	197	1.58	445
3.0	1.72	202	1.52	434
4.0	2.58	227	1.23	371
5.0	3.52	249	0.97	306

method of characteristics the flow in a steady supersonic jet of air issuing at slightly supersonic speed from a circular orifice into a vacuum. Some results of this calculation, contained in Fig. 3.3 of their paper, are reproduced here in Fig. 15. This gives the pressure ratio p/p^* of the actual pressure at the axis of the jet, divided by the "critical pressure" as function of the ratio Z/D. The "critical pressure" p^* is the pressure of the gas when flowing at sonic speed, that is, for $M=1$; it is connected with the "stagnation pressure" in the reservoir by the relation $p^*=p_0[2/(\gamma+1)]^{\gamma/\gamma-1}=p_0\cdot0.528$ (if $\gamma=1.40$).

The curve in Fig. 15 is taken from Owen and Thornhill's paper, the circles are the values obtained from our interferometric measurements for the axis ($R/D=0$, see Fig. 14), replacing p/p_0 by p/p^* which is equal to $p/p_0\times1.893$. Such comparison is possible since the

values calculated for an infinite pressure ratio are universal values insofar as they are applied to any similar jet of cylindrical symmetry, if confined to an area bounded by the circular orifice and the first shock fronts. Also plotted as crosses are values of p/p^* as given in Fig. 3.3 of Owen and Thornhill's paper and taken from the paper by Hartmann and Lazarus (reference 8); they are obtained by pitot measurements along the axis of a jet flowing through a 6-mm orifice from a tank at a pressure of 7 kg/cm². The agreement between the calculated and the measured values is pretty good, the slight

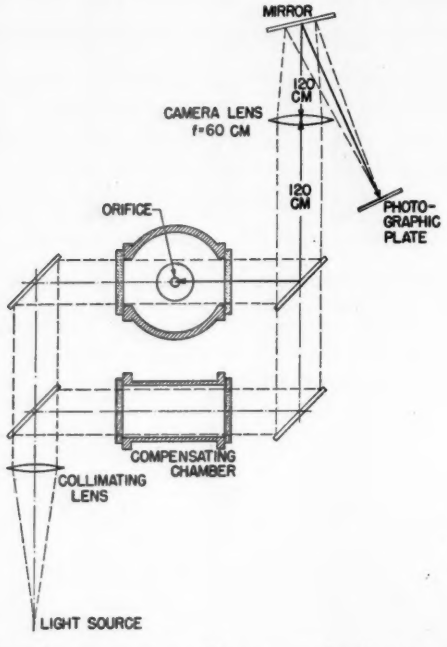

FIG. 8. Sketch of apparatus with vacuum chamber for studying jets at high expansion ratios by interferometry.

deviations, noticeable especially for small distances from the orifices, probably are due to the fact that the calculations start at a Mach angle of 85° ($M=1.004$) at the orifice; whereas, the Mach number at the orifice in the axis of our jets is approximately 1.05, that is somewhat higher than assumed in the calculations, so that the pressure ratios p/p^* are smaller than calculated. The calculations do not permit one of course—as was pointed out before—to determine the characteristic forms of shocks or for that matter the distance from the orifice where the normal shock is formed, since these features depend upon the pressure ratio $p_0:p_{\text{outside}}$, which was assumed in the calculations to be infinite.

C. Prandtl-Meyer Flow at the Edges and the "Valley" Configuration

One prominent feature of the jets is the "valley" which appears in all isopycnic charts, extending up into the jet from the edge of the orifice (see Figs. 5, 6, and 7). This "valley" evidently marks the innermost region influenced by the outside atmosphere. We assume that the expansion of the gas around the edge of the orifice, due to the overpressure in the jet, follows the Prandtl-Meyer type of flow, which very near the corner should be almost the same in the two- as in the three-dimensional case.[h] In the present case the pressure etc. of the air stream and the angular size of the Prandtl-Meyer expansion region, where the stream is turning outward from the orifice toward the atmosphere, depend on the form of the nozzle and the pressure in the reservoir. Assuming sonic velocity in the Z direction at the orifice, then one finds from the Prandtl-Meyer flow equations[i] that along a radius in the direction of the "valley" (dotted lines in Fig. 14) the pressure is less than the external atmospheric pressure. Some recompression, without visible shock waves, must occur between the "valley" and the outer jet boundary to build the jet pressure up to equality with the surroundings. The computed[i] short thin lines in Fig. 14, labeled 40, 60, etc., mark the *atmospheric* pressure point in the Prandtl-Meyer region. If the lines of constant ratio P/P_0 (or ρ/ρ_0) in Fig. 14 could be accurately determined near the orifice edge, they would directly map out the Prandtl-Meyer region, but the resolution of the experimental method does not permit this. The "valley" configuration does not appear to have been predicted from any of the theoretical jet studies so far. It can be approximately located by drawing the Mach line (see

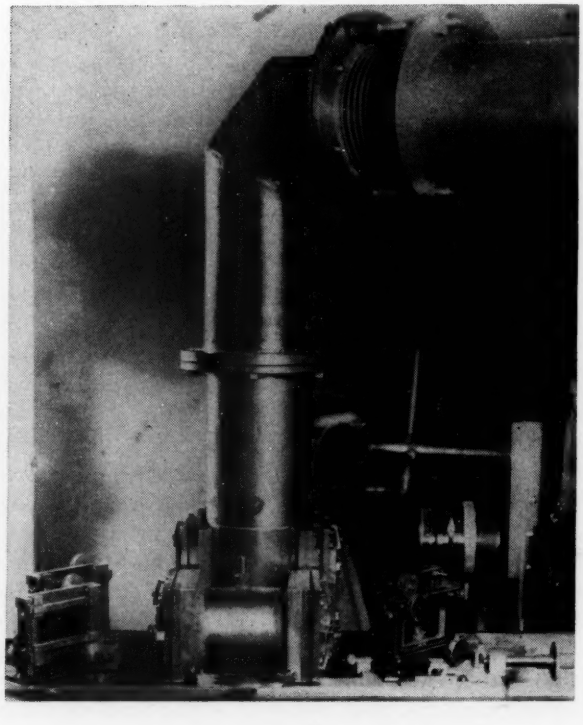

FIG. 9. Photograph of apparatus with vacuum chamber for studying jets at high expansion ratios by interferometry.

[h] See reference e, R. Sauer, p. 143. Also reference 18.
[i] Obtained by using the formulas on pp. 53–58 of R. Sauer's book and his Table II (see reference e).

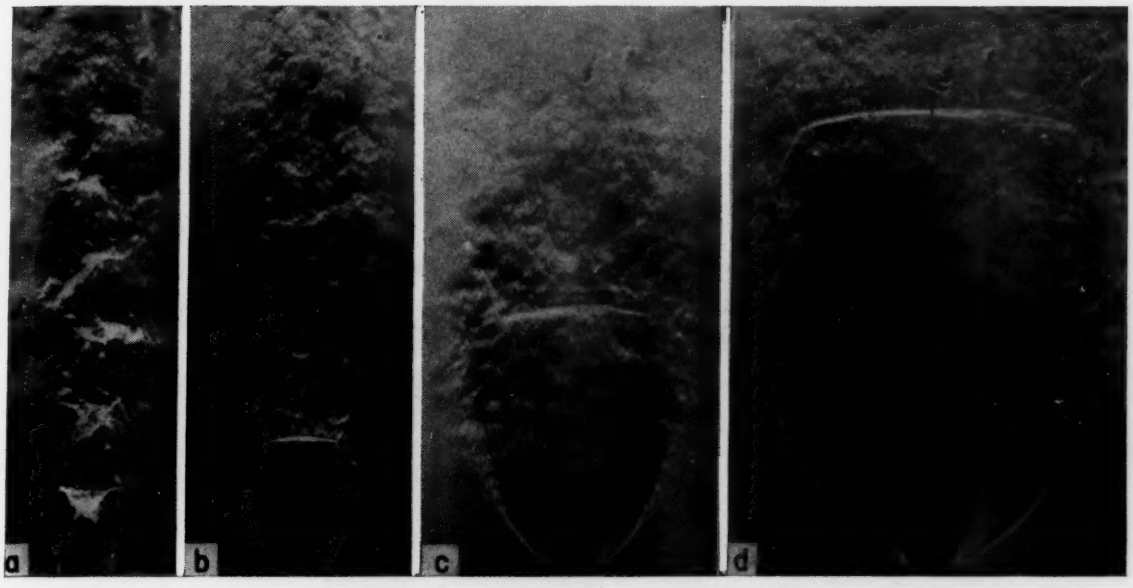

FIG. 10. Schlieren photographs at various expansion ratios, knife edge perpendicular to the flow. Expansion ratios: *a*, 5.1; *b*, 16.9; *c*, 57.5; *d*, 174.

III F) from near the orifice edge, which merges with the weak shock (herein designated shock 1) near the triple point.

D. Shock Waves[j]

The agreement between the measured normal shock strength ρ_2/ρ_1, where ρ_2 and ρ_1 are the densities on the downstream and upstream sides of the shock fronts, and the shock strength calculated from the Rankine-Hugoniot (R-H) relations,[j] is within the errors of the method, as shown in Fig. 13: there the dotted graph connects the values of ρ_2/ρ_0 computed from the R-H relations for a normal shock in the form

$$\frac{\rho_2}{\rho_0}=\frac{\rho_1}{\rho_0}\left[1-\left(\frac{\rho_1}{\rho_0}\right)^{\gamma-1}\right]\frac{\gamma+1}{\gamma-1}, \qquad (1)$$

assuming ρ_1/ρ_0 to be given by the smooth curve through all the experimental points. The normal shock appears clearly in the graphs for the 60-, 80- and 100-lb./in.^{2} jets as a vertical rise of density reaching up to the dotted graph for ρ_2/ρ_0 and confirms therefore the theoretical computations.[k] Small deviations from the R-H relations expected at large shock strength ($\rho_2/\rho_1 > 3.5$) do not show up in our results since the accuracy of evaluation of axially symmetric jets is not sufficient.

Also the oblique shock strength has been compared with the R-H equations, with good success; for example, in the 60-lb./in.^{2} jet, the calculated and observed shock strengths for shock 3 are 1.61 and 1.67, respectively.

[j] For literature on the theory of shock waves see reference e.

[k] The relatively larger deviation for the jet with only 4-mm orifice (60 lb.) may be due to the larger experimental uncertainty connected with the smaller diameter of the orifice.

E. Mach Reflection

It was pointed out in the introduction that the general shock-wave configuration characteristic of jets at the higher pressure ratios bears striking resemblance to the so-called "Mach" reflection of air shocks, first observed by E. Mach in 1878.[12] This phenomenon has been examined experimentally and theoretically in detail in recent years for the case of traveling air shocks with the result that the theory seems to be inadequate.[15] If one considers the oblique collision of a plane shock wave with a wall to be the same as the collision of this shock with its mirror image, one sees that a "simple" reflection at the wall (as in Fig. 16A) is possible over a certain range of strength and angles of the incident shock wave. Outside this range the "Mach" reflection appears, characterized by the point of reflection being away from the wall, and joined more or less normally to it by a third shock wave, as illustrated in Fig. 16B. The similarity between Fig. 16B and the air jets (Fig. 1B) is very great, but the development of the "triple shock" in the two cases may be quite different, as the jets are *stationary* phenomena and are axially symmetric. The Mach configuration, on the other hand, is a transient non-stationary phenomenon, enlarging continually as it moves along the wall, and cannot be brought to rest as a whole by a simple transformation to moving coordinates.

It must also be considered that the "core" of the jet after the normal shock wave is subsonic and therefore may transmit disturbances upstream to the shock region.

In spite of the differences between the triple-shock formation in the present stationary case and the shock formations in transient phenomena, it seemed worth

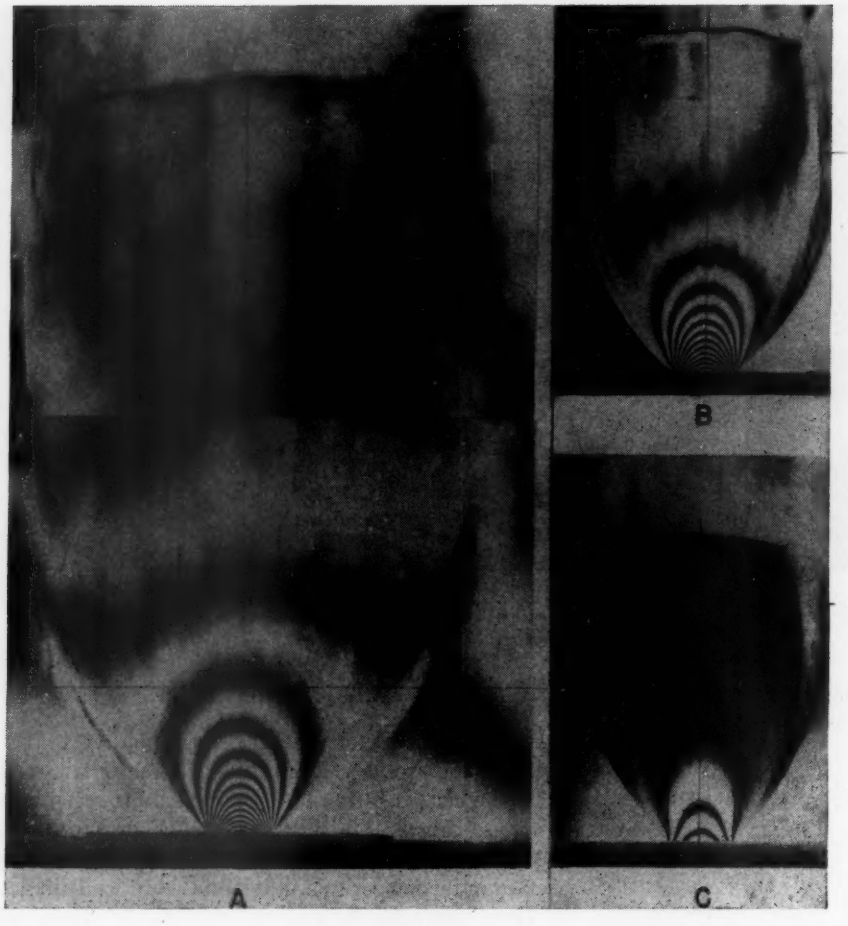

FIG. 11. Interferograms of axially symmetric air jets at high expansion ratios: A, 210; B and C, 60.

while to apply the theory of the triple-shock configuration[15] to the shock formation in jets, assuming that, although the present problem has axial symmetry in three dimensions, it may be considered as a two-dimensional case over a small region. However, preliminary computations have shown that neither the density values near the triple-point nor the shock angles could be measured accurately enough in this series of jets to provide a good check of the theory. For improving the accuracy and for simplifying the conditions, the homogeneous cylindrical jet escaping from a circular Laval nozzle at Mach number 1.7 has been studied as described in Paper I[17] using such tank pressures that triple shocks are formed in the open atmosphere. Figure 17 is an interferogram of a stationary triple shock under these conditions. The evaluation of such interferograms is not yet finished and shall be discussed in another paper.

F. Stream Lines and Mach Lines

A map of stream and Mach lines has been constructed in the case of the 60-lb./in.^{2} jet by step-wise integration of the equations of motion, as described for the stream lines in a previous publication.[17] The Mach lines are constructed in an elementary, approximate way by starting at various points along the axis which coincides with the flow direction. From the measured density at these points the Mach number and Mach angles are computed (as for one-dimensional flow) and so the Mach lines are drawn downstream as well as upstream as straight lines till they cross the next streamline and then the procedure is repeated. In this way Fig. 18 was obtained.

From the behavior of the stream and Mach lines near the orifice it can be concluded that the surface of $M=1$, which theoretically should coincide with the plane of the orifice, is curved back inside the edge, so

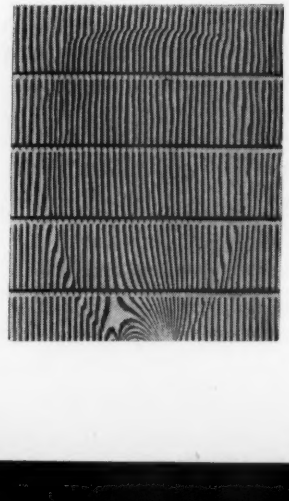

FIG. 12. Interferogram of an axially symmetric air jet at expansion ratio 60.

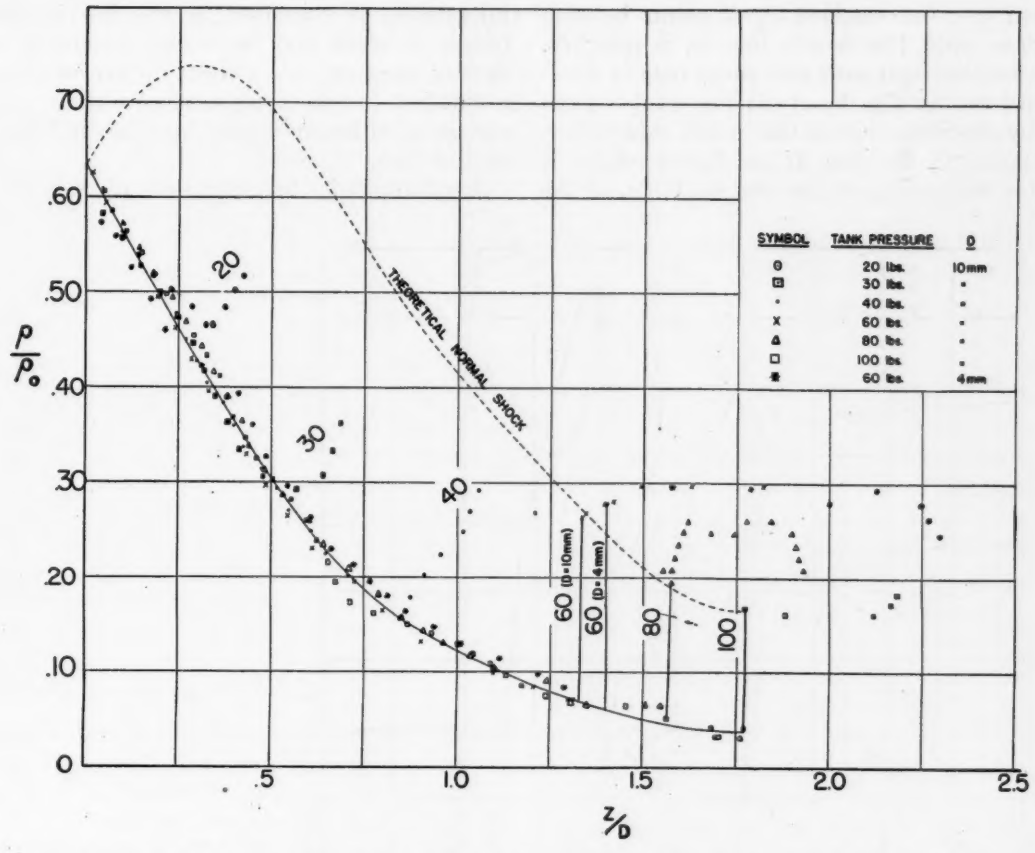

FIG. 13. The ratio ρ/ρ_0 (density at fixed distance R from axis for various jets÷tank density) as a function of the ratio Z/D (distance from orifice÷orifice diameter) for $R/D=0.1$. The graph "Theoretical normal shock" connects the various values of ρ_2/ρ_0 according to Eq. (1) section III-D.

that the air emerges near the edges with higher velocity, and immediately turns outward into the atmosphere. The negative Mach lines (the family with negative slope) diverging from the orifice edge show the three-dimensional Prandtl-Meyer region bounded by the "valley," which was shown in Fig. 14. The rate of expansion then decreases, the streamlines passing an inflection point at the "valley," and the jet reaches its maximum diameter at $Z=8$ mm (Fig. 18). The "bottle" shape of the jet is easily understood, after one has constructed a few streamlines, to be the result of the interaction of the pressure and inertial forces of the outstreaming gas with the atmospheric pressure force to produce an overexpansion and then an overcontraction. This pattern is repeated at successive distances from the orifice, as shown in Mach's and Prandtl's pictures, also in some of the jets of our Fig. 1. However, the turbulence in these jets, which is rather conspicuous due to the short duration of the illuminating spark, destroys part of the repetition phenomena. They are most noticeable when the normal shock is not too large a part of the jet area, otherwise the transition to subsonic flow and corresponding loss of pressure head deteriorates the jet rapidly.

The negative Mach lines beyond the "valley" are not expansion but compression waves due to reflexion at the boundary of the jet where it mixes with the outside air at rest (Fig. 18). When they converge, the pressure gradient steepens so that a shock is produced. This is the weak oblique shock 1 which forms well up in the jet towards the triple point. This shock appears on shadowgrams sometimes as a continuation of the "valley." In the case of jets at low pressure where shock 2 is absent, the "reflected" shock (Fig. 16) may be produced by interference of converging compression waves, which are due to reflexion of expansion waves at the other boundary between jet and air at rest. However, the appearance of the normal shock 2 at higher pressure and the subsonic core downstream from it cannot be understood from such elementary considerations (see Section III-E).[1]

IV. TWO-DIMENSIONAL JETS

The long and arduous reduction process which is inevitable in axial flows suggested the possibility of studying two-dimensional jets, analogous to the three-

[1] Similar conclusions are drawn by K. O. Friedrichs, App. Math. Group, New York University, AMG-NYU No. 47 (1944), from a series of unpublished shadowgrams of jets with various ratios and orifice shapes obtained by R. P. Fraser.

dimensional jets, but confined at all points between parallel glass walls. The density then is, in principle, constant along the light path and varies only in directions normal to this. The density at any point is given uniquely by the fringe shift at that point, independent of other points in the field. If the interferometer is adjusted for fringe contours (see Section II-B), all the information is contained in the interferogram, the fringes of which may be labeled directly in terms of density, pressure, etc., without further measurement or evaluation. In two dimensions, as in three, some reference point of known density must be established in the field of view.

Interferometric investigations of two-dimensional

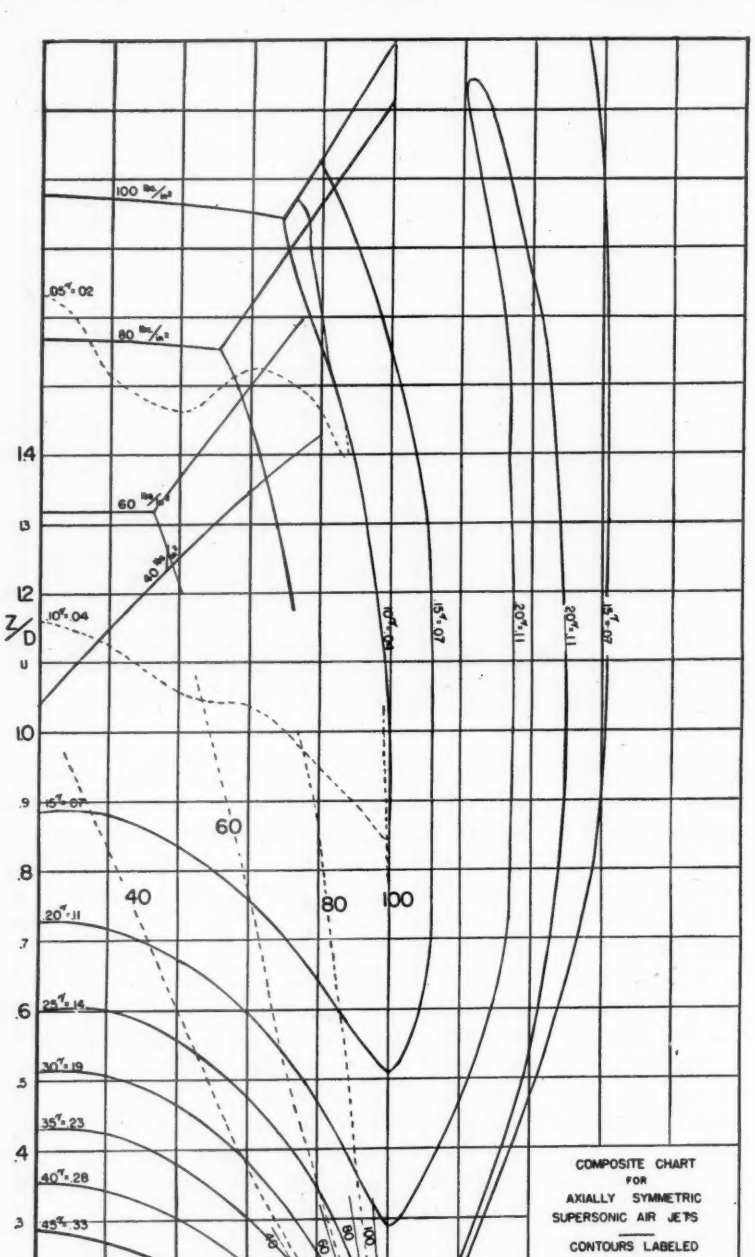

FIG. 14. Composite chart for jets at 40, 60, 80, and 100 lb./in.². Contours labeled in density and pressure ratios $((\rho/\rho_0)^\gamma = P/P_0)$. The over-all figure is for the 100-lb./in.² jet, but it represents also the results of the jets at other pressures in a region bounded by the orifice, the shocks, and the "valleys" (the dotted lines).

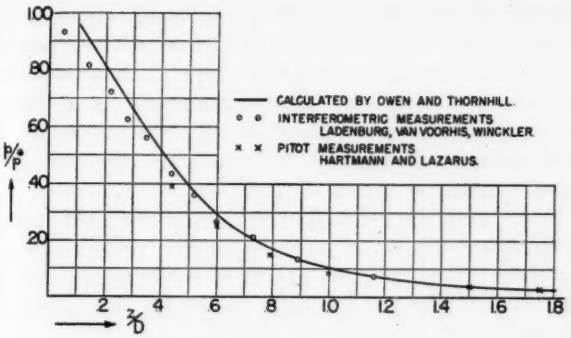

FIG. 15. Axial pressure distribution in supersonic jets as function of the ratio Z/D (distance from orifice divided by orifice diameter). Plotted is the ratio p/p^* of actual pressure divided by "critical pressure" which is the pressure of the gas when flowing at sonic speed.

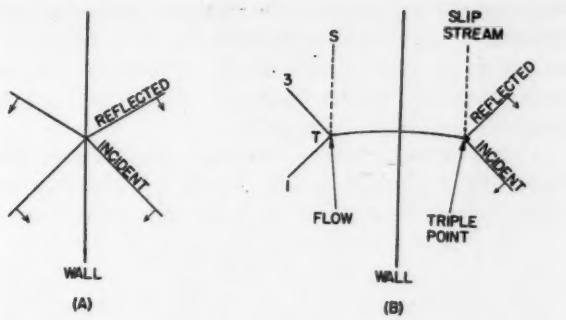

FIG. 16. Schematic drawing (A) of simple reflection and (B) of "Mach" reflection of a shock wave by a wall.

flow, as in standard wind tunnels, permits also the study of a large number of additional phenomena—as, for example, boundary layers and their interaction with shock waves—which are not accessible in axially symmetric jets.

A. Apparatus

A two-dimensional nozzle was constructed, joined to the 1-in.-diameter round tube from the valve by a transition section. The nozzle consisted of two carefully ground and polished steel blocks, 20 mm in thickness along the light path. The nozzle contracted from the end of the 25-mm wide transition section down to the 4-mm orifice, and the blocks were then terminated. A 38-mm-wide region extended upwards from the orifice, which provided space for the jet to expand sidewise. The glass plates were held firmly against the nozzle blocks. The air stream finally discharged into the 4-in. tube leading to the vacuum tank. The flow was kept between the glass plates, with a constant depth along the light path of 20 mm, and could expand only in directions normal to the light beam. A chamber with the compensating glass plates was inserted in the other light beam to equalize the optical paths as in the axially symmetric experiments. The exact shape of the nozzle may be seen in the interferogram, (Fig. 20) and as in the axially symmetric case the nozzle could be raised or lowered to bring various sections of the jet into the interferometer field of view.

B. Experimental Results

An interferogram made by the method of fringe contours of a two-dimensional jet expanding into a partial vacuum is shown in Fig. 19. The jet was found to be unstable, however, apparently due to the tendency of the air stream to exhaust partially the space between the glass windows and side walls into which it expanded, by sweeping air out. The jet would sometimes cling to a side wall or suddenly enlarge and fill nearly the entire space. An example of the latter behavior is given in Fig. 20, which is obtained at the same tank pressure as Fig. 19 but at somewhat lower pressure in the vacuum tank. Figure 20 is a composite view of two sections of

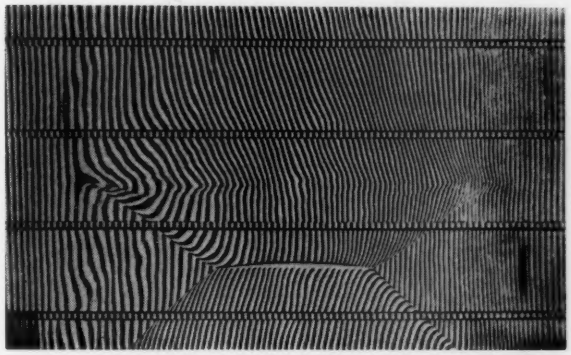

FIG. 17. Interferogram of a stationary "triple-shock configuration" in a homogeneous air jet leaving the orifice of the De Laval nozzle at about one atmosphere with Mach No. = 1.7.

the nozzle. Certain of the fringes have been labeled with their density value in mg/cm³. From the relations

$$\left.\begin{aligned}\Delta s &= \Delta n d/\lambda,\\ \Delta n &= K\Delta\rho\end{aligned}\right\}, \quad \text{and} \qquad (2)$$

where Δs is the number of fringes counted, Δn the corresponding change of refractive index, d the length of light path (2.0 cm), λ the light wave-length ($4.48\cdot10^{-5}$ cm), $\Delta\rho$ the density change and K the Gladstone-Dale factor (0.228), one finds the density increment between adjacent fringes (black to black or white to white) to be 0.103 mg/cm³. The reference point is taken to be the white fringe at the bottom of the photograph, at which point the pressure was measured with a fine hole in the side wall leading to a gauge. The density here is 3.67 mg/cm³, calculated from the tank density and pressure, and assuming an adiabatic expansion to that point.

Theoretically, sonic velocity should be reached at a density of 2.34 mg/cm³ at the throat, and in actuality this occurs very close to the orifice for both Figs. 19 and 20. The density contours there are curves rather

than straight lines across the channel, indicating some departure from uniform conditions. This behavior is analogous to that of the axially symmetric jet, and stems from the section approaching the throat, which probably contracts too rapidly.

A well-defined "valley" extends downstream from the orifice edge, and in Fig. 20 what appears to be a normal shock wave exists in a manner somewhat like the axially symmetric case, except that shock 1 is absent. From the density $\rho_1=0.42$ mg/cm³ just before this normal shock, we find from Eq. (1) that theoretically $\rho_2=1.47$ mg/cm³. This corresponds to a fringe shift across the shock front of 10 units, although a close scrutiny of Fig. 20 shows a shift there of only about $\frac{1}{2}$ unit.

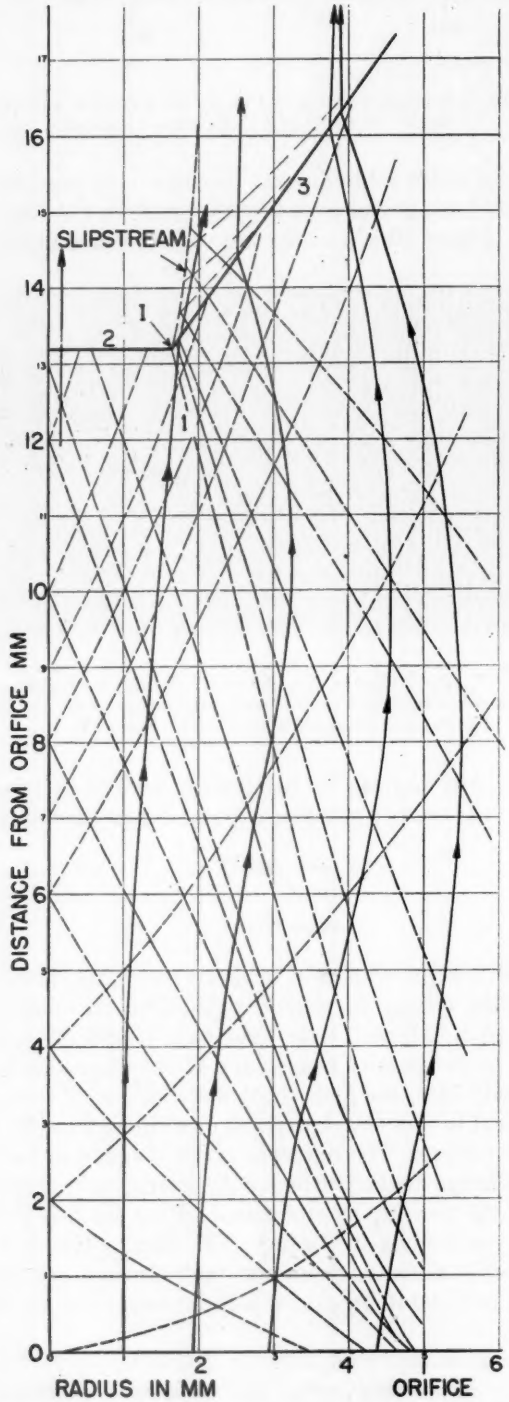

FIG. 18. Chart of computed stream lines and Mach lines for 60-lb./in.² jet.

This discrepancy is not due to an appreciable error in ρ_1, since this value has the correct ratio to ρ_0 as computed from the ratio of the cross-sectional areas of the jet near the shock and at the orifice, according to the equation

$$(A/A_0)^2=\frac{(2/(\gamma+1))^{\gamma+1/\gamma-1}\cdot(\rho_0/\rho_1)^{\gamma+1}}{2[(\rho_0/\rho_1)^{\gamma-1}-1]/(\gamma-1)}. \qquad (3)$$

But the discrepancy between the observed and calculated fringe shift can be understood if the normal shock does not extend completely along the light path between the glass walls, but exists for only a small fraction of it. A reasonable explanation is that the boundary layer, inevitably present on the glass, is separated and enlarged by the pressure gradients of the normal shock, and produces a configuration of oblique shocks which destroys the two-dimensional quality of the flow. This separation phenomenon, if present, makes the observation of stationary shock wave patterns very difficult, as there is an unknown variation of density along the light beam. In fact, because of boundary layer separation, it is probable that the *stationary* Mach reflection in two dimensions is an experimental impossibility, and that one cannot produce in this way a stationary two-dimensional jet analogous to the axially symmetrical, three-dimensional jet.

C. Two-Dimensional Flow in Channels (Experiments carried out by D. Bershader)

In order to avoid the instability of the jet, the latter was discharged not into an evacuated space, but into the atmospheric air after leaving the orifice, and it remained confined by the glass walls in the direction of the optical path. Two different nozzles have been constructed for these experiments; one was a "divergent channel," where the supersonic section was bounded by two plane steel walls, each making an angle of 4° with the axial plane of symmetry, essentially identical with a channel used 40 years ago by Magin in Prandtl's laboratory.[7] The other nozzle was constructed according to the "method of characteristics" in such a way that the supersonic velocity of the gas finally becomes uniform across the entire section. After leaving the correspondingly formed steel walls, the gas stream enters the atmospheric air, but remains between the glass walls. If the overpressure in the reservoir is such that the gas pressure at the orifice is near to atmospheric pressure, the gas stream does not expand sidewise, but

FIG. 19. Interferogram of contour fringes for two-dimensional jet, expansion ratio 6.1:1.

proceeds with nearly the velocity it had reached in the uniform part of the channel.

The details of the experiments carried out with these two channels are reported in the thesis of D. Bershader and are published elsewhere.[20]

Only a few of his results which have a bearing on our foregoing conclusions will be mentioned here: the interferometric pictures of those jets show clearly the effect of the boundary layers along the walls of the channel and between the jet and the quiet air; the fringes, being straight in the main part of the channel, bend suddenly when approaching the edge of the jet, and crowd together; their evaluation permits the quantitative computation of the decrease of density and increase of temperature in the boundary layer and of its velocity profile. Furthermore, by rotating the channel through 90° and taking an interferogram of the light traveling

[20] D. Bershader, Rev. Sci. Inst. **20**, 260 (1949); see further R. Ladenburg, Proc. VII Int. Congress App. Mech. London (in print).

FIG. 20. Interferogram of contour fringes for two-dimensional jet flowing upward from reservoir through nozzle, fringes labeled in mg/cm³. Expansion ratio 9.7:1.

parallel to the glass walls above the orifice, one obtains also the effect of the boundary layer along the glass walls. Except for this boundary layer, the conditions are quite uniform from glass to glass up to a few millimeters above the orifice. However, farther out the pictures show clearly that the boundary layer against the glass begins to separate, destroying the homogeneity in the direction of the light beam, as was concluded before in discussing Fig. 20. The cause of this separation are the oblique shocks, which start at the orifice, and which evidently affect the boundary layer by their pressure gradient.

Our best thanks are due to Dr. H. Panofsky and Miss A. Kenny for very valuable help in carrying out this project.

Internal Pair Formation*

M. E. Rose
Oak Ridge National Laboratory, Oak Ridge, Tennessee
(Received April 20, 1949)

The electron-positron angular correlation and total conversion coefficient are calculated for internal pair formation and for arbitrary multipole order of the electric and magnetic radiation fields. The Born approximation is used and in the region of greatest experimental interest, $Z \lesssim 40$ and gamma-ray energy >2.5 Mev, the consequent error should be negligible. Numerical results are given for multipole fields of order 2^l with $l=1$ through 5 inclusive.

INTERNAL pair formation, as an alternative mode of decay of an excited nucleus competing with gamma-ray emission and (atomic) internal conversion, supplements the latter process in that the pair formation decay rate is largest where the internal conversion rate is smallest. Thus, while the internal conversion coefficients decrease rather rapidly with increasing gamma-ray energy ($k\,mc^2$), the pair formation coefficients increase. Again, the internal conversion coefficients generally increase with Z[1] while the pair formation coefficients are practically independent of Z and in fact decrease slightly with increasing Z.[2] Consequently, in the region of low Z and large k where the internal conversion coefficients will be too small to measure conveniently, the measurement of the pair formation coefficient may prove to be more feasible. Thus, for $Z=40$ the two modes of decay are of roughly equal probability for $k=5.0$ ($\sim$2.5 Mev). The electric internal conversion coefficient (internal conversion electrons per quantum) in this case varies from 5.62×10^{-5} to 3.33×10^{-4} for 2^1 pole to 2^5 pole respectively.[1] The corresponding values[3] of the pair formation coefficients (pairs per quantum), computed for $Z=0$, are 9.93×10^{-4} to 1.77×10^{-4}. Similar results follow for the magnetic multipoles. The contrasting dependence on multipole order is also to be noted and is characteristic. For $Z<40$ and/or $k>5.0$ the internal conversion coefficients will decrease roughly like Z^3 or k^{-n} where n depends on multipole order and parity change and is generally of order 2–3. At the same time the pair formation coefficients increase with k so that at $k=20$, for example, the number of pairs per quantum is of order 10^{-3} for all multipole orders of practical interest, and for both electric and magnetic radiation (see Figs. 3 and 4).

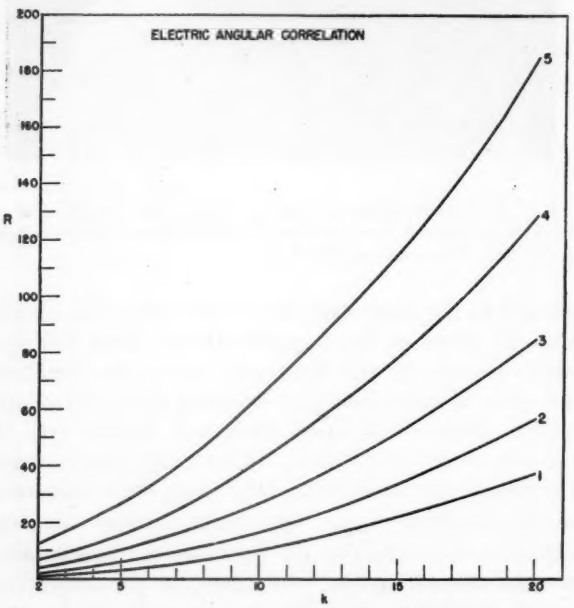

FIG. 1. Ratio (R) of electron-positron coincidence rates for angular separations 0 and $\pi/2$ and for pairs of all energies in the case of electric multipoles. The multipole order 2^l is indicated by the numbers (values of l) affixed to the curves. See Eq. (9).

For the question of utilizing pair formation measurements in order to determine multipole order of nuclear transitions and angular momenta of nuclear energy levels, the sensitivity of the pair formation coefficient with l (2^l is the multipole order) is of importance. Results for the total pair formation coefficients (Figs. 3 and 4) show that a satisfactory degree of sensitivity is obtained for low k but that for large k the ratio of successive multipoles is uncomfortably close to unity.[3] Thus for the largest k for which numerical results are given ($k=20$), the ratio of coefficients for successive multipoles is as low as 1.08 for the ratio of electric 2^4 to 2^5 multipoles and 1.10 for the ratio of magnetic 2^4 to 2^5 multipoles. While a satisfactory dependence is obtained for intermediate gamma-ray energies $k\sim5$ to 10, the situation is considerably improved for all k if

* This document is based on work performed under Contract No. W-7405, eng. 26 for the AEC at the Oak Ridge National Laboratory.

[1] See, Rose, Goertzel, Spinrad, Harr, and Strong, *K-Shell Internal Conversion Coefficients*, to be submitted to the Physical Review. For small k and the larger multipole orders there is a maximum in the Z-dependence of the internal conversion coefficients.

[2] J. C. Jäger and H. R. Hulme, Proc. Roy. Soc. **148**, 708 (1935). This paper gives the electric dipole and quadrupole coefficients calculated with Dirac hydrogen-like wave functions for $Z=84$. The Born approximation ($Z=0$) results for the same multipoles were given by J. R. Oppenheimer and L. Nedelsky, Phys. Rev. 44, 948 (1933). Non-relativistic calculations for these multipoles were carried out by M. E. Rose and G. E. Uhlenbeck, Phys. Rev. 48, 211 (1935). An examination of the accuracy of the approximation methods is given in the last mentioned paper.

[3] This is, of course, due to the fact that for small wave-lengths the pair formation (like the internal conversion) takes place in the far zone of the radiation field so that all dependence on multipolarity (or parity) disappears.

one measures the angular correlation of electron and positron.[4] Accordingly, in Figs. 1 and 2, results are presented for the ratio of coincidence counting rates in the two cases $\Theta=0$ and $\Theta=\pi/2$, where Θ is the angle between the electron and positron. The angular correlation as given here refers to the total counting rates, integrated over the energies of the particles, since this would appear to be the easiest quantity to measure. This *integral* angular correlation is also more accurately predicted by the calculations (see below).

The internal pair formation coefficients, energy and angular distributions and total conversion coefficients, have been calculated for arbitrary multipole fields. The Born approximation is used. An estimate of the error thereby induced may be made by comparing with the results of Jäger and Hulme[2] for $Z=84$. For k as low as 6 the total pair formation coefficient is too large by 20 percent for the electric quadrupole and by 15 percent for the electric dipole. Since we are interested in much smaller Z and k at least as large as the above quoted value the Born approximation should be sufficiently accurate. It should be emphasized, however, that the Born approximation is most accurate for the "integral" features of the pair formation process in which an integration over the energy distribution of the pairs has been carried out. The effect of the Coulomb field is to suppress the number of slow positrons and increase the number of fast ones and upon integration over the energy spectrum these two effects largely cancel out.[2]

In the following we use the system of units with $\hbar=c=m=1$. The energy (including rest energy) and momentum of the particles is $W_\pm$ and $\mathbf{p}_\pm$ respectively where throughout the indices $+$ and $-$ refer to positron and electron respectively. The radiation field is represented by scalar V and vector potentials $\mathbf{A}$ with the following gauge: for the electric 2^l multipole field

$$\mathbf{A}_{lm}=(2/\pi l(l+1))^{\frac{1}{2}}\chi_{l-1}(kr)(r\,\mathrm{grad}+l\mathbf{r}/r)Y_l^m, \quad (1a)$$

$$V=i(2l/\pi(l+1))^{\frac{1}{2}}\chi_l(kr)Y_l^m, \quad (1b)$$

where χ_l is the spherical Hankel function of the first kind

$$\chi_l(x)=(\pi/2x)^{\frac{1}{2}}H_{l+\frac{1}{2}}^{(1)}(x), \quad (1c)$$

and Y_l^m is a normalized spherical harmonic. For the magnetic 2^l multipole field

$$\mathbf{A}_{lm}=-(2/\pi l(l+1))^{\frac{1}{2}}\chi_l(kr)i\mathbf{r}\times\mathrm{grad}Y_l^m, \quad (1d)$$

$$V=0. \quad (1e)$$

With this normalization the number of quanta per second is

$$N_q=1/\pi^2k. \quad (2)$$

Then the ratio of the number of pairs per second with electron and positron traveling in the solid angles $d\Omega_-$ and $d\Omega_+$ and the positron energy between W_+ and W_++dW_+ to the number of quanta per second is

$$d\gamma_l(W_+;\theta_+,\varphi_+;\theta_-,\varphi_-)=\frac{\alpha k}{32\pi^3}p_+p_-W_+W_-$$

$$\times\sum_{s_-s_+}|(\psi_-|V+\boldsymbol{\alpha}\cdot\mathbf{A}|\psi_+)|^2d\Omega_+d\Omega_-dW_+, \quad (3)$$

where α is the fine structure constant, $\boldsymbol{\alpha}$ the Dirac matrix vector and, as indicated, a summation over the spins of both particles is to be performed. In (3) $\theta_\pm$, $\varphi_\pm$ are the polar and azimuth angles of the particles. The wave functions of the particles are

$$\psi_\pm=u_\pm(\mathbf{p}_\pm)\exp(\pm i\mathbf{p}_\pm\cdot\mathbf{r}), \quad (4)$$

where the $u_\pm(\mathbf{p}_\pm)$ are the Dirac spinor amplitudes for a plane wave.

The spin summations are most easily carried out by introducing operators $G_\pm$ defined by

$$\begin{aligned} G_\pm u_\pm&=u_\pm \quad \text{for} \quad W_\pm>0 \\ &=0 \quad \text{for} \quad W_\pm<0, \end{aligned} \quad (5)$$

and summing over the four states, i.e., two spin states and $W_\pm\gtrless 0$.

$$G_\pm=(-\boldsymbol{\alpha}\cdot\mathbf{p}_\pm\mp\beta+W_\pm)/2W_\pm,$$

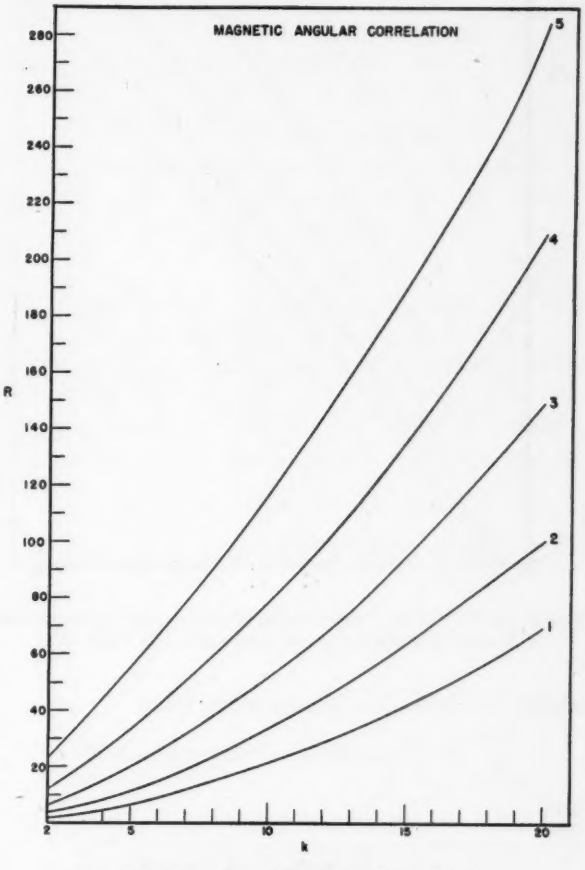

FIG. 2. Same as Fig. 1 for magnetic multipoles.

[4] G. K. Horton, Proc. Phys. Soc. London **60**, 457 (1948). The angular correlation is given for the electric dipole, quadrupole and magnetic dipole for particular division of the total energy between electron and positron. See also, M. E. Rose and G. E. Uhlenbeck, reference 2.

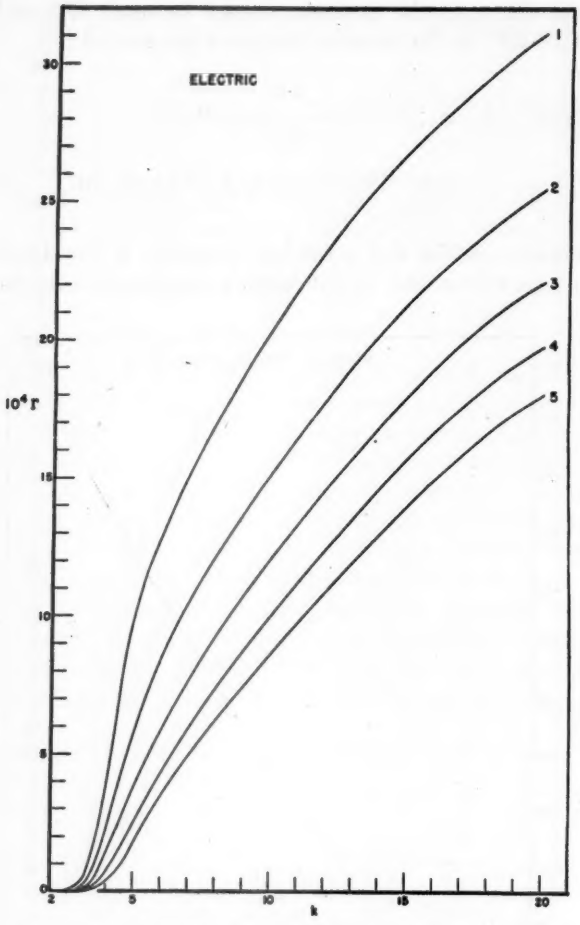

FIG. 3. Total number of pairs per quantum for electric multipoles. The numbers affixed to the curves give the value of l.

where β is the fourth Dirac matrix. Then

$$\sum_{s_+s_-} |(\psi_-|V+\boldsymbol{\alpha}\cdot\mathbf{A}|\psi_+)|^2=\text{Spur}\,(\Lambda G_+\Lambda^+G_-),$$

and

$$\Lambda=\boldsymbol{\alpha}\cdot\int e^{i\mathbf{q}\cdot\mathbf{r}}\mathbf{A}d\tau+\int e^{i\mathbf{q}\cdot\mathbf{r}}Vd\tau,$$

with $\mathbf{q}=\mathbf{p}_++\mathbf{p}_-$ and $d\tau$ is the volume element.

In order to obtain the angular distribution integrations over the two solid angle elements are performed with the subsidiary condition that Θ, the angle between electron and positron, is fixed. This is readily carried out by integrating first over the dihedral angle δ formed by the planes $(\mathbf{z},\mathbf{q})$ and $(\mathbf{p}_+,\mathbf{q})$ where $\mathbf{z}$ is a vector in the direction of the axis of quantization. Here it is useful to use

$$\sin\theta_+e^{\pm i\varphi_+}=e^{\pm i\phi}(\cos\omega_+\sin\theta - \sin\omega_+\cos\theta\cos\delta\mp i\sin\omega_+\sin\delta),$$
$$\cos\theta_+=\cos\omega_+\cos\theta+\sin\omega_+\sin\theta\cos\delta,$$

where ω_+ is the angle between $\mathbf{p}_+$ and $\mathbf{q}$, θ, ϕ the polar and azimuth angles of $\mathbf{q}$; and similar relations for the components of the unit vector in the direction $\mathbf{p}_-$ in which ω_+ is replaced by $\omega_-=\Theta-\omega_+$ and δ by $\pi-\delta$.

After the δ-integration, one integrates over the directions of $\mathbf{q}$ ($d\Omega_+d\Omega_-=\sin\theta d\theta d\phi d\delta\sin\Theta d\Theta$) and, as is to be expected, the result is independent of m. Hence, one obtains the angular distribution giving the number of pairs per unit energy interval, per $|d\cos\Theta|$, per quantum, the energies $W_\pm$ being fixed:

$$\gamma_l(\Theta)=\int(d\gamma_l/d\Omega_+d\Omega_-dW_+)\sin\theta d\theta d\phi d\delta. \quad (6)$$

For electric multipoles

$$\gamma_l(\Theta)=(2\alpha/\pi(l+1))(p_+p_-/q)\frac{(q/k)^{2l-1}}{(k^2-q^2)^2}$$
$$\times\{(2l+1)(W_+W_-+1-\tfrac{1}{3}p_+p_-\cos\Theta)$$
$$+l[(q^2/k^2)-2](W_+W_-1+p_+p_-\cos\Theta)$$
$$+\tfrac{1}{3}(l-1)p_+p_-[(3/q^2)(p_-+p_+\cos\Theta)$$
$$\times(p_++p_-\cos\Theta)-\cos\Theta]\}. \quad (7)$$

For magnetic multipoles

$$\gamma_l(\Theta)=(2\alpha/\pi)(p_+p_-/q)\frac{(q/k)^{2l+1}}{(k^2-q^2)^2}\left\{1+W_+W_- -\frac{p_+p_-}{q^2}(p_-+p_+\cos\Theta)(p_++p_-\cos\Theta)\right\}, \quad (8)$$

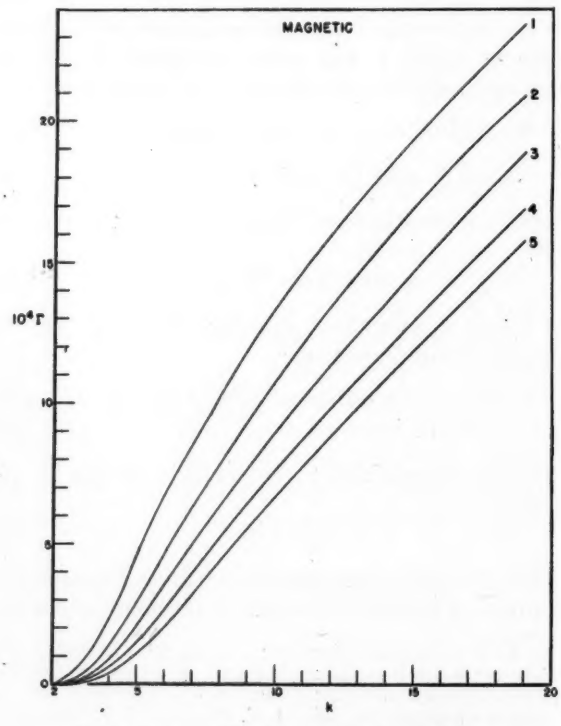

FIG. 4. Same as Fig. 3 for magnetic multipoles.

the angular distribution is, of course, peaked in the forward direction ($\Theta=0$) and the more strongly so the greater the multipole order.

As a convenient index of the angular correlation one may measure the ratio of the electron-positron coincidence rates at $\Theta=0$ and $\pi/2$; since $\gamma_l(\Theta)$ depends only on $\cos\Theta$ it would be permissible to make observations at some small angle instead of at $\Theta=0$. The coincidence rate ratio[5] is then given by

$$R=\int_1^{k-1} dW_+\gamma_l(0)\Big/\int_1^{k-1} dW_+\gamma_l(\pi/2). \quad (9)$$

From (8) $\gamma_l(0)$ and $\gamma_l(\pi/2)$ are easily evaluated and the results for the angular correlation are shown in Fig. 1 for the electric multipoles and in Fig. 2 for the magnetic multipoles.

To obtain the total pair formation coefficients we first integrate (7) and (8) over Θ to obtain the energy distribution

$$\Gamma_l(W_+)=\int_0^{\pi} \gamma_l(\Theta)\sin\Theta d\Theta. \quad (10)$$

For electric multipoles

$$\begin{aligned}\Gamma_l(W_+)=(\alpha/\pi(l+1)k^3)\{&(l/2)k^2J_{l+1}\\&+[2lW_+W_--\tfrac{1}{4}(7l+1)k^2]J_l\\&+[l(W_+^2+W_-^2+1)+1-W_+W_-]J_{l-1}\\&-\tfrac{1}{4}(l-1)(W_+-W_-)^2J_{l-2}\},\end{aligned} \quad (10a)$$

and for magnetic multipoles

$$\begin{aligned}\Gamma_l(W_+)=\alpha/\pi k^3\{&(1+W_+W_-)J_l\\&-(k^2/4)(J_{l+1}-x_1x_2J_{l-1})\},\end{aligned} \quad (10b)$$

where the J_l are the elementary integrals[6]

$$J_l=\int_{x_1}^{x_2} x^l(1-x)^{-2}dx,$$

$$x_1=(p_+-p_-)^2/k^2, \quad x_2=(p_++p_-)^2/k^2.$$

The total pair formation coefficient is then given by

$$\Gamma_l=\int_1^{k-1} dW_+\Gamma_l(W_+).$$

The results for $l=1\cdots5$ are shown in Figs. 3 and 4 for the electric and magnetic multipoles, respectively.

The author is indebted to Mrs. M. K. Hullings of the Computing Panel of Oak Ridge National Laboratory for able assistance in carrying out the numerical work.

[5] Although the ratio of coincidence rates at 0 and π is even more sensitive to l, the number of pairs at $\Theta=\pi$ is very small and would be more difficult to measure.

[6] These are most readily evaluated by using the recurrence formula

$$J_{l+2}-2J_{l+1}+J_l=(x_2^{l+1}-x_1^{l+1})/(l+1),$$

and

$$J_0=p_+p_-, \quad J_1=p_+p_--2\log(1+W_+W_-+p_+p_-)/k.$$

Letters to the Editor

PUBLICATION of brief reports of important discoveries in physics may be secured by addressing them to this department. The closing date for this department is five weeks prior to the date of issue. No proof will be sent to the authors. The Board of Editors does not hold itself responsible for the opinions expressed by the correspondents. Communications should not exceed 600 words in length.

Theory of the Angular Distribution of Photo-Neutrons from Be^9

C. J. MULLIN AND E. GUTH
University of Notre Dame, Notre Dame, Indiana
June 8, 1949

THE simple theory[1] of the photo-disintegration of Be^9 which was adequate for the interpretation of the empirical total cross section *versus* γ-ray energy data,[2] may be used to interpret the data recently obtained on the angular distribution of the photo-neutrons from Be^9. The prospective (loosely bound) photo-neutron is assumed to move in the "effective field" (non-tensor) of the remainder of the nucleus (Be^8). The disintegration process at low energies results from electric dipole transitions from the ground $^2P_{3/2}$ state to S and D states of positive energy. These transitions lead to an angular distribution

$$d\sigma/d\Omega = a + b\sin^2\theta, \tag{1}$$

for the ejected neutrons. a and b are functions of the γ-ray energy and may be expressed in terms of the cross sections for the $P\rightarrow S$ and $P\rightarrow D$ transitions. Values of a/b have been obtained for the following three cases:

(1) The ground state is a $^2P_{3/2}$ state. The $^2D_{5/2}-{}^2D_{3/2}$ splitting of the unbound D doublets may be neglected. Then

$$a/b = (17/12)+(25/12)(\sigma_{PS}/\sigma_{PD}), \tag{2}$$

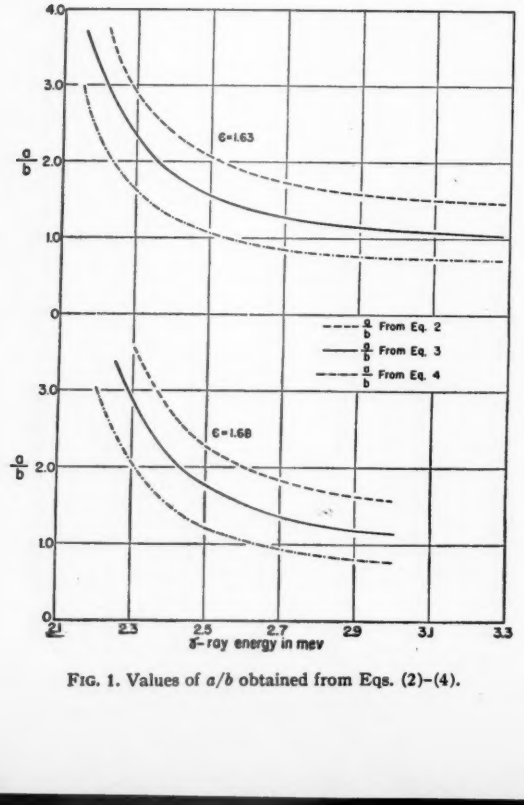

FIG. 1. Values of a/b obtained from Eqs. (2)–(4).

where σ_{PS} is the cross section for the $P_{3/2}\rightarrow S_{1/2}$ transition, and σ_{PD} is the cross section for the $P_{3/2}\rightarrow D_{5/2,3/2}$ transition.

(2) The $D_{5/2}-D_{3/2}$ splitting may not be neglected. For energies less than about 3 Mev, only one D component (the one of lower energy) participates in the transitions. Since the ^2P splitting seems to be inverted, it is reasonable to assume that the ^2D splitting also is inverted; thus the $D_{5/2}$ level should occur at a lower energy than the $D_{3/2}$ level. Using $P_{3/2}\rightarrow S_{1/2}$ and $P_{3/2}\rightarrow D_{5/2}$ transitions only,

$$a/b = 1+(5/3)(\sigma_{PS}/\sigma PD_{5/2}, \tag{3}$$

where $\sigma PD_{5/2}$ is the cross section for the $P_{3/2}\rightarrow D_{5/2}$ transition.

(3) The $P_{3/2}-P_{1/2}$ splitting of the bound P levels and the $D_{5/2}-D_{3/2}$ splitting of the unbound D levels may be neglected. Then

$$a/b = \tfrac{2}{3}[1+(2\sigma_{PS}/\sigma_{PD})]. \tag{4}$$

Some general conclusions may be drawn from Eqs. (2)–(4). Empirical data[2] indicate that the total cross section has a maximum at about $h\nu = 1.7$ Mev, a minimum at about 2.5 Mev, and a subsequent rise beyond 2.5 Mev. Thus for energies somewhat less than 2.5 Mev, $\sigma_{PS} \gg \sigma_{PD}$, and the angular distribution should be spherically symmetrical. For γ-ray energies $\gtrsim 2.5$ Mev, the angular distribution should deviate markedly from spherical symmetry.

Quite recently the angular distribution of the photo-neutrons was measured[3,4] for γ-ray energies of 1.70, 1.81, and 2.76 Mev. The distribution was found to be spherically symmetrical for the 1.70 and 1.81 Mev γ-rays. At 2.76 Mev, Hamermesh, Hamermesh, and Wattenberg obtained $a/b = 1.22$, and Meiners obtained $a/b = 1.15 \pm 0.07$. The experimental values of a/b at 2.76 Mev are consistent with Eq. (3) but do not agree with the results predicted by Eqs. (2) or (4). Equation (2) gives a lower limit of $17/12 \cong 1.4$ for a/b. Since $\sigma_{PS} \ll \sigma_{PD}$ at 2.76 Mev, Eq. (4) predicts a value of a/b which is considerably smaller than the observed value.

In order to obtain numerical values for a/b from Eqs. (2)–(4), σ_{PS}, σ_{PD}, and $\sigma PD_{5/2}$ have been calculated for a nuclear model in which the interaction between the loosely bound neutron and the remainder of the nucleus is represented by a potential well of radius 5×10^{-13} cm. The well depth for S and D states was taken as 3.0 Mev. These parameters were chosen so that the theoretical total cross section *versus* γ-ray energy curve agrees with the experimental one.[5] The well depth for the ground P state was chosen so that the photo-disintegration threshold energy has the correct value. Since there is considerable uncertainty about the value of the threshold energy, two limiting values for this energy, namely, $\epsilon = 1.63$ Mev and $\epsilon = 1.68$ Mev, were used in the calculations. The calculated values for the cross sections have been used to evaluate a/b from Eqs. (1)–(4). The results are shown in Fig. 1. It may be seen that Eq. (3), which is based upon the assumption that the disintegration results from $P_{3/2}\rightarrow S_{1/2}$ and $P_{3/2}\rightarrow D_{5/2}$ transitions, leads to a value for a/b which is in excellent agreement with the empirical results at 2.76 Mev.

An experiment in which γ-rays obtained from the Van de Graaff generator are to be used to determine the angular distribution of the photo-neutrons from Be^9 over an energy interval extending from the threshold energy up to about 3 Mev is underway at Notre Dame.

[1] E. Guth and C. J. Mullin, Phys. Rev. **74**, 833 (1948); Phys. Rev. **76**, 234 (1949).
[2] Russell, Sachs, Wattenberg, and Fields, Phys. Rev. **73**, 545 (1948).
[3] Hamermesh, Hamermesh, and Wattenberg, Phys. Rev. **76**, 611 (1949).
[4] E. Meiners, Private communication; see also Meiners, Smith, and Slack, Phys. Rev. **75**, 1632 (1949).
[5] Actually, the results obtained for the cross section depend chiefly upon the location of the energy levels of the S, P, and D interactions. If these levels are held fixed, the cross sections are rather insensitive to reasonable changes in the well radius or depth. Furthermore, it may be shown for the two body model that the cross section for photo-disintegration at low energies does not depend upon the shape of the effective potential but only upon two parameters: the effective range and the scattering length. The Be^9 problem obviously is very similar to the problems of $N-P$ scattering and photo-disintegration of the deuteron in this respect (J. Blatt and J. D. Jackson, Phys. Rev. **76**, 18 (1949); H. A. Bethe, Phys. Rev. **76**, 38 (1949)).

Double Scattering of Protons in Helium

D. C. Dodder
University of Minnesota, Minneapolis, Minnesota
July 22, 1949

THE phase-shift analysis[1] of the recent Minnesota proton-alpha-scattering experiments[2] reduces the data to three parameters, an s-wave phase shift and two p-wave phase shifts for partial waves of total angular momentum $\frac{1}{2}\hbar$ and $3\hbar/2$. The knowledge of the differential cross section as a function of angle is not sufficient, however, to remove an ambiguity which results in a case of the p-wave phase shifts. The two sets of p-wave phase shifts which satisfy the data correspond to normal and inverted p-doublets in the Li^5 nucleus. For each set, however, the two phase shifts pass through 90° at considerably different energies, so that there is a large range of energies over which the scattered protons are partially polarized. The polarizations at a scattering angle of 90° in the center of mass coordinate system corresponding to the two possible doublets are given as functions of energy in reference 1. Recently Wolfenstein[3] has discussed the possibility of the detection of such scattered polarized protons by means of a second scattering, as had been proposed for the similar case of neutrons and helium by Schwinger.[4] In order to determine the feasibility of performing the experiment of the double scattering with protons, the angular distribution of yield from the second scattering again at 90° in the center of mass system has been calculated as a function of energy for each of the possible doublets.

The amplitudes of scattered waves arising from a single scattering expressed in terms of eigenfunctions of spin-component in the direction of the initial beam may be re-expressed in terms of eigenfunctions of spin-component in the direction of the secondary beam. These amplitudes can now be considered as the amplitudes of plane waves moving in the direction of the secondary beam. They will then be refracted in the same fashion in the second scattering. The final intensity will be the average of the intensities of the waves corresponding to the two initial spin directions.

The final intensity can be written:

$$I=\frac{1}{k^2\bar{k}^2}\{|a\bar{a}|^2+|b\bar{a}|^2+|a\bar{b}|^2+|b\bar{b}|^2+\cos\Phi(\bar{b}^*\bar{a}-\bar{a}^*\bar{b})(b^*a-a^*b)\}$$

where

$$|a|^2=(\tfrac{1}{2}\sin2\delta_0-\eta\cos\eta\ln2)^2+(\sin^2\delta_0-\eta\sin\eta\ln2)^2$$
$$|b|^2=\sin^2(\delta_1^--\delta_1^+)$$
$$b^*a-a^*b=2i\sin(\delta_1^--\delta_1^+)\{\sin\delta_0\sin(\delta_0-\phi_1-\delta_1^+-\delta_1^-)-\eta\sin(\eta\ln2-\phi_1-\delta_1^+-\delta_1^-)\}$$

and where barred quantities are evaluated at the energy, in the laboratory system, of the protons in the secondary beam. Φ is the azimuthal angle about the secondary beam measured from the direction of the initial beam. Other notation is the same as in reference 1.

The product of the differential cross section of the two scatterings in the laboratory system may be written $M+N\cos\Phi$. If M and N are measured in square barns and E is the laboratory energy in Mev of the initial protons in the laboratory system, the results are as given in Table I.

It is seen that, as expected, a measurement of the asymmetry as a function of energy would conclusively decide which doublet exists. Indeed a single measurement at $E=2.8$ Mev would be decisive since for the normal doublet the scattered protons are almost entirely in the direction of the initial beam, while in the inverted doublet they are predominantly in the opposite direction.

Because of the low cross sections the intensity from the double scattering will not be high, but by using a large initial beam, large solid angles, and a high target density a reasonable yield seems feasible. At the 2.8 Mev energy, assuming original current 5 microamperes, solid angles of 0.05 steradians, target density corresponding to a pressure of 1 atmosphere, and effective length of each scattering volume of 1 cm, one obtains a yield of 1.2 scattered proton/sec. This value would seem to indicate that the measurement of the polarization effect by means of the double scattering might be quite possible. Instrumentation for performing the experiment is now under way in the University of Minnesota laboratory.

TABLE I. Angular dependence of products of cross sections for double scattering.

E	1.6	2.0	2.4	2.8	3.2
M	0.008	0.012	0.016	0.021	0.025
			Normal Doublet		
N	−0.001	−0.0055	0.001	0.017	0.011
			Inverted Doublet		
N	−0.001	−0.006	−0.011	−0.011	−0.007

The author wishes to thank Professor C. L. Critchfield for many helpful discussions. The work was supported by the ONR.

[1] C. L. Critchfield and D. C. Dodder, Phys. Rev. 76, 419 (1949).
[2] G. Freier, E. Lampi, W. W. Sleator, Jr., and J. H. Williams, Phys. Rev. 75, 1345 (1949).
[3] L. Wolfenstein, Phys. Rev. 75, 1664 (1949).
[4] J. Schwinger, Phys. Rev. 69, 681 (1946).

A Lower Limit for the Binding Energy of the Deuteron

G. R. Bishop, C. H. Collie, H. Halban, and R. Wilson
The Clarendon Laboratory, Oxford, England
July 12, 1949

A SUMMARY of previous determinations of the binding energy of the deuteron has been given by Stevens[1] who found an average value of $-Q_\gamma=2.187\pm0.011$ Mev. However, recent measurements[2,3] give $-Q_\gamma=2.237\pm0.005$ Mev, in closer agreement with earlier observations.[4,5] A lower limit can be placed upon Q_γ by making measurements on the photo-disintegration of deuterium by the γ-rays from radio-gallium, Ga^{72}, which emits two lines in good intensities with energies of 2.21 Mev, and 2.51 Mev, as well as lower energy lines.[6]

Since the 2.21-Mev line lies between the two values of Q_γ which are in question, it is of interest to observe whether it can produce photo-neutrons from deuterium. If it does, then $-Q_\gamma$ must lie below 2.21 Mev.

This has been investigated by comparing the photo-disintegration produced in deuterium by the γ-rays of radio-gallium and radio-thorium. This can be done in two ways, by measuring either the photo-protons or the photo-neutrons produced. The first is to use an ionization chamber filled with deuterium gas,[7] for which the discriminator bias is chosen to count the photo-protons produced by the 2.51-Mev line of Ga^{72} and the 2.62-Mev line of RdTh, but none of lower energy that may be produced by the 2.21-Mev line of Ga^{72}. The second is to measure the ratio of the rates of production of photo-neutrons by these sources in a sphere of heavy water, by the well-known method of integrating the slow neutron density in a water tank with manganese as detector. This method detects all photo-neutrons independently of their energy, and, in particular, if the 2.21-Mev γ-line of Ga^{72} produces photo-disintegration, the photo-neutron ratio will differ from the photo-proton ratio observed in the ionization chamber.

The radio-thorium source used was a 200-mc standard, enclosed in a platinum cylinder 5 mm in length and 5 mm diameter. The gallium source was a sphere 15 mm in diameter of a gallium-nickel alloy. The alloy contained 12 percent of nickel and remained hard up to 100°C. This was used in preference to pure gallium which melts at 30°C. The source was enclosed in a copper sphere and irradiated with neutrons in the pile at the Atomic Energy Research Establishment at Harwell. The total activity for a long irradiation was 0.6C.

TABLE I.

Ratio: $\frac{\text{RdTh neutrons}}{\text{Ga neutrons}}$	Ratio: $\frac{\text{RdTh protons}}{\text{Ga protons}}$	Ratio: $\frac{\text{Photo-proton ratio}}{\text{Photo-neutron ratio}}$
0.96 ± 0.05	0.98 ± 0.04	1.02 ± 0.08
1.41 ± 0.04	1.43 ± 0.04	$1.01_4 \pm 0.06$

For the photo-proton ratio, the number of counts from the ionization chamber was recorded at the same discriminator bias voltage for each source. A correction for "wall effect" in the chamber has to be considered. If the range of a proton were proportional to its energy, a constant fraction of the photo-protons would be unrecorded. As it is not, the wall effect corrections for the two sets of photo-protons (estimated to be 150 kv and 210 kv) are different. It is possible to adjust the deuterium pressure ($2\frac{1}{2}$ atmos.) so that the total correction is only 10 percent, in which case the uncertainty in the ratio of counts is unlikely to exceed 1 percent.

To integrate the photo-neutron flux, the sources were placed at the center of a sphere of heavy water of 8-cm radius, contained in a thin copper vessel. This was suspended at the center of a cylindrical tank, 60 cm in diameter and 60 cm deep, containing an aqueous solution of $MnSO_4$. After irradiation for a known time, the whole solution was well mixed by a circulating pump and the mean activity determined in an aliquot fraction with a pair of thin glass-walled immersion type Geiger-Müller counters.

Results of two series of measurements are shown in Table I. Clearly the low energy γ-quanta from gallium are not producing many photo-neutrons.

By combining the experimental value[6] of the ratio

$$\frac{\text{2.51-Mev quanta}}{\text{2.21-Mev quanta}}$$

with the theoretical variation in cross section for the photo-disintegration of deuterium near the threshold,[8,9] one can calculate the expected value of the ratio we have measured for any value of Q_γ. For $-Q_\gamma = 2.185$ Mev the value of the ratio would be 1:65; if, as an extreme case, one supposes our results are consistent with a value of 1:1 for the ratio, then Q_γ and the quantum energy of the Ga^{72} γ-ray cannot differ by more than 3 kev, and therefore the binding energy of the deuteron cannot be less than 2.207 Mev.

[1] W. E. Stephens, Rev. Mod. Phys. 19, 19 (1947).
[2] R. E. Bell and L. G. Elliott, Phys. Rev. 74, 1552 (1948).
[3] R. F. Taschek, Phys. Rev. 75, 1268 (1949).
[4] H. Halban, Comptes Rendus 206, 1170 (1938).
[5] R. D. O'Neal, Phys. Rev. 70, 1 (1946).
[6] S. K. Haynes, Phys. Rev. 74, 423 (1948).
[7] Wilson, Collie, and Halban, Nature 163, 245 (1949).
[8] L. Rosenfeld, *Nuclear forces* (North Holland Publishing Company, Amsterdam), p. 178.
[9] L. Hulthén and A. Pais, Cambridge Conference (1946), p. 177.

The Magnetic Moments of Sn^{117}, Sn^{119}, and Pb^{207}*

W. G. PROCTOR
Department of Physics, Stanford University, Stanford, California
July 18, 1949

USING the nuclear induction spectrometer described in a previous letter,[1] the magnetic moments of the nuclei Sn^{117}, Sn^{119}, and Pb^{207} have been remeasured. The results are in good agreement with those from hyperfine structure measurements through which they were previously known, and which indicated for both tin nuclei a spin of $\frac{1}{2}$[2] and a magnetic moment of -0.89 nuclear magneton,[3] and for the nucleus Pb^{207} a spin $\frac{1}{2}$[4] and a magnetic moment of $+0.6$ nuclear magneton.[5]

The tin resonances were observed in the neighborhood of 7 MC, with a magnetic field near 4500 gauss, using a sample consisting of an aqueous solution of 5.3 molar $SnCl_2$ with 1.0 molar $MnCl_2$. These frequencies were compared to that of the resonance of Na^{23} when the above sample was replaced with one consisting of an aqueous solution of 0.69 molar NaCl with 1.0 molar $MnCl_2$. The resonances of Sn^{117}, Sn^{119}, and Na^{23} were observed in that order until six of each had been recorded. After correcting for magnetic field drifts, the ratios of the resonant frequencies in the same field were found to be

$$\nu(Sn^{117})/\nu(Na^{23}) = 1.3464 \pm 0.0004,$$
$$\nu(Sn^{119})/\nu(Na^{23}) = 1.4090 \pm 0.0005,$$
$$\nu(Sn^{119})/\nu(Sn^{117}) = 1.0465 \pm 0.0003.$$

Making a correction for electronic diamagnetism,[6] which here has been assigned an error of 15 percent, and taking $\frac{1}{2}$ for the spin and $+2.217 \pm 0.002$ nuclear magnetons for the magnetic moment of Na^{23},[7] one obtains

$$\mu(Sn^{117}) = -(1.000 \pm 0.001)\mu_N,$$
$$\mu(Sn^{119}) = -(1.047 \pm 0.001)\mu_N.$$

The ratio of this magnetic moments is, of course, given by the ratio of their resonant frequencies. Sn^{117} and Sn^{119} have respectively a natural abundance of 9.1 percent and 9.8 percent,[8] or a ratio of abundance of 0.93; the relative signal amplitudes, when a correction for their different gyromagnetic ratios is made, was 0.86 ± 0.12, which served to identify the isotopes. By comparing the recorded tin signals with the Na^{23} signals, the sign of the magnetic moments of both tin nuclei was seen to be negative, and the signal amplitudes were consistent with spin $\frac{1}{2}$.

Using as a sample an aqueous solution of 1.0 molar $Pb(C_2H_3O_2)_2$ and 0.8 molar $Mn(C_2H_3O_2)_2$, the frequency of the lead resonance which occurred near 5.8 MC at 6600 gauss was repeatedly compared with that of the Na^{23} resonance from the sodium sample above. A resonance frequency ratio of

$$\nu(Pb^{207})/\nu(Na^{23}) = 0.7901 \pm 0.0002$$

was found which leads, in analogy to the above results from the magnetic moments of the tin nuclei, to

$$\mu(Pb^{207}) = +(0.588 \pm 0.001)\mu_N.$$

The sign of the magnetic moment was found to be positive, and the signal amplitudes indicate a spin of $\frac{1}{2}$.

The author wishes to express his appreciation for the frequent and helpful advice of Professor Felix Bloch during the period of these measurements.

* Assisted by the Joint Program of the ONR and the AEC.
[1] W. G. Proctor, Phys. Rev. 75, 522 (1949).
[2] H. Schüler and H. Westmeyer, Naturwiss. 21, 660 (1933).
[3] S. Tolansky, Proc. Roy. Soc. London 144, 574 (1934).
[4] H. Kopfermann, Zeits. f. Physik 75, 363 (1932).
[5] H. A. Bethe and R. F. Bacher, Rev. Mod. Phys. 8, 82 (1936).
[6] W. E. Lamb, Jr., Phys. Rev. 60, 817 (1941).
[7] J. B. M. Kellogg and S. Millman, Rev. Mod. Phys. 18, 323 (1946).
[8] F. W. Aston, Nature 137, 613 (1936).

The Application of Dyson's Methods to Meson Interactions

P. T. MATTHEWS
Clare College, Cambridge, England
June 13, 1949

BY developing a combination of the electrodynamic theories of Schwinger[1] and Feynman,[2] Dyson[3] has given comparatively simple rules whereby the matrix element of the Hamiltonian for an effect such as the Lamb-Retherford shift[4] can be written down directly in terms of invariant functions $D_F(x)$ and $S_F(x)$.

It will be shown here that this technique can be applied even to the more general meson interactions containing derivatives of the field variables which lead to Hamiltonians in the interaction representation which depend explicitly on the direction of the general space-like surfaces.

When there is no external field, the S-matrix can be expressed in the form (reference 3, Section III, Eq. (32))

$$U(\infty)=\sum_{n=0}^{\infty}U_n(\infty)=\sum_{n=0}^{\infty}(-i/\hbar c)^n[1/n!]\int_{-\infty}^{\infty}dx_1\cdots \times\int_{-\infty}^{\infty}dx_n P(H(x_1),\cdots,H(x_n)). \quad (1)$$

As an example the vector interaction of neutral scalar mesons with nucleons will be considered. The Hamiltonian is[5]

$$H(x)=(1/c\kappa)j_\mu(x)\partial\phi(x)/\partial x_\mu+(1/2c^2\kappa^2)(j_\mu(x)n_\mu(x))^2, \quad (2)$$

where $j_\mu(x)=ig\bar{\psi}(x)\gamma_\mu\psi(x)$ and $n_\mu(x)$ is the normal to a one-parameter family of space-like surfaces $\sigma(x)$.

Now

$$[\phi(x),\phi(x')]=i\hbar c\Delta(x-x') \quad (3)$$

and

$$\langle\{\phi(x),\phi(x')\}\rangle_0=\hbar c\Delta^{(1)}(x-x'). \quad (4)$$

Also, in the "natural" coordinate system (with time axis in the direction $n_\mu(x)$), $\partial\Delta(x)/\partial x_4=i\delta(x_1)\delta(x_2)\delta(x_3)$. And for the function $\epsilon(x)$ defined by Schwinger,[1] $\partial\epsilon(x)/\partial x_4=-2i\delta(x_0)$. Hence

$$j_\mu(x)j_\nu(x')\langle P(\partial\phi(x)/\partial x_\mu,\partial\phi(x')/\partial x_\nu')\rangle_0 =\tfrac{1}{2}\hbar c j_\mu(x)j_\nu(x')\left(\frac{\partial^2}{\partial x_\mu\partial x_\nu'}\Delta^{(1)}(x-x')+i\epsilon(x-x')\frac{\partial^2}{\partial x_\mu\partial x_\nu'}\Delta(x-x')\right).$$

The factor $\epsilon(x-x')$ can be taken under the differential sign and the additional terms subtracted explicitly. These can be evaluated in the "natural" coordinate system and then expressed in general coordinates, giving

$$j_\mu(x)j_\nu(x')\langle P(\partial\phi(x)/\partial x_\mu,\partial\varphi(x')/\partial x_\nu')\rangle_0 =\tfrac{1}{2}\hbar c j_\mu(x)j_\nu(x')(\partial^2/\partial x_\mu\partial x_\nu')\Delta_F(x-x') +(\hbar c/i)(j_\mu(x)n_\mu)(j_\nu(x')n_\nu')\delta_4(x-x').$$

The terms of order g^n in $U_n(\infty)$ are

$$\left(\frac{-i}{\hbar c^2\kappa}\right)^n\frac{1}{n!}\int_{-\infty}^{\infty}dx_1\cdots\int_{-\infty}^{\infty}dx_n P\left(j_\mu(x_1)\frac{\partial\varphi}{\partial x_{1,\mu}},\cdots,j_\nu(x_n)\frac{\partial\phi}{\partial x_{n,\nu}}\right). \quad (5)$$

The matrix element for an effect in which there are $n-2$ free mesons will have one pair of meson operators combining to give a vacuum effect. This pair can be chosen in $n(n-1)/2$ ways and the term is thus

$$\begin{aligned}&\frac{1}{2}\left(\frac{-i}{\hbar c^2\kappa}\right)^n\frac{1}{(n-2)!}\int dx_1\cdots\int dx_n P\left(j_\mu(x_1)\frac{\partial\phi}{\partial x_{1,\mu}},\cdots,\right.\\ &\left.j_\nu(x_{n-2})\frac{\partial\phi}{\partial x_{n-2,\nu}},j_\rho(x_{n-1}),j_\pi(x_n)\left\langle P\left(\frac{\partial\phi}{\partial x_{n-1,\rho}},\frac{\partial\phi}{\partial x_{n,\pi}}\right)\right\rangle_0\right.\\ =&\frac{1}{2}\left(\frac{-i}{\hbar c^2\kappa}\right)^n\frac{1}{(n-2)!}\left\{\int dx_1\cdots\int dx_n P\left(j_\mu(x_1)\frac{d\varphi}{\partial x_{1,\mu}}\right),\cdots,\right.\\ &j_\nu(x_{n-2})\frac{\partial\varphi}{\partial x_{n-2,\nu}},j_\rho(x_{n-1}),j_\pi(x_n)\frac{1}{2}\hbar c\frac{\partial^2}{\partial x_{n-1,\rho}\partial x_{n,\pi}}\Delta_F(x_{n-1}-x_n)\\ &+\frac{\hbar c}{i}\int dx_1\cdots\int dx_{n-1}P\left(j_\mu(x_1)\frac{\partial\varphi}{\partial x_{1,\mu}}\right),\cdots,\\ &\left.j_\nu(x_{n-2})\frac{\partial\phi}{\partial x_{n-2,\nu}},(j_\rho(x_{n-1})n_\rho(x_{n-1}))^2\right\}. \quad (6)\end{aligned}$$

The only other contribution to this element of this order is from $U_{n-1}(\infty)$. By a similar argument this can be shown to be just the term required to cancel the n_μ-dependent part of (6), leaving an invariant expression independent of the surface σ. For an effect involving $n-4$ free mesons there will be two terms dependent on n_μ from $U_n(\infty)$. These can be shown to cancel with similar terms from $U_{n-1}(\infty)$ and $U_{n-2}(\infty)$ leaving an invariant expression as before. A similar cancelation of the n_μ-dependent terms occurs for any effect and up to any order. The calculation of matrix elements is now no more complicated than in the electrodynamic case. The Hamiltonian can be taken to be

$$H(x)=(1/c\kappa)j_\mu(x)\partial\varphi(x)/\partial x_\mu \quad (7)$$

and effectively

$$\langle P(\partial\phi(x)/\partial x_\mu,\partial\phi(x')/\partial x_\nu')\rangle_0=\tfrac{1}{2}\hbar c(\partial^2/\partial x_\mu\partial_\nu')\Delta_F(x-x'). \quad (8)$$

Using these formulas, the graphical methods of Dyson[3] can be employed with only trivial changes. The Hamiltonian should of course contain two additional terms to allow for the renormalization of both the nucleon and the meson masses.

An exactly similar analysis is possible for all meson interactions with either nucleons or photons. Dyson[6] has shown that the particular case dealt with above leads to no physical effects. It serves here as a simple example of the formalism.

[1] J. Schwinger, Phys. Rev. **74**, 1492 (1948); **75**, 651 (1949).
[2] R. P. Feynman, Rev. Mod. Phys. **20**, 367 (1948); Phys. Rev. **74**, 939, 1430 (1948).
[3] F. J. Dyson, Phys. Rev. **75**, 486 (1949).
[4] W. E. Lamb and R. C. Retherford, Phys. Rev. **72**, 241 (1947).
[5] Y. Miyamoto, Prog. Theor. Phys. **3**, 124 (1948).
[6] F. J. Dyson, Phys. Rev. **73**, 929 (1948).

Electromagnetic Induction in a Superconductor

W. V. HOUSTON AND C. F. SQUIRE
Rice Institute, Houston, Texas
July 18, 1949

ACCORDING to London's formulation of the macroscopic equations for a superconductor, a negligible electromotive force should be induced in a figure of rotation turned about its axis in a magnetic field. The field should penetrate only a very small distance into the rotating body and the electromotive force induced by this penetrating field would be very small.

To test this conclusion a lead ellipsoid was turned about a vertical axis in a cryostat at speeds between 3000 and 9000 r.p.m. A vertical field of 30 to 70 gauss was produced by a solenoid, and sliding contacts enabled the induced electromotive force to be measured with a potentiometer. Above the transition temperature the observed electromotive force had the expected value with an uncertainty of less than 5 percent. This uncertainty was apparently due to thermal and other extraneous electromotive forces.

When the ellipsoid was superconducting, the induced electromotive force was definitely less than 5 percent of its value above the transition temperature. It may therefore be concluded that the description by London's equations, which suggests about 10^{-3} percent of the normal effect, is consistent with this experimental result.

Preliminary results already reported as showing the full induced electromotive force were in error.[1] The rotation of the ellipsoid apparently produced enough heat in the bearings and at the sliding contacts to destroy the superconductivity while a potentiometer setting was being made. This heat was developed in the rotating system and was neither evidenced in the thermometers, nor effectively absorbed by a neighboring bath of liquid helium. It was possible to reduce the rate of development of this heat by reducing the pressure on the sliding contacts and loosening the bearings. In this way the rotor could be kept superconducting for two to five minutes.

In the final measurements, the superconductivity was checked by means of a pick-up coil concentric with and close to the circumference of the rotor. The flux through this coil due to the applied field was measured by a ballistic galvanometer. It dropped to about one-third of its value when the rotor became superconducting. This value was quite consistent with complete exclusion of the field from the rotor, since there was some space between the pick-up coil and the rotor.

An attempt to use an a.c. method of measuring the flux through the pick-up coil brought to light a curious coincidence. The increasing conductivity of the lead, and the corresponding increase in eddy currents as the temperature was lowered, reduced the 60 cycle a.c. voltage induced in the pick-up coil just above the transition temperature to only 10 percent above its value just below the transition. This made the transition difficult to detect by use of a.c., although it was clearly marked in the d.c. ballistic measurement.

[1] W. V. Houston and C. F. Squire, Science **109**, 439 (1949); Wexler and Corak have just communicated to us results in agreement with our present observations.

The Microwave Spectra of CD_3Cl and CD_3I*

JAMES W. SIMMONS
Department of Physics, Emory University, Atlanta, Georgia
July 22, 1949

IN order to obtain further microwave data to make possible the complete solution of the structure of methyl chloride and methyl iodide, preliminary investigations have been made of the pure rotational transitions $J=0\rightarrow1$ for CD_3Cl and $J=1\rightarrow2$ for CD_3I using a single crystal detecting system.[1] The frequencies of the hypothetical, unsplit rotational lines, ν_0, for each transition and the resulting moments of inertia are given in Table I. The ratio of the intensities of the absorption lines for the transitions $K=0\rightarrow0$ and $K=1\rightarrow1$ in the spectrum of CD_3I has been found to agree well with that predicted by the theory of Dennison[2] when the spin of D is taken as one.

TABLE I. Pure rotational frequencies and molecular constants for the ground vibrational state.

Molecule	J Transition	ν_0 (mc/sec.)	I_B (10^{-40} g-cm^2)
$C^{12}D_3Cl^{35}$	$0\rightarrow1$	21688 ± 5	77.36_5
$C^{12}D_3Cl^{37}$	$0\rightarrow1$	21325 ± 5	78.68_8
$C^{12}D_3I^{127}$	$1\rightarrow2$	24162 ± 2	138.8_9

In Table II are given the molecular dimensions evaluated by combining the above data with that given by Gordy, Simmons, and Smith[3] in equations which follow from the geometry of the molecules. The results are seen to be in good agreement with the values in the earlier determination,[3] the trend in d_{CH} and $\angle$HCH being definitely established. It is felt, however, that the large value of $\angle$HCH obtained for CH_3I is not consistent with a d_{CH} equal to the methane distance, probably due to differences in the zero-point vibrational energies of CH_3I and CD_3I.

In the structure determinations it was assumed that the distances and angles in the ground vibrational state are the same for all isotope combinations. Since this is not strictly correct, the molecular dimensions are not exact solutions of the equations. In this case of methyl chloride the four equations for $C^{12}H_3Cl^{35}$, $C^{12}H_3Cl^{37}$, $C^{12}D_3Cl^{35}$, and $C^{12}D_3Cl^{37}$, respectively, are satisfied to better than 6 parts in 10^5 by the dimensions given in the table.** The methyl iodide dimensions satisfy the equations for $C^{12}H_3I^{127}$, $C^{13}H_3I^{127}$, and $C^{12}D_3I^{127}$ to about 12 parts in 10^5. In addition, use has been made of the I_A values of 5.52 for methyl chloride and 5.50 for methyl iodide as used by Gordy, Simmons, and Smith[3] in fixing the relative magnitudes of d_{CH} and $\angle$HCH. The availability of more accurate values of I_A would enable a closer determination of these two quantities.

TABLE II. Molecular dimensions of methyl chloride and methyl iodide.*

Molecule	d_{CX} (10^{-8} cm)	d_{CH} (10^{-8} cm)	$\angle$HCH
CH_3Cl	1.786_4	1.10_0	111° 24′
CH_3I	2.144_0	1.09_3	112° 3′

* The values of all physical constants used here have been taken the same as those of reference 3 with $M_D=2.01473$ as given by R. T. Birge, Rev. Mod. Phys. 13, 233 (1941).

Measurements are now being made of the spectra of $C^{13}H_3Br$ and $C^{12}D_3Br$ in order to determine more accurately the structure of the methyl bromide molecule.

I wish to thank Dr. Walter Gordy for helpful discussions and Mr. V. E. Pilcher who assisted in the construction of the microwave system.

* This work was supported by grants from the Research Corporation of New York and the University Center in Georgia. The deuterium compounds were obtained from the Texas Research Foundation on allocation from the Isotopes Division, U. S. Atomic Energy Commission.

** This agreement also holds for the equations of $C^{13}H_3Cl^{35}$ and $C^{13}H_3Cl^{37}$ resulting from the B_0 values just published by Dailey, Mays, and Townes, Phys. Rev. **76**, 137 (1949).

[1] W. Gordy and M. Kessler, Phys. Rev. **72**, 644 (1947); W. Gordy, Rev. Mod. Phys. **20**, 668 (1948).

[2] D. M. Dennison, Rev. Mod. Phys. **3**, 280 (1931); G. Herzberg, *Infrared and Raman Spectra of Polyatomic Molecules* (D. Van Nostrand Company, Inc., New York, 1945), p. 28.

[3] Gordy, Simmons, and Smith, Phys. Rev. **74**, 243 (1948).

Erratum: The Influence of the Length of a Hot Wire on the Measurements of Turbulence

[Phys. Rev. **75**, 1263 (1949)]

F. N. FRENKIEL
Naval Ordnance Laboratory, White Oak, Silver Spring, Maryland
July 22, 1949

IN the particular case when $R_x=\exp(-\pi x^2/4L_x^2)$ the factor $I_b=(L_x/l)erf\{[(\pi)^{\frac{1}{2}}/2]l/L_x\}$ [and not=1]. In this case $R_{b,x}=R_x$ and $\lambda/\lambda_{b,x}=1$ and no correction is necessary for the correlation coefficient.

The Excited State of Li^7 and the Angular Yield in $Li^6(d,p)Li^{7*}(\gamma)Li^7$

S. S. HANNA
Department of Physics, The Johns Hopkins University, Baltimore, Maryland
July 22, 1949

THE recent discussions[1-3] concerning the nature of the 480-kev excited state of Li^7 make it desirable to seek additional experimental evidence which will contribute to the interpretation. On the basis of the existing evidence it appears probable[3] that the state has $I=5/2$. Feld[4] has proposed the measurement of a possible angular correlation in successive $\alpha-\gamma$-emission in the $B^{10}(n,\alpha)Li^{7*}(\gamma)Li^7$ reaction as a means of testing the various assignments which have been proposed for the excited state. The most significant result is that a definite angular correlation of the form $1+A\cos^2\phi$ in this experiment would exclude the possibility of $I=\frac{1}{2}$ for the excited state, but would allow $I\geq\frac{3}{2}$.

In this $B^{10}(n,\alpha)Li^{7*}(\gamma)Li^7$ reaction, the incident thermal neutrons have $l=0$. As a result both the alpha-yield and the gamma-yield when measured independently of each other must be spherically symmetric. This is in contrast to the $Li^6(d,p)Li^{7*}(\gamma)Li^7$ reaction, in which the angular distribution of the protons has been measured[5] and found to be of the form $1+\alpha\cos\theta+\beta\cos^2\theta+\gamma\cos^3\theta+\delta\cos^4\theta$ at several deuteron energies between 400 and 900 kev. It follows from this that the angular yield function of the gammas

may include all terms up to and including $\cos^4\theta$ which are allowed by the multipole character of the radiation and by the spin of the excited state. Since the parity of the excited state is almost certainly the same as that of the ground state (odd), the radiation is either magnetic dipole or electric quadrupole,[6] both of which give rise[7] to a distribution function of the form $Y(\theta)=1+A\cos^2\theta+B\cos^4\theta$. If now the spin of the excited state is I, then the maximum exponent in this expression cannot exceed $2I$. For $I=\frac{1}{2}$ one obtains $Y(\theta)=1$, for $I=\frac{3}{2}$ the expression is $1+A\cos^2\theta$, while for $I=5/2$ all the terms are allowed. Accordingly a simple determination of the complexity of the angular distribution function of the gammas in $Li^6(d,p)Li^{7*}(\gamma)Li^7$ at a deuteron energy between 400 and 900 kev should provide definite information about the spin of the excited state.

[1] D. R. Inglis, Phys. Rev. **74**, 1876 (1948).
[2] E. Feenberg and H. Primakoff, private communication. See reference 4.
[3] S. S. Hanna and D. R. Inglis, Phys. Rev. **75**, 1767 (1949).
[4] B. T. Feld, Phys. Rev. **75**, 1618 (1949).
[5] Krone, Hanna, and Inglis, Phys. Rev. **75**, 335 (1949).
[6] The measured lifetime of the excited state makes it probable that the radiation is magnetic dipole. L. G. Elliott and R. E. Bell, Phys. Rev. **74**, 1869 (1948). See also reference 3.
[7] C. N. Yang, Phys. Rev. **74**, 764 (1948).

The Energy Levels of the N^{14} Nucleus

H. A. Wilson
Rice Institute, Houston, Texas
July 14, 1949

THE resonances observed in the bombardment of carbon by deuterons[1,4] can be explained on the nuclear spherical shell theory[2] proposed by the writer.

According to this theory nuclei at high excitation energies have equally spaced levels with separations 0.387 Mev. The resonances when C^{12} is bombarded by deuterons should therefore be equally spaced with separations $0.387\times14/12$ or 0.452 Mev.

Table I gives values of $1.30+0.452n$ with $n=0, 1, 2, 3, 4$ and of observed resonances.

The observed and calculated values agree very closely. The chance that such exact agreement is accidental is clearly small.

The writer has suggested[3] that there may also be rotation vibration levels with rotational energies equal to $cj(j+1)$ where c is a constant and j is the rotation quantum number.

The value of the constant c for the N^{14} resonances on the shell theory is equal to 0.052 Mev. The resonances should therefore be given by $1.30+0.452n+0.052j(j+1)$. Table II gives the calculated and observed values.

There is no calculated value corresponding to the resonance at 1.23. The resonances are based on seven sets of experiments none of which shown more than one resonance between 0.93 and 1.30 although the resolving power was probably good enough to separate resonances differing by 0.07. It is possible therefore that the six results between 0.93 and 1.30 all belong to the same resonance. The mean of the six results is 1.18 which agrees nearly with the calculated value 1.16.

The three resonances 2.90, 2.95, and 3.01 are based on four results between 2.82 and 3.11. None of the experiments gave more than one resonance between 2.82 and 3.11. It is therefore possible that the three values 2.90, 2.95 and 3.01 all belong to one resonance. The mean of these three is 2.95 which agrees nearly with the calculated value 2.97.

The value 2.72 quoted in Table II seems to be a misprint since the graph on page 1149 of reference 1 shows this resonance at 2.76 in agreement with the calculated value.

Heydenburg *et al.*[1] point out that when the virtual levels are together, the resonances may not be observed exactly at the positions corresponding to the levels and also that the differences may not be the same for different modes of observation. This may be the reason why several different values were found for the resonances at 1.16 and 2.97. It is possible therefore that some of the differences between the observed and calculated values in Table II are real and not due to experimental errors. In any case the general agreement between the observed and the calculated values is satisfactory.

Table I. Certain observed and calculated values of the energy levels of N^{14}.

n	Calculated	Observed
0	1.30	1.30
1	1.752	1.75
2	2.204	2.20
3	2.656	2.66
4	3.108	3.11

Table II. Observed and calculated values of the energy levels of N^{14}.

n	j	Calculated	Observed*	Observed**
−1	1	0.95	0.93	0.91
−1	2	1.16	1.16, 1.23 } 1.18?	1.16 1.14
0	0	1.30	1.30	1.30
0	1	1.40	1.43	1.435
0	2	1.61	1.66	
1	0	1.75	1.75	
1	1	1.86	1.81	
1	2	2.06	2.09	
2	0	2.20	2.20	
2	1	2.31	2.34	
2	2	2.52	2.53	
3	0	2.66	2.66	
3	1	2.76	2.72 2.76?	
2	3	2.83	2.82, 2.90	
3	2	2.97	2.95, 3.01 } 2.95?	
4	0	3.11	3.11	
4	1	3.21	3.20	
3	3	3.28	3.31	

* See reference 1.
** See reference 4.

[1] Heydenburg, Inglis, Whitehead, and Hafner, Phys. Rev. **75**, 1147 (1949).
[2] H. A. Wilson, *Modern Physics*, 3rd edition (1948), p. 273.
[3] H. A. Wilson, Phys. Rev. **74**, 351, 352 (1948).
[4] Phillips, Bonner, and Richardson, Phys. Rev. **76**, 169 (1949).

Rotation Levels of the Na^{24} and Ca^{41} Nuclei

H. A. Wilson
Rice Institute, Houston, Texas
May 23, 1949

THE neutron resonance levels of sodium and calcium reported by Adair, Barschall, Bockelman, and Sala[1] can be explained as rotation levels of the compound nuclei. The resolving power was about 20 kev.

Table I gives values of $150+c(j(j+1)-\frac{3}{4})$ with $c=8$ and of the observed levels in calcium.

Table I. Calculated and observed values of the energy levels in calcium.

j	Calculated	Observed	Area	l
		kev		
$\frac{1}{2}$	150	150	50	3 or 4
$1\frac{1}{2}$	174	185	40	2 or 3
$2\frac{1}{2}$	214	220	80	1 or 2
$3\frac{1}{2}$	270	255	260	0 or 1
$4\frac{1}{2}$	342	335	300	0 or 1
$5\frac{1}{2}$	430	440	90	1 or 2
$6\frac{1}{2}$	534	505*	40	2 or 3

* The highest neutron energy used was 523 kev so that a resonance at the calculated value 534 could not have been observed.

TABLE II. Calculated and observed values of the energy levels in sodium.

j	Calculated	Observed	Area	l
		kev		
0	666	—	15(?)	1 or 2
1	708	710	100	0 or 1
2	792	790	60	0 or 1
3	918	920	30	1 or 2

The differences between the observed and calculated values are probably not greater than the probable errors.

We have $\hbar^2/8\pi^2K=c\times1.6\times10^{-9}\times(A-1)/A$. With $K=\frac{2}{5}Amr^2$ this gives for the radius of a nucleus of mass number A, $r=177\times10^{-13}(c(A-1)^{-\frac{1}{3}})$. With $A=41$ and $c=8$ this gives $r=9.9\times10^{-13}$. The spherical shell theory[2] formula $r=4.65\times10^{-13}(Z^2/A)^{\frac{1}{3}}$ gives $r=9.95\times10^{-13}$.

The fourth column gives rough estimates of the areas of the resonances above the background. The fifth column gives values of l the orbital angular momentum number of the incident neutrons assuming the spin of Ca^{40} to be 4. The areas decrease as l increases but the areas for the larger values of l are greater than would have been expected.

Table II gives values of $666+21j(j+1)$ and of the observed levels, above 600 kev, in sodium. No resonance was found at 666 kev. According to the Breit-Wigner theory the resonance at $j=0$ should be about one-third as high as that at $j=1$. An examination of the observed graph shows that a low resonance at 666 kev could have been obscured by the high resonance at 710 and the broad low rise in the graph near 600 kev.

The formula $r=177\times10^{-13}(c(A-1)^{-\frac{1}{3}})$ with $A=24$ and $c=21$ gives $r=8.04\times10^{-13}$ cm. The formula $r=4.65\times10^{-13}(Z^2/A)^{\frac{1}{3}}$ gives $r=8.0\times10^{-13}$.

The last two columns give the areas of the resonances and the values of l. The areas decrease as l increases about as would be expected.

Several low resonances between 0 and 600 kev were found with sodium. These resonances probably have rather large spin numbers and do not all belong to the same set so it is not possible to assign spin numbers to them with any certainty. Table III gives the values of the constant c for all the sets of nuclear rotation levels so far found.[3]

TABLE III. Values of the constant c and calculated values of nuclear radii.

Element	c	r from c	r calculated
		$\times10^{13}$	$\times10^{13}$
Na^{24}	21	8.04	8.0
Si^{28}	16.15	8.47	8.90
Al^{28}	21	7.43	8.47
Ca^{41}	8	9.90	9.95
Fe^{57}	5	10.6	10.6
Ni^{59}	4.1	11.5	10.8

The last two columns give the nuclear radii got from the values of c and from $r=4.65\times10^{-13}(Z^2/A)^{\frac{1}{3}}$.

It would be interesting to see if similar rotation resonances appear when elements of higher mass number are bombarded by fast neutrons. For example with arsenic As^{76} rotation resonances with $c=3.28$ might be expected. With bismuth Bi^{210} rotation resonances with $c=0.68$ might be expected but could not be separated with a resolving power of 20 kev.

[1] Adair, Barschall, Bockelman, and Sala, Phys. Rev. **75**, 1124 (1948).
[2] H. A. Wilson, *Modern Physics*, 3rd edition (1948), p. 273.
[3] H. A. Wilson, Phys. Rev. **74**, 351, 352 (1948).

On the Production of Mesons

H. KOPPE
Department of Physics, University of British Columbia, Vancouver, Canada
July 18, 1949

IN a recent paper[1] a simple method has been given for the calculation of the yield of mesons produced by the interaction of light nuclei. It was based on the assumption of a strong interaction between mesons and nucleons, which should make it possible, to treat a nucleus as a "black body" with regard to mesonic radiation and to calculate the probability for emission of a meson by statistical methods.

If a nucleus of mass M_1 and kinetic energy U hits a target nucleus of mass M_2, then the probability for the emission of a meson of mass μ is given by

$$\eta=\frac{240}{11\pi^2}\frac{e}{k}\exp\left[-\frac{\mu c^2}{kT_0}\right]. \tag{1}$$

Here T_0 is the temperature corresponding to an excitation energy $U_0=U\cdot M_2/(M_1+M_2)^2$ of the compound nucleus, and C its specific heat. Originally, it was assumed, that the nucleus could be treated as a degenerate Fermi-gas; hence the relation between T_0 and U_0 would have been[2]

$$kT_0=3.8(U_0)^{\frac{1}{2}} \tag{2}$$

giving kT_0 in Mev if U_0 is expressed in Mev. It turned out, however, that the resultant temperatures are so high, that the classical

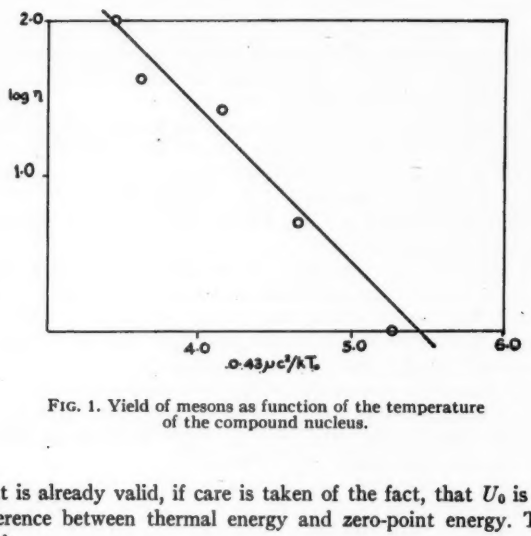

FIG. 1. Yield of mesons as function of the temperature of the compound nucleus.

limit is already valid, if care is taken of the fact, that U_0 is the difference between thermal energy and zero-point energy. This yields

$$U_0=3kT_0/2-3.51 \tag{3}$$

and, combined with (1)

$$\eta=\frac{360}{11\pi^2}(M_1+M_2)\exp\left\{-\frac{3\mu c^2}{2(U_0+3.51)}\right\}. \tag{4}$$

The relative yields of π-mesons (produced by bombarding carbon atoms by protons) as a function of proton energy, which have been obtained by Jones and White,[3] make it possible, to test Eq. (4). Since only relative values have been obtained, in Fig. 1 $\log\eta$ is plotted against $0.43\mu c^2/kT_0=94.7/(U_0+3.51)$. The empirical points should then fit into a straight line with a slope of 45°. It can be seen, that the comparison between theory and experiment is quite satisfactory.

[1] H. Koppe, Zeits. f. Naturforschung **3**(a), 251 (1948).
[2] See E. Bagge, Ann. d. Physik (5) **33**, 389 (1938).
[3] Stanley B. Jones and R. Stephan White, Bull. Am. Phys. Soc. **24** (No. 6), 8 (1949).

The Beta-Spectrum of O^{15}*

V. Perez-Mendez and H. Brown
Pupin Physics Laboratories, Columbia University, New York, New York
July 18, 1949

O^{15} HAS long been known to be a positron emitter,[1] but its short half-life has hitherto prevented an accurate measurement of the spectrum. Using a hollow probe[2] and a beta-spectrometer for gaseous emitters,[3] this spectrum has now been obtained.

Oxygen^{15} was produced by the $N^{14}(d,n)$ reaction using nitrogen gas continuously circulated. The gas passes through the probe and is bombarded through a thin window by 8 Mev deuterons, the current being about 15 microamp. It is then pumped to a disintegration chamber along with the gaseous products of the bombardment, and recirculated.

Six decay curves were taken over a period of 10 half-lives (covering a counting rate variation of 1000), by alternately counting and waiting for 30 sec. periods, beginning 30 sec. after the end of the bombardment. A simple decay curve, corrected for counter background and deadtime, is shown in Fig. 1. The half-life of O^{15} as obtained from the entire series is 118.0 ± 0.7 sec., which is somewhat lower than previous values.[4,5] The linearity of the logarithmic plot of the decay curve indicates that only one activity is present, as would be expected on the basis of the isotopic abundances and relative cross sections involved in the competing reactions.

For the measurement of the energy spectrum, the bombarded gas was pumped through a source chamber, which was fitted with a thin Cellophane window and inserted into a semicircular focusing magnetic spectrometer. The amount of activity in the source chamber so used was monitored by placing a counter next to the pumping line about 5 cm from the chamber. By subtracting backgrounds and taking the ratio of the counts by the spectrometer counter to those by the monitor counter as the magnetic field was varied, the O^{15} spectrum was obtained.

The resulting Fermi plot is shown in Fig. 2. This gives an end point (corrected for the source window absorption at high energies) of 1.683 ± 0.005 Mev, which is in good agreement with the results of cloud chamber[1] and absorption measurements.[5] The graph shown is the result of four runs, normalized to the same value in the intermediate energy region (400–800 kev). The Fermi plot is essentially linear down to an energy of about 300 kev. Below this energy, it deviates sharply. This could be due to an additional group of beta-rays, but is more probably caused by the thickness of the gaseous source (about 0.7 mg/cm²) and window (about 2.5 mg/cm²). Calculations carried out on the basis of the experiments of White and Millington[6] indicate that the straggling of the beta-particles in their passage through this window should produce a perceptible excess of low energy positrons at about 300 kev, as observed. We conclude that the spectrum is of the allowed type. The *ft*. value calculated from $E_0=1.683$ Mev, $\gamma_{\frac{1}{2}}=119.0$ sec., and $Z=7$, is 3910 which would tend to confirm this result.

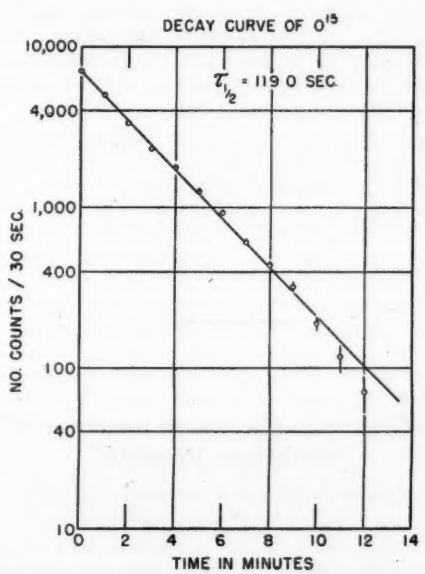

FIG. 1. Decay curve of O^{15}. Each point represents number of counts over a 30 sec. period, corrected for background and counter deadtime. When the statistical error is greater than the size of the points, it is shown by the vertical lines.

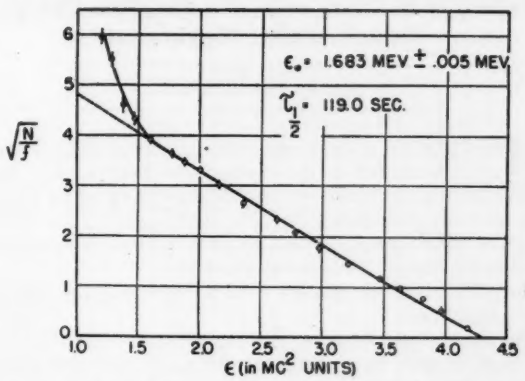

FIG. 2. Kurie plot of the O^{15} spectrum. ϵ is the total energy (rest and kinetic) in units of Mc^2. N is the number of electrons per unit momentum interval. f is the Fermi function $\eta^2F(z,\eta)$. $(N/f)^{\frac{1}{2}}$ is plotted in arbitrary units. Where the statistical error is greater than the size of the points, it is shown by vertical lines.

* Work done under AEC Contract AT-30-1-Gen 72.
[1] Fowler, Delsasso, Lauritsen, Phys. Rev. **49**, 561 (1936).
[2] H. Brown and V. Perez-Mendez, Phys. Rev. **75**, 1286 (1949).
[3] H. Brown and V. Perez-Mendez, Phys. Rev. **75**, 1276 (1949).
[4] W. Bethe and W. Gentner, Zeits. f. Physik **112**, 45 (1939).
[5] Sherr, Meuther, and White, Phys. Rev. **75**, 282 (1949).
[6] White and Millington, Proc. Roy. Soc. A **120**, 701 (1928).

Erratum: The Production of Mesons by Photons and Electrons

[Phys. Rev. **76**, 134 (1949)]

Herman Feshbach
Department of Physics, Massachusetts Institute of Technology, Cambridge, Massachusetts
and
Melvin Lax
Department of Physics, Syracuse University, Syracuse, New York
July 18, 1949

THE Editor regrets that, due to an oversight, certain changes which the authors of the above article had requested were not made. The title should have read, "The Production of Positive Mesons by Photons and Electrons." The following note should have been added to the paper:

"The above discussion applies only to the production of positive mesons where the corrections due to the neglect of the relativistic terms in the meson-nucleon Hamiltonian that we have made are unimportant. In the production of negative mesons this is not true, as has been pointed out to us by M. L. Goldberger, so that even at threshold there is a larger production of negative pseudoscalar mesons than positive pseudoscalar mesons. This correction is of the order of μ_0/M and therefore can be appreciable."

A Difficulty in Using $mk^{\frac{1}{2}}$ as a Residual Charge to Explain Stellar Magnetism

P. D. P. SMITH
Montreal, Quebec, Canada
July 20, 1949

MARIANI has pointed out recently[1] that a residual charge of amount $mk^{\frac{1}{2}}$ e.s.u., associated with all masses, would explain Babcock's results[2] on the Zeeman splitting of spectral lines from rotating stars. The difficulty in accepting a residual charge of this magnitude is that *the forces of electrostatic repulsion would cancel those of gravitational attraction.*

Mariani derived the relation $e=\pm mk^{\frac{1}{2}}$ by using the appromation[1] $\frac{1}{2}\Delta^2 g_{44}\simeq u_4$.

This needs closer attention. Calling $\bar{\sigma}=k/c^2\int\rho_0\cdot dv/r$ (ρ_0 being the mass density) in a static gravity field[3] $u_4=g_{44}u^4=(1-2\bar{\sigma})\cdot cdt/ds$. Also $c\cdot dt/ds=(1-2\bar{\sigma}-(1+2\bar{\sigma})v^2/c^2)^{-\frac{1}{2}}$. Hence to the first power in v^2/c^2

$$u_4=1-\bar{\sigma}+\tfrac{1}{2}v^2/c^2.$$

Making use of Mariani's Eq. (3),

$$\Delta^2 u_4=\Delta^2(\tfrac{1}{2}v^2/c^2-\bar{\sigma})=\sigma_0/\rho_0c^2\cdot\Delta^2\varphi_4,$$

or

$$\Delta^2\{\tfrac{1}{2}\rho_0v^2-k\rho_0\int\rho_0'dv/r+\sigma_0\int\sigma_0'dv/r\}=0,$$

which is simply the classical conservation of energy in differential form. It can also be written

$$\Delta^2\{\tfrac{1}{2}\rho_0v^2\}=4\pi(\sigma_0^2-k\rho_0^2),$$

in a region where all particles have the same e/m. Thus it appears that Mariani's result means simply that the kinetic energy is constant when electrostatic repulsions balance gravitational attractions, rather than that $\sigma_0=\pm k^{\frac{1}{2}}\rho_0$.

[1] J. Mariani, Phys. Rev. **73**, 78 (1948).
[2] H. Babcock, Phys. Rev. **72**, 83 (1947).
[3] A. Einstein, *The Meaning of Relativity* (Princeton University Press, Princeton, N. J., 2nd Edition, 1946), pp. 101–102.

A New Measurement of the $Pt^{195}-Cu^{65}$ Packing Fraction Difference*

HENRY E. DUCKWORTH
Scott Laboratory, Wesleyan University, Middletown, Connecticut
July 15, 1949

MASS spectra of the doublet formed by singly-charged Cu^{65} and triply-charged Pt^{195} were first obtained by A. J. Dempster[1] in 1938. His measurement of the doublet spacing permitted a calculation of the packing fraction difference between these two nuclides, and provided an important link between the elements of medium atomic weight and the very heavy ones. The author, working in Dempster's laboratory and using Dempster's mass spectrograph, remeasured[2] the doublet spacing in 1942. The mass spectra used in the present measurement have been obtained with a large Dempster-type mass spectrograph which has recently been completed at Wesleyan University.[3] These results should serve as a check of previous work, and may be of special interest since they have been obtained with different equipment.

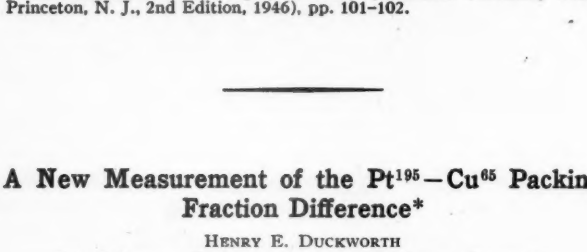

FIG. 1. Mass spectrum showing the doublet formed by singly-charged Cu^{65} and triply-charged Pt^{195}. Magnification 6×.

TABLE I. Values of the packing fraction difference between Pt^{195} and Cu^{65} for six doublets. The probable errors are based on the internal consistency of the measured values.

Mass scale	(f of $Pt^{195}-f$ of Cu^{65})×10⁴ #1	#2	#3	#4	#5	#6	Mean
$Cu^{63}-Cu^{65}$	9.13	9.30	9.58			9.36	9.34±0.07
$Pt^{194}-Pt^{195}$	9.07	9.21	9.52	9.51	9.05	9.22	9.26+0.06
$Pt^{194}-Pt^{196}$	8.85	9.05	9.54	8.95	8.95	9.00	9.11+0.07
$Pt^{195}-Pt^{196}$	9.16	9.27	9.50	9.27	9.27	9.32	9.36+0.05

Mean of 22 measurements on 6 doublets 9.26±0.03

Triply-charged platinum and singly-charged copper ions were produced in a spark between a platinum electrode and a gold electrode containing one percent copper. The doublets formed at mass 65, of which a typical one is shown in Fig. 1, were well matched in intensity, and were secured with exposure times ranging from two to four minutes. It can be seen that suitable mass scales are provided by the Cu^{63} and Cu^{65} lines, by Pt^{194} and Pt^{195}, by Pt^{194} and Pt^{196}, and by Pt^{195} and Pt^{196}. Measurement of six doublets gave the values shown in Table I.

It was also possible, on four of the exposures, to locate Pt^{194} and Pt^{196} with respect to the copper lines, thereby permitting a calculation of the difference in packing fractions of these nuclides and the average packing fraction of the copper isotopes (if the copper packing fractions are unlike, which is unlikely, this average must be replaced by an appropriate weighted mean).[2] The value of $\Delta f\times10^4$ for the $Pt^{194}-\overline{Cu}$ difference is 8.89±0.10 and for the $Pt^{196}-\overline{Cu}$ is 9.44±0.20.

The mean value of the $Pt^{195}-Cu^{65}$ packing fraction difference of (9.26±0.03)×10⁴ is to be compared with Dempster's value of 8.93±0.1[1] and the author's earlier value of 10.74±0.20.[2] In the present measurement the two lines are somewhat better matched than were those in previous doublets. This advantage, plus the greater resolution and dispersion of the new instrument (about two and one-third times those of Dempster's original mass spectrograph), should give fair weight to the present work. It is hoped that other mass measurements, now in progress, will yield packing fraction differences for other significant doublets.

The author wishes to thank Mr. Richard Woodcock, Mr. Howard Johnson, and Mr. Clifford Geiselbreth for assistance in these experiments. He is also grateful to Professor Carl Stearns, Chairman of the Astronomy Department of Wesleyan University, for the use of the comparator.

* This letter is based on work done at Wesleyan University under Contract AT(30-1)-451 with the AEC.
[1] A. J. Dempster, Phys. Rev. **53**, 64 (1938).
[2] H. E. Duckworth, Phys. Rev. **62**, 19 (1942).
[3] A description of the mass spectrograph will be proposed shortly for publication in the Review of Scientific Instruments.

Microwave Absorption Spectrum of Methylene Bromide*

WILLIAM J. PIETENPOL AND JOHN D. ROGERS
Ohio State University, Columbus, Ohio
July 21, 1949

USING a Stark-effect-modulation spectrograph recently developed here, we have observed sixteen absorption lines in the spectrum of the asymmetrical-top molecule CH_2Br_2. Preliminary results on the frequencies and the relative intensities of

TABLE I. Microwave absorption spectrum of CH_2Br_2.

Frequency	Observed Intensity
25223 mc/sec.	m
25203	m
25170	m
25160	w
25152	w
25147	w
25128	s
25090	m
25072	s
25042	s
25013	m
25002	w
24982	m
24972	w
24943	w
24908	m

the observed lines are given in Table I. Previously a single line had been observed in this region by Turner,[1] who gave the frequency of this line as 25,056 mc/sec. We are extending our measurements to higher frequencies and are attempting an interpretation of the observed spectrum.

* The work described in this paper was carried out under contract between the Cambridge Field Station of the Air Materiel Command and the Ohio State University Research Foundation.

[1] T. E. Turner, Thesis, McGill University (1948).

Nuclear Spin and Quadrupole Moment of Cl^{36}*

C. H. TOWNES AND L. C. AAMODT
Pupin Physics Laboratories, Columbia University, New York, New York
July 18, 1949

EXAMINATION of the hyperfine structure of the $J=1\rightarrow2$ rotational transition of the molecule $Cl^{36}C^{12}N^{14}$ allows determination of the Cl^{36} nuclear spin as 2 and its nuclear quadrupole moment as $-0.0172\pm0.0004\times10^{-24}$ cm^2.

The $J=1\rightarrow2$ transition of $Cl^{36}CN$ occurs near 23635 mc/sec. The upper two curves of Fig. 1 show recordings of its hyperfine structure. The lower of these two curves represents the higher resolution, or the lower gas pressure. In the top curve resolution is somewhat poorer but random fluctuations are essentially eliminated. The other curves represent theoretical envelopes of the spectrum assuming different values of nuclear spin and resolutions approximately equal to that actually obtained. The upper curves for spin 2 and 3 and the curve for spin 1 correspond to line widths (total width at half-maximum) of 2 mc/sec. and the two lower curves for spins 2 and 3 are for line widths of 1 mc. Theoretical positions and relative intensities of each line is also shown. Magnitudes of quadrupole coupling constants for Cl^{36} are chosen for each value of spin to obtain the best fit of the experimental spectrum. The observed curve agrees very well with the theoretical curves assuming a spin of 2 but can be seen to disagree in a number of respects with those for spins of 1 and 3. Some small deviations in relative intensities of the components of the higher resolution experimental curve from those theoretically expected for a spin of two are caused by saturation effects, which depress the peaks of the stronger lines.

Measurements of relative intensities and separations of the three most evident components of the hyperfine pattern, labeled *a*, *b*, and *c* on Fig. 1, were made on approximately thirty recordings of this spectrum. Results are listed in Table I, which again shows very good agreement with theoretical expectations for a spin of 2. Intensity and spacing ratios for similar features of the theoretical spectrum assuming a spin of 1 are in clear disagreement with the results listed in Table I. Although the expected spectrum for a spin of 3 differs in general appearance from the observed spectrum, we have considered the outer bump on the right-hand side of the spin 3 spectrum as corresponding to com-

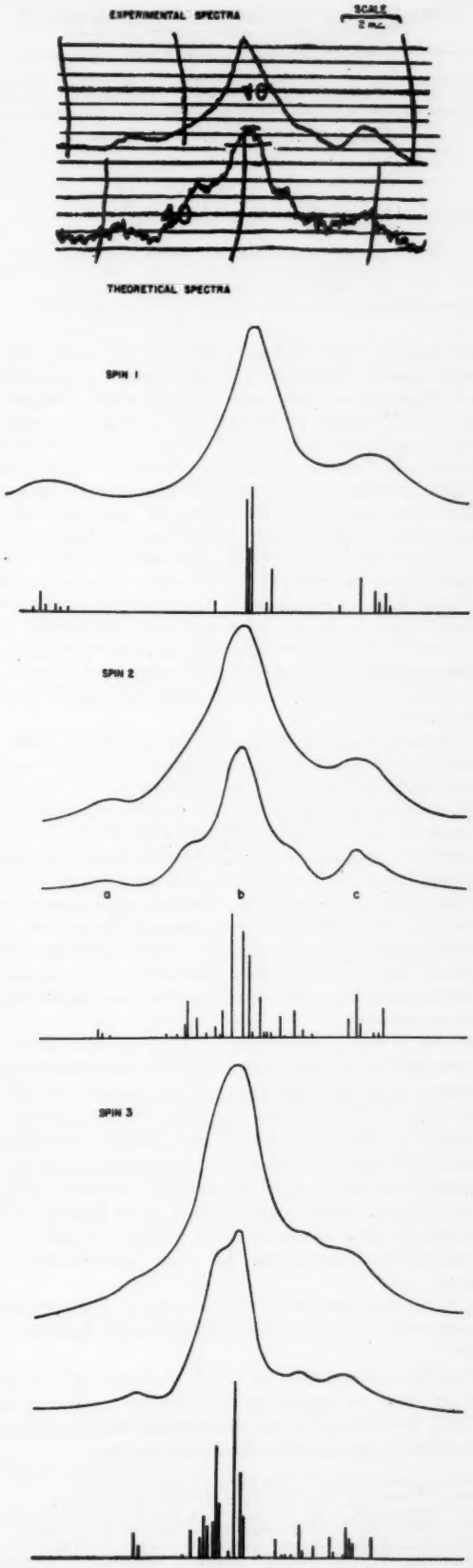

FIG. 1. Comparison of observed hyperfine structure of the $J=1\rightarrow2$ transition of $Cl^{36}CN$ and theoretically expected structures for various assumed values of the Cl^{36} spin.

TABLE I. Intensity and spacing ratios. Designation of components as a, b, and c is shown in Fig. 1.

Intensity ratios	Measured	Theoretical for Spin 2	Theoretical for Spin 1	Theoretical for Spin 3
$\frac{a}{c}$	0.22±0.03	0.20	0.43	0.50
$\frac{b}{c}$	4.05±0.2	4.2	3.6	4.3
Spacing ratio				
$\frac{a-b}{b-c}$	1.17±0.03	1.15	1.65	0.82

ponent c and the weak left-hand component to a, and given their theoretical relative intensities and positions for a comparison in Table I. Experimental measurements again clearly disagree with a spin of 3. Cl^{36} is, oddly, the first nucleus found to have a spin of 2.

N^{14} is present in the molecule ClCN and its quadrupole moment complicates the hyperfine pattern observed. However, the N^{14} quadrupole coupling constant in ClCN is accurately known[1] and its effect was included in the theoretical patterns. An exact calculation was made of energy levels and frequencies for the case of spin 2, although since the quadrupole coupling of Cl^{36} is five times larger than that of N^{14}, the exact frequencies differed only slightly from those obtained by a first-order calculation.[2] In the cases of spin 1 and 3, only a first-order calculation.[2] In the cases of spin 1 and 3, only a first-order calculation (assuming the N^{14} coupling small compared to the Cl^{37} coupling) has been made, since an exact computation would produce only minor changes in the theoretical curves.

The average frequency difference between the two weak components of the hyperfine pattern obtained from a number of spectral tracings is 9.08 mc/sec. This, combined with a knowledge of the Cl^{35} quadrupole moment[3] and its coupling constant[1,4] in the same molecule ClCN, allows a determination of the Cl^{36} nuclear quadrupole moment as $-0.0172\pm0.0004\ 10^{-24}$ cm². This moment equals one-quarter of the average quadrupole moments of Cl^{35} and Cl^{37} within experimental accuracy. The ratio one-quarter would be expected if it is assumed that only the odd proton and neutron in d orbits[5] contribute to the nuclear moments and that Cl^{36} is in a $^3F_2$ state. This agreement may well be fortuitous, however, in view of the sizable quadrupole moment[6] of the neighboring odd neutron nucleus S^{33}.

The $Cl^{36}CN$ was prepared from a dilute solution of 70 mg of HCl furnished by the Oak Ridge National Laboratory. Isotopic abundance of Cl^{36} was approximately 0.8 percent. The HCl was titrated with NaOH and then evaporated to a volume of 5 cc. Two grams of MnO_2 were added, then concentrated H_2SO_4 introduced slowly and the evolved Cl_2 condensed in a dry ice bath. The mixture was heated to 80° to complete evolution of Cl_2. The resulting Cl_2 was mixed with an equal molal amount of HCN and a drop of water to obtain ClCN which, although not pure, was sufficiently concentrated to allow spectroscopic measurements.

The microwave spectrometer used was a Stark modulation instrument with a phase detecting amplifier and Esterline Angus recorder.[7]

The authors are indebted to Dr. B. P. Dailey for advice and Mr. A. F. Byas for assistance with chemical problems, and to Mrs. Zelda Droshnicop for the considerable amount of computation involved in obtaining the theoretical spectra.

* Work supported jointly by the Signal Corps and ONR.
[1] Townes, Holden, and Merritt, Phys. Rev. **74**, 1113 (1948).
[2] See J. Bardeen and C. H. Townes, Phys. Rev. **73**, 97 (1948).
[3] Davis, Feld, Zabel, and Zacharias, Phys. Rev. **73**, 525 (1948).
[4] Smith, Ring, Smith, and Gordy, Phys. Rev. **74**, 370 (1948).
[5] E. Feenberg, Phys. Rev. **75**, 320 (1949). L. Nordheim, to be submitted for publication in Phys. Rev.
[6] C. H. Townes and S. Geschwind, Phys. Rev. **74**, 626 (1948).
[7] W. Low and C. H. Townes, Phys. Rev. **75**, 529 (1949).

Radioactivity of Chlorine^{36}*

C. S. Wu, C. H. Townes, and L. Feldman
Pupin Physics Laboratories, Columbia University, New York, New York
July 18, 1949

THE half-life of the Cl^{36} activity has been estimated as $\sim10^6$ yr.[1] and 2×10^6 yr.[3]. The maximum energy of the beta-radiation from absorption measurements was given as 0.64[2] to 0.66[1] Mev. Cl^{36} has also been reported to decay in the three parallel paths[2] of β^-, β^+ and K-capture. However, recent investigation[4] of the maximum positron to negatron ratio in the decay of Cl^{36} by gamma-ray absorption method puts an upper limit of the ratio of positron-to-negatron-emission at less than 3×10^{-4}. No nuclear gamma-rays have been reported. We have redetermined the half-life of Cl^{36} as $(0.44\pm0.05)\times10^6$ yr. by determining the specific disintegration rate of Cl^{36}. In addition, a search for positron and gamma-ray emission has been made with negative results.

The isotopic concentration of Cl^{36} was obtained from intensity measurements of the microwave absorption spectrum of $Cl^{36}CN$. Part of a dilute solution of HCl containing Cl^{36} was converted to $Cl^{36}CN$ as described in the preceding letter. A number of spectra of the $J=1\rightarrow2$ transitions of $Cl^{36}C^{12}N^{14}$ and of $Cl^{35}C^{13}N^{14}$ were taken on a recording spectrometer and the ratio of total area (integrated intensity) of the absorption lines due to the two transitions was measured from the recording. A variety of conditions of gas pressure and spectrometer adjustments were used, but for all intensity measurements the pressure was high enough so that hyperfine components of the $Cl^{36}C^{12}N^{14}$ line were not resolved, and only certain well-separated hyperfine components of the $Cl^{35}C^{13}N^{14}$ transition were resolved. Intensities and frequencies of the two absorption lines compared differed only slightly. Assuming the natural abundance of Cl^{35} to be 75.40 percent and C^{13} to be 1.12 percent, the abundance of Cl^{36} obtained for two different batches of HCl was 0.675 percent and 0.835 percent as shown in Table I. Accuracy of these determinations is thought to be ±5 percent.

The absolute beta-disintegration rate was measured on a mica window (5–6 mg/cm²) G-M counter. The geometrical efficiency of the counter was calibrated with the help of several RaE standards from the Bureau of Standards. The procedure of preparing source and calculating the exact Cl^{36} content in the source is as follows. A careful titration of the HCl solution received from Oak Ridge with an NaOH solution of known normality gives the exact amount of chlorine contained in the solution. The neutralized solution is then slowly evaporated to dryness under an infra-red lamp. The total solid content of this neutralized solution is weighed on a microbalance. After weighing, the total solid is redissolved in a minimum amount of distilled water and several cc of pure alcohol or acetone are added to obtain a suspension. The particles in suspension are allowed to settle on a 1.24 cm² area of a standard silver disk which is the same as the RaE sources of the Bureau of Standards. After these sources are thoroughly dried, the weight is again determined on a microbalance. The Cl^{36} content in the source is then easily calculated.

The different amounts of backscatterings of the beta-radiations of Cl^{36} and RaE from the standard disks are determined experi-

TABLE I. Half-life determinations of Cl^{36}.

Group	Sample	Isotopic concentration	Sample weight	Half-life
1	a	0.675	0.836 mg	0.428×10^6 yr.
1	b	0.675	0.536 mg	0.394×10^6 yr.
2	c	0.835	0.431 mg	0.480×10^6 yr.
2	d	0.835	0.262 mg	0.494×10^6 yr.
2	e	0.835	2.236 mg	0.425×10^6 yr.
				Average $=0.444\times10^6$ yr.

mentally by measuring the ratio of the radiations from extremely thin Cl^{36} and RaE sources deposited on collodion films of ~12 microgram/cm² when they are either backed or not backed with the standard silver disks.

The absorption in the counter window and the air path between the source and the counter and also the self-absorption of the source are corrected by extrapolating the beginning of the absorption curve to zero thickness. Since the curvature of the absorption curve at the beginning is small, the error introduced in extrapolating should not be appreciable.

Five different sources were prepared from two different batches of HCl. The half-life determinations are listed in Table I.

The half-life of sample *b* was also determined in a low absorption counter[5] giving good agreement with the above result. We conclude that the half-life of Cl^{36} is $(0.44\pm0.05)\times10^6$ yr., where the error of approximately 10 percent is thought to include possible systematic errors.

To recheck the possibility of positron emission in a Cl^{36} source, a strong $LiCl^{36}$ source was placed in the spectrometer and the energy region from 20 kev to 700 kev carefully scanned for electrons and positrons. Figure 1 shows that when the spectrometer is adjusted for positrons, the counting rate remained at background throughout the whole energy region in spite of the high electron activity. Judging from the ratio of the areas under the electron curve and the positron curve, the ratio of positrons to electrons emitted is less than 10^{-4}. Although positrons from Cl^{36} were observed[2] in the cloud chamber, observations of numerous positron tracks from a thick pure electron emitter such as P^{32} in a cloud chamber have been frequently reported in the literature, but these positron tracks seem to disappear[6] when a thin source is used.

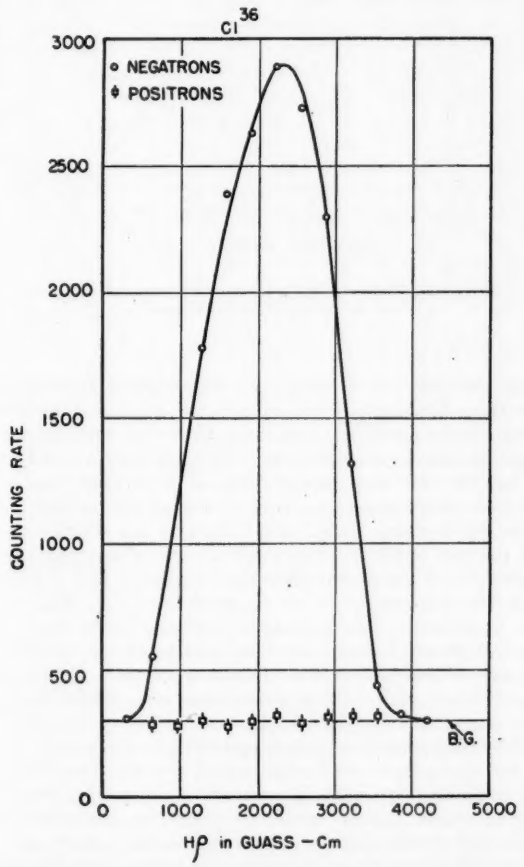

FIG. 1. Search of positrons from Cl^{36} by beta-ray spectrometer.

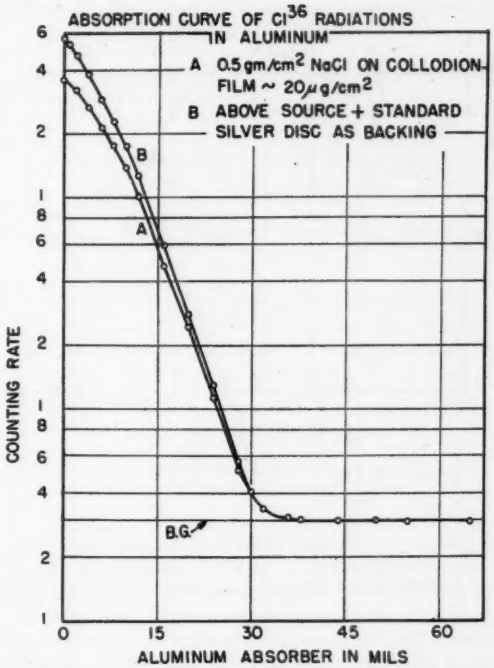

FIG. 2. Absorption curves of Cl^{36} radiations in aluminum.

The absorption curve of the Cl^{36} beta-radiation in Al foils is shown in Fig. 2. Curve A shows the absorption curve of a Cl^{36} source on a thin collodion film; curve B is the absorption curve of the same Cl^{36} source except with the standard silver disk right behind the collodion film. The steeper initial slope of curve B is probably due to the softness of the back-scattered radiation. At 38 mils of Al, both curves show only background counts which give the upper energy limit of 0.73 Mev in good agreement with the spectrometer determination of 0.713 Mev. For absorber thicknesses greater than 38 mils of Al, no point lies outside of the statistical fluctuations of the background rate which is 0.02 percent of the total number of counts. Therefore, no gamma-rays are associated with the disintegration of Cl^{36} unless they are of very low energy (<20 kev) or of low intensity (<5 percent of disintegration if gamma-ray were of the order of 1 Mev).

* Work supported jointly by the AEC Contract AT-30-1-Gen 72, the Signal Corps and the ONR.

[1] Overman (Radioactivities Produced in Neutron Irradiation of Chlorine), AECD 857.
[2] D. C. Grahame and H. J. Walke, Phys. Rev. **60**, 909 (1941).
[3] Hughes, Eggler and Goldstein, P. P. R., CP-3801, p. 17 (1947).
[4] F. Johnston and J. E. Willard, Phys. Rev. **75**, 528 (1949).
[5] L. D. Norris and M. G. Inghram, Phys. Rev. **73**, 350 (1948).
[6] Bradt, Heine and Scherrer, Helv. Phys. Acta. **16**, 491 (1943). L. Smith and G. Groetzinger, Phys. Rev. **70**, 96 (1946). T. H. Pi and C. Y. Chao, Phys. Rev. **72**, 639 (1947).

The Beta-Ray Spectrum of Chlorine[36]*

C. S. WU AND L. FELDMAN
Pupin Physics Laboratories, Columbia University, New York, New York
July 18, 1949

RECENTLY, a strong source of radioactive Cl^{36} was obtained from the Atomic Energy Commission Isotope Division at Oak Ridge. The specific activity of the chlorine was given as 0.0003 mc/mg which is high enough to permit an investigation of its β-spectrum. The new baffle system[1] of the solenoid magnetic

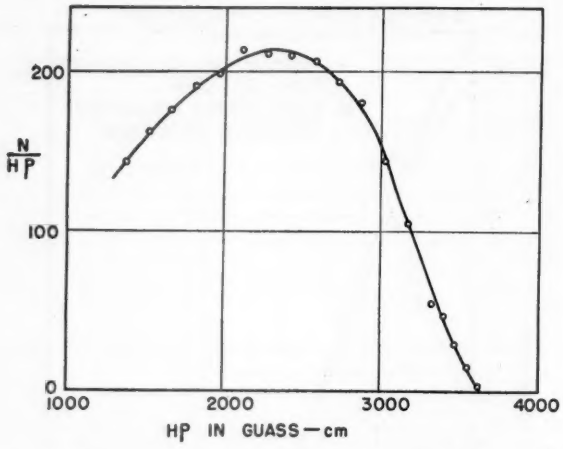

FIG. 1. Momentum distribution of Cl^{36} beta-spectrum. Thickness of the $LiCl^{36}$ source is around 0.3 mg/cm².

β-spectrometer of Columbia University designed according to the ring-focus principle offers a large transmission of the electron beam of 6 to 7 percent with a resolution of 4 percent, defined as the full width at half-maximum intensity. Under these favorable conditions, a Cl^{36} β-ray source of the order of magnitude of 0.01 μc will yield a reasonably accurate spectrum without special efforts. The radioactive chlorine is supplied by Oak Ridge in the form of an HCl solution. It is a by-product of the production of S^{35} ($Cl^{35}(n,p)S^{35}$). The HCl solution is neutralized to LiCl and chemical separation of S^{35} is carried out. Several LiCl sources varying from 300 μg/cm² to 1 mg/cm² were used in this investigation. Both collodion and Nylon window counters were used to cover the whole range. Figure 1 shows the momentum distribution curve of Cl^{36} β-spectrum. It is interesting to note that the maximum of the distribution is shifted more to the higher energy region than is expected from a symmetrical distribution curve. For an element of low atomic number such as Cl^{36}, the allowed beta-ray momentum distribution curve should be fairly symmetrical. The effects of the Coulomb correction or of the slowing down of electrons in the source itself would be to shift the maximum of the curve to the lower energy region. A superposition of two β-spectra would also cause a shift opposite to the one actually observed. Figure 2 shows the conventional Fermi plot of the Cl^{36} data treated as an allowed transition. The Fermi plot exhibits pronounced curvature toward the energy axis down to the very low energy region. This is the first shape of this kind ever observed among the forbidden spectra. The marked curvature between the upper energy limit down to ~180 kev was identical within the experimental uncertainty for sources varying in thickness from 300 μg/cm² to 1 mg/cm². The energy region below 180 kev was not extensively investigated as its true shape is probably distorted by the comparatively unfavorable source thickness used. A Cl^{36} source of higher specific activity would be preferred for this low energy region.

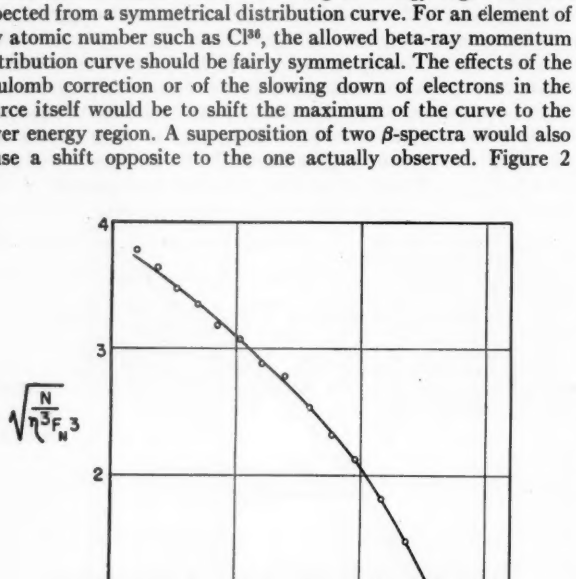

FIG. 2. Conventional Fermi plot for Cl^{36} beta-spectrum.

The spin of Cl^{36} was not known when the β-spectrum of Cl^{36} was first observed. Following the usual procedure of interpreting a forbidden shaped spectrum, a perfect fit (see Fig. 3) was found

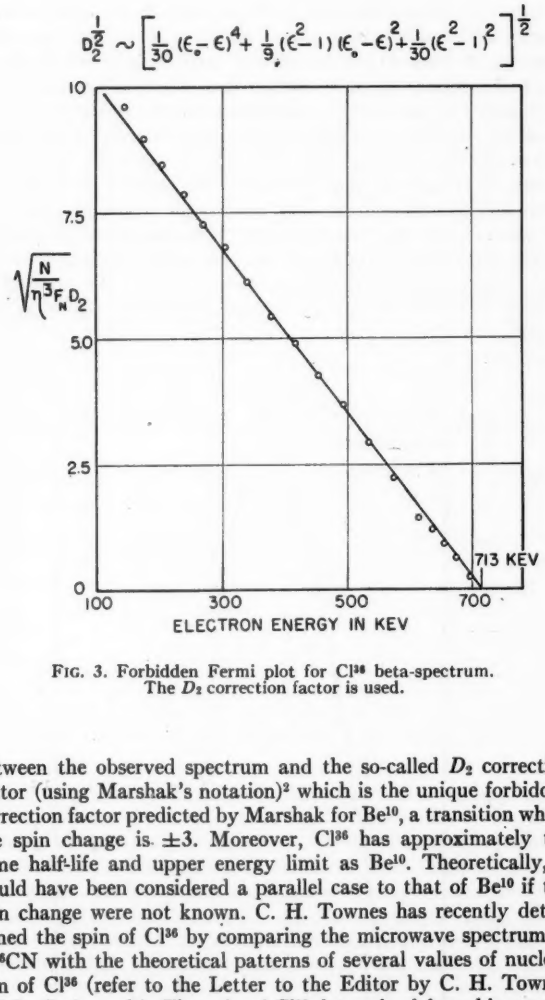

FIG. 3. Forbidden Fermi plot for Cl^{36} beta-spectrum. The D_2 correction factor is used.

between the observed spectrum and the so-called D_2 correction factor (using Marshak's notation)[2] which is the unique forbidden correction factor predicted by Marshak for Be^{10}, a transition where the spin change is ± 3. Moreover, Cl^{36} has approximately the same half-life and upper energy limit as Be^{10}. Theoretically, it would have been considered a parallel case to that of Be^{10} if the spin change were not known. C. H. Townes has recently determined the spin of Cl^{36} by comparing the microwave spectrum of $Cl^{36}CN$ with the theoretical patterns of several values of nuclear spin of Cl^{36} (refer to the Letter to the Editor by C. H. Townes and L. C. Aamodt). The spin of Cl^{36} determined from his experiments is definitely 2. Since argon 36 contains an even number of both neutrons and protons, its spin is probably zero. With a spin change of 2, and parity change either yes or no, a β-transition can be any one of the many transitions as allowed by the selection rules. The correction factors of all possible transitions were calculated and the ratios of the nuclear matrix elements were adjusted to try to fit the experimental spectrum. Refer to the letter following this one. But no fitting between the theoretical and experimental curves could be considered as satisfactory as that given by the D_2 factors or the correction factors from the linear combinations of S and T, V and A, and V and T interactions.

The authors wish to thank Professor J. R. Dunning, Dr. W. W. Havens, Jr., and Dr. L. J. Rainwater for their constant interest and encouragement. We are also indebted to Mrs. Zelda Droshnicop for her assistance with the numerical calculations.

* Work done under AEC Contract AT-30-1-Gen 72.
[1] L. Feldman and C. S. Wu, Phys. Rev. 76, 180 (1949).
[2] R. E. Marshak, Phys. Rev. 75, 513 (1949).

On the Spin and Beta-Spectrum of Cl^{36}*

C. LONGMIRE, C. S. WU, AND C. H. TOWNES
Pupin Physics Laboratories, Columbia University, New York, New York
July 18, 1949

THE results presented in the preceding three letters may be used to eliminate much of the arbitrariness concerning the type of interaction in β-ray theory.

The recent discoveries of β-spectra (Y^{91}, Y^{90}, Sr^{90}, Sr^{89}, and Cs^{137}) having shapes which agree with theoretical shapes for the first forbidden transitions ($\Delta S=\pm 2$, yes) on the tensor (T) or axial vector (A) interaction are fair evidence that part of the true interaction must be either T or A, and agree with the apparent requirement of Gamow-Teller selection rules. However, these spectra give no information as to whether the two interactions contain any scalar (S), polar vector (V), or pseudoscalar (P) parts.

When the spectrum of Cl^{36} was first measured, it was noticed that the shape agreed very well with the theoretical spectrum for the second forbidden transition (3→0, no), again for T or A. However, since an apparently reliable measurement of the spin of Cl^{36} gives the value 2, we have tried to fit the spectrum with theoretical spectra for the transition 2→0 (the final nucleus A^{36}, is even-even, and search indicated that there were no γ-rays). Table I shows the matrix elements which permit the transition 2→0 with the associated parity changes. The correction factors (by which the "allowed" number of electrons must be multiplied) for these matrix elements have been given by Konopinski and Uhlenbeck, and by Greuling. Figure 1 shows that no single one of these correction factors agree with the experiment. For $2V$ and $2T$, there is some arbitrariness in the correction factor, since the ratio of the two possible matrix elements in each case may be varied. Thus, (e.g.) for $2T$ one may take

$$a(|T_{ij}|^2 \text{ shape})+b(|A_{ij}|^2 \text{ shape})+c(T_{ij}A_{ij} \text{ shape}),$$

where a, b, and c are arbitrary real numbers except that

$$a\geqslant 0, \quad b\geqslant 0, \quad c\leqslant 2(ab)^{\frac{1}{2}}.$$

(There are, of course, upper limits to the magnitudes of the matrix elements, but we have not relied upon them.) Even with this arbitrariness, one cannot fit the data. The closest possible fit with $2T$ is shown in Fig. 1; $2V$ would give almost identical results. Thus, no single interaction fits the experimental data.

The next step was to try combinations of interactions. Such combinations give cross-terms with new shapes. Fierz[1] found that the cross-terms seriously modified the shape of even allowed spectra if S is combined with V, or T with A; such combinations are therefore ruled out. Also, $2P$ will not combine with other second forbidden matrix elements, since P has opposite parity requirements. Therefore, in fitting the spectrum, one need try only combinations of two interactions at a time, namely ($2S$, $2A$) ($2S$, $2T$) ($2V$, $2T$) ($2V$, $2A$) ($2P$, $3V$).

We have calculated the correction factors for the first four of these combinations, using Marshak's spherical harmonic method. This work was rather tedious, but an excellent check was had by comparing the quadratic terms with their values as already given by Konopinski and Uhlenbeck.

TABLE I. Matrix elements which permit the transition 2→0 with the associated parity changes.

Interaction	First forbidden	Second forbidden	Third forbidden
S		R_{ij} No	
V		R_{ij}, A_{ij} No	Yes
T	B_{ij} Yes	T_{ij}, A_{ij} No	
A	B_{ij} Yes	T_{ij} No	
P		$\gamma^5 R_{ij}$ Yes	

The results are shown in Fig. 2. The combinations ($2S$, $2T$) and ($2A$, $2V$) are almost identical and fit the data quite well. (In addition, these combinations will not alter spectra for Y^{91}, Y^{90}, Sr^{90}, Sr^{89}, and Cs^{137}.) For the combination (S, T) the data was best fitted by taking:

$$C_S R_{ij}=iC_T(0.175)A_{ij},$$
$$C_T T_{ij}=2iC_S R_{ij}.$$

It may be interesting to note that with this choice of the constants, the large $(\alpha Z/2\rho)^2$ and $2Z/\rho$ terms drop out of the correction factor; the result depends on the nuclear radius only through a factor multiplying the entire expression. For the ($2V$, $2T$) combination, we were able to fit the data only by arranging for an almost exact cancellation among all the ten curves available; we do not regard this fit as satisfactory, although we cannot rule out ($2V$, $2T$).

The last combination ($2P$, $3V$) was not worked, since ($2P$, $2V$) would not provide Gamow-Teller selection rules. In addition, the most reasonable guess is that the transition does not involve a change of parity, because the nucleons involved are presumably in D states.

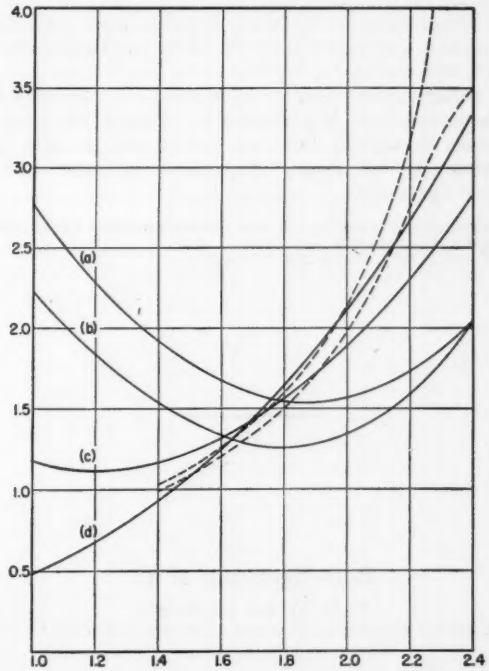

FIG. 1. Correction factors for Cl^{36} electrons. The area between the dashed curves represents the experimental data. Curve (a) is for $2T(T_{ij})$ and (approximately) $\frac{1}{2}2V(R_{ij})$; curve (b), same scale as (a), is for $2A(T_{ij})$ and (approximately) $\frac{1}{2}2S(R_{ij})$; curve (c) is for $2T(A_{ij})$ and $2V(A_{ij})$; curve (d) is best fit with $2T$, or $2V$ (approximately). The correction factor for $3V$ has roughly the same shape as (b). Ordinate scale is arbitrary.

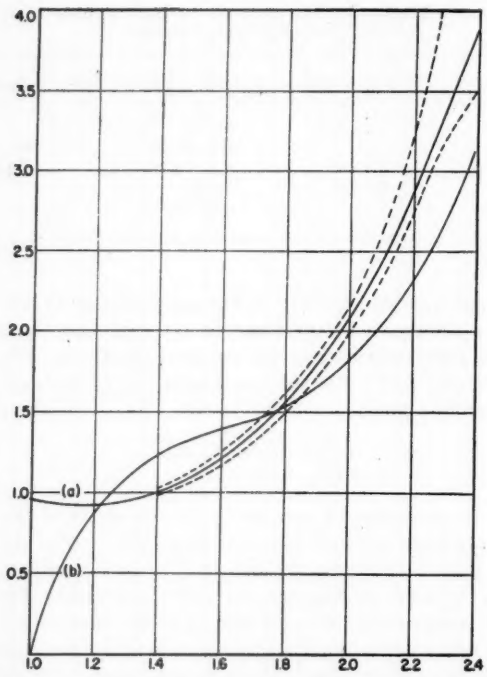

FIG. 2. Correction factors for Cl^{36} electrons. The area between the dashed curves represents the experimental data. Curve (*a*) is for the combination (2*S*, 2*T*), or (approximately) for the combination (2*A*, 2*V*). Curve (*b*) is the closest fit for the combination (2*S*, 2*A*).

Summing the results, it seems that the forbidden spectrum of Cl^{36} cannot be explained by any single type of interaction and spin change of two. It can be interpreted by three of the combinations of interactions; namely, (2*S*, 2*T*), (2*V*, 2*T*), (2*V*, 2*A*), but not by the combination (2*S*, 2*A*). Moreover, these combinations of interactions give agreement with the observed spectra for Y^{91}, Y^{90}, Sr^{90}, Sr^{89}, and Cs^{137}.

The authors are indebted to Professors R. E. Marshak, G. E. Uhlenbeck, and E. P. Wigner for their valuable discussions and suggestions throughout this investigation and to Mrs. Zelda Droshnicop for her greatly appreciated assistance with the numerical calculations.

* Work supported jointly by the AEC Contract Number AT-30-1-Gen 72, the Signal Corps and ONR.

[1] M. Fierz, Zeits. f. Physik **104**, 553 (1937).

Beta-Spectrum of Y^{91}

C. S. WU AND L. FELDMAN
Pupin Physics Laboratories, Columbia University, New York, New York
July 18, 1949

THE beta-spectrum of Cl^{36} [1] was observed to be radically different from allowed shape or the forbidden type exhibited by RaE. An attempt was made to fit it with an $(p^2+q^2)^{\frac{1}{2}}$ [2] correction factor. This unique correction factor is the same as the one for transitions of $\Delta J = \pm 2$, (yes) as in Y^{91}, Y^{90}, Sr^{89}, Sr^{90}, etc.

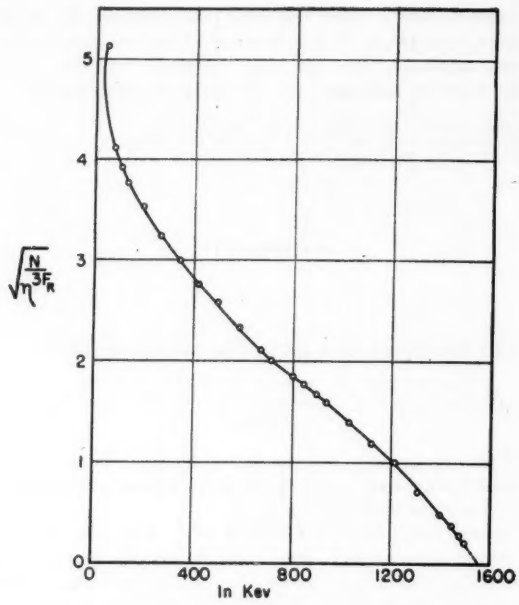

FIG. 1. Conventional Fermi plot for Y^{91} beta-spectrum.

However, the difference between the two curves is quite pronounced. In order to check the distinctiveness of these two forbidden shapes, the beta-spectrum of Y^{91} was investigated in the solenoid magnetic spectrometer under conditions identical with those for the investigation of Cl^{36}, except that the thickness of the Y^{91} source was less than 100 mg/cm². Baffle systems of resolution of 2.5 percent and 4 percent both were used and yielded identical results.

Figure 1 is a Fermi plot of the Y^{91} beta-spectrum treated as an allowed transition. This curve shows a definite inversion point around the energy region of 500 kev as expected from the $(p^2+q^2)^{\frac{1}{2}}$ correction factor, but the concavity of the curve at the high energy region is much less pronounced than in the case of Cl^{36}.

When each point of the curve in Fig. 1 is divided by its corresponding $(p^2+q^2)^{\frac{1}{2}}$ correction factor all the points thus calculated fit a straight line, as shown in Fig. 2, from the upper energy limit

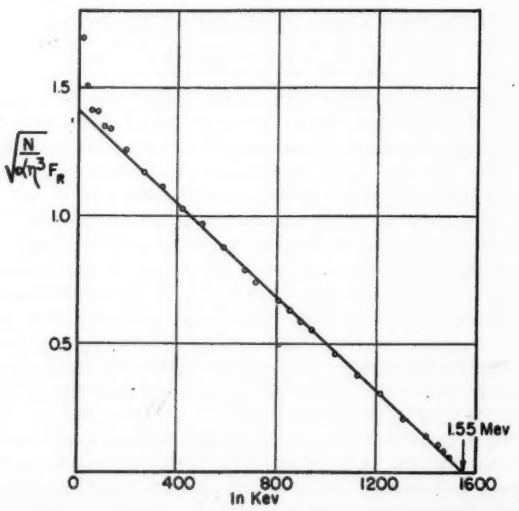

FIG. 2. Fermi plot of Y^{91} corrected by $(\alpha)^{\frac{1}{2}} \sim [(\epsilon^2-1)+(\epsilon_0-\epsilon)^2]^{\frac{1}{2}}$.

to about 200 kev. Even below 200 kev, the deviation from the straight line is very small. The upper energy limit determined from the forbidden Fermi plot is 1.55±0.01 Mev and is in good agreement with the result of Langer and Price.[3]

This investigation demonstrated the distinct difference between Cl^{36} and Y^{91} spectra. It is also interesting to observe that two completely different types of spectrometers and one spectrometer using two different resolutions can reproduce a forbidden spectrum such as that of Y^{91} in complete detail.[3]

The theoretical interpretation of the forbidden spectrum of Y^{91} is based on Feenberg and Hammack's analysis[4] of the shell structure in nuclei and was presented in detail in the Letter to the Editor by Langer and Price.[3] However, in view of the findings in the case of Cl^{36}, it would be highly desirable to have the spin of Y^{91} actually determined experimentally.

We wish to thank Dr. W. W. Havens, Jr., Dr. L. J. Rainwater, and Professor J. R. Dunning for the kind interest and valuable help rendered to us throughout this work. To Dr. C. Longmire, his enlightening discussions are deeply appreciated.

[1] C. S. Wu and L. Feldman, Phys. Rev. 76, 693 (1949).
[2] E. J. Konopinski and G. E. Uhlenbeck, Phys. Rev. 60, 308 (1941).
[3] L. M. Langer and H. C. Price, Jr., Phys. Rev. 75, 1109 (1949).
[4] E. Feenberg and K. C. Hammack, Phys. Rev. 75, 1877 (1949).

Interpretation of Beta-Spectra from Thick Sources*

L. FELDMAN AND C. S. WU
Pupin Physics Laboratories, Columbia University, New York, New York
July 18, 1949

IT has been demonstrated[1] in the past that the beta-spectrum of an allowed transition as obtained from a thick source shows definite deviation from the expected straight line on the Fermi plot. The effect of the source thickness is to shift the energy of some of the electrons to lower values and to give an increased (energy dependent) back scattering effect. Therefore, a thick source invariably distorts an allowed straight Fermi plot to a convex curve toward the energy axis; its exact curvature depending on the upper energy limit, shape of the spectrum and the thickness of the source.

By this reasoning, one would therefore conclude that when a spectrum obtained from a thick source shows an allowed distribution, it is most likely that the Fermi plot of the true distribution is actually a concave curve towards the energy axis, at least in the high energy region.

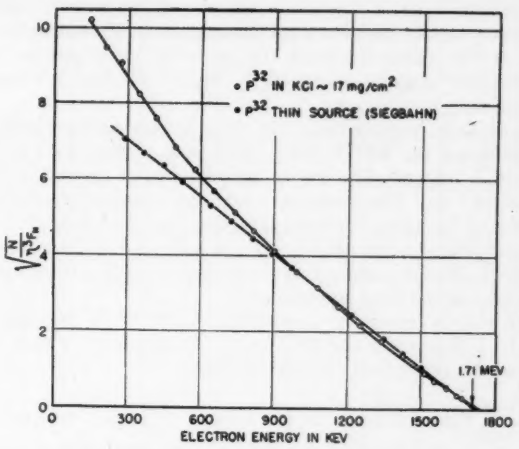

FIG. 2. Kurie plots of P^{32} from thin and thick sources. The thick source is in KCl of 17 mg/cm².

We have investigated the spectrum of three beta-emitters having radically different spectrum shapes, under exactly the same experimental conditions except for the thickness of the source. The same diluting material (KCl) was used in all cases to increase the thickness of the source.

In our investigation, the beta-spectra of Y^{91}, P^{32} and RaE were used. The upper energy limit of these three spectra are 1.55, 1.71 and 1.17 Mev respectively. Small amounts (less than 100 μg/cm²) of each of these radioactive substances are mixed thoroughly with inactive KCl to make sources of thickness around 15–20 mg/cm². While the thin source of Y^{91} gives a spectrum[2] according to the $(p^2+q^2)^1$ correction factors, a source of ~20 mg/cm² exhibits straight Fermi plot to 600 kev (Fig. 1). The P^{32} is known to show straight Fermi plot,[3] but a thick source of 17 mg/cm² distorted the spectrum to a convex curve (Fig. 2). The spectrum obtained from a thick source of RaE~22 mg/cm² also shows much greater curvature than that[4] of the thin sources (Fig. 3).

It is interesting to observe that the effect of the source thickness has definitely demonstrated the tendency to increase the second derivative of the conventional Fermi plot and therefore strongly supports the reasoning outlined above.

In view of this conclusion, it is interesting to reexamine the results recently reported by Alburger[5] on the beta-ray spectrum of K^{40}. The average thickness of the source used is around 18.5 mg/cm². The Fermi plot is straight from the upper energy limit 1.40 Mev to 450 kev. In view of the findings presented above, it seems reasonable to conclude that the true distribution of the

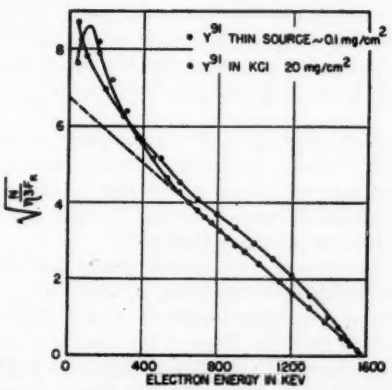

FIG. 1. Kurie plots of Y^{91} from thin and thick sources. The thin source is less than 0.1 mg/cm². The thick source is in KCl of 20 mg/cm².

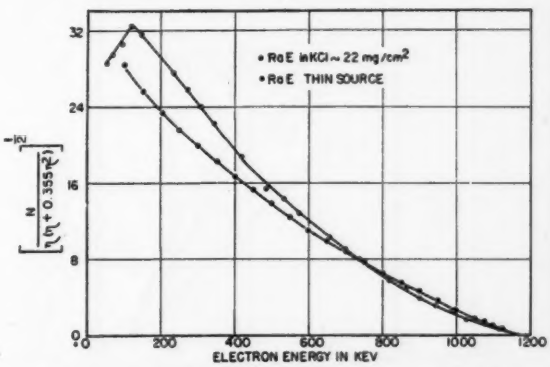

FIG. 3. Kurie plots of RaE from thin and thick sources. The thin source is in <0.1 mg/cm². The thick source is KCl of 22 mg/cm².

K^{40} beta-radiation is most likely not allowed but actually exhibits a concave curve which has been distorted to nearly a straight line due to the source thickness. In order to investigate its true distribution without distortion, a highly enriched K^{40} source (~50 percent) is desirable.

In all these investigations, the thick sources were prepared by precipitating the KCl inactive salts from alcohol on a plastic film of 2 mg/cm². The source area is circular in form with a radius of 1 cm. The resolution under this operating condition is calibrated by using internal conversion lines and is around 8–9 percent defined as the full width at the half-value of the maximum intensity. The thin sources were investigated with a resolution of 4 percent of the same spectrometer.

We wish to express our appreciation to Dr. W. W. Havens, Jr., Dr. L. J. Rainwater and Professor J. R. Dunning for their help and advice throughout this investigation.

* Work supported by the AEC, Contract Number AT-30-1-Gen 72.

[1] A. W. Tyler, Phys. Rev. **56**, 125 (1939); J. C. Lawson, Phys. Rev. **56**, 131 (1939).
[2] L. Langer and H. Price, Jr., Phys. Rev. **75**, 1109 (1949); C. S. Wu and L. Feldman, Phys. Rev. **76**, 696 (1949).
[3] K. Sieghahn, Phys. Rev. **70**, 127 (1946).
[4] L. Langer, Phys. Rev. **75**, 328 (1949); R. Morrissey and C. S. Wu, Phys. Rev. **75**, 1288 (1949).
[5] D. E. Alburger, Phys. Rev. **75**, 1442 (1949).

The Beta-Spectrum of Be^{10}*

C. S. Wu and L. Feldman
Pupin Physics Laboratories, Columbia University, New York, New York
July 18, 1949

RECENT determination[1] of the spin of the ground state of B^{10} of three units has aroused great interest concerning the energy distribution of the beta-ray spectrum from Be^{10}. According to Marshak's theoretical investigation,[2] the beta-spectrum of Be^{10} should be fitted by an unique D_2 spectrum (using Marshak's notation) which is very different from an allowed spectrum. On the other hand, Hughes[3] and his co-workers investigated the beta-spectrum of Be^{10} by absorption methods and found its distribution in disagreement with the D_2 shape but in agreement with the allowed spectrum within experimental error. If the allowed distribution interpreted from the absorption method is real, then the present theories of beta-decay will have to undergo serious revision.

Because of the extremely long life and small activation cross section, the specific activity of Be^{10} by the ordinary method of preparation is rather poor. When a thick beta-source is used in investigating its spectrum, the true distribution is inevitably distorted due to the effects of slowing down, absorption and back scattering of the electrons in the source itself. Nevertheless, the distortion of the Kurie plot due to source thickness follows a definite trend. This trend can be reasonably explained and interpreted as presented in the preceding letter[4] in the case of Y^{91}, P^{32} and RaE.

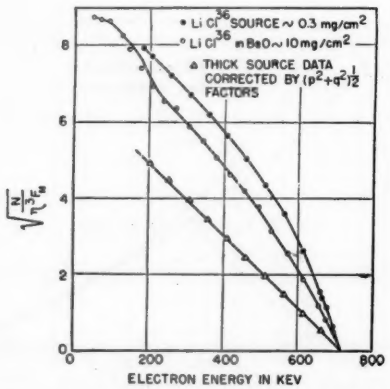

FIG. 1. Kurie plots of beta-spectra of Cl^{36} in thin and thick sources.

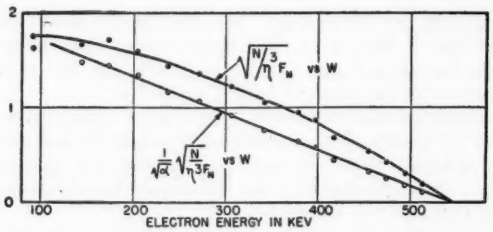

FIG. 2. The upper concave curve represents the conventional Fermi plot of Be^{10} beta-spectrum from a thick source of BeO of 12 mg/cm². The lower linear curve represents the forbidden Fermi plot after being corrected by the α-factor $[\alpha^2 \sim (p^2+q^2)^{\frac{1}{2}}]$.

The beta-spectrum of Be^{10} has an upper energy limit of around 550 kev, a comparative study of the spectra of Cl^{36} (713 kev), Be^{10} (550 kev) and Cu^{64} (ε^- 571 kev; ε^+ 657 kev) in thick BeO sources should shed some lights on the true distribution of the beta-spectrum from Be^{10}.

The active $Be^{10}O$ source used in this investigation was kindly loaned to us through the courtesy of Professor Stephens of the University of Pennsylvania. No more chemistry was done on the BeO after it was received. The specific activity of Be^{10} used in this investigation in only 3×10^{-4} μc/mg of BeO. A rather thick source of around 10 mg/cm² of an area of 3 cm² has to be used. For comparison, both the Cl^{36} and Cu^{64} are thoroughly mixed with inactive BeO to form beta-sources of around 10 mg/cm² of an area of 3 cm². The resolution under this operating condition is 8–9 percent.

Figure 1 shows the Kurie plots of Cl^{36} from thin and thick sources. The spectrum of Cl^{36} from thin source has been shown[5] to follow the unique D_2 spectrum closely, but the curvature of the Kurie plot from a thick source shows much less concave toward the energy axis as compared with that from a thin source. In fact, the Kurie plot is well matched by an α-spectrum[6] $[\alpha \sim (p^2+q^2)^{\frac{1}{2}}]$. Although the exact fitting of the α-correction factors is rather a chance coincidence, it does strongly demonstrate the general trend that a thick source invariably distorts a D_2 spectrum to a less concave curve such as an α-spectrum.

Figure 2 shows the Kurie plot of the beta-spectrum of Be^{10} from a BeO source of around 12 mg/cm². The upper energy limit of the spectrum is 550±10 kev. The Kurie plot is definitely concave toward the energy axis and is well fitted by an α-spectrum. By comparing the data on Be^{10} with the Kurie plot of Cl^{36} from a thick source, one is inclined to conclude that the true distribution of the Be^{10} beta-spectrum is more concave than an α-spectrum and may well be a D_2 spectrum as predicted theoretically.

We also investigated the Cu^{64} electron and positron spectra from a thick BeO source. In this case, the straight allowed shapes are both distorted to convex curves due to the finite source thickness. Therefore, it seems to us that the spectrum of Be^{10} can not be interpreted as an allowed spectrum.

Although this type of comparative studies does not give the detailed distribution of a spectrum, it does help to guide the interpretation of a spectrum obtained from a thick source. At least, it serves to limit the shape of the spectrum to only a few possible known shapes. It is needless to say that a highly enriched Be^{10} source would be most desirable for further investigation in this case.

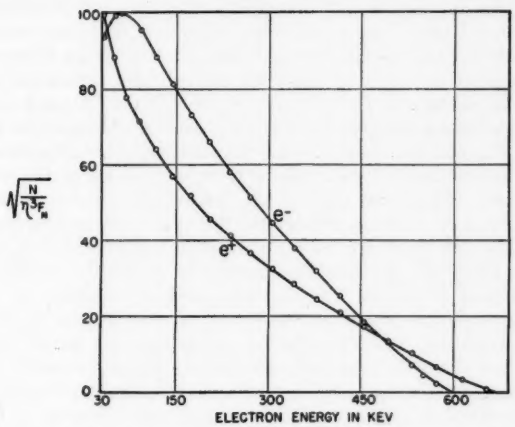

FIG. 3. Kurie plots of Cu^{64} electron and positron spectra from BeO of 11 mg/cm².

We wish to thank Professor W. E. Stephens for his kindness in sharing his radioactive $Be^{10}O$ with us. The constant interest and encouragement of Dr. L. J. Rainwater, Dr. W. W. Havens, Jr. and Professor J. R. Dunning are greatly appreciated.

* Work was supported by the AEC Contract Number AT-30-1-Gen 72.

[1] Gordy, Ring and Burg, Phys. Rev. **74**, 1191 (1948).
[2] R. E. Marshak, Phys. Rev. **75**, 513 (1949).
[3] Hughes, Eggler, and Huddleston, Phys. Rev. **75**, 515 (1949).
[4] L. Feldman and C. S. Wu, Phys. Rev. **76**, 697 (1949).
[5] C. S. Wu and L. Feldman, Phys. Rev. **76**, 693 (1949).
[6] E. J. Konopinski and G. E. Uhlenbeck, Phys. Rev. **60**, 308 (1944).

Photoelectric Disintegration of the Deuteron

J. S. LEVINGER
Cornell University, Ithaca, New York
July 18, 1949

THE cross section for the photoelectric disintegration of the deuteron has been calculated by many authors, with various assumptions as to the size, shape, and exchange character of the neutron-proton potential.[1] Recent measurements on neutron-proton scattering at high energies are consistent with a Yukawa potential of range $\mu^{-1}=1.18\times10^{-13}$ cm, about half exchange force, and half ordinary force.[2] The combination of half exchange and half ordinary force gives no force on states of odd orbital quantum number, thus greatly simplifying the calculation of the photoelectric cross section.

In this note we shall further simplify the calculation by assuming central forces, and by using an approximate wave function for the Yukawa potential.[3] The calculation is then very similar to the derivation of the Bethe-Peierls formula[4] for zero range of nuclear forces. We shall follow Bethe's notation.[4]

The cross section for the dipole term of the photoelectric effect is

$$\sigma=8\pi^3\nu|M_{OE}|^2/c, \tag{1}$$

where the electric dipole moment between ground state 0 and excited state E is

$$M_{OE}=\tfrac{1}{2}e\int U_{OZ}U_E d\tau. \tag{2}$$

For the ground state of the deuteron we use the wave function[3]

$$U_O=[\alpha\beta(\alpha+\beta)/2\pi(\alpha-\beta)^2]^{\frac{1}{2}}[\exp(-\alpha r)-\exp(-\beta r)]/r. \tag{3}$$

For the excited state, we use the free wave function

$$U_E=\frac{3^{\frac{1}{2}}}{2\pi\hbar}\cos\theta\left(\frac{M}{k}\right)^{\frac{1}{2}}\frac{1}{kr^2}(\sin kr-kr\cos kr). \tag{4}$$

In Eq. (1), $\alpha=(M\epsilon)^{\frac{1}{2}}/\hbar$, where ϵ = binding energy of the deuteron. We shall use $\beta/\alpha=5.47$[6] corresponding to $\mu^{-1}=1.18\times10^{-13}$ cm, or effective range[5] $b=2.5\times10^{-13}$ cm; k is the wave number of the emitted proton.

The only changes from the Bethe-Peierls derivation are in the wave function for the ground state. Our Eq. (3) as compared to Bethe's Eq. (44c)[4] $U_O=(\alpha/2\pi)^{\frac{1}{2}}\exp(-\alpha r)/r$ has the extra term $\exp(-\beta r)$ and a different normalization factor. Our 4 equations give us

$$\sigma=\left[\frac{\beta(\alpha+\beta)}{(\alpha-\beta)^2}\right]\left[1-\left(\frac{\alpha^2+k^2}{\beta^2+k^2}\right)^2\right]^2\left[\frac{8\pi}{3}\frac{e^2}{\hbar c}\frac{\hbar^2}{M}\frac{\epsilon^{\frac{1}{2}}E^{\frac{3}{2}}}{(E+\epsilon)^3}\right]$$
$$=20.4\left[1-\left(\frac{\gamma}{29+\gamma}\right)^2\right]^2(\gamma-1)^{\frac{1}{2}}\gamma^{-3}\text{ millibarns}. \tag{5}$$

Here γ = photon energy/binding energy of the deuteron.

The term $\beta(\alpha+\beta)/(\alpha-\beta)^2$ in Eq. (5) represents our use of a different normalizing factor[6] for the bound wave function from that used by Bethe. The term $[1-(\alpha^2+k^2)^2/(\beta^2+k^2)^2]^2=[1-\gamma^2/(29+\gamma)^2]^2$ represents the effect of the $\exp(-\beta r)$ term in the wave function for the ground state. This interference term, due to the finite range of nuclear forces, greatly reduces the cross section at high energies. For $\gamma\gg29$, the cross section varies as $\gamma^{-7/2}$, instead of as $\gamma^{-\frac{3}{2}}$ in the Bethe-Peierls formula. The interference effect is very small for $\gamma\ll29$, or photon energy much less than 65 Mev. The term $(8\pi/3)(e^2/\hbar c)(\hbar^2/M)[\epsilon^{\frac{1}{2}}E^{\frac{3}{2}}/(E+\epsilon)^3]$ in Eq. (5) is the Bethe-Peierls formula for zero range of nuclear forces.

In Fig. 1, we show the photoelectric cross section as a function of photon energy, both as given by Eq. (5), and as given by the Bethe-Peierls formula. This dipole term for the photoelectric cross section should be a fair approximation to the total photo-disintegration cross section between photon energies of about 6 Mev and about 100 Mev. At energies near the threshold for photo-disintegration the photomagnetic cross section is of importance.

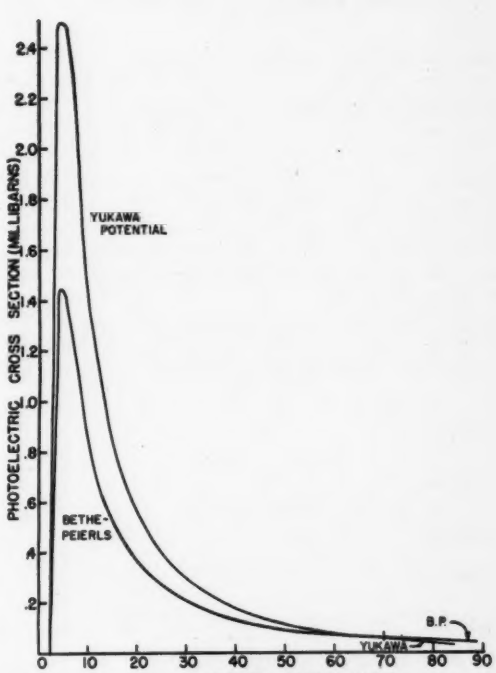

FIG. 1.

At high energies quadrupole and higher multipoles must be considered; and at very high energies relativistic and mesonic effects are important. Also our approximation of central forces may give poor results at moderately high energies.[7]

This work was done while the author was employed under an ONR contract.

[1] Latest calculation by Hu and Massey, Proc. Royal Soc. **196**, 135 (1949); they give references to literature. See also M. E. Rose and G. Goertzel, Phys. Rev. **72**, 749 (1947), for a calculation of high energy photo-effect for a square well potential.

[2] Hadley, Kelly, Leith, Segrè, Wiegand, and York, Phys. Rev. **75**, 351 (1949).

[3] L. Hulthen, Arkiv 28A, No. 5; L. Rosenfeld, *Nuclear Forces* (Interscience Publishers, New York, 1948), p. 76; G. Chew, Phys. Rev. **74**, 809 (1948). The wave function $[\exp(-\alpha r)-\exp(-\beta r)]/r$ is an exact solution of Hulthen's potential $V=-V_0\exp[-(\beta-\alpha)r]/(1-\exp[-(\beta-\alpha)r])$. Since Hulthen's potential is similar to the Yukawa potential $V=-V_0e^{-\mu r}/\mu r$, the exact solution to Hulthen's potential is a good approximate wave function for the Yukawa potential. Chew states that $[\exp(-\alpha r)-\exp(-\beta r)]/r$ agrees with the exact solution for the Yukawa potential to within 3 percent for all values of r. The value of β/α is adjusted by the variational method to give the greatest binding energy for a given μ; it varies with μ approximately as $(1+\mu/\alpha)$.

[4] H. A. Bethe and R. F. Bacher, Rev. Mod. Phys. **8**, 82 (1936), formula (16).

[5] Blatt and Jackson, Phys. Rev. **76**, 18 (1949).

[6] Using $\beta/\alpha=5.476$, as given by Chew, this term $=1.77$. This value should be compared with the factor $(1+\alpha b)=1.57$ given by Bethe in reference 4; or $1/(1-\alpha b)=2.35$ found by Bethe using the method of effective ranges ($\alpha=0.230\times10^{13}$ cm^{-1}, $b=2.5\times10^{-13}$ cm) for the increase in the low energy photoelectric cross section as compared with the Bethe-Peierls formula.

[7] Hu and Massey, reference 1, compare total cross sections for central *vs.* non-central forces. For a square well of range 2.62×10^{-13} cm, and symmetrical meson theory ($\frac{1}{2}$ exchange $+\frac{1}{2}$ ordinary force) non-central forces cause only a 4 percent decrease in the photoelectric cross section for photons of 17.5 Mev, but a 40 percent increase in the cross section for photons of 28.8 Mev.

Evidence on Nuclear Moments of Stable Ge and Si Isotopes from Microwave Spectra*

C. H. Townes, J. M. Mays, and B. P. Dailey
Columbia University, New York, New York
July 12, 1949

A previous letter[1] reported measurements on the $J=1\rightarrow2$ rotational transition of SiH_3Cl and the $J=2\rightarrow3$ transition of GeH_3Cl. Absorption lines due to the eight stable isotopes of Si and Ge were found, and a sizable nuclear quadrupole coupling noted in the case of Ge^{73}. An examination of hyperfine structure in the spectra of these molecules allows a determination of the spins of the even Ge isotopes, Ge^{70}, Ge^{72}, Ge^{74}, and Ge^{76} as zero, the spin of Ge^{73} as 9/2, and the nuclear quadrupole moment of Ge^{73} as $-0.21\pm0.10\times10^{-24}$ cm^2. Less certain evidence is obtained that the spins of the even isotopes of Si, Si^{28} and Si^{30}, are zero, and the spin of Si^{29} is $\frac{1}{2}$.

Hyperfine structure of the $J=2\rightarrow3$ transition of $Ge^{73}H_3Cl$ near 1 cm wave-length is rather complex because both Ge^{73} and the Cl nuclei show quadrupole coupling and spectra for $K=0$, 1, and 2 are superimposed. Consequently the considerably simpler transition $J=0\rightarrow1$ transition at 3.6 cm wave-length was studied in order to obtain the Ge^{73} spin and quadrupole coupling. Observed hyperfine structures were fitted by theoretically calculated patterns assuming the Ge^{73} has a spin of 9/2 and a quadrupole coupling constant $eqQ=-95\pm3$ mc. Coupling constants for Cl^{35} and Cl^{37}, obtained from measurements of hyperfine structure of lines due to GeH_3Cl molecules with even isotopes of Ge, were taken as -46 ± 1 and -36 ± 1 mc, respectively. These are consistent with and more accurate than the value -34 mc previously given for Cl^{37}. Both relative intensities and positions of lines were calculated.[2] The line positions agree well as shown in Fig. 1. The lowest frequency Cl^{35} line was partially obscured by the adjoining $Ge^{74}H_3Cl^{35}$ pattern and thus its measurement is somewhat uncertain. Although relative intensities could not be accurately measured, they agreed with theoretical expectations within experimental errors. Hyperfine patterns computed for spins of 3/2, 5/2, and 7/2 for several different assumed values of the Ge^{73} coupling constant show that these values of spin cannot give a reasonable fit of the observed patterns. Calculations for a spin of 11/2 have not yet been completed, but this value of spin is very improbable.

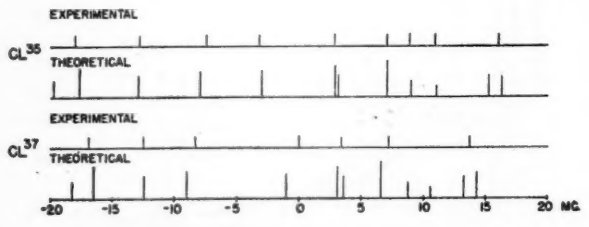

Fig. 1. Experimental and theoretical hyperfine structure patterns for $J=0\rightarrow1$ transition of $Ge^{73}H_3Cl^{35}$ and $Ge^{73}H_3Cl^{37}$. Origins correspond to position of unsplit transition, $Ge^{73}H_3Cl^{35}$ 8700 mc and $Ge^{73}H_3Cl^{37}$ 8389 mc.

It can be shown[3] that the value of q or $(\partial^2V/\partial z^2)$ for an atom in a molecule depends principally upon the number of "unbalanced" p electrons along the molecular axis. The GeCl bond has been assigned[1] 45 percent ionic and 15 percent double bond character. In the single and double bond structures the three p orbitals of the Ge atom are assumed to be equally populated by bonding electrons and thus not to contribute appreciably to q. The ionic structure $H_3Ge^+Cl^-$, however, corresponds to a deficiency of $0.75p$ electrons and thus produces a q equal to 0.34 of that for GeII. This latter quantity can be calculated[3] using the doublet separation $\Delta\nu=1768$ cm^{-1} [4] for GeII. The resulting value of the Ge^{73} nuclear quadrupole moment is $-0.21\pm0.10\times10^{-24}$ cm^2. The large limits of error allow for uncertainties in the GeH_3Cl structure, as well as errors in the approximations involved.

The spin of Ge^{73}, which has 41 neutrons and an even number of protons, is the same as the spin of Cb^{93} which has 41 protons and an even number of neutrons. Furthermore Ge^{73} is the lightest nucleus with a known spin as large as 9/2. These facts fit very well into the nuclear shell scheme proposed by Mayer,[5] where the first neutron or proton which goes into the $5g9/2$ shell is the 41st. The Ge^{73} spin can also fit into other[6,7] nuclear shell schemes.

No evidence of a quadrupole moment for the Ge^{70}, Ge^{72}, Ge^{74}, or Ge^{76} nuclei was observed. A rough calculation based on the observed line widths and the splitting to be expected for various spin values shows that the quadrupole moments of these nuclei must be less than 1/30 of the Ge^{73} quadrupole moment, or $Q=0.007^{-24}$ cm^2. This appears to be very good evidence that the spins of the even Ge isotopes are zero, since then no quadrupole moment is observable.

In the case of Si moments the spectrum of SiH_3Cl has so far given less clear-cut evidence. No hyperfine structure due to Si nuclei has been observed, which suggests the Si^{28} and Si^{30} spins are zero and the Si^{29} spin is $\frac{1}{2}$. It is possible, however, that these spins are not correct and that the nuclei have very small quadrupole coupling constants. It is hoped that projected work with a high resolution microwave spectrometer and with other silane derivatives will make certain the assignment of spins for the Si nuclei.

The authors are indebted to Mrs. Zelda Droshnicop for assistance in calculation of the theoretical hyperfine patterns.

* Work supported jointly by the Signal Corps and ONR.

[1] Dailey, Mays, and Townes, Phys. Rev. **76**, 136 (1949).
[2] J. Bardeen and C. H. Townes, Phys. Rev. **73**, 97 (1948).
[3] C. H. Townes and B. P. Dailey, J. Chem. Phys., in press.
[4] R. F. Bacher and S. Goudsmit, *Atomic Energy States* (McGraw-Hill Book Company, Inc., New York, 1932).
[5] Maria Goeppert Mayer, Phys. Rev. **75**, 1969 (1949).
[6] Eugene Feenberg and Kenyon C. Hammack, Phys. Rev. **75**, 1877 (1949).
[7] L. W. Nordheim, Phys. Rev. **75**, 1894 (1949).

The Specific Ionization of the Cosmic Radiation above the Atmosphere*

S. F. SINGER
Applied Physics Laboratory, Johns Hopkins University, Silver Spring, Maryland
July 18, 1949

A DIRECT measurement of the average primary specific ionization of the cosmic rays above the atmosphere has been conducted in order to gain more information about the nature of the primary radiation. The results presented are based on one rocket flight and are of preliminary character.

A counter telescope (Fig. 1) containing a low efficiency counter was installed in a V-2 rocket launched at the White Sands Proving Ground ($\lambda=41°$) on February 17, 1949. The low efficiency counter B' had an effective length of 14.5 cm, an effective diameter of 2.38 cm, and was filled with pure hydrogen to a pressure of 5 cm Hg; it required an external quenching circuit. The other counters in the telescope were constructed similarly, but filled with a standard mixture of argon and alcohol. Their measured efficiency was better than 99.3 percent. The following triple coincidences were telemetered: telescope counts (ABC), ($AB'C$), and guard counts (ACG). The solid angle of the telescope was covered by about 1 g/cm² of aluminum. The same telescope had been installed in an Aerobee rocket in November 1948 in a much "cleaner" environment but was transferred to the V-2 after postponement of the Aerobee firing.

The efficiency of a G-M counter is given by the well-known expression

$$\eta=1-\exp\{-(\text{prim. spec. ioniz.})\times(\text{path length through counter})\times(\text{counter pressure})\}.$$

This dependence of efficiency on primary specific ionization has been used in cosmic-ray investigations at low altitudes.[1-3] In the present experimental arrangement, the efficiency of counter B' for single particles is the ratio $ABB'C/ABC$.** At Silver Spring (altitude 120 m) and at White Sands (altitude 1200 m), the experimental efficiency was 0.585±0.019.*** The rocket spent 238 seconds on the high altitude cosmic-ray plateau (above 55 km).[4] The measured efficiency on the plateau was 0.689±0.027. The guard count correction in the high altitude case was about 40 percent; however, we believe that the shower protection was adequate since most of the material near the telescope was disposed at its side. Furthermore, with all guard counts subtracted out, the telescope counting rate yielded an average intensity above the atmosphere $j=0.10/\text{sec.}-\text{cm}^2-\text{steradian}$, in substantial agreement with previous measurements.[4] In any case, leaving in all shower counts did not appreciably affect the value for the high altitude efficiency. However, the following corrections need to be considered:

(i) A geometrical correction has to be made to the efficiency since the average path length through counter B' increases in going above the atmosphere, as the zenith angle distribution of the radiation changes from a $\cos^2\theta$ dependence to a more nearly isotropic distribution. This correction for our particular case is less than 0.02.

(ii) The knock-on correction amounts to about 0.01 but is already present in the low altitude value for efficiency.

(iii) The burst correction has been estimated from the transition curve of the primaries in aluminum[5] to be less than 0.01. We can safely assume that most bursts tripped a guard counter and have, therefore, been already subtracted.

On the basis of these considerations, the best value for the high altitude efficiency is 0.670±0.027, compared to a low altitude value of 0.585±0.019.

Insofar as we can believe in the validity of these results—and indeed it seems reasonable to do so in view of the arguments advanced earlier, in spite of the large shower correction—their interpretation leads to rather interesting consequences:

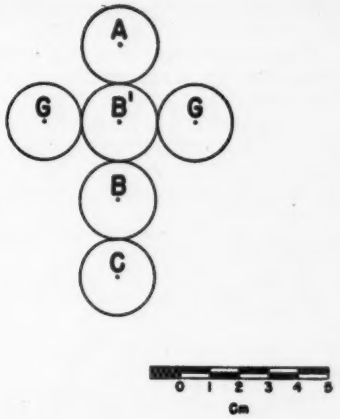

FIG. 1. Inefficient telescope.

(i) The principal conclusion one can draw is that the *ionizing radiation above the atmosphere* is predominantly *singly charged* and has an average primary specific ionization appreciably higher than minimum.

On the over-simplified assumption (see below) that the radiation above the atmosphere consists exclusively of primary rays, we can estimate from the theoretical geomagnetic cut-off and the observed latitude effect an average momentum for any assumed type of particle.

(ii) *The data are then in clear disagreement with the hypothesis of a pure electronic primary radiation.* Hereford[6] has demonstrated experimentally the rise in primary ionization for electrons of energy higher than 1.5 Mev. 10-Bev electrons should be detected with an efficiency of about 0.80 by our arrangement. It may be remarked that, aside from the general burden of other evidence against this hypothesis, there are the recent balloon cloud-chamber results of the Minnesota group that electrons do not represent more than 1 percent of the primary beam.[7]

(iii) *The data are not consistent with the assumption of a pure proton beam of primaries.* Since the primary ionization of a 10-Bev proton is about the same as the average sea level meson (about 1 B :v) there should have been no appreciable difference between low altitude and corrected high altitude values of efficiency.

We can finally proceed to examine the consequences of a mixture of particles in the primary radiation:

(iv) *For an assumed proton-electron mixture the data require the electron intensity to be 41+6 percent of the primary beam.* This possibility is excluded on other grounds, as under (ii).

(v) *For an assumed proton-alpha-particle mixture the data give an alpha-particle intensity of 20±8 percent.* This fraction is consistent with the estimate made by the Minnesota group based on cloud-chamber data at balloon altitudes.[8]

The data obtained in the present experiment do not furnish a basis for excluding more complex mixtures. More importantly, there is evidence that secondary radiation from the earth's upper atmosphere contributes significantly to the intensity observed above the atmosphere. Thus, it is more realistic to attribute the measured average specific ionization to a mixture of primary and secondary particles. The zenith angle dependence of the efficiency may make possible a separation of primary and secondary contributions. The subject is being pursued in further experiments

using different telescope arrangements and counters of different efficiencies.

At any rate, conclusion (i) is independent of detailed assumptions and may be regarded as the principal result of this preliminary work.

It is a pleasure to acknowledge my indebtedness to Dr. J. A. Van Allen in the planning and interpretation of the experiment and to Messrs. L. W. Fraser, R. S. Ostrander, B. J. Chaffee and D. W. Hamlin for technical assistance.

* This work was supported by the Navy Bureau of Ordnance under Contract NOrd 7386.

[1] W. E. Danforth and W. E. Ramsey, Phys. Rev. **49**, 854 (1936).
[2] M. G. E. Cosyns, Bull. Acad. Belg. **5**, 498 (1937).
[3] F. L. Hereford, Phys. Rev. **75**, 923 (1949).

** More precisely

$$\eta = \frac{(AB'C)\cdot(ABC) - (AB'C)\cdot(ABC)\cdot(ACG)}{[(AB'C)\cdot(ABC) - (AB'C)\cdot(ABC)\cdot(ACG)] + [(ABC) - (ABC)\cdot(ACG)]}.$$

*** All errors quoted are standard errors.

[4] Gangnes, Jenkins, and Van Allen, Phys. Rev. **75**, 57 (1949).
[5] Fraser, Ostrander, Van Allen, Echo Lake Conference (June 1949).
[6] F. L. Hereford, Phys. Rev. **74**, 579 (1948).
[7] E. P. Ney, Echo Lake Conference (June 1949).
[8] Freier, Lofgren, Ney, and Oppenheimer, Phys. Rev. **74**, 1818 (1948).

Spontaneous Neutron Emission from Uranium and Samarium

HERMAN YAGODA AND NATHAN KAPLAN
Laboratory of Physical Biology, Experimental Biology and Medicine Institute, National Institutes of Health, Bethesda, Maryland

May 13, 1949

EXPERIMENTS with 200-micron Ilford C2 plates show that about 15 mg of B^{10} and 2 mg of Li^6 can be incorporated per ml of emulsion after soaking for 2 hours in a solution containing 10 g of lithium borate and 3 ml of glycerine per 100 ml without causing appreciable loss in sensitivity for densely ionizing particles.[1,2] The high concentration of B^{10} and Li^6 nuclei, coupled with the large cross section for slow neutron capture, provide an exceedingly sensitive recording medium for the measurement of slow neutron flux. Thus, a detector plate situated 1.3 cm from a ~4-mc Po-Be disk enclosed in the paraffin cylinder described in Fig. 1 recorded a population of 8.38×10^3 tracks per ml of emulsion originating from the $B^{10}(n,\alpha)Li^7$ reaction after only a 15-min. exposure. Counts of proton recoil tracks show that the source emitted a total of 3.85×10^6 fast neutrons during the same interval, indicating the registration of 1 $(B^{10}+n)$-track per ml of emulsion per 460 ± 24 fast neutrons generated.

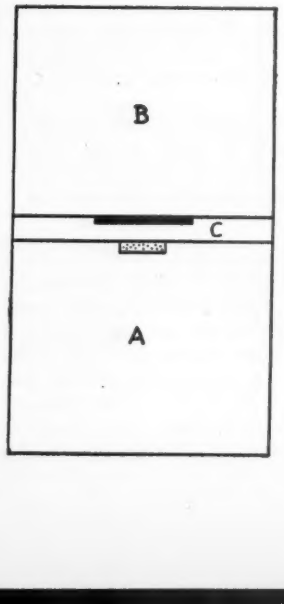

FIG. 1. Paraffin cylinder for slow neutron measurement. Two 1-lb. iron tobacco cans are each filled flush with 1450 g of molten paraffin. *A* serves as a sample holder and *B* as a neutron reflector. The plate holder *C* is a paraffin disk 16 mm thick carrying a 1×2-inch plate wrapped in paraffined-black paper. The cylindrical arrangement was chosen for convenience, and its efficiency has not been compared with a cubical or spherical disposition.

TABLE I. $(B^{10}+n)$-track counts from U and Sm.

Experiment	Exposure hours	Volume surveyed	Track count	Counts per ml per day
A—Blank	449	0.0155 ml	19	66
B—36.4 g U	449	0.0216	111	276
C—18.6 g Sm_2O_3 powder	449	0.0126	16	68
D—18.6 g Sm_2O_3 pellet	689	0.0080	21	92
E—20 g rare earth oxide pellet	689	0.0089	16	63
F—31.8 g U metal	689	0.0085	55	227

The calibration data suggest that by extending the exposure to 500 hours flux of the order of 2×10^{-6} slow neutron per sec. per cm² could be measured with an uncertainty less than 20 percent. As a test, three identical paraffin cylinders were assembled. *A*—containing paraffin only served as a control for cosmic-ray neutrons, *B*—contained a disk of uranium of approximately the same volume as the Po—Be source, and in *C*—a 25-ml cavity was filled with Sm_2O_3 powder. The units were stored in the subbasement of a sea level building in which prior measurements showed an evaporation rate of 0.29 star per ml per day.[8] The $(B^{10}+n)$ tracks were counted with a 98× fluorite objective and 7.5× compensating oculars. High magnification is essential in order to discern the short tracks of 6- to 7-micron length at all angles of incidence and to differentiate them from occasional rod-shaped artifacts in the gelatin. The alpha-triton tracks from the $Li^6(n,\alpha)H^3$ reaction were noted, but were too few in number to constitute a quantitative check for the boron slow neutron reaction.

The differential counts between *B* and *A* (Table I) indicate the emission of 2660 fast neutrons per day per g of U. If this be attributed to spontaneous fission of U^{238} with one neutron released per fission, the count corresponds to a half-life of 1.8×10^{15} yr. This is in good agreement with the value of $(2.5\pm0.6)10^{15}$ yr. observed by Maurer and Pose[4] employing a cylinder of uranium weighing 8.82 kg.

As a check on the reproducibility of the method, the experiment was repeated with a smaller mass of uranium and an extension of exposure time. Also the samarium oxide was compressed into a pellet of 10-ml volume to provide better geometry, and a similar pellet of mixed rare earth oxides from Norwegian gadolinite was employed as a monitor. This measurement showed the emission of 2370 fast neutrons per day per g of U corresponding to a half-life of 2.0×10^{15} yr. The deviation from the mean value of $(1.9\pm0.1)10^{15}$ yr. indicates a reproducibility of about 5 percent.

Compression of the samarium oxide powder increased the track count by 39 percent. If this be attributed to fast neutron emission from the samarium preparation, the half-life of the process is estimated at 10^{16} yr. In view of the small differential count and that neutrons may have originated by interaction of samarium alpha-particles with light nuclei impurities in our preparation, confirmation of the effect must be made using larger quantities of samarium specifically purified from beryllium, boron, and other elements with a large cross section for (α,n) interaction. The observed neutron production, if attributed to $Be^9(\alpha,n)C^{12}$, would necessitate the presence of about 1 percent BeO as impurity in the Sm_2O_3. This degree of contamination is improbable in a rare earth preparation isolated from monazite sand.

Estimate of cosmic-ray neutron contribution to observed neutron emission from uranium.—An analysis of one of the $Li_2B_4O_7$-loaded plates from the same batch employed in the measurements revealed a B^{10} concentration of 9.3×10^{20} atoms per ml. The plate exposed in the blank cylinder (*A*) exhibited 66 tracks per ml per day arising from the $B^{10}(n,\alpha)Li^7$ reaction. This affords a measure of the average cosmic-ray slow neutron flux in our laboratory during the period of the exposures:

$$\text{slow neutron flux} = \frac{66}{3525\times10^{-24}\times9.3\times10^{20}} = 20.1 \text{ cm}^{-2}/\text{day}.$$

This value permits an estimate of the induced fission rate assuming 2×10^{-24} cm² for the fission cross section of normal isotopic uranium. In a mass of 36.4 g of the metal the number of induced fissions per day will be approximately:

$$20.1\times9.25\times10^{22}\times2\times10^{-24}=3.71.$$

If each fission releases between 1 and 3 fast neutrons, about 4 to 11 fast neutrons will be generated in the test mass of uranium per day of exposure. Since the plate records one track for each 460 fast neutrons, the correction seems too small for consideration.

Neutron yield from Sm-alpha-particles interaction with Be⁹.— The average cross section of the $Be^9(\alpha,n)C^{12}$ reaction was approximated from the relationship $\sigma=\pi R^2\bar{G}$. The average Gamow factor $\bar{G}$ for alpha-particle energies between 2.1 and 0 Mev is estimated at 0.067 using the Mattauch and Fluegge tables.

$$\sigma=\pi(2\times10^{-13}Z^{\frac{1}{2}})^2\times0.067=0.021\times10^{-24}\text{ cm}^2.$$

The 18.6 g Sm_2O_3 emit:

$$18.6\times\frac{300}{348}\times89\times3600\times24=1.23\times10^8\text{ alpha-particles per day.}$$

The differential count between Experiments D and $E=92-63=29$ boron tracks per cc per day corresponds to the emission of $29\times460=13.3\times10^3$ fast neutrons. If these be attributed to (α,n) on Be^9, the number of the latter must be:

$$\frac{13.3\times10^3}{0.021\times10^{-24}\times1.23\times10^8}=5.16\times10^{21}\ Be^9\text{ atoms in 18.6 g of }Sm_2O_3$$

equivalent to a concentration of 0.37 percent Be or 1 percent BeO.

It is unlikely that our Sm_2O_3 pellet contains as much as 1 percent BeO. However, the additive effect of traces of Be, B, Mg, and Al may contribute in part to the observed neutron emission.

[1] H. Yagoda and N. Kaplan, Phys. Rev. **75**, 1328 (1949).
[2] H. Yagoda, *Radioactive Measurements with Nuclear Emulsions* (John Wiley and Sons, Inc., New York, 1949).
[3] Yagoda, Kaplan, and Conner, Phys. Rev. **76**, 171 (1949).
[4] W. Maurer and H. Pose, Zeits. f. Physik **121**, 285 (1943).

Nuclear Spin and Quadrupole Coupling of S^{35}*

VICTOR W. COHEN, W. S. KOSKI,** AND T. WENTINK, JR.
Brookhaven National Laboratory, Upton, Long Island, New York
July 22, 1949

THE rotational absorption transition $J=1\rightarrow2$ of carbonyl sulfide, OCS, containing S^{35} has been observed at 23461 ± 5 mc/sec. This frequency agrees with the value calculated from bond distances and isotopic masses given in the literature, and directly from interpolation of the published frequencies of $O^{16}C^{12}S^{32}$, $O^{16}C^{12}S^{33}$, $O^{16}C^{12}S^{34}$, and $O^{16}C^{12}S^{36}$.[1-3]

Complete resolution of the spectrum was not attained. However, sufficient resolution of groups of hyperfine components was realized to permit a determination of the spin of S^{35}, the sign of the quadrupole coupling and an estimate of the magnitude of the coupling constant.

A typical record of the $J=1\rightarrow2$ transition with its associated hyperfine and Stark structure is shown in Fig. 1. Immediately below the experimental curve is the theoretical hyperfine structure pattern expected for a nuclear spin of $\frac{3}{2}$. All Stark components give negative deflections due to the properties of the phase-sensitive detector used. Comparison of our experimental results with theoretical patterns that would be expected for higher nuclear spins[3] indicates that our results are not compatible with any spin value other than $\frac{3}{2}$. The frequency separation between the strong central components and the weaker components are 5.0 and 3.8 mc/sec., with the larger frequency separation on the high frequency side of the central components. The ratio of these

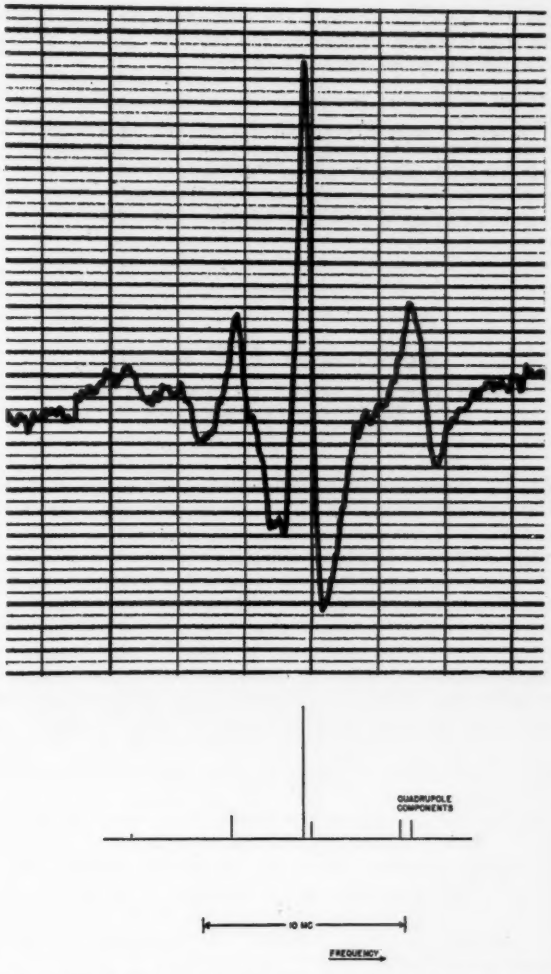

FIG. 1. *Above*: the experimental curve showing the partially resolved spectrum of COS^{35}. *Below*: the theoretical pattern calculated for a spin of 3/2 for S^{35}.

separations is approximately 1.3, which agrees within our experimental error with the theoretical value of 1.43 for a spin of $\frac{3}{2}$. Comparison of our curves obtained from S^{35} and S^{33} which also has a spin of $\frac{3}{2}$ show that the patterns are mirror images, indicating that the quadrupole moment in S^{35} is positive, or opposite in sign to that of S^{33}. We have estimated the electric quadrupole coupling constant eqQ[4,5] as $+20\pm4$ mc/sec. The corresponding value of S^{33} in OCS is -28.5 ± 0.7 mc/sec.

The principal error in the quadrupole interaction was due to the absolute error in determining the dispersion of the recorded spectrum. This was measured with a wave meter at many points, and compared with the observed, know spectra of COS^{33} and the Stark pattern of COS^{34}.

The detection system was a Stark modulation spectroscope operating at 100 kc/sec. and used a phase-sensitive or "lock-in" detector which drove an ink recorder. The 2K33 Klystron used was swept in frequency by a low speed mechanical drive operated by a synchronous motor. The absorption cell, cooled by dry ice, was 14 feet of K-band wave guide in which the Stark electrode was supported by quartz spacers.

The frequency of the central component was measured with a wave meter.

The OCS^{35} was prepared from H_2SO_4 obtained from Oak Ridge. The ratio of S^{35} to S^{32} at the time of use was about 0.004 and because of gaseous impurities the concentration of the OCS^{35}

used was about 0.1 percent. The pressure in the absorption cell was approximately 70 microns and the total number of COS^{35} molecules was of the order of 3×10^{16}.

* Work performed at Brookhaven National Laboratory under contract with the AEC.
** Permanent address: Chemistry Department, Johns Hopkins University, Baltimore, Maryland.
[1] Dakin, Good, and Coles, Phys. Rev. **71**, 640 (1947).
[2] Low and Townes, Phys. Rev. **75**, 529 (1949).
[3] Townes and Geschwind, Phys. Rev. **74**, 626 (1948).
[4] J. Bardeen and C. H. Townes, Phys. Rev. **73**, 97 (1948).
[5] B. T. Feld, Phys. Rev. **72**, 1116 (1947).

Confirmation of Cl^{39} Activity

R. N. H. Haslam, L. Katz, H. E. Johns, and H. J. Moody
Department of Physics, University of Saskatchewan, Saskatoon, Saskatchewan, Canada
July 15, 1949

In an attempt to discover the activity of the isotope A^{39}, pure argon was irradiated by the University of Saskatchewan betatron, at a pressure of 10 atmospheres and at a betatron energy of 23 Mev. The irradiated gas was then allowed to expand into a counting chamber surrounding a thin-walled beta-counter. An activity of half-life of about 110 minutes was present, due to A^{41}. It was noticed however, that the apparent half-life of this activity was always less than the expected 110 minutes[1] and varied considerably from run to run. It was surmised that this deviation was caused by the presence of an activity of somewhat similar half-life which might be due to A^{39} or Cl^{39}. A plug of glass wool saturated with antimony powder was introduced into the tube connecting the irradiation and counting chambers to absorb any chlorine present. The activity measured in the counting chamber, and thus due to the filtered argon, was then found to have a half-life of exactly 110 minutes, and the glass wool-antimony filter carried a β^--activity of 55.5 ± 0.2 minutes (curve *A*, Fig. 1). This is ascribed to the isotope Cl^{39} produced in the reaction $A^{40}(\gamma,p)Cl^{39}$. This isotope is listed in the table of Seaborg and Perlman[2] as having a half-life of one hour. This result is based on unpublished data.

A careful chemical separation confirmed the assignment of the activity to a chlorine isotope.

A greatly increased count is obtained by washing the glass wool filter and the inside of the brass irradiation chamber with dilute HCl, precipitating with $AgNO_3$ and filtering out the active AgCl precipitate. When this is done, there is evidence of a long period activity which may be due to A^{39} formed by the disintegration of Cl^{39} (curve *B*). At present the evidence is not conclusive and further work is in progress to test this assumption, and, if it is valid, to measure the half-life of A^{39}. However, it appears certain that the 4-minute activity ascribed to A^{39} in the above-mentioned table[2,3] and given an *F* rating does not occur. Such an activity would easily have been detected in our experiments, for in general the cross section for a (γ,n) reaction is greater than that for the (γ,p) reaction in the same isotope.

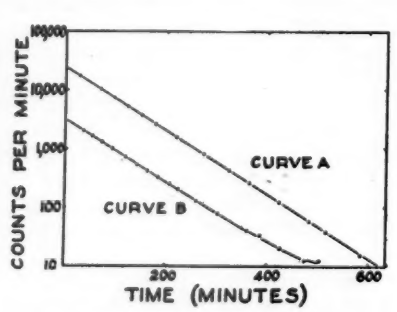

FIG. 1. Decay curve of Cl^{39}. Half-life—55,5 m,

Aluminum absorption curves show that if only one β^- is present in the Cl^{39} decay, it has an energy of 2.5 Mev. A more exact analysis is in progress to determine the disintegration scheme of this isotope.

The authors express their thanks to Dr. K. J. McCallum of the Chemistry Department of the University of Saskatchewan for performing the chemical separations and for much valuable advice. This work was carried out with the aid of a grant from the Canadian National Research Council whose assistance is gratefully acknowledged.

[1] A. H. Snell, Phys. Rev. **49**, 555 (1936).
[2] G. T. Seaborg and I. Perlman, Rev. Mod. Phys. **20**, 585 (1948).
[3] Pool, Cork, and Thornton, Phys. Rev. **52**, 239 (1937).

Detection of X-Ray Quanta by a Cadmium Sulphide Crystal Counter

Samuel G. Zizzo and Joseph B. Platt
University of Rochester, Rochester, New York
July 18, 1949

We have observed voltage pulses of the order of 50 μvolts from a CdS crystal irradiated with 0.5A x-rays.

A single crystal of CdS 7×10^{-3} cm thick with flat faces of 1 mm^2 area was prepared for use as a counter by applying Aquadag coatings to opposite faces and attaching a fine copper wire to each coating. The crystal was inserted in a metal tube so that it was located directly behind an end window of 5×10^{-4} cm silver foil. The other end of the tube was fastened to the can containing the first stage of amplification. One lead was attached to the input grid and the other to a 21 v battery which supplied the voltage across the crystal.

The circuit diagram of the first preamplifier is shown in Fig. 1. The voltage pulses were amplified further by a commercial pre-amplifier and linear amplifier[1] and the amplified pulses were fed to a discriminator and scaler.[2] The system was calibrated with step function input pulses over the region from 20 to 500 microvolts. The background level under operating conditions was such that approximately two counts/minute were observed of amplitude greater than 20 microvolts. The input capacity of the first stage plus crystal was found to be 8 $\mu\mu$f.

The crystal was inserted in a beam of x-rays from a molybdenum target x-ray tube operated at 20 ma and 45 kv peak voltage, self-rectified. Pulses were obtained of amplitudes up to 68 microvolts. Absorption curves were taken by inserting aluminum absorbers in the beam, and yielded the familiar concave upward plot for heterochromatic radiation. (Fig. 2.)

At higher intensities, corresponding to counting rates in excess of 10^6 per minute, a direct current through the crystal was detected. This current was measured by placing a microammeter in the plate lead to the first amplifier tube. The plate current was known as a function of grid voltage from a previous calibration, so a reading of the plate current yielded the grid voltage and hence the current through the grid resistor. A plot of change in crystal current *vs.* absorber thickness yielded a logarithmic plot of approximately the same slope as the one obtained by counting.

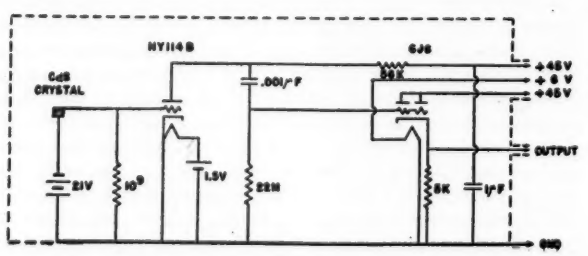

FIG. 1. First pre-amplifier schematic and counter.

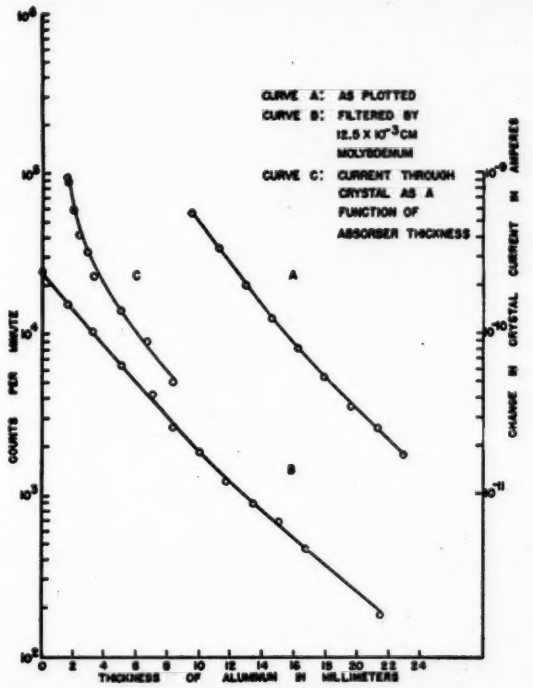
CURVE A: AS PLOTTED
CURVE B: FILTERED BY 12.5 X 10⁻³ CM MOLYBDENUM
CURVE C: CURRENT THROUGH CRYSTAL AS A FUNCTION OF ABSORBER THICKNESS
COUNTS PER MINUTE
CHANGE IN CRYSTAL CURRENT IN AMPERES
THICKNESS OF ALUMINUM IN MILLIMETERS

FIG. 2. Absorption curve for radiation from molybdenum target x-ray tube.

The effective wave-length, as determined from the slope of the absorption plot, varied from 0.60 to 0.35A as the aluminum filtering was increased from 8 mm to 22 mm. The crystal should be expected to detect higher energy radiation selectively because of the Cd absorption edge at 0.46A and because the larger quantum energies presumably give larger voltage pulses.

The absorption curve was taken by counting pulses of amplitude greater than 33 μvolts. By matching curves, one finds that 10^5 counts/minute correspond roughly to a current through the crystal of 6×10^{-11} ampere. About 1 percent of the observed current is therefore accounted for by the integrated charge per second from detectable pulses. It seems reasonable to assume many more pulses of amplitude less than 33 μvolts.

The maximum number of counts observed per second was also compared with an estimate of the number of quanta absorbed per

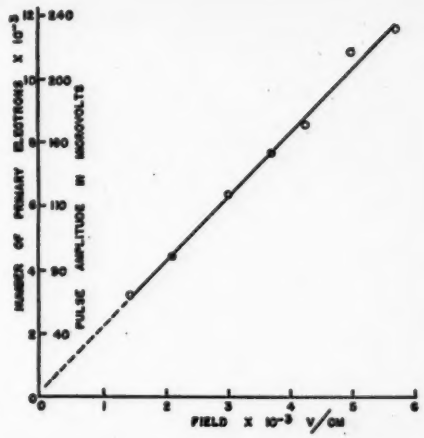

FIG. 3. Maximum amplitude of pulses from radium E beta-rays as a function of field strength in crystal. The two points at higher field strengths were taken while there was occasional evidence of breakdown in the crystal.

second in the crystal,[3] making allowance for pulses too small to be observed, and an order of magnitude agreement was obtained. These observations are consistent with the assumption that each voltage pulse was caused by the absorption of one x-ray quantum. The rise and fall time of the observed pulses were identical with the rise and fall times of the amplifier, i.e., 1 μsec. and 4 μsec.

Assuming the largest pulses (68 μvolts) to be due to 45 kev quanta, one obtains a value of 14 electron volts for the energy necessary to produce one conduction electron. A plot of maximum pulse amplitude *vs.* field strength in the crystal (Fig. 3), taken with RaE β-rays, shows, however, that at least for β-radiation the crystal is not saturated. The value of 14 electron volts may therefore be too high.

The cadmium sulphide crystal was prepared by Dr. Rudolph Frerichs.[4] We wish to thank Professor R. J. Cashman (Northwestern University), Director, Navy Contract N065 45068, and Dr. Bruce Billings of Baird Associates for making the crystal available to us.

This research was supported in part by the joint program of the ONR and the AEC.

[1] Atomic Instruments Models 204C and 205.
[2] R. Hofstadter, Nucleonics **4**, 22–25 (1949).
[3] Compton and Allison, *X-rays in Theory and Experiment* (D. Van Nostrand and Company, Inc., New York, 1936), Second Ed., p. 90.
[4] Rudolph Frerichs, Phys. Rev. **72**, 594 (1947).